SCHOOL OF ENGINEERING
CARDIFF UNIVERSITY

Serviceability Assessments of Masonry Arch Bridges

Lufang Wu

BSc, MSc

THESIS SUBMITTED TO CARDIFF UNIVERSITY IN CANDIDATURE FOR THE DEGREE OF DOCTOR OF PHILOSOPHY

AUGUST 2010

ProQuest LLC
789 East Eisenhower Parkway
P.O. Box 1346
Ann Arbor, MI 48106-1346

DECLARATION

This work has not previously been accepted in substance for any degree and is not being concurrently submitted in candidature for any degree.

Signed.....Lufang Wu.....(Lufang Wu)

Date.....16/09/2010.....

STATEMENT 1

This thesis is the result of my own investigations, except where otherwise stated. Other sources are acknowledged by provision of explicit references.

Signed.....Lufang Wu.....(Lufang Wu)

Date.....16/09/2010.....

STATEMENT 2

I hereby give consent for my thesis, if accepted, to be available for photocopying and for inter-library loan, and for the title and summary to be made available to outside organisations.

Signed.....Lufang Wu.....(Lufang Wu)

Date.....16/09/2010.....

To my parents
Zhenghe Wu and Xianfei Dai

AKNOWLEDGEMENTS

Firstly I would like to thank my supervisor Professor Tim Hughes for his great assistance, support and encouragement during the research work.

The facilities provided by the Cardiff School of Engineering, are hereby gratefully acknowledged.

Most importantly, I would like to thank my family, particularly my wife, my parents and my brother for their continued support and encouragement throughout the course of this research.

ABSTRACT

Masonry arch bridges continue to play an important role in the UK's transport infrastructure, forming a significant proportion of road, rail and waterway crossings. Many of these bridges are relatively old and are still in service in their original configuration.

Increasing vehicle loads and speeds have highlighted the need for reliable estimates of both ultimate and serviceability load levels. Most experimental work and assessment methods have so far been carried out under ultimate load. Only limited work has been undertaken to date on serviceability assessment methods, this project therefore aims to develop a systematic method to assess the serviceability load of masonry bridges under a series of different serviceability criteria.

A complex spreadsheet was developed as the main analytical tool for the serviceability assessment and was an encastered elastic analysis based on Castigliano's complementary energy method.

The geometric data from a large number of real masonry bridges data was gathered and analysed to develop suitable distribution statistics. Three independent serviceability criteria were then developed based on an attempt to replicate, on average, the existing assessment methods. These three criteria are stress, deflection and cracking depth.

Finally, a serviceability assessment method system was fully established within the developed spreadsheet.

INDEX

TABLES

FIGURES

NOTATION

A	sectional area
a	new elastic length of arch ring section after thinning or constant in regression function
a_1	tensile part of new elastic length of arch ring section after thinning
a_2	compressive part of new elastic length of arch ring section after thinning
b	new crack length or anti-thinning length of arch ring section or constant in regression function
b_t	total crack length before thinning or anti-thinning of arch ring section
c	new yield length or anti-thinning yield part length of arch ring section or constant in regression function
c_t	total yield length before thinning or anti-thinning of arch ring section
C_s	serviceability criterion
c_t	total compressive yield length of arch ring section
cw	carriageway width
d	current elastic length of the arch ring
d_o	original depth of the arch ring
d_s	incremental length along the arch
E	Young modulus of the material
E_a	modulus of arch

E_f	modulus of fill material
G	shear modulus
H	horizontal force
h	fill depth including the pavement at the crown
H_A	abutment horizontal force
H_L	live load thrust
I	arch ring inertia
K	shear coefficient
k	Constant coefficient
k_0	coefficient of earth pressure at rest
k_a	coefficient of active pressure
k_p	coefficient of passive pressure
k_s	modulus of subgrade reaction of the fill
L	span
lw	Lane width
M	bending moment
M_A	abutment moment
M_L	bending moment at the crown
M_n	new bending moment
n	nominal numbers of lane
P_s	serviceability load

P_u	ultimate load
R	correlation coefficient between the outcomes and their predicted values, or distance from the force
r	middle rise of arch bridge
r_q	quarter rise of arch bridge
S	shear force
SS_{err}	the sum of squared errors
SS_{tot}	the total sum of squares
T	thrust force
U	energy
V	vertical force
V_A	abutment vertical force
w	effective width
wl	width between loads
x_j	x coordinate of current element j
x_{jnew}	new x coordinate of current element j
y_j	y coordinate of current element j
y_{jnew}	new y coordinate of current element j
z	vertical distance from the force
γ	unit weight
δ	deflection
θ	distribution angle or arch element angle

ν	Poisson ratio of material
ρ_a	density of arch
ρ_f	density of fill
σ	stress in the material
σ_a	stress of arch
σ_b	Boussinesq load distribution stress
σ_c	masonry ultimate compressive stress
σ_e	equivalent stress
σ_h	horizontal stress
σ_{max}	maximum compressive stress
σ_{min}	minimum stress (tensile defined as negative)
σ_p	stress determined by load distribution by angle
σ_t	masonry ultimate tensile stress
σ_v	vertical stress
ϕ	angle of internal friction

1 Introduction

1.1 Background

Masonry arch bridges represent a significant part of the transport system around the world. There are about 40,000 masonry arch bridges in use in the UK, and the majority of them were built between the 17th and the 19th centuries.

The world's longest single span masonry arch bridge, Jiuxigou Bridge, was built in Sichuan, China, in 1972 with span, rise, and width of 116m, 14.5m, and 7.5m respectively. The ring thickness varies from 1.6m to 2.15m, this represents a substantial slender structure. The arch was built in random stonework and took only one year to complete.

Masonry arch bridges continue to play an important role in the UK's transport infrastructure, forming a significant proportion of road, rail and waterway crossings.

Many of these bridges are relatively old and are still in service in their original configuration. Increasing vehicle loads and speeds have highlighted the need for reliable estimates of both ultimate and serviceability load levels.

Most experimental work and the assessment methods so far developed, have been undertaken under ultimate loading conditions.

Little has been done to date on the development of serviceability assessment methods, this project aims to develop a systematic method to assess the serviceability load of masonry bridges under a series of different serviceability criteria.

Most current approaches to masonry arch bridge assessment are based on either a direct or on a factored, ultimate load analysis. Whilst from a safety perspective this approach provides a measure of confidence to bridge owners it fails to capture the more fundamental issue of progressive deterioration. With large numbers of masonry arch bridges, that still contribute significantly to the transport infrastructure, a serviceability approach is a more sustainable long term solution.

Ideally the development of a serviceability approach would be based on a detailed investigation of the longevity of the existing arch bridge stock when compared to the historic loading (if known) and a detailed elastic based analysis of

each structure. It is considered unlikely that records are sufficiently detailed for such a study. An alternative approach could be to use the same detailed elastic based analysis of each structure together with a detailed understanding of the long term mechanical/fatigue properties of the, as-constructed materials. This approach also requires the historic loading to predict the deterioration. Although this approach is being used it suffers from real difficulties in our understanding of the loads the materials actually endure and also our limited understanding of the actual material testing necessary to properly capture its long term deterioration.

The approach adopted in this project recognises these difficulties and the current dominance of the ultimate limit load approach to arch bridge assessment. It utilises a Castigliano thinning analysis to investigate stress, deformation and thinning (joint/crack opening) as serviceability parameters and seeks, in the first instance, to determine the limiting values as those parameters which would, on average, produce a similar overall system performance. That is, a bridge owner would get the same number of failures but now the criteria for failure would be service based. This approach allows different materials/geometries to be identified, as likely to result in premature failure, and it is considered that this more general information will really assist bridge owners in starting to classify the types of bridges that are more at risk. This approach would also provide the bedrock from which the earlier approaches suggested could be better developed.

1.2 Objectives

The particular objectives of this thesis were:

- To review existing methods related to the assessment of masonry arch bridges.
- To develop a suitable analytical tool for the serviceability assessment of masonry arch bridges that was transparent to the user and capable of user modification/development.
- To obtain reasonable geometric and material parameter values for masonry arch bridges for later numerical analysis, these parameters to be based on the distribution statistics from a bridge database.

- To study serviceability criteria affects on the assessment of masonry arch bridges and to develop suitable serviceability based assessment criteria.
- To assess a series of real masonry arch bridges using the serviceability criteria developed.

1.3 Layout

This thesis is divided into 8 chapters:

Chapter 1 contains the background, the aims of the research and finally outlines the contents of the thesis.

A fairly brief review of theoretical, experimental and serviceability work on arch bridges is presented in chapter 2. The analysis and assessment method are presented and then experimental works on masonry arch bridges is considered. The final section of this chapter covers serviceability related research on masonry arch bridges.

Chapter 3 describes the theory of the Castigliano elastic cracking model including yield. This includes forces and moments' solution, deflections, soil pressure, the load distribution, yield model, thinning models, equivalent elastic stress model of compressive yield stress model, and iterative solutions for thinning (that is joint/crack opening) and anti-thinning (that is joint/crack closing) models.

Chapter 4 details the development of the spreadsheet. The first section of this chapter includes the input data layout and explanation. It then detailed how to use these data and the theory developed in the last chapter to obtain the result, the development of each part of the spreadsheet is detailed. Finally, there is a description of the result data and result graphs.

Chapter 5 details the development of the statistics of masonry arch bridge geometric parameters. This includes the bridge database explanation, and the statistics of the parameters.

Chapter 6 contains the development of serviceability criteria. This chapter is the main part of the work. This includes the development of the three criteria based on stress, deflection and opening depth (that is the depth to which the joint/crack opens

under load). These three serviceability criteria are compared to ultimate load in order to obtain the compatibility between ultimate load and serviceability load and finally a systematic serviceability assessment method is established.

Chapter 7 presents the assessment of a number of experimental tested bridges. This includes description of the assessment method, comparison of ultimate load to the failure load, and the serviceability assessment of these bridges.

Chapter 8, the final chapter presents the main conclusions from the work and recommendations for further research.

2 Literature review

2.1 Introduction

Masonry structures have been used for centuries. They have excellent aesthetic appeal and long-term durability. Many of these historic masonry structures have survived for centuries[1].

Masonry arch bridges are perhaps the most important masonry structures. They are widely used, particularly in the railway and highway networks. Many of these bridges are relatively old and are being subjected to increasing demands in terms of vehicle size. Howe[2] believed that Chinese built the first arches. There are many very old arch bridges in China many of them are still in use.

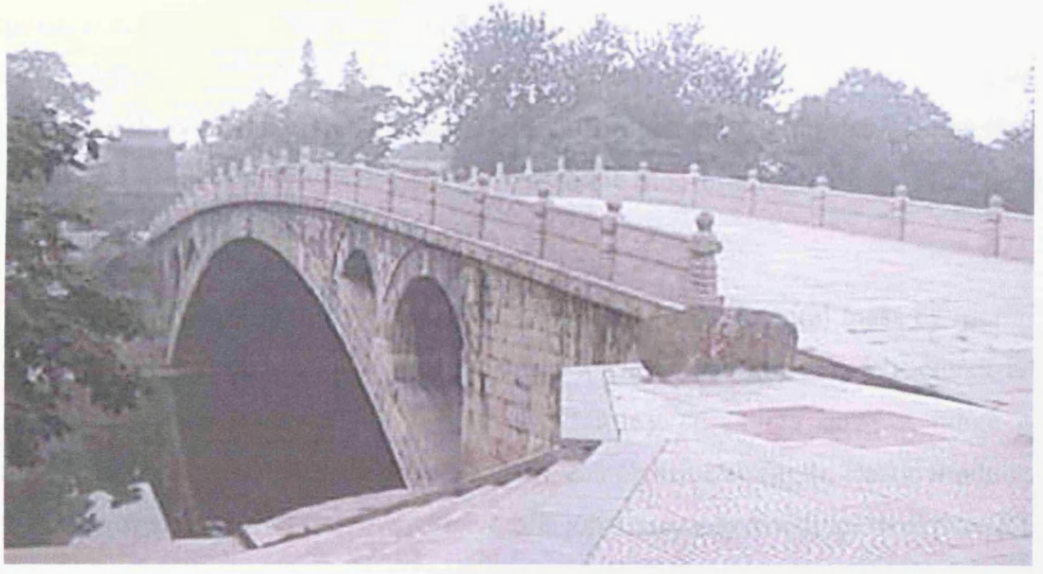

Figure 2.1 Zhaozhou Bridge (Completed between AD 595-605)

The Zhaozhou Bridge was constructed in the years 595-605 during the Sui Dynasty. It is the oldest standing bridge in China. The bridge also is one of the world's oldest open-spandrel segmental arch bridges. Zhaozhou Bridge is 50.82 metres long and 9.6 metres wide. It stands 7.3 metres tall and the span of the large stone arch in the middle measuring 37.37 metres, span to rise ratio of 5.25 and ring thickness 1.03m, is still in use[3,4] . Since it was built, it has withstood 10 floods, 8 battles, and many earthquakes including a 7.2 Richter scale earthquake in 1966. Yet,

the support structure remains intact and the bridge is still in use. Only the ornamental railings have been replaced every few hundred years.

Masonry arch bridges continue to play an important role in the UK's transport infrastructure, forming a significant proportion of road, rail and waterway crossings. Many of these bridges are relatively old and are still in service in their original configuration.

At present there are more than 100,000 road bridges in the UK and masonry arches bridge form an important part of them with some 40 percent of the total bridges. Durability and low maintenance of the masonry arch bridges, compared with the steel and concrete bridges as built today, provides a stimulus for the structural form to be reconsidered as a viable option. When maintenance is taken in the whole life analysis of these structures they are cheaper than other structures. Cox[5] has shown that the whole life cost of an 8 metre span arch, 120 years old, is about 12% less than the same arch in concrete or steel. For this reason some masonry bridges have recently been built, for instance Ellerbeck Bridge on Carleton road, Monk New Bridge in Lancashire, Prestwood Bridge near to the Stourbridge, Shinafoot Bridge in Tayside Region and Kimbolton Bridge[6].

Masonry work is stone or brick being bonded into an integral mass by mortar, it is often considered to be a homogeneous construction. Masonry structures are dominated by their composite behaviour. Masonry structures have a range of mechanical and geometric properties, such as compressive strength, elastic modulus, geometry of arch, thickness, orientation of the joint, masonry bonding, workmanship, curing, environment and age etc. Properties of the masonry unit and mortar also will affect the behaviour of the structure. Fatigue of the masonry and the masonry unit is become an important property in the serviceability of masonry arch bridges[7,8,9,10,11].

Masonry is a heterogeneous composite material made from structural units (bricks, stone and concrete blocks) bonded together with mortar[12,13]. In general masonry possesses significant compressive strength (up to around 30 N/mm^2) but negligible tensile strength. Numerous experimental and theoretical investigations[14,15] have indicated that the compressive strength of masonry depends upon many parameters including the compressive strength of the structural units and mortar, the

nature of the applied loading (uniform, linearly varying, concentrated) and environmental conditions (degree of saturation).

Structural elements of a typical masonry arch bridge are shown in Figure 2.2. The figure has the following elements resisting the loading.

1) The arch ring is the basic structure element of the arch.

2) The backfill transfers load from the pavement to the backfill and is then distributed on to the arch ring.

3) The backfill also resists the lateral movement of the arch under asymmetric loading. It has been shown that backfill material properties and interaction between arch and fill is a significant parameter in an arch load capacity[16,17].

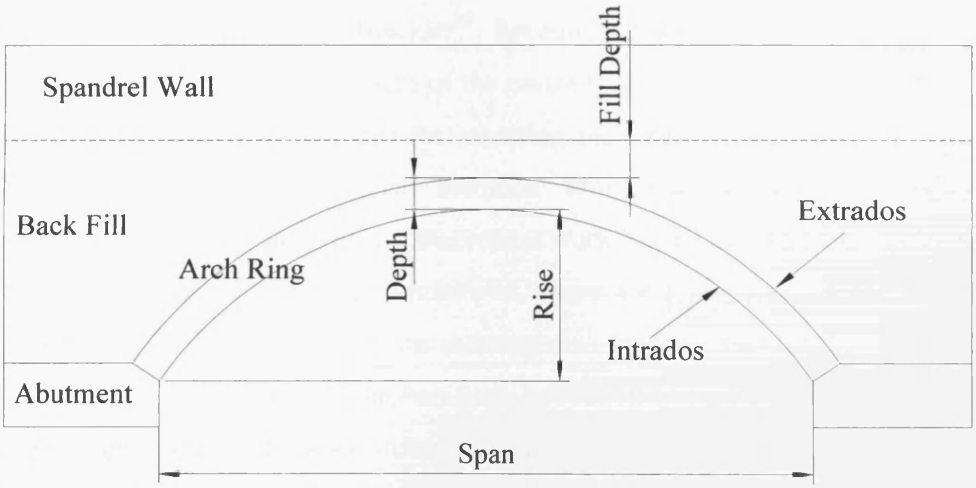

Figure 2.2 Typical masonry arch bridge

A series of models tests carried out by Royles[16] indicated that the spandrel and wing walls have a significant role in arch load bearing capacity. But traditionally the contribution of spandrel and wing walls to the stiffness and load capacity of the bridges is ignored[6]. This is because in many arch bridges the spandrel walls are detached from the barrel during their lifetime or because the connection cannot be guaranteed.

This literature review considers the analysis and assessment methods, experimental research including small scale testing and full scale testing, and finally reviews the serviceability assessment of masonry arch bridge including studying the masonry unit material fatigue, criteria developed in theoretical and experimental studies and criteria developed from empirical methods.

2.2 Analysis and assessment of masonry arch bridges

For many centuries masonry arch bridges were built by trial and error, using simple rules of thumb. Reviews of the early literature relating to the analysis and design of arch bridges by Heyman[18,19] and other researchers has been given by Crisfield and Page[6, 20]. A review on the UK masonry arch bridge assessment method was presented by Hughes and Blackler[21]. Recently, Orban[22] undertook a review for the UIC project, and the assessment of the masonry arch bridges was included. The three principal analytical methods for assessing the structural capacity of masonry arch bridges were semi-empirical methods, limit analysis methods and solid mechanics methods. In this section theoretical work on the analysis and assessment method of masonry arch bridge is reviewed. There are a few researchers who used statistic based methods to analyse the masonry arch bridges, such as Schueremans et al. [23,24] and Casas[25], they used probabilistic or reliability-based methods to analyse masonry arch bridges. However, these methods are not widely accepted, so they are not considered further in this review.

2.2.1 Semi-empirical methods

Pippard[26] and his co-workers made a significant contribution to the development of using elastic theory in arch assessments. A series of experiments on model arches was conducted and the voussoir arch was seen to behave elastically within certain limiting loads. It was demonstrated that the collapse of arch bridges was due to the formation of hinges as a result of cracking. In this context cracking is considered as the opening of a joint between masonry units and is variously called

thinning (the effective section becomes thinner), opening (the joint opens) or cracking (a crack within the masonry or the joint material opens). An expression relating the span, rise, and thickness and fill depth over the crown to vehicle type was derived. This simple approach to assess the arch bridge was used during the wartime. Pippard ignored the possibility of the formation of the third hinge and analysed the arch as a two-hinged structure. The analysis assumed the arch was parabolic, loaded with a point load P at the crown and the analysis was confined to the case where the rise at the quarter span was 0.75 times the rise at the half of the span. Pippard's actual and idealized arch are presented in Figure 2.3.

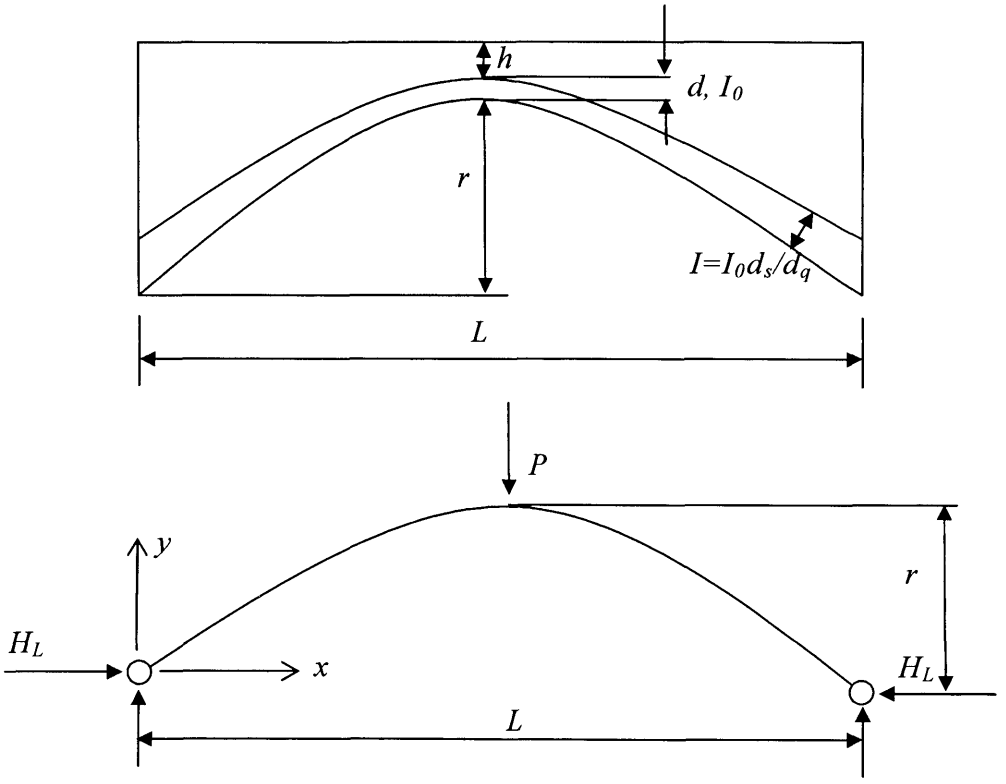

Figure 2.3 Pippard real and analytical arch models [26]

For the loading shown in Figure 2.3 the value of the live load thrust H_L and the corresponding value of bending moment at the crown M_L are given by Page[6] as detailed in equations (2.1) and (2.2).

$$H_L = \frac{25}{128}\left(\frac{PL}{r}\right) \tag{2.1}$$

$$M_L = -\frac{7}{128} PL \tag{2.2}$$

Where the negative sign indicates that the thrust line lies above the arch rib. The numerical values resulting from the above equations must be added on to the corresponding values for the self weight.

Pippard[26] used the moment equation to derive the rules of assessment. As larger and larger values of P are imposed at the crown of the bridge, the second part of the equation increased and it proceeds to develop tensile stresses. They argued that a less restrictive criterion might be based on the middle-half rule, in which the limiting value of P would be given by the solution of equation (2.3) and (2.4)

$$P_2 = \frac{\frac{256fhd}{L} + 128\gamma Lh\left(\frac{r}{28d} - \frac{1}{21} - \frac{h+d}{4r}\right)}{\left(\frac{25}{r} + \frac{42}{d}\right)} \tag{2.3}$$

$$f = \frac{H_L}{2dh} - \frac{3M_L}{hd^2} \tag{2.4}$$

Pippard then took a range of numerical examples and the full scale tests results made by the Building Research Station[27] and this resulted in the use of equation (2.3). For arches the soil cover h is generally less than 0.6m so the effective width would be less than the 1.2m. Thus the safe axle load P_A for a vehicle of normal arch width may be taken as given in equation (2.5)

$$P_A = 2\,P_2 \tag{2.5}$$

Pippard constructed tables for single span parabolic arches with span to rise ratio of 4, for unit weight of arch ring =21.65 kN/m^2 and with a limiting compressive stress= 1.39 N/mm^2.

Equation (2.3) was then modified by the Military Engineering Experimental Establishment (MEXE) to form a nomogram and this is still currently recommended by the Department of Transport[28,29]. In the current method the load-carrying capacity of the arch is assessed without the effect of the spandrel and wing walls, backfill,

abutment condition etc. and then the effect of these elements is added to the assessed load by use of additional factors. The provisional axle load can be calculated based on geometric data by using the equation (2.6) (or a nomogram). The loading is designated provisional because the value of the provisional axle load (*PAL*) is then modified by a series of modifying factors.

$$PAL = \frac{740(d+h)^2}{L^{1.3}} \tag{2.6}$$

This formula can be used for bridges with spans above 1.5m and up to 18m, (it may be too conservative for spans bigger than 12 m), and 0.25 m to 1.8 m for d+h.

The *PAL* is then modified by the following factors[28]:

1. Span/rise factor F_{sr}: deep arches are stronger than flat ones so it considers F_{sr} =1 for an arch with span/rise 4 or less, decreasing for span/rise ratios greater than 4.

2. Profile factor F_p: takes into account arch shape. The presumed ideal arch profile is parabolic and for this shape the rise a quarter-point is given by r_q /r=0.75. Any arch profile different to this is modified by this factor.

3. Material factor F_m: this factor takes into account the type of backfill and arch ring materials.

4. Joint factor F_j: by this factor the effect of joints (size and condition) and the quality of mortar is considered.

5. Condition factor F_{cM}: this factor is determined by the engineering judgement of the assessing engineer. Zero is applicable to a bridge in very poor condition with a lot of defects and 1 is suitable for an arch in good condition.

The modified axial load can be calculated by applying these factors to the previous calculated *PAL* as given in equation (2.7*)*.

Modified axle load $= F_{sr}\ F_p\ F_m\ F_j\ F_{cM}\ PAL$ (2.7)

This method is simple and easy to use for assessment engineers but is now considered by some to be conservative, particularly for longer spans[20]. The method also relies on the experienced judgement and may result in different arch capacities for a unique bridge with different engineers. The method also provides no information about stresses or deflections and it is difficult to incorporate the effects or strengthening other than through the condition factor.

2.2.2 Limit analysis methods

Before the development of modern mechanism method, there are some older analysis methods based on the thrust line and no tension model. Hughes[30] recently reviewed the analysis of William Edwards Bridge, by George Snell entitled 'Stability of Arches' and details a complex, no-tension masonry analysis from 1846.

Pippard[31, 32, 33] developed a tabulated mechanism method for assessment of a single span standard arch of parabolic profile with a span/rise ratio of 4. In Figure 2.4, according to his assumption the collapse load P can be found by statics and is directly related to the weight of the three blocks which have contributions from both the arch ring and the associated fill.

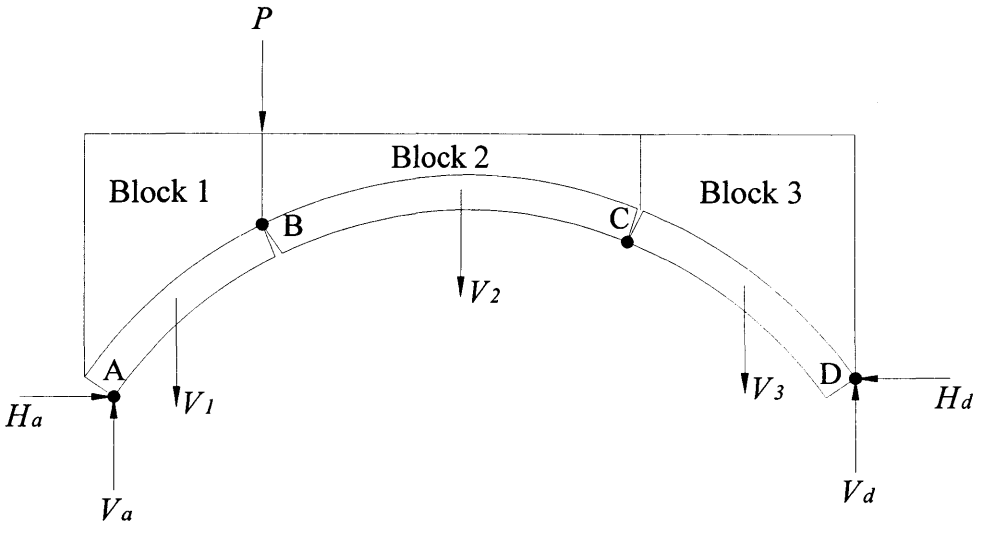

Figure 2.4 Mechanism with equilibrating forces [6]

Pippard assumed that the hinges form at B, under the load position, and at D at the far springing. The positions of the other two hinges had to be obtained by trial and error using a tabular method of computation.

He did not use the terminology plastic method directly in his mechanism analysis.

Heyman[18, 19] related his work to plasticity theory. According to Heyman's work if a thrust line can be found for the complete arch, which is in equilibrium with the external loading (including self weight), and which lies every where within the masonry of the arch ring, then the arch is safe[19]. He gave an approximate approach, which enabled a quick assessment to be made for the strength of a given bridge. The method computes the load necessary to just transform an arch into a hinged mechanism.

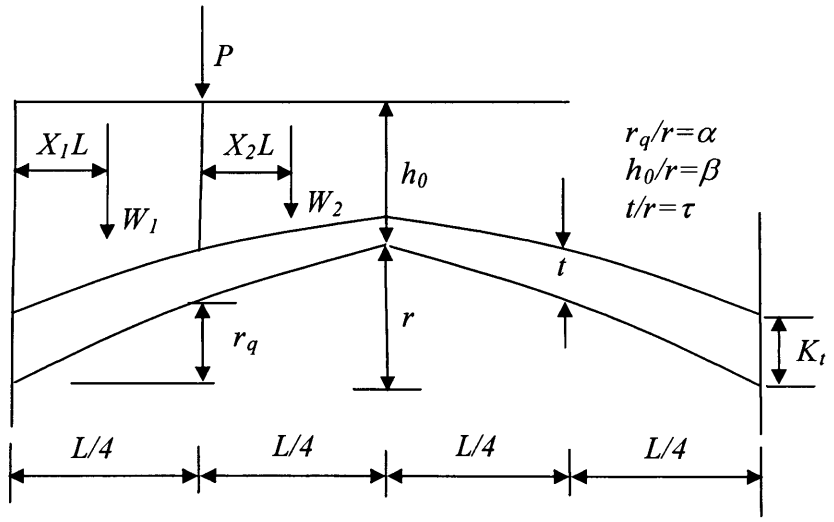

Figure 2.5 Heyman's arch model[19]

Figure 2.5 shows the dimension of arch assumed by Heyman. The road surface is assumed horizontal and the fill is assumed to have no strength and to transmit the live load P to the arch ring without any dispersion. The same unit weight is assumed for both the fill and ring. The calculations are normalised with respect to the rise at the crown (r) so that the parameter r_q/r gives a measure of the shape of the arch and h_0/r gives a measure of the depth of the bridge (fill depth + ring thickness) at the

crown and t/h_c is a measure of the vertical thickness of the arch ring at the quarter-span. Considering the statically determinate equations of equilibrium gives the value of live load that would just cause the arch to collapse[19] as given by equation (2.8).

$$P = 16\frac{W_2 X_2\left\{\alpha+\left(1-\frac{1}{4}k\right)\tau\right\}-\left(W_1 x_1+\frac{1}{4}W_2\right)\left[(1-\alpha)-\left(1+\frac{1}{4}k\right)\tau\right]}{(3-2\alpha)-(2+k)\tau} \tag{2.8}$$

A further approximation was made in order to get equation (2.8) into a form suitable for general application, the weights of W_1 and W_2 were calculated from trapezium, in which the intrados of the bridge has been replaced by a straight line. Then by considering the unit width of the arch equation (2.9) [19] was developed.

$$p = \frac{P}{\gamma L r/6} = \frac{(1+3\beta-\alpha)[\alpha+(1-\frac{1}{4}k)\tau]-(6+9\beta-5\alpha)[(1-\alpha)-(1+\frac{1}{4}k)\tau]}{(3-2\alpha)-(2+k)\tau} \tag{2.9}$$

The constant k, expressing the vertical thickness of the arch ring at the springing, is taken unity, so that equation (2.9) gives the intensity of the line load per unit width of bridge necessary to cause collapse, in terms of the α, β and τ. Harvey[34] used a similar mechanism method and developed a numerical model, named ARCHIE. This program is easy to use and widely used by engineers. Later, Sharman and Harvey[35] assessed a very special long span bridge Castle Bridge using this method.

Both Heyman[19] and Pippard[31] ignored the effect of fill on the load capacity of arches, but later work showed that fill can have a significant effect on the strength of an arch. Crisfield and Packham[36] developed a computer program based on the mechanism method. They used the virtual work equation instead of the static equilibrium equations and included two options for distributing the live load through the fill. The first procedure applied a uniform pressure over a horizontal line at the level of intersection with the arch directly under the load. The second had a linearly varying distribution between two points. They used the concept of passive resistance for considering the lateral earth pressure. Their study showed that the assumption of supporting lateral earth pressure may overestimate the collapse load by as much as

25% in some cases, particularly for arches where for deep arches where the soil resistance is important.

Livesley[37] developed a discrete rigid block method. This method was thought to be the first significant conceptual progress in the limit analysis of arch. The analysis of rigid-plastic structural frames was adapted to provide a formal procedure for finding the limit load of any structure formed from rigid blocks. He then applied this method specifically to the collapse analysis of masonry arch bridges[38]. Furthermore, he developed a computational model for this method applicable to three dimensional masonry structures[39].

The discrete rigid block method divides the structure into a large number of discrete rigid blocks connected by zero thickness and zero tensile strength joints and all the possible combinations of virtual displacements, compatible with the kinematic laws of the system of rigid blocks, are considered. All possible configurations are considered, and plastic theorems were applied. Gilbert et al.[40,41,42,43,44,45,46,47,48,49] developed this method step by step and into a commercial software package named RING and continue to improve the software, recently moving into the geotechnical area.

Gilbert and Melbourne[41] initially described a conceptually simple and computationally efficient method of determining the collapse load of structures comprising of a number of masonry blocks. The method uses the upper-bound theory of plasticity in conjunction with geometrical compatibility criteria to obtain solutions to problems involving single- and multi-span arches; well established rigorous linear programming methods were used to obtain solutions. Gilbert et al. [42, 44] and Melbourne et al. [43] applied this method to multi-ring arch bridges.

Finally, Gilbert[45] developed the software based on Livesley rigid block analysis method, is his first version of RING. This software's improvement was carried by Gilbert and Ahmed[46].

Further development of the rigid block method was a simple iterative procedure which involves the successive solution of linear programming sub-problems was developed by Gilbert et al. [47]. Using the procedure a specially modified

Mohr-Coulomb failure surface was adopted at each contact interface, with all failure surfaces updated at each iteration until a converged solution was obtained.

More recently the review of limit analysis and further development was undertaken[48]. Soil-arch interaction also was studied by the Particle Image Velocimetry (PIV) method[49]. This experimental technique has also been compared with rigid block method analysis of masonry arch bridges.

Other researchers also benefited significantly from application of the rigid block method. Begg and Fishwick[50] released the restriction of the associated flow rule, or normality condition, for masonry arches, including sliding shear failure. This aspect was also addressed by Baggio and Trovalusci[51] in a general formulation for rigid block limit analysis. It is noted that extending the formulation to non-associated flow, results in a nonlinear mathematical problem of a significantly larger size, in comparison with the lower size linear problem resulting from the classical theory. This method is also used by Orduna and Lourenco[52] to assess ancient masonry structures.

Hughes et al[53] used a spreadsheet as a tool to solve simple masonry arch limit analysis problems. This made use of the inbuilt 'Solver' optimising function within Microsoft Excel to indentify critical hinge and load positions.

Hughes[54] also used limit analysis method to analyse multi-span masonry arch bridges. He also created a function to fit the parameters with the ultimate load thus for the first time creating a geometry based MEXE type multispan factor.

Harvey and Maunder[55] also used a spreadsheet to analyse complex masonry structures using a thrust line.

Recently, Brencich, Gambarotta and Sterpi[56] studied the stochastic compressive strength effect to the load carrying capacity of masonry arches. This approach enhanced the Kinematic Limit Analysis (Mechanism Method).

2.2.3 Solid mechanics methods

Navier developed the straight line law for the distribution of pressure across a surface, and demonstrated that the resulting line of force had to be within the middle third of the surface to prevent tension arising[6]. Castigliano[57] developed an elastic method based on the minimum strain energy. He assumed that provided the line of pressure fell within the middle third of the arch ring, the ring would behave as a continuous elastic rib[6]. Based on Castigliano strain energy Bridle and Hughes[58] developed a commercial computer program known as CTAP[59,60]. It is capable of analysing all normal arch geometries under live loads. The arch ring is treated as linear elastic material fixed at both ends. The arch ring is discretised into a number of elements and loads are applied to the arch barrel and the resulting member forces determined. These are used to determine the stress state and deformations of the arch. The stresses are used to identify the tensile area. This area then has a reduced effective depth of ring. This iterative process is continued until the formation of incipient hinges as the live load increases. This method has an ability to calculate the deformation of arch under load. Soil/masonry interaction is also considered in this analysis by incorporating active and passive pressure around the arch extrados within the iterative process.

Garrity, Toropov and Turovtsev[61] developed an elastic-brittle model incorporating the non-linear stress-strain relations, failure criterion and unloading-reloading behaviour of masonry. An energy method was used in this model. This energy approach was used to analyse a large deflection problem of a beam with a slight initial deflection and subjected to a sinusoidal lateral load. The results showed that the energy method used was an effective and simple tool for stress or deformation analysis of masonry structures.

Molin and Roca[62,63] developed a method flexibility based method based on a nonlinear Generalized Matrix Formulation (GMF) for curved members with variable cross section. The Generalized Matrix Formulation (GMF) is an extension of a conventional matrix calculation for the study of masonry spatial structures composed of curved, spatial members with variable cross section. This method included non-linear material behaviour such as cracking in tension, yielding and crushing in

compression and second order equilibrium. Monlin et al. [64,65] specially used this method for the simulation of the service and ultimate response of open-spandrel masonry arch bridges. Energy methods and flexibility methods were discussed by Roca et al. [66]

Finite element analysis is a widely used and widely accepted modern method of analysis for masonry arch bridges. The first attempt of the application of the finite element method to masonry arch was carried out by Towler[67,68] and Sawko[69,70] who compared their own theoretical solutions with experimental results on a series of brickwork model arches, following a no-tension approach. In these works, the backfill was simply a dead load over the bridge, masonry and fill interaction was ignored. In further developments, a shear failure criterion was included allowing the numeric modelling of ring separation for the first time. Crisfield[71,72] showed that, in these circumstances, the finite element should give lower collapse loads than the mechanism method. Non-linear springs were used in the finite element models to simulate the lateral resistance of the backfill[73,74].

Choo et al. [75] used tapered beam elements in a two dimensional model, and in addition to neglecting regions of tensile stress, limited the magnitude of the compressive stress. Horizontal fill elements were used to represent the passive resistance of the soil around the masonry arch. This model resulted in reasonable predictions of the response of full-scale tests of masonry arch bridges.

Loo and Yang's[76] procedure incorporated several additional concepts into a two dimensional model. The material cracking in the arch ring was examined in more detail than in previous models. A von Mises failure envelope was developed for two dimensional stresses. Stress-strain curves for a variety of failure conditions were used to more accurately represent the state of stress in the arch ring during loading. Rather than distinguishing between individual properties the entire masonry/mortar assembly was modelled. The horizontal and vertical forces on the arch ring from the fill were found using a second finite-element model. This model replaced the arch /fill interface with a series of hinge supports. The horizontal and vertical reactions found at these supports from the weight of the fill elements were then applied to the standard finite element model of the arch ring.

Boothby et al. [77] and Fanning et al.[78] used an ANSYS commercial finite element package to study the service load response of masonry arch bridges. The masonry arch finite element mesh used five different element types to duplicate the behaviour of a system of discrete blocks under fill. Four-node isoparametric elements were used for the voussoirs, while gap and hinge elements provided the necessary mesh connectivity between blocks. Cable elements were used to simulate the resistance to arch movements provided by the fill and spring elements were placed at the abutments to control the amount of abutment spread under load. Joints between voussoirs in a masonry arch were able to transmit negligible tension and form hinges under eccentric thrust. This behaviour was modelled by a combination of gap and hinge elements at the intrados and the extrados. The gap elements transmit compression but not tension. The gap elements, however, do not allow rotation. This shortcoming was overcome by locating a hinge element immediately adjacent to each gap. Boothby et al.[79] and Fanning et al.[80] also studied the transverse behaviour of masonry arch bridges.

Three dimensional nonlinear finite element models of different masonry arch bridges were generated using a commercially finite element package (ANSYS) by Fanning and Boothby [78, 81]. The behaviour of the masonry was replicated by use of a solid element that can have its stiffness modified by the development of cracks and crushing. The fill material was modelled as a Drucker-Prager material, and the interface between the masonry and the fill was characterised as a frictional contact surface. The bridges were modelled under service loads, and the model results were compared to the results of a programme of a field testing of the structures. It is found that the assumption of the structure, implemented through a program of three dimensional nonlinear finite element analysis enable good predictions of the actual behaviour of a masonry arch bridge.

Three dimensional finite element method has also been widely used by a number of researchers[82,83,84]. Middleton et al. [82] undertook a three dimensional finite element analysis of masonry arch bridge using a homogenisation model. The result showed this approach was highly efficient and permits the accurate analysis of general three dimensional masonry structures. Frunzio et al.[83] used a three dimensional nonlinear finite element model to analyse a Roman arch bridge

including the spandrel walls and filling effects. More recently, Kaminski[84] developed a three dimensional finite element model based on predetermined planes of weakness. This model took into account transverse effects of the arch bridges.

Ng K.H et al[85] carried out finite element analysis using a commercial finite element package. Three full-scale bridges collapse tests were modelled and the results compare with available field test data. Comparisons were also made with results obtained from other arch bridge assessment methods. Eight–noded quadrilateral elements were used to model the arch, backfill and extrados interface. The behaviour of backfill and interface elements was elasto-plastic with failure defined by Mohr-Coulomb yield criterion. The arch was simulated by a stress-dependent von Mises constitutive law enabling different tensile and compressive material to be specified.

The features of a non-linear finite element approach suitable for the progressive failure analysis of masonry arch bridges are summarised by Loo[86]. According to his study from various properties of materials, only the masonry tensile strength and the strain softening parameter N have a significant influence on the failure behaviour of the arch bridge. Based on the collapse load result of five full-scale bridges tested in Britain, a comparative study was carried out by him and the best values for these parameters was suggested for both brick and stone bridge. For the cracking and failure analysis of the arch rib, the masonry can be modelled as a strain softening material and Loo was proposed a stress-strain relationship for the masonry. At a given point of masonry arch, when the state of stress reaches a certain value, there are three possible modes of local failure:

1. Cracking in both principal stress directions. This occurs when the state of stress is of the biaxial tension-tension type and both the tensile principal stresses are beyond the tensile–failure envelope. In this situation the material loses its tensile strength completely.

2. Cracking in one direction occurs when the state of stress is of the tension-compression type and a principle stress exceeds the limiting value prescribed by the tensile –failure surface.

3. Crushing. The crushing occurs when the state of stress is biaxial compression-compression and the stress level is beyond the simplified Von miss failure surface.

Using the above assumption a finite element programme was developed by Loo and calibrated based on the five full-scale test results. From this calibrated study he concluded that for a good estimate of the ultimate strength of a stone arch bridge, the masonry tensile strength may assume a value of 1.6MPa and the strain softening parameter N=12. The recommended values for brickwork arches are 0.3 and 4 respectively. These values to be used in conjunction with the experimental values of E_0 and s_c for the stones or bricks, as appropriate. Since the collapse load computed using the proposed analysis is rather insensitive to E_0 and s_c, their estimated values may also be acceptable in the absence of experimental data.

Brencich, Francesco and Gambarotta[87,88,89,90,91] developed a non-linear elasto-plastic collapse analysis method to analyse multi-span masonry arch bridge. This method assumes masonry as a no tensile resistant material, with perfect elasto-plastic response in compression, and the algorithm is implemented by standard programming of a commercial finite element code. They[89] found the elasto-plastic response of masonry has a significant effect on the limit load of both shallow and deep arches.

Cavicchi and Gambarotta[92] studied the contribution of arch fill interaction to the load carrying capacity of masonry arch bridge by a two-dimensional statically admissible finite element model and a numerical procedure.

Hughes and Baker[93] developed a macro finite element model specially to deal with masonry arch behaviour.

Sicilia et al. [94,95,96,97,98] used a homogenised three dimensional nonlinear finite element model to analyse the centrifuge model of William Edwards Bridge at Pontypridd.

Betti et al. [99] developed two finite element models both with fill interaction. The first model the geometry of the arch was divided into a number of unilateral

contact interfaces which simulate potential cracks. The second model was a two dimensional finite element model. When tensile stress appeared, the corresponding elements were replaced by nonlinear gap elements which represent cracks. The results showed the first model was the best model to predict the ultimate load reliably.

The finite element has been widely used in a number of famous long span masonry arch bridges. Chiorino et al [100] analysed a 50m span bridge named Mosca's Bridge. The finite element method has also been widely used in bridge testing analysis. Oliveira et al. [101] used a finite element model to analyse a limestone masonry bridge located in Leiria, Portugal. The load test procedure was simulated use this model.

Cucchiara et al.[102] developed a numerical model of masonry arches with interfaces. The model was applied and the results showed the finite element model developed with a code implemented with the interface law agreed with the experimental data.

Dede and Ural[103] developed a finite element computer program in MATLAB code, which can analyse masonry structures.

The finite element was also used to study the soil interaction in masonry arch bridges. Wang and Melbourne [104] undertook two models to understand the soil interaction in masonry arch bridges. The simple model was mainly used to get the parameters within the service loading range. The full bridge model was created to predict the failure of the same corresponding experiment. The result showed that the relative stiffness of the arch and the soil was a very important factor and the model was very sensitive to the material properties like density, cohesion of soil, the internal angle of friction etc.

Shin and Pande[105] developed an intelligent finite element method, this method introduced artificial intelligence in to the finite element codes used for load-deformation analysis of masonry structures.

Lemos[106,107] studied the masonry structures using the Discrete Element Method(DEM). This method models structures composed of multiple blocks or

particles using a discontinuous series of individual blocks. Two dimensional and three dimensional numerical models based on DEM were used to study the carrying capacity of a masonry arch bridge[106]. Lemos[107] also applied this method to study the seismic behaviour of stone masonry arches.

More recently, Rouxinol, Providencia and Lemos[108] applied DEM to the analysis of the loading capacity of Bridgemill Bridge one of the arches tested in the UK in the early 90s.

2.3 Experimental work on arch bridges

The span, rise, width, arch shape including distortions, arch thickness, depth of fill, arch material including defects, fill material including surface, quality of mortar, thickness of spandrel and wing walls, degree of bond between arch and spandrel walls, strength and stiffness of foundations, and applied load including its position, form and distribution through the fill and surfacing all affects the capacity of an arch. So there was no possibility that the full scale experimental works could include all of these parameters, and so test programs tend to focus on some of these variations. Literature reviews have shown a lot of experimental work on determining the effect of one or some of these parameters on the load capacity and assessment of arch bridges. Some of these experiments were carried out on real arches (most of them redundant bridges), some on full scale models, built in a controlled condition in labs and some carried out on small scale models. An overview of experimental masonry arch bridge research in UK was presented by Melbourne[103]. In this section, a brief review on experimental works on arch bridges is presented.

2.3.1 Load test on full-scale bridges

The use of load testing to understand the behaviour and assessment of arch bridge is well known. Davey[27] at the Building Research Station in Britain carried out a early series of serviceability and failure load tests on real arch bridges. In his failure tests he observed the significant effect of backfill on bridge capacity. For

instance he observed for one test the collapse load was 2.5 times higher in the presence of the fill than in its absence.

Chettoe and Henderson[110] carried out elastic tests on 13 real bridges in Britain. The maximum applied load was limited to 90 tonne to avoid any damages. All bridges were in a good condition. The load deflection measurements were elastic, and they concluded that the behaviour of bridges were elastic under the test conditions. A comprehensive review on load tests on arch bridges was presented by Page[6]. He identified 13 tests on full-scale bridges and 77 load tests on model scale bridges.

A number of tests have been carried out under the direction of the Transport Research Laboratory (TRL) to examine the validity of the MEXE method for the assessment of arch bridge capacity. Eight of these TRL tests were on redundant bridges[111,112], Page[113,114,115], two were laboratory full-scale tests[116,117] and in additional included in the study were three from the earlier tests that were carried out before the second war[112]. The results of these tests have shown that non-linear behaviour was observed from the very start of loading but in all cases the load at which the first visible signs of damage occurred was recorded, which is a different for each bridge when compared to the failure load. In some cases this point was quite near to the failure load[20].

The problem with full-scale tests (especially on redundant bridges) is that the properties of the bridge components are not well known. Masonry properties (brick, concrete block, stone and mortar) fill materials and even the exact geometry of arch may not be available, especially the arch ring thickness. Also understanding the effect of interaction the soil and masonry in these tests is difficult. Any attempt to install stress gauges would have caused a significant disturbance to the fill and changed the initial condition of the bridges. To avoid this problem two full-scale model were carried out under TRL contracts. The first one was a semi-circular arch with 4m span that was built of bricks at the laboratory at Dundee University[116]. The thickness of barrel was 0.25m and the depth of fill over crown was 0.2m. The soil pressures were measured using 48 pressure cells on the extrados of arch barrel. The result of this test showed that the assumption of stress dispersal at an angle 45° was

apparent in low loads. The second test, a flat arch with a 6.0m span, 1.0m rise and with two ring of brickwork, was built as a part of TRL programme in Bolton[117]. Loading was applied at the quarter span across the full width of the bridge. Test results showed that the arch failed due to the formation of a four-hinge mechanism and the spandrel walls provided a significant restrain to the arch barrel. Ring separation was observed at the quarter point under a load of about 30% of the failure load and no ring separation was recorded at the unloaded quarter point until after the arch reached the maximum load. Fill pressures were recorded by 34 pressure cells. The result showed the backfill did provide a significant lateral resistance to the arch. The pressure cells beneath the KEL showed a good agreement with the 45° load distribution angle. The load deflection response was identified as being initially linear until hinging of the barrel occurred.

Fairfield and Ponniah[17,118] focused on the soil-structure interaction effect, load dispersal angle, lateral soil pressure in arch bridges. They worked with the TRL to install pressure gauges at Kimbolton Bridge during the building period and monitored the pressure in the fill during the building period and after. The bridge is a single 8m span with a 2m rise brick arch. The arch was built in four rings with a 440mm thickness. Two different types of pressure cells were used. One was used to measure the vertical pressure within the soil fill, and the other to monitor the interaction between the barrel and soil.

Melbourne[119] undertook a full scale laboratory test on a two-span 45 degree skewed brickwork arch bridge. The two span bridge with each nominally 3m span, had a nominal square span/rise ratio of 4 i.e. a rise of 0.75m. The experiment produced lots of important results. The bridge was weaker than the equivalent three span square two ring brickwork arch bridge. Strains commensurate with cracking were induced in the intrados below the point load of 42% of failure load.

Roca P. and Molins[120] undertook two short span full-scale experiments. The aim of this experiment was to provide additional experimental evidence useful for the validation of numerical tools for the structural analysis of masonry arch bridges.

2.3.2 Load test on model scale bridges

The literature review has shown that there has been a wide range of laboratory tests on scale model arches. A variety of arch spans, span to rise ratios, single and multi ring arches, single and multiple spans, square and skew arches with different materials have all been tested. A review of these tests has been reported elsewhere[6]. Short reviews of some of these tests are repeated here. Many models were built without spandrels or wing walls. The result of these test have been used to calibrate numerical models, but some models were tested as three dimensional tests with spandrel walls to understand the behaviour of different parts of an arch under load.

The first significant research work in this area was carried out by Pippard et al.[31] A series of segmental arches were built using steel voussoirs. Hanging equivalent weights at the centre of each voussoir simulated the dead load of the fill. He concluded that a voussoir arch behaves elastically within a limiting load and then fails by a four hinged mechanism. In the second series of Pippard's tests 26 arches with the same geometry but using mass concrete voussoirs were built. The results showed that the arches failed in the similar manner by a four-hinge mechanism. From these tests Pippard concluded that it was reasonable to analyse an arch as a linear elastic material.

Royles and Hendry[16] carried out a series of tests on 24 model arch bridges with spans of 1.0, 2.1 and 2.5m. The object of these tests was to examine the general behaviour of these structures, which had span to rise ratios between 2 and 6.4, and in particular to establish the effect on the strength of the arch of the fill material and wing-wall masonry. The models were built from masonry materials with sand or gravel fill. The dimensions of the models were selected based on three actual bridges, Bridgemill, Bargower and a bridge across the Carron River in the Highland Region. Each bridge vault was built three times and tested with fill material, the fill material plus the spandrel masonry, the fill material, the spandrel masonry plus the wing walls. One-third scale clay bricks were used for both the vault and the spandrels for Bridgemill. Concrete bricks and one-third scale clay bricks were used to model the Carron river bridge and finally the Bargower model was built with concrete bricks. The fill material in the models was graded from sand to 20mm crushed stone. The

abutments of all models tests were rigid. Test results show a significant effect of the various different components of the bridges on their load capacity. For example, in the Bridgemill model the vault only achieved 50% of the complete model failure load, vaults and fill test achieved 59% and the model with spandrel unrestrained wall achieved 77% of the capacity of the fully restrained model. For Carron River arch bridge model, vault, vault plus fill, vault plus fill and unrestrained spandrel, achieved 24%, 28%, 41% of the failure capacity of complete arch model (with fill, spandrel and wing walls) respectively. The test results on the Bargower arch model also showed the significant component effect on the load carrying capacity. The load deflection from these tests showed non linearity of arches under load, but it might be assumed linear up to about one third of the maximum load. Models that were constructed with different strength bricks failed at virtually the same load, therefore the strength of the material used for the construction of the arch was not thought critical. The main conclusion from these tests was the significant effect of the spandrel, wing wall and fill. The extent of this effect is greatest in arches with a high ratio of rise to span i.e. in arches approaching semicircular profile. In this case, the failure load of the complete structure was about twelve times that of the vault only.

Significant research work has been carried out at the Bolton Institute by Melbourne et al[43,121,122,123]. These tests included small-scale and full-scale models. In full-scale model, the work focused on single span arch, the effect of defects, multi ring and skewed arch bridges.

Fairfield and Ponniah[17] carried out a series of tests on arches of span of 700mm constructed in timber with 25 voussoirs and a span to rise ratio of 4. Polythene film was used to minimise the friction between the fill and sidewalls. The fill was a medium density, uniformly graded dry silica sand with rounded particles. In all 88 tests were carried out, of which 3 were use to establish the end walls boundary condition and 4 on the semicircular arch to determine the regions of fill displacement. Three tests on the semicircular arch were carried out with various fill densities. Finally 60 tests were carried out as part of the parametric study of both semicircular and span to rise ratio of 4. Some of the above tests were undertaken twice to check the repeatability of the tests. The results showed a distance of about 33% of arch span from the spring to end walls as being sufficient. Collapse loads

increased 13% for a 3% density increase. They also concluded that the collapse load increased with increasing fill depth. Increased vertical stresses increase lateral pressures which prevent arch movement into the fill on the side of arch remote from the load. So increased dead load increases the live load needed to cause collapse. Generally they concluded that soil-structure interaction contributed significantly to the capacity of the model arches.

Hughes et al. [124,125,126], Davies et al. [127], Burroughs et al.[128] and Taunton[129] have successfully undertaken small scale models using a geotechnical centrifuge to study the soil effects and masonry material influence on masonry arch bridges. These works studied the soil effects and involved the determination of the properties of a range of brickwork composed of different model mortars in a number of different geometric test configurations. The work contains comparisons with the full-scale behaviour of masonry constructed with essentially the same constituent unit and mortars. These works demonstrates that not only are the modes of failure properly established at small scale but also that detailed behaviour is properly considered. This work opened the way for consideration of modelling the overall response of quite large masonry structures within centrifuges.

Overall the results provide initial evidence that small-scale models are a suitable vehicle for investigating structural brickwork behaviour. Whilst it will clearly not be possible to built models of the same prototype materials and expect an exact scaled response, scale models are suitable for calibrating numerical models.

Gilbert et al. [130,131] studied the soil interaction both by small scale and full scale. The results showed that small scale tests can be performed rapidly and inexpensively, and with care can provide consistent results.

2.4 Serviceability assessment

Masonry arch bridges continue to play an important role in the UK's transport infrastructure, forming a significant proportion of road, rail and waterway crossings. Many of these bridges are relatively old and are still in service in their original configuration. Increasing vehicle loads and speeds have therefore highlighted the need for reliable estimates of both ultimate and serviceability load levels[132].

Recent experimental and theoretical investigations of the behaviour of masonry arch bridges have generally been directed towards the determination of their ultimate or failure load[21]. Some studies have started to investigate further the serviceability requirements for brick masonry arch bridges, based on representative cyclic loading tests on brick masonry test specimens[7,8,9,10,11]. However, it has been suggested[23] that if the applied loads are kept to a level less than 50% of the calculated failure load, then no lasting damage to the structure will occur. This 50% limit has been reinforced by a series of cyclic loading tests on laboratory dry brick masonry[8] which indicate a fatigue or run out limit at approximately 50% of the compressive strength.

The current Department of Transport Standard for the Assessment of Highway recommends that older structures need not be assessed for the serviceability limit state, structures built after 1965 should normally be checked for the serviceability limit state as well as the ultimate. Examination of typical load deformation curves shows that deformations increase rapidly as the applied load exceeds approximately half the ultimate failure load. So a serviceability limit of half of the ultimate load was initially suggested, pending a detailed investigation.[28]

Melbourne and Walker[117] have suggested that the formation of the first structural hinge should be taken as the serviceability limit state as this represents the onset of plastic, as opposed to linear elastic behaviour.

A number of tests to failure have been carried out on redundant arch bridges and full scale laboratory models[6].

Material properties and the current state of stress can be influenced significantly by long term environmental effects and ground movements. High cycle fatigue tests on stocky brick masonry columns, reported by Clark[15], also indicate a fatigue or run out limit for laboratory dry test specimens at approximately 50% of the static compressive strength. However, stress levels corresponding to 50% of the ultimate load and to 50% of the static compressive strength are unlikely to be equal.

Masonry arch bridges are mass dominated structures that owe much of their structural integrity to compression between the structural units induced by gravitational forces. Users are therefore unlikely to experience any ill effects due to

excessive deflections and vibrations. However, long term movements, particularly of the abutments, and high frequency vibrations that have a tendency to dislodge damaged material and structural units, may adversely affect serviceability.

A recent experimental investigation of the quasi-static and high cycle fatigue strength of brick masonry, sponsored by Network Rail, identified several aspects requiring further investigation[8]. The main conclusions drawn from the investigation were as follows.

1. The static compressive strength of brick masonry subjected to non-uniform loading is significantly greater than its compressive strength under uniform loading. This conclusion is consistent with the results of previous investigations reviewed by Page and Hendry[133] and Hendry[134]. However, at present there appears to be no simple physical or analytical model for quantifying this phenomenon.

2. The fatigue strength of laboratory dry brick masonry at 108 cycles is approximately 50% of its static strength under similar loading conditions. This conclusion is consistent with previous experimental investigations[15].

3. The static compressive strength of saturated brick masonry is approximately equal to the static compressive strength of laboratory dry brick masonry.

4. The fatigue strength of initially saturated brick masonry is significantly less than the fatigue strength of laboratory dry brick masonry. This conclusion is consistent with the results of previous experimental investigations[15] but is not compatible with the approximately equal static compressive strengths.

5. The fatigue strength of initially saturated brick masonry at 108 cycles is approximately 50% of its static compressive strength. This conclusion is compatible with previous investigations for laboratory dry test specimens, but not for saturated test specimens. Previous investigations[15] indicate that the fatigue strength of saturated brick masonry tends to zero at just over 106 cycles. This discrepancy may be due to differences in the degree of saturation and loading frequency. The specimens tested by Roberts et al[7] may have dried

out to some extent during the course of the tests, which were conducted at a frequency between 1 and 2 cycles per second. The specimens tested by Clark[10] were kept very wet throughout the tests, which were conducted at a frequency of 5 cycles per second. The hydraulic pressures generated in the tests conducted by Clark[15] are therefore likely to have been more damaging than those generated during the tests conducted by Roberts et al. [8]

The failure of brick masonry subjected to uniform compression is invariably initiated by tensile cracking of the structural units[10]. The physical explanation of this phenomenon is significant for the current study and is illustrated in Figure 2.6. When loading is applied normal to a mortar joint the relatively flexible mortar has a tendency to expand laterally far more than the structural units. This gives rise to interfacial shearing stresses, which induce compression in the mortar joint and tension in the structural units, normal to the axis of loading. It is the tensile stresses generated in the units that initiate the failure.

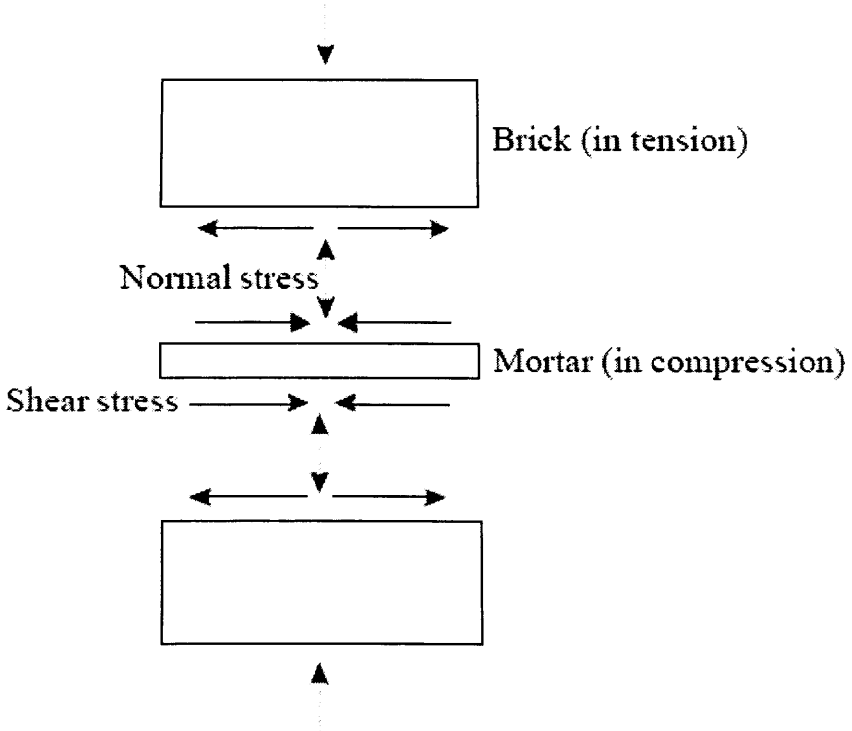

Figure 2.6 Stresses in brick masonry induced by uniform compression[7]

While in principle it is possible to predict theoretically the compressive strength of masonry[136] such analyses are complex and require specification of the pseudo elastic properties, and compressive and tensile strengths, of both the mortar and structural units.

The compressive strength of masonry subjected to non-uniform and localised loading depends also upon the nature of the applied loading[133, 134, 135, 137]. Experimental evidence indicates that the compressive strength of masonry under both types of loading is significantly greater than that under uniform compressive loading.

2.4.1 Cyclic compressive strength and cyclic load

Experimental studies of the response of masonry to cyclic loading have focused primarily on low cycle high stress fatigue loading[138, 139, 140]. Such studies are concerned with the behaviour of masonry under extreme forms of cyclic loading such as induced by earthquakes. Tests are conducted during which the amplitude of the cyclic loading is increased incrementally to induce failure in a relatively small number of cycles (typically ten or less). Such tests provide valuable information concerning the strength, ductility, energy absorption and post peak softening of masonry subjected to extreme cyclic loading.

A series of high cycle fatigue tests, on brick masonry subjected to concentric and eccentric compressive loading, has been reported by Clark[15]. These tests provided valuable information concerning the high cycle fatigue strength of both laboratory dry and saturated brick masonry. The loading applied to the test specimens was a relatively narrow line load, distributed through, what appears to be, a relatively flexible, 12 mm thick steel plate. The nature of the applied loading was therefore likely to be more localised than assumed in the theoretical analysis of stress levels. The tests were also conducted at a frequency of 5 cycles per second, which may have induced relatively high excess pore pressures in the saturated test specimens[9].

Melbourne et al. [141, 142] carried a series of full scale multi-ring masonry arch bridges experimental under cyclic load. The results showed that the classical mode of

failure of arches under static loading is the four-hinge-mechanism, all arches within this test series under cyclic loading have failed by ring separation over middle section of the arch. Cyclic loading therefore influences the mode of failure.

Lemos[143] used discrete element formulation method to analyse the experimental stone masonry arch and pillar structure under cyclic loading. The comparison of numerical and experimental cyclic force-displacement curves indicates a good agreement.

2.4.2 Dynamic characteristics

An extensive study of the influence of various parameters on the natural frequencies and modes of vibration of masonry arch bridges, based on a combination of dynamic testing and theoretical predictions, has been reported by Brown[144]. The main aim of the study was to investigate whether or not changes in the natural frequencies of vibration provide a reliable indication of progressive damage and reduced serviceability. The main conclusions of the investigation are as follows.

Variations in the natural frequencies of vibration of masonry arch bridges, due to normal environmental temperature and moisture content changes, are generally of the order of 3%. However, frequency changes under freezing conditions may be as high as 10%, a frequency shift comparable to that caused by major damage. Consequently, excluding freezing conditions, any change in natural frequency exceeding 5% should be viewed with concern and prompt further investigation.

Transverse cracking and ring separation in the arch barrel can cause significant shifts in natural frequencies. For transverse cracking the natural frequencies were found to decrease by up to 10% before the damage was so severe as to impair serviceability of the structure. Large amounts of ring separation caused frequency shifts approaching 50%. Smaller de-laminations, affecting about 20% of the arch barrel, caused frequency shifts of up to 10%.

It appears therefore that changes in the natural frequencies of masonry arch bridges may provide a reliable indication of progressive damage and reduced serviceability. However, the extent of the damage required to induce detectable

changes in the natural frequencies is relatively large, and may be more readily detectable by visual or other less sophisticated means, such as monitoring deflections. In this context it is worth noting that natural frequencies are proportional to the square root of the stiffness, while deflections are directly proportional to the stiffness. Deflections are therefore more sensitive than natural frequencies to changes in stiffness produced by damage. Also, at present, there appears to be no way of either locating or characterising the nature of the damage from changes in natural frequencies and mode shapes.

Bintrim et al. [145] tested three masonry arch bridges using seismometers and LVDTs to measure the dynamic testing response. The bridges were loaded using calibration trucks, random traffic, and a drop-weight device. These vibrations could indicate large cracks in the structure causing a separation of the arch ring. The result showed it was suitable to using vibration testing to determine the position of localized damage in less complex masonry arch bridges. However, vibration studies were not the quick answer to masonry arch assessment.

Harvey and Houghton[146] investigated one group of small arches under dynamic load. Deflections were measured simultaneously at many points on the arch soffit. And the results showed that arches suffer load induced deterioration at loading levels substantially below ultimate capacity. They suggested indentifying real serviceability limits for arches.

2.4.3 Serviceability limits

Nowadays structures are generally designed in accordance with well established limit state principles. The initial design is carried out for the ultimate limit state, under the action of factored loads, to ensure an adequate factor of safety against immediate failure. Various checks are then conducted for the serviceability limit state, to ensure that the structure performs satisfactorily under the action of service loads, both in the short and long term.

Serviceability limits on deflections and vibrations are intended to ensure that users of the structure do not experience any ill effects, and to avoid damage to essentially non-structural components such as cladding, spandrel walls and parapets.

Serviceability limits on stresses are intended to safeguard against progressive damage due to low and high cycle fatigue.

The establishing of serviceability limits for masonry arch bridges is by no means straightforward. Many of these structures are relatively old and owe their existence more to intuition and experience than engineering design. While the majority of the research to date has been directed towards a definition of the ultimate limit state, several authors have also considered the serviceability limit state[15, 29, 72, 147, 148].

Harvey[147] advocated the use of deflection and cracking criteria, despite the difficulties associated with their prediction, detection and measurement. The majority of other authors have advocated load or stress limitations. BD 21/01[29] advocates limiting the service load to 50% of the predicted ultimate load. This conclusion is based on the general results of numerous large and full scale tests, which were summarised to indicate that the load deflection response of masonry arch bridges remains approximately linear up to 50% of the ultimate load. Although this is a different phenomenon, high cycle fatigue tests on stocky brick masonry columns, reported by Clark[15] also indicate a fatigue or run out limit for laboratory dry test specimens at approximately 50% of the static compressive strength.

Little research has been undertaken into the creep effect in masonry arches. Mola and Palermo[149] studied the long-term analysis of segmental arch bridges subjected to loads, imposed deformations and delayed restraints. Their approach was based on a range of rate of creep models and they undertook three case studies applying these models. Hughes and Wu[150, 151] used the finite element analysis method to analyse the effect of long term creep in masonry tunnel. The results showed the creep could relax the initial high stress in the tunnel arches. Creep is also a factor to the serviceability limit load.

Choo & Hogg[148, 152] undertook two experiments to try to quantify the serviceability state of masonry arch bridges, and to define suitable criteria for their serviceability. But it was a very limited study to quantify the serviceability limit, because the experiments only loaded at the quarter point loading and did not include moving the load.

Recently, Melbourne et al.[153] developed a new method, the Sustainable Masonry Arch Resistance Technique (SMART) assessment method. They discussed limit state and suggested a new permissible limit state specific for masonry. The method is based on the long-term fatigue performance of masonry arch bridges subjected to cyclic loading.

Brook and Mullet[154] undertook a set of service loading tests and finite element model to analyse these tests. They tried to understand serviceability limit state by doing the strengthening used in to this tests and analysis. They set serviceability criterion as deflection, strains and stress ranges.

2.5 Conclusions

From the literature review above almost all the analysis and assessment methods use ultimate limit to define the allowable load. Most of the experiments were based on the static ultimate load, because it is easy to load and measure when using the static ultimate load.

However, there are still a few researchers who suggest developing a serviceability assessment method to apply to the masonry arch bridges' assessment.

Most current approaches to masonry arch bridge assessment are based on either a direct or on a factored, ultimate load analysis. Whilst from a safety perspective this approach provides a measure of confidence to bridge owners it fails to capture the more fundamental issue of progressive deterioration. With large numbers of masonry arch bridges, that still contribute significantly to the transport infrastructure, a serviceability approach is a more sustainable long term solution.

Ideally the development of a serviceability approach would be based on a detailed investigation of the longevity of the existing arch bridge stock when compared to the historic loading (if known) and a detailed elastic based analysis of each structure. It is unlikely that records will be sufficiently detailed for such a study. An alternative approach could be to use the same detailed elastic based analysis of each structure together with a detailed understanding of the long term mechanical properties of the, as-constructed materials.

So, this thesis is trying to approach a new systematically based serviceability assessment method of masonry arch bridges.

From the review, it is clear that finite element models are very well accepted and used, however, it is still considered as "overkill" for routine bridge assessments. One of the principle problems with the acceptance of new approaches to bridge assessment is the combination of suitable pre and post processors, to allow easy application and interpretation of the results, with an analysis "engine" which is well understood and trusted by the assessment engineer.

Limit Analysis based assessment methods can be "transparent" but are quite simplistic. The move from assessments based solely on ultimate load towards assessments undertaken on the basis of serviceability requires the development of suitable "transparent" elastic based assessment tools. This approach is developed in the next chapter.

3 Theory

3.1 Introduction

From the previous chapter it is apparent that serviceability criteria based assessment method requires some elastic analysis, plastic analysis is only applicable at ultimate load and could only be used in some factored analyses. Complex finite element analysis whilst entirely appropriate for developing complex understanding of difficult individual structures is too complex for use as a large scale assessment tool. It was therefore decided that some form of curved one dimensional analysis was required. Although plain linear elastic analysis is an acceptable method in the current UK Highways Agency standard[23] for ultimate load assessment the literature suggest that limiting compressive or tensile stress in a linear (non cracking) model is not a good predictor of an arch's overall strength. It was therefore decided that a one dimensional cracking elastic analysis was required for serviceability based assessments.

The theory to be used in the current study is based on Castigliano's[51] energy method. The energy method has previously been used by Bridle and Hughes[52].for ultimate load assessment. The analyse requires the arch to be divided into a number of elements and then Castigliano's theorem II is applied to generate the matrix to determinate the forces and moments. Castigliano's theorem II is then applied to determine the deflections of each of the discretised elements. The soil pressure is determined from the deflection and its direction. Active and passive soil pressures are applied in this theory. The load distribution methods developed are combined from two normally used methods. The theory modifies the arch geometry and stiffness to model the effects of the masonry's ability to sustain cracked tensile stress and yield compressive stress.

Castigliano's energy only applies to the elastic (linear) part of the arch ring, so the cracked part and the yield part need to be treated separately as external

parts/forces on the elastic part, the forces and the self weight of the external parts being added to the elastic part as external forces.

The analysis itself is linear elastic stress analysis, however, because of the thinning of the ring depth, this produces a non-linear effect.

3.2 Forces and moments solution

The arch ring (elastic part) is divided into a number of discrete elements. The whole ensemble of elements is treated as a curved beam with each of the elements subjected to forces that can be resolved into axial, shear and moment components, as illustrated in Figure 3.1.

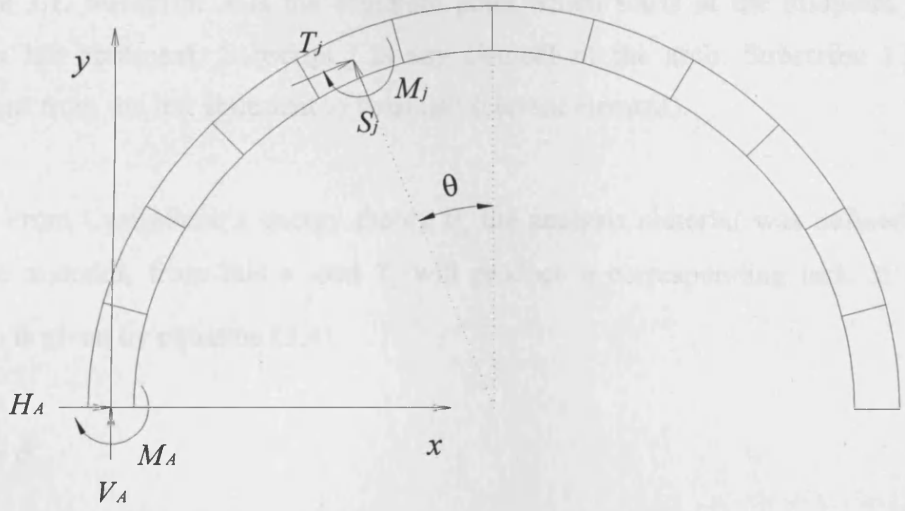

Figure 3.1 The bridge arch's elements and their forces and moments

The energy in an elastic material is expressed in equation (3.1).

$$U = 0.5\frac{\sigma^2}{E} \tag{3.1}$$

The integrations contained in the equations which follow are undertaken only from the left side abutment to any element j and then to right side abutment.

The whole energy U resulting from the bending, axial and shear forces in the beam is written in equation (3.2).

$$U = \int \frac{M^2 ds}{2EI} + \int \frac{T^2 ds}{2EA} + k\int \frac{S^2 ds}{2GA} \tag{3.2}$$

here G is determined by the equation (3.3).

$$G = \frac{E}{2(1+\nu)} \tag{3.3}$$

The co-ordinate and force direction definition are as follows.

M_A V_A H_A are shown in Figure 3.1 in a positive direction. V_j is the reverse direction to V_A, H_i has the same direction with H_A. M_j, T_j and S_j are also show in Figure 3.1. Subscript A is the abutment point which starts at the midpoint of the arch's left abutment. Subscript j is any element of the arch. Subscribe i is any element from the left abutment to j element (current element).

From Castigliano's energy theory II, the analysis material was defined as an elastic material, from this a load T_j will produce a corresponding lack of fit, δ_j which is given by equation (3.4).

$$\frac{\partial U}{\partial T_j} = \delta_j \tag{3.4}$$

The moment M_j at any point j in the arch is given by the equilibrium equation (3.5).

$$M_j = V_A x - H_A y + M_A - \sum V_i (x - x_i) - \sum H_i (y - y_i) \tag{3.5}$$

The axial compressive force T_j at any point j is then given by equation (3.6).

$$T_j = (V_A - \sum V_i)\sin\theta + (H_A + \sum H_i)\cos\theta \tag{3.6}$$

And lastly the shear force S_j is given by equation (3.7).

$$S_j = (V_A - \sum V_i)\cos\theta + (H_A + \sum H_i)\sin\theta \tag{3.7}$$

Considering the left hand abutment, the displacement and angular rotation of any element j can be determined by taking the differential coefficients of equation (3.1) with respect to H_A, V_A and M_A.

Applying equation (3.2), equation (3.3), equation (3.4) and equation (3.5) or equation (3.6) or equation (3.7), and differentiating with respect to V_A, H_A and M_A results in equation (3.8) or equation (3.10) or equation (3.12); these are equal to the abutment deflections δ_x or δ_y or δ_r.

$$\begin{aligned}
\frac{\partial U}{\partial V_A} = \delta_y &= \frac{1}{E}\int \frac{M}{I}\frac{\partial M}{\partial V_A}ds + \frac{1}{E}\int \frac{T}{A}\frac{\partial T}{\partial V_A}ds + \frac{k}{G}\int \frac{S}{A}\frac{\partial S}{\partial V_A}ds \\
&= \frac{1}{E}\sum \frac{dx}{I\cos\theta}\left[V_A x - H_A y + M_A - \sum V_i(x - x_i) - \sum H_i(y - y_i)\right] \\
&+ \frac{1}{E}\sum \frac{dx}{A\cos\theta}\sin\theta\left[(V_A - \sum V_i)\sin\theta + (H_A + \sum H_i)\cos\theta\right] \\
&+ \frac{k}{G}\sum \frac{dx}{A\cos\theta}\cos\theta\left[(V_A - \sum V_i)\cos\theta - (H_A + \sum H_i)\sin\theta\right]
\end{aligned} \tag{3.8}$$

Transferring equation (3.8) to equation (3.9), equation (3.9) can readily be put in a matrix form.

$$\begin{aligned}
\delta_y = E\frac{\partial \bar{U}}{\partial V_A} &= \left(\sum \frac{dx}{I\cos\theta}x^2 + \sum \frac{dx}{A\cos\theta}\sin^2\theta + 2k(1+\nu)\sum \frac{dx}{A\cos\theta}\cos^2\theta\right)V_A \\
&+ \left(-\sum \frac{dx}{I\cos\theta}xy + \sum \frac{dx}{A\cos\theta}\sin\theta\cos\theta - 2k(1+\nu)\sum \frac{dx}{A\cos\theta}\cos\theta\sin\theta\right)H_A \\
&+ \left(\sum \frac{dx}{I\cos\theta}x\right)M_A \\
&+ \left\{\sum \frac{dx}{I\cos\theta}x\left[-\sum V_i(x - x_i) - \sum H_i(y - y_i)\right]\right\} \\
&+ \left[\sum \frac{dx}{A\cos\theta}\sin\theta(-\sum V_i\sin\theta + \sum H_i\cos\theta)\right] \\
&+ 2k(1+\nu)\left[\sum \frac{dx}{A\cos\theta}\cos\theta(-\sum V_i\cos\theta - \sum H_i\sin\theta)\right]
\end{aligned} \tag{3.9}$$

Differentiating with respect to H_A gives equation (3.10).

$$\begin{aligned}
&\frac{\partial U}{\partial H_A} = \delta_x = \frac{1}{E}\int \frac{M}{I}\frac{\partial M}{\partial H_A}ds + \frac{1}{E}\int \frac{T}{A}\frac{\partial T}{\partial H_A}ds + \frac{k}{G}\int \frac{S}{A}\frac{\partial S}{\partial H_A}ds \\
&= \frac{1}{E}\sum \frac{dx}{I\cos\theta}(-y)\left[V_A x - H_A y + M_A - \sum V_i(x-x_i) - \sum H_i(y-y_i)\right] \\
&+ \frac{1}{E}\sum \frac{dx}{A\cos\theta}\cos\theta\left[(V_A - \sum V_i)\sin\theta + (H_A + \sum H_i)\cos\theta\right] \\
&+ \frac{k}{G}\sum \frac{dx}{A\cos\theta}(-\sin\theta)\left[(V_A - \sum V_i)\cos\theta - (H_A + \sum H_i)\sin\theta\right]
\end{aligned} \tag{3.10}$$

Transferring equation (3.10) to equation (3.11), equation (3.11) is readily put in matrix form.

$$\begin{aligned}
&\delta_x = E\frac{\partial U}{\partial H_A} = \left(\sum -\frac{dx}{I\cos\theta}xy + \sum \frac{dx}{A\cos\theta}\cos\theta\sin\theta - 2k(1+\nu)\sum \frac{dx}{A\cos\theta}\cos\theta\sin\theta\right)V_A \\
&+\left(\sum \frac{dx}{I\cos\theta}y^2 + \sum \frac{dx}{A\cos\theta}\cos^2\theta + 2k(1+\nu)\sum \frac{dx}{A\cos\theta}\sin^2\theta\right)H_A \\
&+\left(\sum \frac{dx}{I\cos\theta}(-y)\right)M_A \\
&+\left\{\sum \frac{dx}{I\cos\theta}y\left[\sum V_i(x-x_i) + \sum H_i(y-y_i)\right]\right\} \\
&+\left[\sum \frac{dx}{A\cos\theta}\cos\theta(-\sum V_i\sin\theta + \sum H_i\cos\theta)\right] \\
&+2k(1+\nu)\left[\sum \frac{dx}{A\cos\theta}(-\sin\theta)(-\sum V_i\cos\theta - \sum H_i\sin\theta)\right]
\end{aligned} \tag{3.11}$$

Differentiating with respect to M_A gives equation (3.12).

$$\begin{aligned}
&\frac{\partial U}{\partial M_A} = \delta_r = \frac{1}{E}\int \frac{M}{I}\frac{\partial M}{\partial M_A}ds \\
&= \frac{1}{E}\sum \frac{dx}{I\cos\theta}\left[V_A x - H_A y + M_A - \sum V_i(x-x_i) - \sum H_i(y-y_i)\right]
\end{aligned} \tag{3.12}$$

Transferring equation (3.12) to equation (3.13), equation (3.14) is also readily put in a matrix form.

$$\delta_r = E\frac{\partial U}{\partial M_A} = \left(\sum \frac{dx}{I\cos\theta} x\right) V_A + \left(-\sum \frac{dx}{I\cos\theta} y\right) H_A + \left(\sum \frac{dx}{I\cos\theta}\right) M_A + \left\{\sum \frac{dx}{I\cos\theta}\left[-\sum V_i(x-x_i) - \sum H_i(y-y_i)\right]\right\} \tag{3.13}$$

From the above equations (3.9), equation (3.11) and equation (3.13), the abutment reaction: V_A, H_A and M_A can be solved using the standard compatibility approach. This can be readily undertaken by arranging the equations of the abutment movements in matrix form as given in Table 3.1, and this was reunited to *ds* in Table 3.2.

The resulting set of three simultaneous equations, as arranged in Table 3.2 are solved for the abutment reactions H_A, S_A and M_A and then these reactions are subsequently used in determining the total axial force T_j, shear force S_j and the moment M_j at each element of the arch from equation (3.5), equation (3.6) and equation (3.7).

3.3 Deflections

Having determined the forces in the whole structure, these are then used in evaluating the deflections at any point j in the structure.

Castigliano theorem II is written in equation (3.4). The energy of the arch is expressed in equation (3.2). Applying equation (3.4) to equation (3.2), then the horizontal deflection δ_{jx} is therefore given by equation (3.14). Here because the shear energy is small in comparison to the moment and axial compressive energy[52] just those two parts of the full equation are retained.

Table 3.1 Matrix solution of V_A, H_A and M_A expressed by dx

$\sum \frac{dx}{I\cos\theta}x^2$	$-\sum \frac{dx}{I\cos\theta}xy$	$\sum \frac{dx}{I\cos\theta}x$			$\delta_y+\sum \frac{dx}{I\cos\theta}x\left[\sum V_i(x-x_i)+\sum H_i(y-y_i)\right]$
$\sum \frac{dx}{A\cos\theta}\sin^2\theta$	$\sum \frac{dx}{A}\sin\theta$	/		V_A	$\sum \frac{dx}{A\cos\theta}\sin\theta(\sum V_i\sin\theta-\sum H_i\cos\theta)$
$2k(1+\nu)\sum \frac{dx}{A}\cos\theta$	$-2k(1+\nu)\sum \frac{dx}{A}\sin\theta$	/			$2k(1+\nu)\left[\sum \frac{dx}{A}(\sum V_i\cos\theta+\sum H_i\sin\theta)\right]$
$\sum -\frac{dx}{I\cos\theta}xy$	$\sum \frac{dx}{I\cos\theta}y^2$	$\sum \frac{dx}{I\cos\theta}(-y)$			$\delta_x-\left\{\sum \frac{dx}{I\cos\theta}y\left[\sum V_i(x-x_i)+\sum H_i(y-y_i)\right]\right\}$
$\sum \frac{dx}{A}\sin\theta$	$\sum \frac{dx}{A}\cos\theta$	/		H_A	$\sum \frac{dx}{A}(\sum V_i\sin\theta-\sum H_i\cos\theta)$
$-2k(1+\nu)\sum \frac{dx}{A}\sin\theta$	$2k(1+\nu)\sum \frac{dx}{A\cos\theta}\sin^2\theta$	/			$2k(1+\nu)\left[\sum \frac{dx}{A\cos\theta}(-\sin\theta)(-\sum V_i\cos\theta-\sum H_i\sin\theta)\right]$
$\sum \frac{dx}{I\cos\theta}x$	$-\sum \frac{dx}{I\cos\theta}y$	$\sum \frac{dx}{I\cos\theta}$			$\delta_r+\sum \frac{dx}{I\cos\theta}\left[\sum V_i(x-x_i)+\sum H_i(y-y_i)\right]$
/	/	/		M_A	/
/	/	/			/

Table 3.2 Matrix solution of V_A, H_A and M_A expressed by ds

$\sum \frac{ds}{I} x^2$	$-\sum \frac{ds}{I} xy$	$\sum \frac{ds}{I} x$			$\delta_y + \sum \frac{ds}{I} x\left[\sum V_i(x-x_i) + \sum H_i(y-y_i)\right]$
$\sum \frac{ds}{A} \sin^2\theta$	$\sum \frac{ds}{A} \cos\theta \sin\theta$	/		V_A	$\sum \frac{ds}{A} \sin\theta(\sum V_i \sin\theta - \sum H_i \cos\theta)$
$2k(1+\nu)\sum \frac{ds}{A} \cos^2\theta$	$-2k(1+\nu)\sum \frac{ds}{A} \cos\theta\sin\theta$	/			$2k(1+\nu)\left[\sum \frac{ds}{A} \cos\theta(\sum V_i \cos\theta + \sum H_i \sin\theta)\right]$
$\sum -\frac{ds}{I} xy$	$\sum \frac{ds}{I} y^2$	$\sum \frac{ds}{I}(-y)$			$\delta_x - \left\{\sum \frac{ds}{I} y\left[\sum V_i(x-x_i) + \sum H_i(y-y_i)\right]\right\}$
$\sum \frac{ds}{A} \cos\theta \sin\theta$	$\sum \frac{ds}{A} \cos^2\theta$	/		H_A	$\sum \frac{ds}{A} \cos\theta(\sum V_i \sin\theta - \sum H_i \cos\theta)$
$-2k(1+\nu)\sum \frac{ds}{A} \cos\theta\sin\theta$	$2k(1+\nu)\sum \frac{ds}{A} \sin^2\theta$	/	=		$2k(1+\nu)\left[\sum \frac{ds}{A}(-\sin\theta)(-\sum V_i \cos\theta - \sum H_i \sin\theta)\right]$
$\sum \frac{ds}{I} x$	$-\sum \frac{ds}{I} y$	$\sum \frac{ds}{I}$			$\delta_r + \sum \frac{ds}{I}\left[\sum V_i(x-x_i) + \sum H_i(y-y_i)\right]$
/	/	/		M_A	/
/	/	/			/

$$\delta_{jx} = \frac{\partial U}{\partial H_j} = \int M \frac{\partial M}{\partial H_j} \frac{ds}{EI} + \int T \frac{\partial T}{\partial H_j} \frac{ds}{EA} \tag{3.14}$$

Similarly the vertical deflection δ_{jy} is given by equation (3.15)

$$\delta_{jy} = \frac{\partial U}{\partial V_j} = \int M \frac{\partial M}{\partial V_j} \frac{ds}{EI} + \int T \frac{\partial T}{\partial V_j} \frac{ds}{EA} \tag{3.15}$$

The deflection due to the axial force at the j element is then given by equation (3.16) and equation (3.17).

$$\delta_{ajy} = -T_j \frac{ds_j}{2} \frac{\sin\theta_j}{EA_j} \tag{3.16}$$

$$\delta_{ajx} = -T_x \frac{ds_j}{2} \frac{\cos\theta_j}{EA_j} \tag{3.17}$$

The deflection due to the bending action of the j element is the given by equation (3.18) and equation (3.19).

$$\delta_{bjy} = -\frac{1}{8} dx M_j \frac{ds_j}{EI_j} \tag{3.18}$$

$$\delta_{bjx} = -\frac{1}{8} dy M_j \frac{ds_j}{EI_j} \tag{3.19}$$

The vertical and horizontal deflections at any point are therefore given by the sum of the various components given above i.e. as shown in equation (3.20) and equation (3.21).

$$\delta_{jx} = \sum \delta_x + \delta_{ajx} + \delta_{bjx} \tag{3.20}$$

$$\delta_{jy} = \sum \delta_y + \delta_{ajy} + \delta_{bjy} \tag{3.21}$$

The axial force and bending moments calculated at each section previously are then used to determine the section stress distribution. This is used assuming a linear elastic strain distribution so as to coincide with the strain energy approach assumed.

If applying the nonlinear geometry, the deflections determined above can be used in conjunction with the reduction in the effective arch ring geometry. The new arch ring geometry is then determined using equation (3.22) and equation (3.23).

$$x_{jnew} = x_j + \delta_{jx} \tag{3.22}$$

$$y_{jnew} = y_j + \delta_{jy} \tag{3.23}$$

3.4 Soil pressure

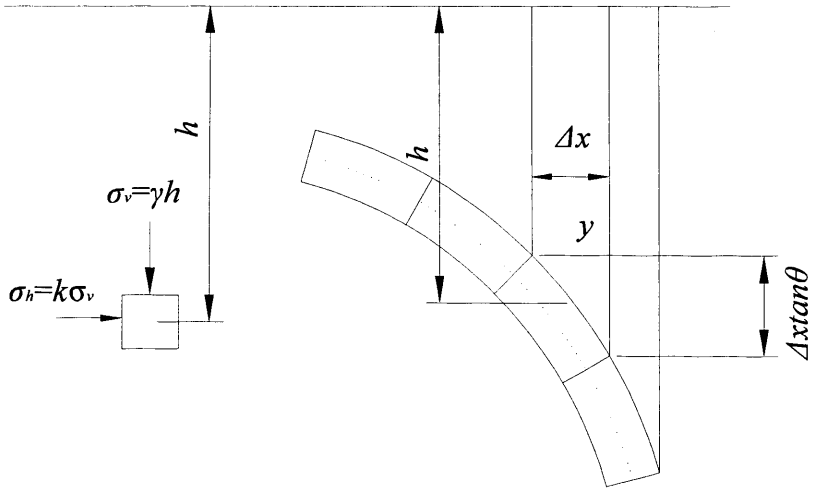

Figure 3.2 Soil forces and soil pressures

In Figure 3.2 the vertical force applied to the arch by the column of soil is $\gamma h \Delta x$.

Depending on the direction of the deflection the lateral soil pressures changes. It is initially assumed to be at-rest under dead load only and depending on the

direction of movement it moves into the passive or active zone, the value of k therefore always lies between k_a and k_p., the Rankine active and passive coefficient limits.

The proposed analysis considers the effect of lateral soil pressures acting on the arch. These were considered using the concept of the modulus of subgrade reaction (k_s) of the fill, being essentially the elasticity of the soil. The concept assumed is that, the horizontal stress imposed by the earth is linearly related to the horizontal deflection, so the horizontal stress is given by equation (3.24) within the previously discussed Rankine limits.

$$\sigma_h = k_s \delta_{jx} \tag{3.24}$$

At zero deflection of the arch ring, the earth pressure is said to be that due to the soil at rest. This is given by equation (3.25).

$$\sigma_h = k_0 \gamma h \tag{3.25}$$

As the arch ring deflects into the soil body it is resisted by a soil pressure which increases with the horizontal deflection. This is limited to a deflection that achieves a pressure which is equal to the passive limit of the soil, given by equation (3.26).

$$\sigma_h = k_p \gamma h \tag{3.26}$$

As the arch deflects away from the soil, the reverse happens and the pressure reduces to the limiting active value given by equation (3.27).

$$\sigma_h = k_a \gamma h \tag{3.27}$$

The adopted soil model detailed above is diagrammatically shown in Figure 3.3 with the two limiting values. The values of k_0 and k_p are also given in Figure 3.3.

The slope of he line connecting the earth pressure at rest and the passive limit is taken to be the modulus of subgrade reaction k_s.

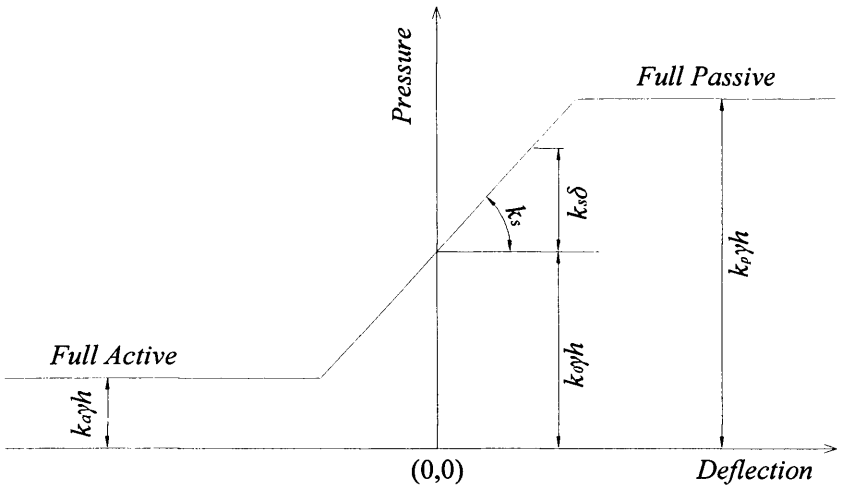

Figure 3.3 Typical soil pressures

The Rankine models are only simple approximations of the behaviour of the real back fill in arch bridges.

The deflections as determined above are therefore seen to be dependent on the soil fill depth. Although k_s can be assumed to vary with depth, it had been assumed to be constant in the present analysis.

Consideration was given to including the effect of the increased lateral pressure under the live loading component but whilst likely there was no experimental evidence in any of the arch tests to support or provide quantification of this.

3.5 Live load distribution

The author is not aware of any simple standard method for use in three dimensions, this ignores the benefit the arch gets from three dimensional effects. Loads are therefore distributed both longitudinally and laterally to the arch. The longitudinal load distribution distributes the loads to all the elements over the arch.

The lateral (transverse) load distribution is also important in determining the effective width of the arch bridge.

3.5.1 Longitudinal load distribution

The live load applied to the surface is discretised into a number of individual loadings, which are equally spaced. The load is then allowed to disperse through the fill assuming both of the following criteria:

1. The assumption of a fixed angle specified, through which the load is allowed to disperse before reaching the surface of the arch ring, illustrated in Figure 3.4.

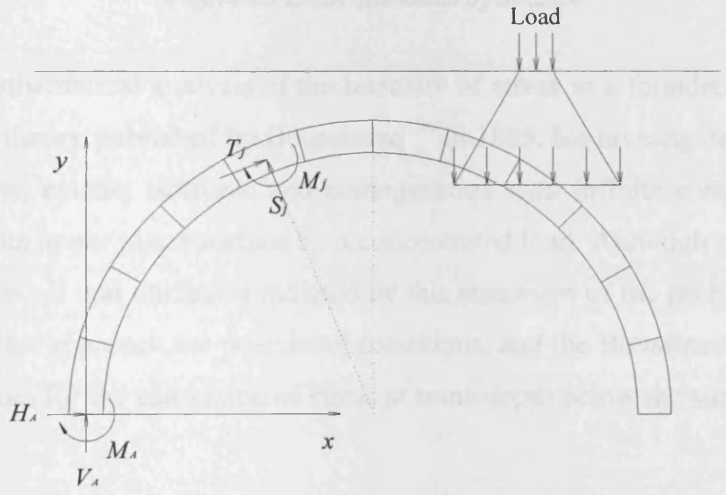

Figure 3.4 Loads distributed by angle

This load distribution can be expressed by the equation (3.28).

$$P = \sum P_i \tag{3.28}$$

P_i is the loading in the arch elements between the disperse angle.

2. Load dispersion based on semi infinite elastic theory. This allows for a means of calculating the stress distribution with respect to depth for a reasonably homogeneous soil. It applies for a point load or for a pattern of uniformly distributed load at the surface and is illustrated in Figure 3.5.

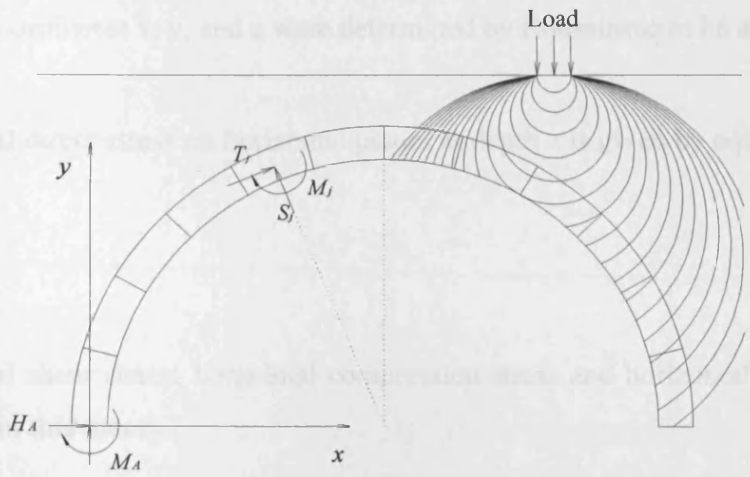

Figure 3.5 Loads distributed by distance

The mathematical analysis of the intensity of stress in a foundation material is based on the theory published by Boussinesq[155] in 1885. He investigated the stress in a semi-infinite, elastic, isotropic and homogeneous semi infinite continuum loaded normally on its upper plane surface by a concentrated load. Although no soils can be said to possess all that attributes indicted by this statement of the problem, yet many clays do at least approach the postulated conditions, and the Boussinesq figures form a valuable basis for the estimation of stress at some depth below the surface.

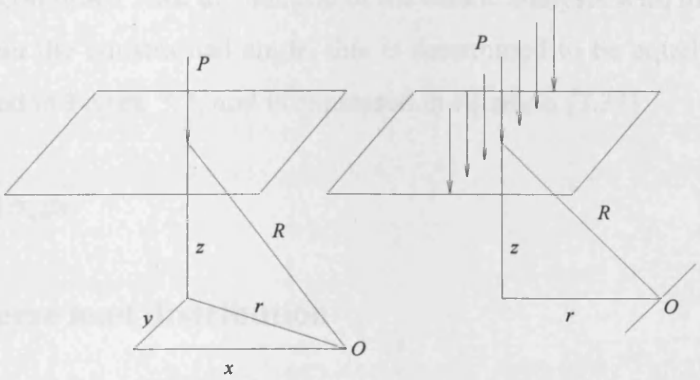

(a) Point load (b) Line load

Figure 3.6 Boussinesq point load and line load distribution

For a point load, see Figure 3.6 (a), the intensities of the stresses at point O, defined by coordinates x, y, and z were determined by Boussinesq to be as follows:

Vertical direct stress on horizontal planes at depth z is given by equation (3.29).

$$\sigma_v = \frac{3Pz^3}{2\pi R^5} \tag{3.29}$$

Vertical shear stress, horizontal compression stress and horizontal shear stress is neglected in this theory.

When the load is a line load, see Figure 3.6 (b), then the stress at point O is given by equation (3.30).

$$\sigma_v = \frac{2Pz^3}{\pi R^4} \tag{3.30}$$

The proposal load distribution applied is a combination of these two frequently used load distribution methods.

The distribution of the applied load in the current model uses the distance to decide the load combined with the integral of the elastic analysis with the loads being distributed within the constrained angle, this is determined to be equal to the whole load, is illustrated in Figure 3.7, and is expressed in equation (3.31).

$$P = \int \sigma_p dx = \int k\sigma_b dx \tag{3.31}$$

3.5.2 Transverse load distribution

There are three different transverse load distributions. The first one is recommended by Department of Transport[29]. The second one is recommended by Mott MacDonald Ltd. [60] The third one is recommended by author.

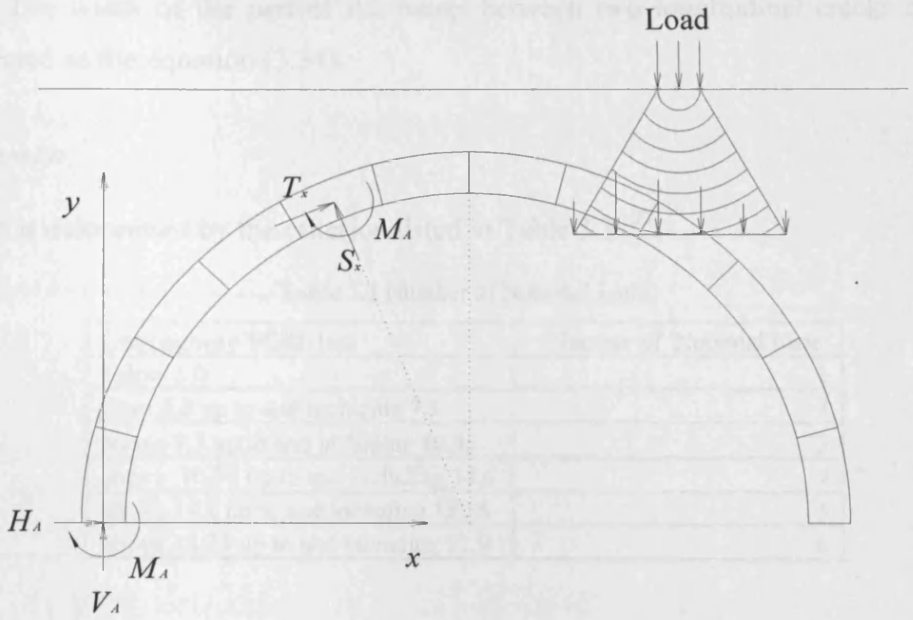

Figure 3.7 Loads distributed by combination

3.5.2.1 Department of Transport distribution

The analysis of an arch is generally carried out for a unit width of barrel. The effective width of the arch barrel carrying a wheel load applied at any position along the span can be derived as shown in Figure 3.8 from the equation (3.32)[23].

$$w = h + 1.5 \tag{3.32}$$

where h is the fill depth at the point under consideration and both w and h are in metres. The effective width for a number of wheel loads located transversely on the carriageway is the combined effective width. It is that between the outer points, as shown in Figure 3.9, the overall width of the barrel or the width of the part of the barrel between two longitudinal cracks, whichever is the least.

The combined effective width can be expressed in equation (3.33) or the width of the part of the barrel between two longitudinal cracks.

$$w = wl + h + 1.5 \tag{3.33}$$

The width of the part of the barrel between two longitudinal cracks can be expressed as the equation (3.34).

$$lw = cw / n \tag{3.34}$$

here n is determined by the criterion listed in Table 3.3. [23]

Table 3.3 Number of Notional Lanes

Carriageway Width (m)	Number of Notional Lane
below 5.0	1
from 5.0 up to and including 7.5	2
above 7.5 up to and including 10.95	3
above 10.95 up to and including 14.6	4
above 14.6 up to and including 18.25	5
above 18.25 up to and including 21.9	6

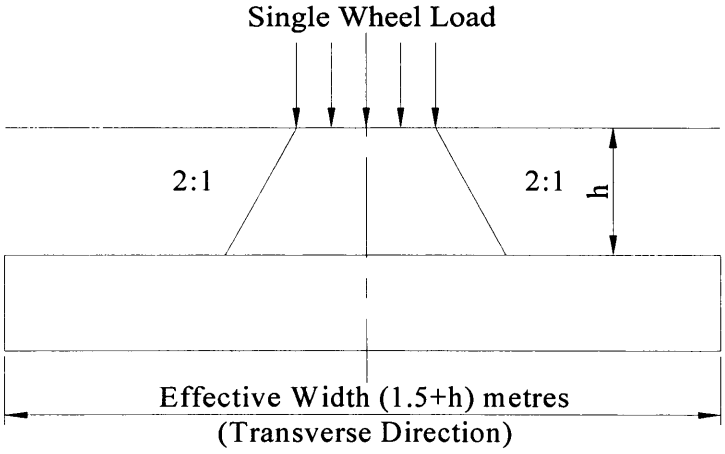

Figure 3.8 Effective width under a wheel load[29]

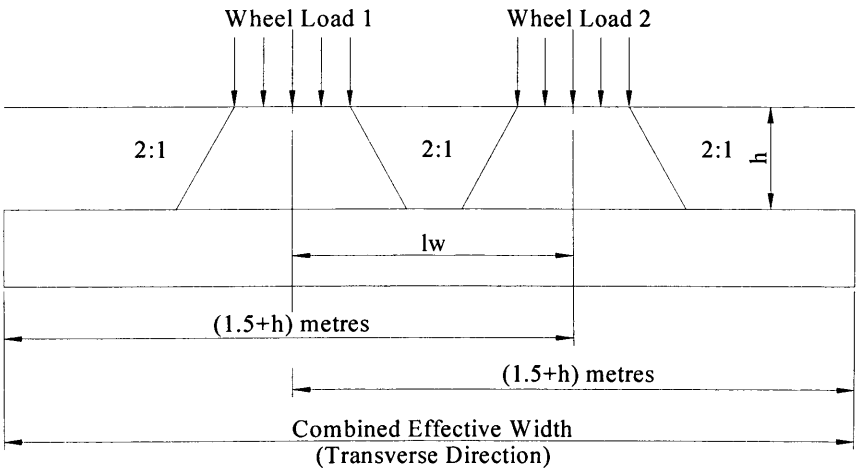

Figure 3.9 Combined effective width[29]

3.5.2.2 Mott MacDonald Ltd. distribution

It is suggested that the following approach be used[60]:

For construction and use vehicles, lane width shall be taken as 2.5 m, irrespective of lane width based on notional number of lanes. One axle load with 1.8 shall be taken between adjacent axles. The full effects of loading from axles in two adjacent lanes only shall be considered, with axle loading in other lanes factored by 0.6. The transverse disposition of the axles is to be such as to cause the most adverse effect on the bridge cross section.

In addition to the axle loads described above, a UDL shall be applied to any fractional part of the lane which remains after the carriageway has been divided into 2.5m widths. The UDL shall be given a value of $5kN/m^2$. A footway loading of $5kN/m^2$ shall also be considered in combination with the carriageway loading where appropriate.

An illustration of the transverse disposition of axle pattern is given in Figure 3.10.

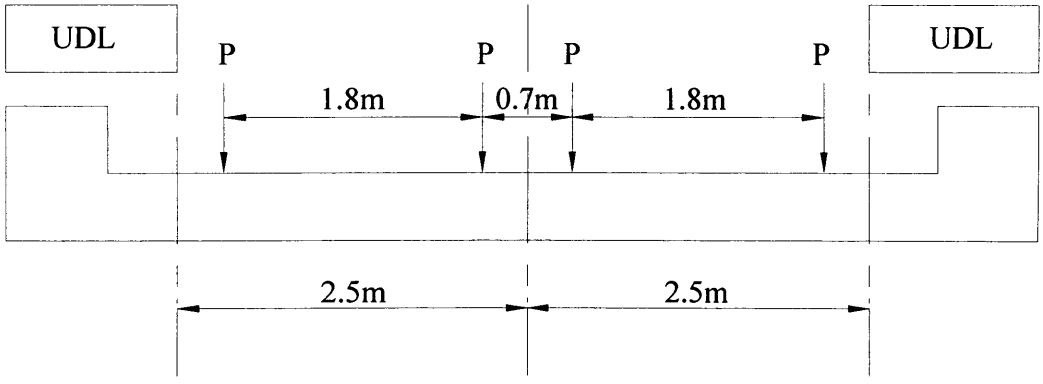

Figure 3.10 Transverse distribution of live loads[54]

3.5.2.3 Author recommended distribution

The author recommends the application of carriageway loading across the full width of the bridge. The reason is the crack between two lane divides the bridges in several bridges with lane width naturally created by cracks. These cracks are more common in railway bridges where the load lines are rigidly fixed. This cracked form develops because the high level loading and the different direction loading lead to the deflections and stresses are totally different and in different direction, this creates very high shear stress between different direction lanes. Between these bridges no other cracks would be found. So the individual bridge created by cracks is a new bridge which can carry all loads include dead loads and live loads from the bridge above. So the whole bridge carriage width can carry the total loads above all these new bridges. The whole width is the sum of the new bridges is equal to the carriageway width, as illustrated in Figure 3.11.

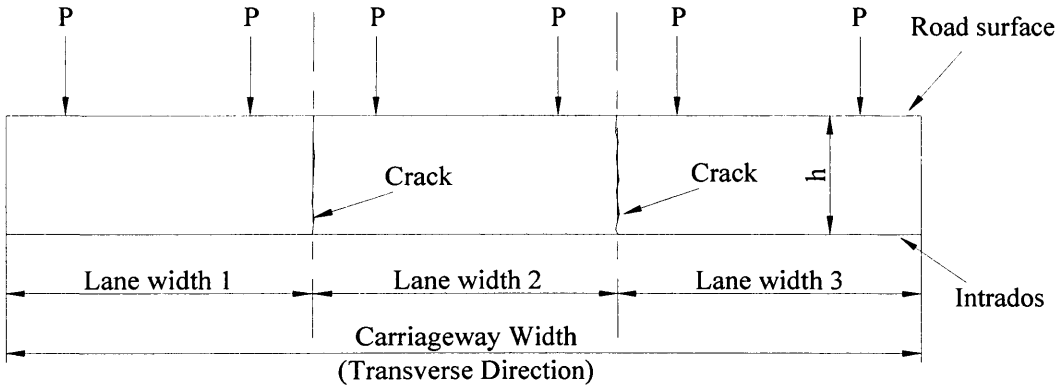

Figure 3.11 Author commended transverse distribution of live loads

Normally the bridge has no more cracks between the lane width cracks or crack to the edge of the bridge. In this condition, the suggested carriageway width is used as the nominal bridge width, especially for serviceability load. Here the live load can be distributed by bending moment and shear stress to the part which is not within the live load distributed part in the lane width.

The recommended distribution is different with the previous two methods which gives us different distribution width.

3.6 Castigliano theory applied to compressive yield models

The force carried by the compressive yield area in the yielded section is $\sigma_c \cdot c_t$, so the new force in the elastic part is $T_j - \sigma_c \cdot c_t$. To the calculated elastic length d, the yielded part carries a force which looks like an external force. The moment about the middle of the ring section elastic length d is $M_j - \sigma_c \cdot c_t(d/2 - c_t/2)$ when the yield is in the extrados, and $M_j + \sigma_c \cdot c_t(d/2 - c_t/2)$ when the yield is in the intrados, as illustrated in Figure 3.12. Applying these forces and moments to the elements in the equation (3.2), Table 3.4 would be created.

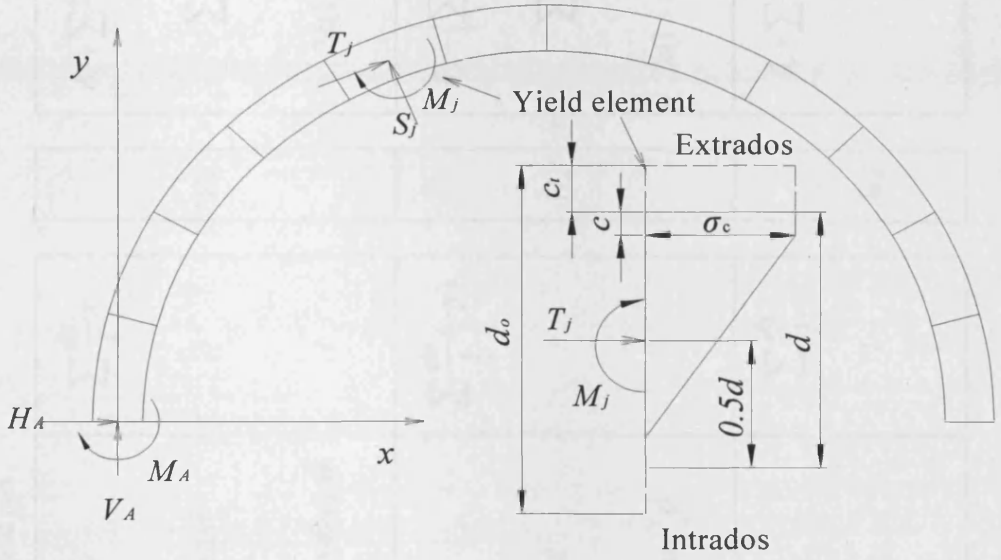

Figure 3.12 Castigliano theory applied to compressive yield models

3.7 Thinning models

3.7.1 Introduction

Normally, a typical model of masonry uses zero tensile strength and unlimited compressive strength, as shown in Figure 3.13(a). The current proposal theory can however use a limited tension cracked model, see Figure 3.13 (b), or a limited compressive yield with limited tension cracked model, see Figure 3.14 (b).

Table 3.4 Matrix type of V_A, H_A and M_A solution with yield part

$\sum \frac{ds}{I} x^2$	$-\sum \frac{ds}{I} xy$	$\sum \frac{ds}{I} x$			$\delta_y + \sum \frac{ds}{I} x \left[\sum V_i (x - x_i) + \sum H_i (y - y_i) + \sigma \cdot c_t (\frac{d}{2} + \frac{c_t}{2}) \right]$
$\sum \frac{ds}{A} \sin^2 \theta$	$\sum \frac{ds}{A} \cos\theta \sin\theta$	/		V_A	$\sum \frac{ds}{A} \sin\theta (\sum V_i \sin\theta - \sum H_i \cos\theta + \sigma \cdot c_t)$
$2k(1+\nu) \sum \frac{ds}{A} \cos^2 \theta$	$-2k(1+\nu) \sum \frac{ds}{A} \cos\theta \sin\theta$	/			$2k(1+\nu) \left[\sum \frac{ds}{A} \cos\theta (\sum V_i \cos\theta + \sum H_i \sin\theta) \right]$
$\sum -\frac{ds}{I} xy$	$\sum \frac{ds}{I} y^2$	$\sum \frac{ds}{I} (-y)$			$\delta_x - \left\{ \sum \frac{ds}{I} y \left[\sum V_i (x - x_i) + \sum H_i (y - y_i) + \sigma \cdot c_t (\frac{d}{2} + \frac{c_t}{2}) \right] \right\}$
$\sum \frac{ds}{A} \cos\theta \sin\theta$	$\sum \frac{ds}{A} \cos^2 \theta$	/		H_A =	$\sum \frac{ds}{A} \cos\theta (\sum V_i \sin\theta - \sum H_i \cos\theta + \sigma \cdot c_t)$
$-2k(1+\nu) \sum \frac{ds}{A} \cos\theta \sin\theta$	$2k(1+\nu) \sum \frac{ds}{A} \sin^2 \theta$	/			$2k(1+\nu) \left[\sum \frac{ds}{A} (-\sin\theta)(-\sum V_i \cos\theta - \sum H_i \sin\theta) \right]$
$\sum \frac{ds}{I} x$	$-\sum \frac{ds}{I} y$	$\sum \frac{ds}{I}$			$\delta_r + \sum \frac{ds}{I} \left[\sum V_i (x - x_i) + \sum H_i (y - y_i) + \sigma \cdot c_t (\frac{d}{2} + \frac{c_t}{2}) \right]$
/	/	/		M_A	/
/	/	/			/

These tension models can be used as the condition of the new bridge in an experiment or in a repaired bridge with a brittle material that can support an applied tensile stress.

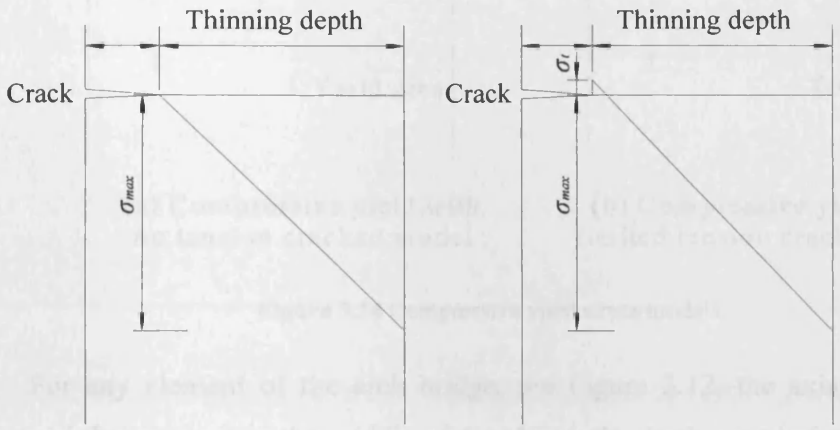

(a) No tension model (b) Limited crack tension model

Figure 3.13 Unlimited compressive stress models

The last, but not the least, is the model that includes compressive yield with a no tension cracked model, see Figure 3.14 (a). This model is normally applied to most masonry arch bridges. Because most masonry arch bridges have been built a hundred years before, the cracks have already existed in these structures, then no tension can be carried by masonry arch bridges.

When applying a limited tensile stress, the cross section is still cracked and thinned. The model with a tensile strength allows a larger effective depth to be determined and naturally results in a larger live load capacity.

When applying a compressive yield stress method, it is similar to thinning but the yield area has a constant compressive stress. The rest of the cross section still works as an elastic material, the energy method can be then be applied. The yield field is applied as an external force applied to the compressive thinning section, as illustrated in Figure 3.14.

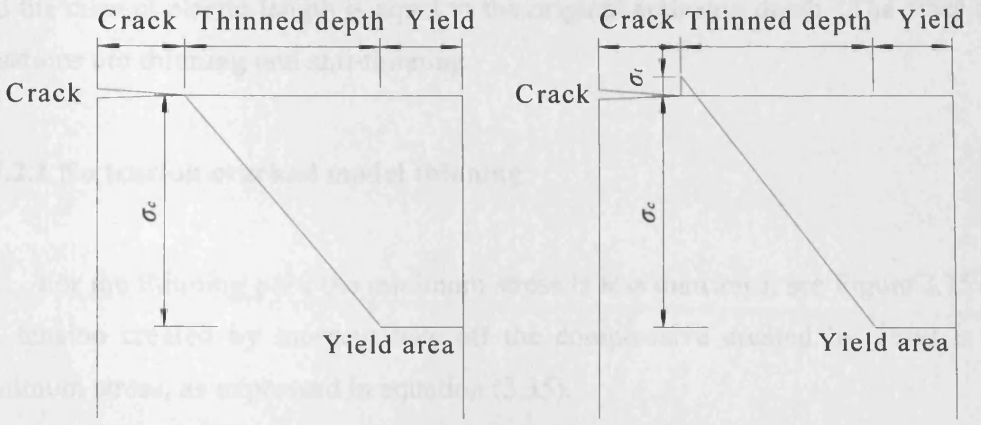

(a) Compressive yield with no tension cracked model

(b) Compressive yield with limited tension cracked model

Figure 3.14 Compressive yield stress models

For any element of the arch bridge, see Figure 3.12, the axial compressive force and the moment in the middle of the element's elastic part before thinning are known. The yielded part length is also known before thinning and anti-thinning (joint closing). The total lengths shown in Figure 3.13 and 3.14 are elastic length parts before thinning. The other three parts in every section are lengths after thinning.

This proposed method can thin and anti-thin the element section. If the minimum stress of the element in calculation is tensile in a no tension cracked model or the tensile stress in the calculation is more than the allowable ultimate tensile stress with tension model, then thinning begins, else if the elastic length in the iterative calculation is less than the total length the anti-thinning starts. In the yield model, if the maximum compressive stress is greater than allowable ultimate compressive stress then yield thinning starts, else if total yield length is already greater than zero, then yield anti-thinning starts.

3.7.2 No tension cracked model

There are three thinning and anti-thinning situations in this model. The first situation is the no thinning situation, where the minimum stress is greater than zero

and the current elastic length is equal to the original arch ring depth. The other two situations are thinning and anti-thinning.

3.7.2.1 No tension cracked model thinning

For the thinning part, the minimum stress is less than zero, see Figure 3.15 (a), the tension created by moment take off the compressive created by thrust is the minimum stress, as expressed in equation (3.35).

$$\sigma_{\min} = \frac{T}{d} - \frac{|M|\,d}{2I} < 0 \tag{3.35}$$

Where d is limited as given in equation (3.36).

$$d < \frac{6|M|}{T} \tag{3.36}$$

If this meets the equation (3.36) criterion, then thinning starts. The cracked length of the element is the most important value to be determined once thinning starts. If the bending moment is positive, the crack is in intrados, else the crack is in extrados.

The moment in the middle of the element is given by equation (3.37), as illustrated in Figure 3.15 (a).

$$|M| = \left(\frac{d}{2} - \frac{a}{3}\right) \cdot T \tag{3.37}$$

From equation (3.37) the length of the no tension elastic part can be determined from the equation (3.38).

$$a = 3\left(\frac{d}{2} - \frac{|M|}{T}\right) \tag{3.38}$$

So then the cracked length is given by equation (3.39).

$$b = d - a \tag{3.39}$$

The maximum stress in the element can then be determined by equation (3.40).

$$\frac{1}{2} a \sigma_{max} = T \tag{3.40}$$

Giving a stress as determined for equation (3.41).

$$\sigma_{max} = \frac{2T}{a} \tag{3.41}$$

The length a can then be used as the new elastic length of the element to determine the whole structure's new thrusts, shears and moments. This is a non linear iterative process.

3.7.2.2 No tension cracked model anti-thinning

This proposed model can also anti-thin the element, when the minimum stress is greater than zero, i.e. equation (3.42).

$$\sigma_{min} = \frac{T}{d} - \frac{|M| d}{2I} > 0 \tag{3.42}$$

Where d is limited as given in equation (3.43).

$$d > \frac{6|M|}{T} \tag{3.43}$$

If the criterion of equation (3.43) is met, then anti-thinning starts. The moment in the middle of the element is given by equation (3.37), as illustrated in Figure 3.15 (b).

The length of the no tension elastic part also can be determined from equation (3.38).

If the new length of the element *a,* in equation (3.38), is less then the original ring depth d_o, it is determined from equation (3.38), otherwise $a=d_o$, $b=d_o-d$, and the new bending moment in the middle of new length, new minimum stress, and new maximum stress are determined from equations (3.44) , equation (3.45) and equation (3.46).

$$|M_n| = |M| + T(\frac{a}{2} - \frac{d}{2}) \tag{3.44}$$

$$\sigma_{\min} = \frac{T}{d} - \frac{|M_n|a}{2I} \tag{3.45}$$

$$\sigma_{\max} = \frac{T}{d} + \frac{|M_n|a}{2I} \tag{3.46}$$

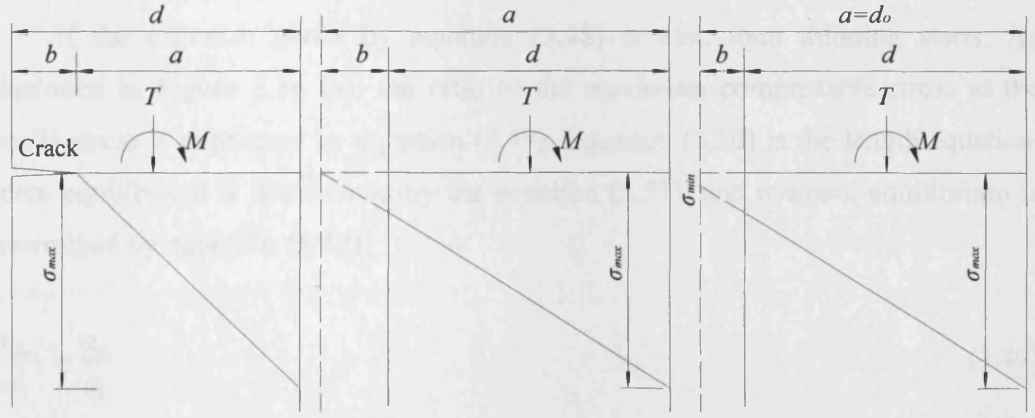

(a) No tension model thinning (b) Anti-thinning $a>d_o$ (c) Anti-thinning $a=d_o$

Figure 3.15 No tension cracked model

3.7.3 Limited Tension cracked model

There are three thinning situations in this model. The first situation is the no thinning situation, when the minimum stress is greater than the tensile stress (tensile

stress defined as negative) and the current elastic length is equal to the original arch ring depth. The other two situations are thinning and anti-thinning.

3.7.3.1 Tension cracked model thinning

If applied to the tension cracked model, see Figure 3.16, when the tension is greater than the ultimate tensile strength, then thinning begin, expressed in equation (3.47).

$$\sigma_{\min} = \frac{T}{d} - \frac{|M|d}{2I} < -\sigma_t \tag{3.47}$$

Where d is limited as given in equation (3.48).

$$d < \frac{6|M|}{T + \sigma_t d} \tag{3.48}$$

If the criterion given by equation (3.48) is met, then thinning starts. As illustrated in Figure 3.16 (a), the ratio of the maximum compressive stress to the tensile stress is expressed by equation (3.49). Equation (3.50) is the length equation. Force equilibrium is determined by the equation (3.51), and moment equilibrium is determined by equation (3.52).

$$\frac{\sigma_{\max}}{\sigma_t} = \frac{a_2}{a_1} \tag{3.49}$$

$$a = a_1 + a_2 \tag{3.50}$$

$$T = \frac{1}{2}\sigma_{\max} a_2 - \frac{1}{2}\sigma_t a_1 \tag{3.51}$$

$$|M| = \frac{1}{2}\sigma_{\max} a_2 \left(\frac{d}{2} - \frac{a_2}{3}\right) + \frac{1}{2}\sigma_t a_1 \left(a - \frac{d}{2} - \frac{a_1}{3}\right) \tag{3.52}$$

From equations (3.49), equation (3.50), equation (3.51) and equation (3.52), the length of the limited tension elastic part can be determined from equation (3.53).

$$\sigma_t a^2 - 2Ta + 3Td - 6M = 0 \tag{3.53}$$

Because the tensile stress is not equal to zero in this model, a new elastic length can be determined from equation (3.54).

$$a = \frac{2T - \sqrt{4T^2 - 4\sigma_t(3Td - 6M)}}{2\sigma_t} \tag{3.54}$$

So the cracked length is then given by equation (3.55).

$$b = d - a \tag{3.55}$$

From equation (3.49), equation (3.50) and equation (3.51) the maximum stress can be determined as given in equation (3.56).

$$\sigma_{max} = \frac{2T}{a} + \sigma_t \tag{3.56}$$

3.7.3.2 Tension cracked model anti-thinning

This proposed model can also anti-thin the element. When the minimum stress is greater than the tensile stress (tension is negative), the tension created by the moment is subtracted from the compressive created by the axial thrust and is the minimum stress, these are greater than ultimate tensile stress, i.e. equation (3.57), and $d<d_o$.

$$\sigma_{min} = \frac{|M|d}{2I} - \frac{T}{d} > -\sigma_t \tag{3.57}$$

Where d is limited as given in equation (3.58).

$$d > \frac{6|M|}{T + \sigma_t d} \tag{3.58}$$

If the criterion from equation (3.58) is met then anti-thinning starts. As illustrated in Figure 3.16 (b), similar to Figure 3.16 (a), the ratio of maximum

compressive stress to the tensile stress is expressed by equation (3.49). Equation (3.50) is length equation. Force equilibrium is determined by equation (3.51), and moment equilibrium is determined by equation (3.52).

From equation (3.49), equation (3.50), equation (3.51) and equation (3.52), the length of the limited tension elastic part can be determined from equation (3.53).

Because the tensile stress is not equal to zero in this model, a new elastic length can be determined by equation (3.54).

So the anti-cracked length is given by equation (3.59).

$$b = a - d \tag{3.59}$$

If the new length of the element a in equation (3.54) is less then the original ring depth d_o, it is calculated by the equation (3.54), otherwise $a=d_o$, $b=d_o-d$, as illustrated in Figure 3.16 (b), and the new bending moment in the middle of new length, new minimum stress, and new maximum stress are determined in equation (3.44), equation (3.45) and equation (3.46).

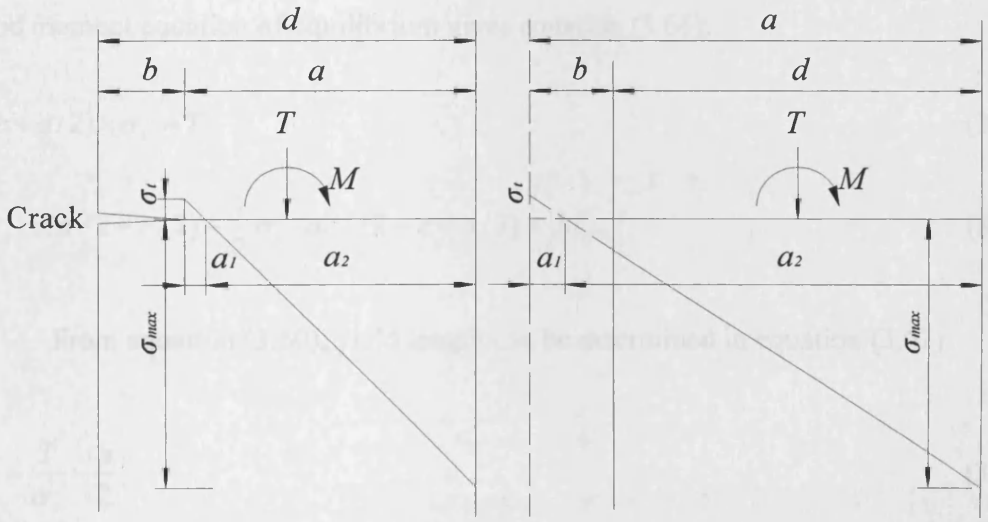

(a) Tension model thinning (b) Tension model anti-thinning

Figure 3.16 Limited tension cracked model

3.7.4 Compressive yield with no tension cracked model

In this section, the compressive yield with the no tension cracked model is detailed. Thinning and anti-thinning are applied to the model, as illustrated in Figure 3.17 (a), (b), (c) and (d). There are four thinning and anti-thinning situations: crack thinning and yield thinning, crack thinning and yield anti-thinning, crack anti-thinning and yield thinning, and crack anti-thinning and yield anti-thinning.

There are five no thinning combinations with thinning and anti-thinning situations. Three of these situations are as simple as the no tension cracked model, and their maximum stresses are all less than the ultimate compressive stress. So no yield thinning and anti-thinning will happen. The other two situations are no thinning with yield thinning and no thinning with yield anti-thinning.

3.7.4.1 Cracked thinning and yield thinning

When the minimum stress is less than zero and the maximum stress greater than ultimate compressive stress, then cracked thinning and yield thinning starts, as illustrated in Figure 3.17 (a). Force equation of equilibrium gives equation (3.60) and moment equation of equilibrium gives equation (3.61).

$$(c+a/2)\times\sigma_c = T \tag{3.60}$$

$$\sigma_c \cdot c(d/2-c/2)+\frac{1}{2}\sigma_c \cdot a(d/2-c-a/3)=|M| \tag{3.61}$$

From equation (3.60), yield length can be determined in equation (3.62).

$$c=\frac{T}{\sigma_c}-\frac{a}{2} \tag{3.62}$$

This replaces the c in the equation (3.61) and results in equation (3.63):

$$\frac{a^2}{24}+(\frac{T^2}{2\sigma_c^{\ 2}}-\frac{Td}{2\sigma_c}+\frac{|M|}{\sigma_c})=0 \tag{3.63}$$

Because a>0, then a new elastic length can be determined from equation (3.64).

$$a=\sqrt{24(\frac{T\cdot d}{2\sigma_c}-\frac{1}{2}(\frac{T}{\sigma_c})^2-\frac{|M|}{\sigma_c})} \tag{3.64}$$

Then the new yield part c can be determined by equation (3.62) and the cracked length b can be determined by equation (3.65), as illustrated in Figure 3.17(a).

$$b=d-a-c \tag{3.65}$$

3.7.4.2 Cracked thinning and yield anti-thinning

When the minimum stress is less than zero and the maximum stress is less than the ultimate compressive stress, and if the yield length c is greater than zero, then crack thinning and anti-yield thinning starts, as illustrated in Figure 3.17 (b). If the yield length is zero, then only cracked thinning starts, this case has been detailed in section 3.7.2.1.

As illustrated in Figure 3.17(b), force equation of equilibrium gives equation (3.66) and moment equation of equilibrium gives equation (3.67).

$$\frac{\sigma_c a}{2}=T+\sigma_c c \tag{3.66}$$

$$\frac{1}{2}\sigma_c\cdot a(d/2+c-a/3)=|M|+\sigma_c c(d/2+c/2) \tag{3.67}$$

From equation (3.66), yield length can be determined in equation (3.68).

$$c=\frac{a}{2}-\frac{T}{\sigma_c} \tag{3.68}$$

This replaces the c in the equation (3.67) and results in equation (3.69).

$$\frac{a^2}{24}+(\frac{T^2}{2\sigma_c^{\ 2}}-\frac{Td}{2\sigma_c}+\frac{|M|}{\sigma_c})=0 \tag{3.69}$$

Because $a>0$, then the new elastic length can be determined from equation (3.70).

$$a=\sqrt{24(\frac{T\cdot d}{2\sigma_c}-\frac{1}{2}(\frac{T}{\sigma_c})^2-\frac{|M|}{\sigma_c})} \tag{3.70}$$

Then the new yield anti-thinning part c can be determined by equation (3.68) and the cracked length b can be determined by equation (3.71), as illustrated in Figure 3.17 (b).

$$b=d+c-a \tag{3.71}$$

Comparing equations (3.66) – (3.71) to equations (3.60) – (3.65), if c is defined as negative in equation (3.66) – (3.71), these two groups of equations are the same. However, when the yield anti-thinning length is greater than total yield thinning length, then the maximum stress will not be the ultimate compressive stress, but the anti-thinning length will equal to the total yield thinning length. Then the force equation of equilibrium gives equation (3.72) and the moment equation of equilibrium also gives equation (3.73).

$$\frac{\sigma_{\max}a}{2}=T+\sigma_c c_t \tag{3.72}$$

$$\frac{1}{2}\sigma_{\max}a(\frac{d}{2}+c_t-\frac{a}{3})=|M|+\sigma_c c_t\frac{d+c_t}{2} \tag{3.73}$$

From equation (3.72), maximum stress can be determined in equation (3.74).

$$\sigma_{\max}=\frac{2T}{a}+\frac{2\sigma_c c_t}{a} \tag{3.74}$$

This then replaces σ_{max} in the equation (3.73) results in equation (3.75).

$$a = \frac{3d}{2} + 3c_t - 3\frac{|M| + \sigma_c c_t \frac{d + c_t}{2}}{(T + \sigma_c c_t)} \tag{3.75}$$

3.7.4.3 Cracked anti-thinning and yield thinning

When the minimum stress is greater than zero and maximum stress greater than the ultimate compressive stress, then crack anti-thinning and yield thinning starts, as illustrated in Figure 3.17 (c). If the anti-thinning length is less than the total cracked thinning length, then the shape of the stress is the same as the cracked thinning one. Force equation of equilibrium gives equation (3.60) and moment equation of equilibrium gives equation (3.61).

From equation (3.60), yield length c can be determined in equation (3.62).

Because a>0, then a new elastic length can be determined from equation (3.64).

Then the new cracked length b can be determined by equation (3.72), as illustrated in Figure 3.17(c). If the length b is negative, then this length can also be determined from equation (3.76)

$$b = a + c - d \tag{3.76}$$

If the anti-thinning cracked length calculated in equation (3.76) is greater than the total cracked thinning length b_t, then the new total cracked length is zero and the new cracked anti-thinning length is b_t, the new elastic length is determined by equation (3.77), Force equation of equilibrium gives equation (3.78) and moment equation of equilibrium gives equation (3.79).

$$a = d + b_t - c \tag{3.77}$$

$$a/2\times(\sigma_c+\sigma_{\min})+\sigma_c c=T \tag{3.78}$$

$$\sigma_c c\frac{d-c}{2}+\frac{1}{2}(\sigma_c-\sigma_{\min})a(\frac{d}{2}-c-\frac{a}{3})+\sigma_{\min}a(\frac{d}{2}-c-\frac{a}{2})=|M| \tag{3.79}$$

From equation (3.78), the minimum stress can be determined from equation (3.80).

$$\sigma_{\min}=\frac{2(T-\sigma_c c)}{a}-\sigma_c \tag{3.80}$$

This replaces $\sigma_{\min}$ in equation (3.79) results in equation (3.81).

$$c=\frac{(d+b_t)^2-(d+4b_t)\frac{T}{\sigma_c}-6\frac{|M|}{\sigma_c}}{\frac{2T}{\sigma_c}-2d-2b_t} \tag{3.81}$$

3.7.4.4 Cracked anti-thinning and yield anti-thinning

3.7.4.4.1 Free cracked anti-thinning length and free yield anti-thinning

When the minimum stress is greater than zero and the maximum stress less than the ultimate compressive stress, then crack anti-thinning and yield anti-thinning starts, as illustrated in Figure 3.17 (d). If the cracked anti-thinning length is less than the total cracked thinning length and the yield anti-thinning length is less than the total yield thinning length, then the shape of stress is the same as cracked thinning and yield thinning one, as illustrated in Figure 3.17 (a). Force equation of equilibrium gives equation (3.60) and moment equation of equilibrium gives equation (3.61).

From equation (3.60), the yield length c (which is negative) can be determined from equation (3.62).

Because $a>0$, then the new elastic length can be determined from equation (3.64).

The new cracked length b is also negative, and this length can also be determined in equation (3.65)

3.7.4.4.2 Limited cracked anti-thinning length and free yield anti-thinning

If the anti-thinning cracked length calculated in equation (3.72) (which is positive) is greater than the total cracked thinning length b_t, and the yield anti-thinning is less than the total yield length, the new total cracked length is zero and the new cracked anti-thinning length is b_t, he new elastic length is determined by equation (3.77). Then force equation of equilibrium gives equation (3.78) and moment equation of equilibrium gives equation (3.79).

From equation (3.78), the maximum stress can be determined from equation (3.80), and this replaces σ_{max} in the equation (3.79) and results in equation (3.81).

3.7.4.4.3 Free cracked anti-thinning length and limited yield anti-thinning

If the anti-thinning cracked length calculated in equation (3.72) is less than the total cracked thinning length b_t, and the absolute value of the yield anti-thinning determined in equation (3.62) is greater than total yield length, so the new total cracked length is zero, the new cracked anti-thinning length is b_t, and the new elastic length is determined by equation (3.75). The new bending moment is in the middle of the new elastic length and the new maximum stress is determined from equation (3.74).

3.7.4.4.4 Limited cracked anti-thinning length and limited yield anti-thinning

If the anti-thinning cracked length calculated in equation (3.72) is greater than the total cracked thinning length b_t, and the absolute value of the yield anti-thinning determined in equation (3.62) is greater than the total yield length, then the new total cracked length is zero, the new cracked anti-thinning length is b_t, the new total yield length is zero, and the new yield anti-thinning length is c_t. The total elastic length is then determined from equation (3.82).

$$a = d + b_t + c_t \tag{3.82}$$

Force equation of equilibrium gives equation (3.83) and moment equation of equilibrium gives equation (3.84).

$$\frac{d+b_t+c_t}{2}(\sigma_{\max}+\sigma_{\min}) = T + \sigma_c c_t \tag{3.83}$$

$$\begin{aligned}&\frac{1}{2}(\sigma_{\max}-\sigma_{\min})(d+b_t+c_t)(\frac{d}{2}+c_t-\frac{d+b_t+c_t}{3})\\&+\sigma_{\min}(d+b_t+c_t)(\frac{d}{2}+c_t-\frac{d+b_t+c_t}{2}) = |M| + \sigma_c c_t \frac{d+c_t}{2}\end{aligned} \tag{3.84}$$

From equation (3.83), the maximum stress can be determined from equation (3.85).

$$\sigma_{\max} = \frac{2(T+\sigma_c c_t)}{d+b_t+c_t} - \sigma_{\min} \tag{3.85}$$

This replaces $\sigma_{\max}$ in equation (3.84) and results in equation (3.86).

$$\sigma_{\min} = \frac{(T+\sigma_c c_t)(d+4c_t-2b_t) - 3\sigma_c c_t(d+c_t) - 6|M|}{(d+b_t+c_t)^2} \tag{3.86}$$

3.7.4.5 Yield thinning only

When the minimum stress is greater than zero and the total cracked length is zero, and the maximum stress is greater than the ultimate compressive stress, then only yield thinning starts, as illustrated in Figure 3.17 (e). The force equation of equilibrium gives equation (3.87), the moment equation of equilibrium gives equation (3.88), and the geometry relation equation (3.89).

$$\sigma_c c + \frac{a}{2}(\sigma_c + \sigma_{\min}) = T \tag{3.87}$$

$$\sigma_c c(\frac{d}{2}-\frac{c}{2})+\frac{1}{2}(\sigma_c-\sigma_{\min})a(\frac{d}{2}-c-\frac{a}{3})+\sigma_{\min}a(\frac{d}{2}-c-\frac{a}{2})=|M| \tag{3.88}$$

$$c=d-a \tag{3.89}$$

From equation (3.87) and equation (3.89), the yield length can be determined from equation (3.90).

$$\sigma_{\min}=\frac{2T-\sigma_c(2d-a)}{a} \tag{3.90}$$

This replaces the $\sigma_{\min}$ and c in equation (3.88) and results in equation (3.91):

$$a=\frac{3d}{2}-\frac{3|M|}{\sigma_c d-T} \tag{3.91}$$

3.7.4.6 Yield anti-thinning only

When the minimum stress is greater than zero and the total cracked length is zero, and the maximum stress is less than the ultimate compressive stress, and the total yield length c_t *is* greater than zero, then only yield thinning starts, as illustrated in Figure 3.17 (f). Then force equation of equilibrium gives equation (3.78) and moment equation of equilibrium gives equation (3.79).

From equation (3.78), the maximum stress can be determined from equation (3.80), and this replaces $\sigma_{\max}$ in the equation (3.79) and results in equation (3.81).

If the absolute value of the yield anti-thinning, determined in equation (3.62), is greater than the total yield length, so the new total cracked length is zero, the new total yield length is zero, and the new yield anti-thinning length is c_t.

The total elastic length is determined by equation (3.92).

$$a = d + c_t \tag{3.92}$$

Force equation of equilibrium gives equation (3.93) and moment equation of equilibrium gives equation (3.94).

$$\frac{d+c_t}{2}(\sigma_{\max} + \sigma_{\min}) = T + \sigma_c c_t \tag{3.93}$$

$$\begin{aligned}&\frac{1}{2}(\sigma_{\max} - \sigma_{\min})(d+c_t)(\frac{d}{2} + c_t - \frac{d+c_t}{3}) \\ &+ \sigma_{\min}(d+c_t)(\frac{d}{2} + c_t - \frac{d+c_t}{2}) = |M| + \sigma_c c_t \frac{d+c_t}{2}\end{aligned} \tag{3.94}$$

From equation (3.83), the maximum stress can be determined in equation (3.95).

$$\sigma_{\max} = \frac{2(T + \sigma_c c_t)}{d + c_t} - \sigma_{\min} \tag{3.95}$$

This replaces $\sigma_{\max}$ in equation (3.94) results in equation (3.96).

$$\sigma_{\min} = \frac{(T + \sigma_c c_t)(d + 4c_t) - 3\sigma_c c_t (d + c_t) - 6|M|}{(d + c_t)^2} \tag{3.96}$$

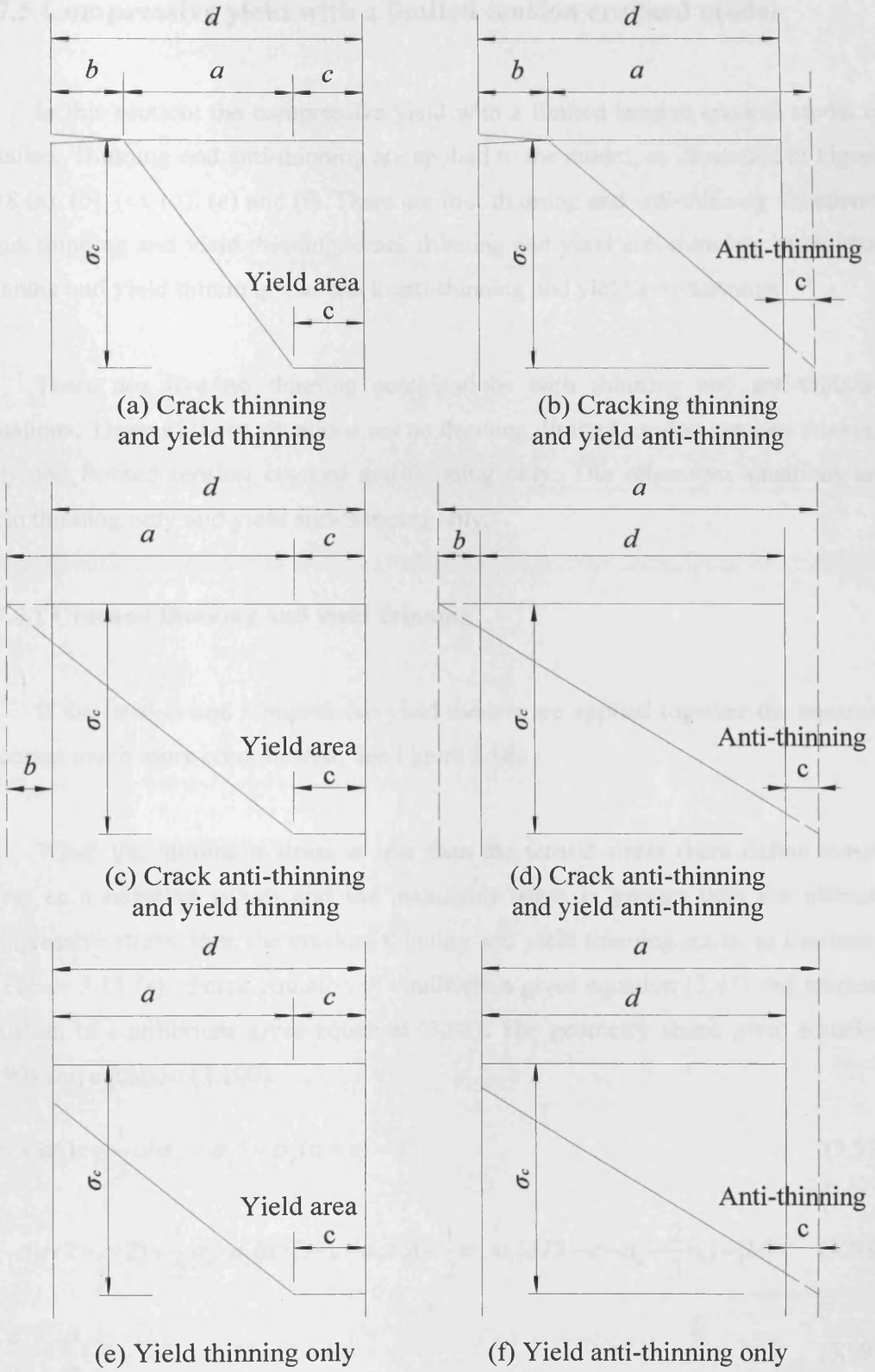

Figure 3.17 Compressive yield with no tension models thinning and anti-thinning

3.7.5 Compressive yield with a limited tension cracked model

In this section, the compressive yield with a limited tension cracked model is detailed. Thinning and anti-thinning are applied to the model, as illustrated in Figure 3.18 (a), (b), (c), (d), (e) and (f). There are four thinning and anti-thinning situations: crack thinning and yield thinning, crack thinning and yield anti-thinning, crack anti-thinning and yield thinning, and crack anti-thinning and yield anti-thinning.

There are five no thinning combinations with thinning and anti-thinning situations. Three of these situations are no thinning, limited tension cracked thinning only and limited tension cracked anti-thinning only. The other two situations are yield thinning only and yield anti-thinning only.

3.7.5.1 Cracked thinning and yield thinning

If the tension and compressive yield models are applied together the equation becomes much more complicated. See Figure 3.18.

When the minimum stress is less than the tensile stress (here define tensile stress as a negative value) and the maximum stress is greater than the ultimate compressive stress, then the cracked thinning and yield thinning starts, as illustrated in Figure 3.18 (a). Force equation of equilibrium gives equation (3.97) and moment equation of equilibrium gives equation (3.98). The geometry shape gives equation (3.99) and equation (3.100).

$$(\sigma_c+\sigma_t)c+\frac{1}{2}a(\sigma_c+\sigma_t)-\sigma_t(a+c)=T \tag{3.97}$$

$$\sigma_c\cdot c(d/2-c/2)+\frac{1}{2}\sigma_c\cdot a_2(d/2-c-a_2/3)-\frac{1}{2}\sigma_t\cdot a_1(d/2-c-a_2-\frac{2}{3}a_1)=|M| \tag{3.98}$$

$$\frac{a_1}{a_2}=\frac{\sigma_t}{\sigma_c} \tag{3.99}$$

$$a=a_1+a_2 \tag{3.100}$$

From equation (3.97), equation (3.98), equation (3.99) and equation (3.100), the new elastic length a can be calculated and is given in equation (3.101).

$$\left[-\frac{1}{8}\frac{(\sigma_c-\sigma_t)^2}{\sigma_c}+\frac{1}{4}\frac{\sigma_c-\sigma_t}{\sigma_c+\sigma_t}\sigma_c-\frac{1}{6}\frac{\sigma_c^3}{(\sigma_c-\sigma_t)^2}-\frac{1}{4}\frac{(\sigma_c-\sigma_t)\sigma_t^2}{(\sigma_c+\sigma_t)\sigma_c}+\frac{1}{2}\frac{\sigma_c\sigma_t^2}{(\sigma_c+\sigma_t)^2}+\frac{1}{3}\frac{\sigma_t^3}{(\sigma_c+\sigma_t)^2}\right]a^2$$
$$+\left[-\frac{d}{4}(\sigma_c-\sigma_t)+\frac{T}{2\sigma_c}(\sigma_c-\sigma_t)+\frac{\sigma_c^2 d}{4(\sigma_c+\sigma_t)}-\frac{T\sigma_c}{2(\sigma_c+\sigma_t)}-\frac{d\sigma_t^2}{4(\sigma_c+\sigma_t)}+\frac{T\sigma_t^2}{2\sigma_c(\sigma_c+\sigma_t)}\right]a \qquad (3.101)$$
$$-|M|+\frac{Td}{2}-\frac{T^2}{2\sigma_c}=0$$

From equation (3.97) the yield length can be determined as equation (3.102).

$$c=\frac{T-0.5a(\sigma_c-\sigma_t)}{\sigma_c} \qquad (3.102)$$

3.7.5.2 Cracked thinning and yield anti-thinning

When the minimum stress is less than the ultimate tensile stress and the maximum stress is less than the ultimate compressive stress, and if the yield length c is greater than zero, then the crack thinning and anti-yield thinning starts, as illustrated in Figure 3.18 (b). The force equation of equilibrium gives equation (3.97) and the moment equation of equilibrium gives equation (3.98). The new elastic length a can be calculated from equation (3.101). The yield length can be determined from equation (3.102).

When the yield anti-thinning length is greater than the total yield thinning length, then the maximum stress will not be the ultimate compressive stress, but the anti-thinning length will equal to the total yield thinning length. The force equation of equilibrium gives equation (3.103) and the moment equation of equilibrium gives equation (3.104).

$$\frac{\sigma_{max}-\sigma_t}{2}a = T + \sigma_c c_t \tag{3.103}$$

$$\frac{\sigma_{max}+\sigma_t}{2}a(\frac{d}{2}+c_t-\frac{a}{3})-\sigma_t a(\frac{d}{2}-c-\frac{a}{2}) = |M| + \sigma_c c_t \frac{d+c_t}{2} \tag{3.104}$$

From equation (3.103), the maximum stress can be determined from equation (3.105).

$$\sigma_{max} = \frac{2T}{a} + \frac{2\sigma_c c_t}{a} + \sigma_t \tag{3.105}$$

This replaces σ_{max} in equation (3.104) results in equation (3.106).

$$\sigma_t a^2 - 2(T+\sigma_c c_t)a + (T+\sigma_c c_t)(3d+6c_t) - 6|M| - 3\sigma_c c_t(d+c_t) = 0 \tag{3.106}$$

If tensile stress is not equal to zero, the elastic length can be determined by equation (3.107).

$$a = \frac{(T+\sigma_c c_t) - \sqrt{(T+\sigma_c c_t)^2 - \sigma_t(3d+6c_t)(T+\sigma_c c_t) + 6|M|\sigma_t + 3\sigma_c\sigma_t c_t(d+c_t)}}{\sigma_t} \tag{3.107}$$

3.7.5.3 Cracked anti-thinning and yield thinning

When the minimum stress is greater than the ultimate tensile stress and the maximum stress is greater than the ultimate compressive stress, then crack anti-thinning and yield thinning starts, as illustrated in Figure 3.18 (c). The force equation of equilibrium gives equation (3.97) and the moment equation of equilibrium gives equation (3.98). The new elastic length a can be calculated from equation (3.101).

From equation (3.97), the yield length c can be determined from equation (3.102).

If anti-thinning then the cracked length is greater than the total cracked thinning length b_t, so the new total cracked length is zero, the new cracked anti-thinning length is b_t, and the new elastic length is determined by equation (3.77). The force equation of equilibrium gives equation (3.78) and the moment equation of equilibrium gives equation (3.79), therefore, the minimum stress can be determined from equation (3.80) and the new yield length determined from equation (3.81).

3.7.5.4 Cracked anti-thinning and yield anti-thinning

3.7.4.4.1 Free cracked anti-thinning length and Free yield anti-thinning

When the minimum stress is greater than zero and the maximum stress is less than the ultimate compressive stress, then crack anti-thinning and yield anti-thinning starts, as illustrated in Figure 3.18 (d). If the cracked anti-thinning length is less than the total cracked thinning length and the yield anti-thinning length is less than the total yield thinning length, then the shape of stress is the same as the cracked thinning and yield thinning one, as illustrated in Figure 3.18 (a). The force equation of equilibrium gives equation (3.97) and the moment equation of equilibrium gives equation (3.98). So the new elastic length can be determined from equation (3.101), and the yield length c (which is negative) can be determined from equation (3.102).

3.7.4.4.2 Limited cracked anti-thinning length and free yield anti-thinning

If the anti-thinning cracked length is greater than the total cracked thinning length b_t, and the yield anti-thinning is less than the total yield length, so the new total cracked length is zero, the new cracked anti-thinning length is b_t, and the new elastic length is determined by equation (3.77). The force equation of equilibrium gives equation (3.78) and the moment equation of equilibrium gives equation (3.79).

From equation (3.78), the maximum stress can be determined in equation (3.80), let this replace σ_{max} in the equation (3.79) and this results in equation (3.81).

3.7.4.4.3 Free cracked anti-thinning length and limited yield anti-thinning

If the anti-thinning cracked length is less than the total cracked thinning length b_t, and the absolute value of the yield anti-thinning determined in equation (3.62) is greater than the total yield length, so the new total cracked length is zero, the new cracked anti-thinning length is b_t, the new elastic length is determined by equation (3.107) and the new bending moment is in the middle of the new elastic length and the new maximum stress can be determined from equation (3.105).

3.7.4.4.4 Limited cracked anti-thinning length and limited yield anti-thinning

If the anti-thinning cracked length is greater than the total cracked thinning length b_t, and the absolute value of yield anti-thinning is greater than the total yield length, so the new total cracked length is zero, the new cracked anti-thinning length is b_t, the new total yield length is zero, and the new yield anti-thinning length is c_t. The total elastic length is then determined from equation (3.82). The force equation of equilibrium gives equation (3.83) and moment equation of equilibrium gives equation (3.84), so the maximum stress can be determined from equation (3.85) and the minimum stress can be determined from equation (3.86).

3.7.5.5 Yield thinning only

When the minimum stress is greater than zero and the total cracked length is zero, and the maximum stress is greater than the ultimate compressive stress, then only yield thinning starts, as illustrated in Figure 3.18 (e). This situation is the same as the situation detailed in section 3.7.4.5, so the same equations can be used to determine the stresses and lengths.

3.7.5.6 Yield anti-thinning only

When the minimum stress is greater than the tensile stress (here tensile stress defined as negative) and the total cracked length is zero, and the maximum stress is

less than the ultimate compressive stress, and the total yield length c_t is greater than zero, then only yield thinning starts, as illustrated in Figure 3.18 (f). This situation is the same as the situation detailed in section 3.7.4.6, so the same equations can be used to determine the stresses and lengths.

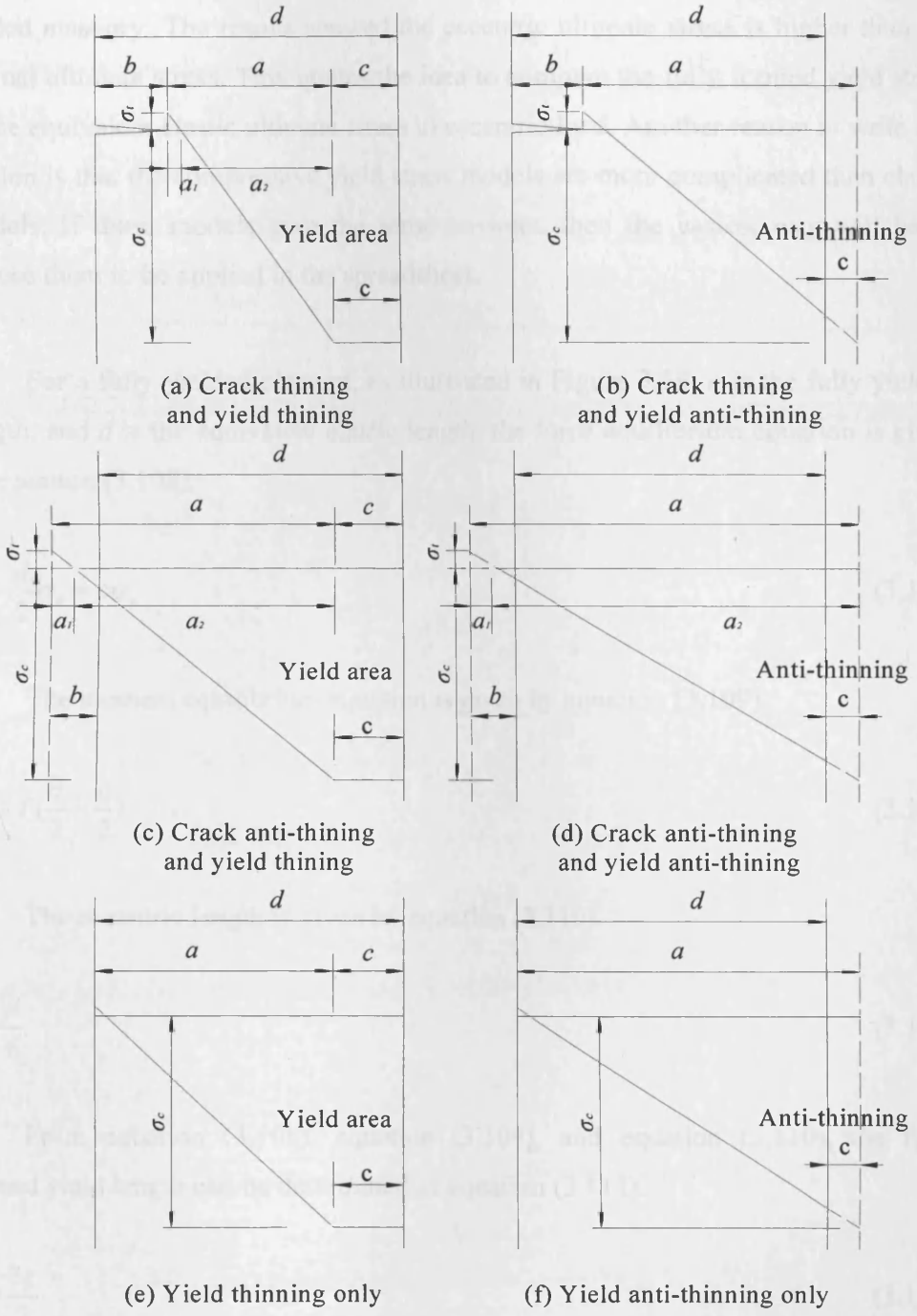

Figure 3.18 Compressive yield with limited tension models thinning and anti-thinning

3.8 Equivalent elastic stress model of compressive yield stress model

Roberts and Hughes[156] investigated the compressive strength of eccentric loaded masonry. The results showed the eccentric ultimate stress is higher than the normal ultimate stress. This ignites the idea to compare the fully formed yield stress to the equivalent elastic ultimate stress in eccentric load. Another reason to write this section is that the compressive yield stress models are more complicated than elastic models. If these models give the same answers, then the easiest way will be to choose them to be applied in the spreadsheet.

For a fully yielded element, as illustrated in Figure 3.19, c is the fully yielded length, and d is the equivalent elastic length, the force equilibrium equation is given by equation (3.108).

$$T = \frac{d}{2}\sigma_e = c\sigma_u \tag{3.108}$$

The moment equilibrium equation is given by equation (3.109).

$$Te = T(\frac{d}{2} - \frac{c}{2}) \tag{3.109}$$

The eccentric length is given by equation (3.110).

$$e = \frac{d}{6} \tag{3.110}$$

From equation (3.108), equation (3.109), and equation (3.110), the fully formed yield length can be determined as equation (3.111).

$$d = \frac{3c}{2} \tag{3.111}$$

The equivalent elastic stress from the fully formed yield stress can then be determined by equation (3.112).

$$\frac{\sigma_e}{\sigma_c} = \frac{2c}{d} = \frac{4}{3} \tag{3.112}$$

This result shows the equivalent stress is 33.33% higher than the ultimate compressive stress.

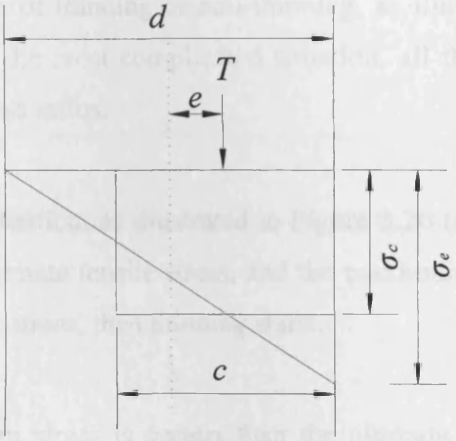

Equivalent stress of fully yield

Figure 3.19 Equivalent stress of fully yield compression

This equivalent model could be used in a spreadsheet, because the fully yield elements are very limited in extent over the arch and the length of the fully yield part is very thin about 5% of the original depth, so the energy in this part is relatively small. This idea is investigated further in the next section.

3.9 Iterative solutions for thinning and anti-thinning models

Because thinning and anti thinning of any element affects the processes in the other elements it was decided to investigate iterative solutions for thinning and anti-thinning to replace the range of separate models by a simpler iterative solution.

In this section a simple spreadsheet is introduced to explain how iterative solutions can determine the same answers as all models developed in the thinning models sections.

3.9.1 Theory

An iterative solution was developed that calculated the minimum and maximum stress using the current elastic length, and then according to the stress ratio determined a new length of thinning or anti-thinning, as illustrated in Figure 3.20. Figure 3.20 only shows the most complicated situation, all the other situations can also be solved by the stress ratios.

For the thinning situation, as illustrated in Figure 3.20 (a), when the minimum stress is less than the ultimate tensile stress, and the maximum stress is greater than the ultimate compressive stress, then thinning starts.

When the minimum stress is greater than the ultimate tensile stress, and the maximum stress is less than the ultimate compressive stress, then anti-thinning starts, as illustrated in Figure 3.20 (b).

The ratio of length can be determined by the ratio of stress, as expressed in equation (3.113), equation (3.114) and equation (3.115).

$$\frac{\sigma_c - \sigma_t}{\sigma_{\max} - \sigma_{\min}} = \frac{a}{d} \tag{3.113}$$

$$\frac{\sigma_t - \sigma_{\min}}{\sigma_{\max} - \sigma_{\min}} = \frac{b}{d} \tag{3.114}$$

$$\frac{\sigma_{\max} - \sigma_c}{\sigma_{\max} - \sigma_{\min}} = \frac{c}{d} \tag{3.115}$$

Here, positive b and c , means thinning, otherwise anti-thinning .

$$T_n = T - \sigma_c c \tag{3.116}$$

Where c is negative and anti-thinning.

$$M_n = M - \sigma_c c(d/2 - c/2) - T_n(d/2 - a/2 - c) \tag{3.117}$$

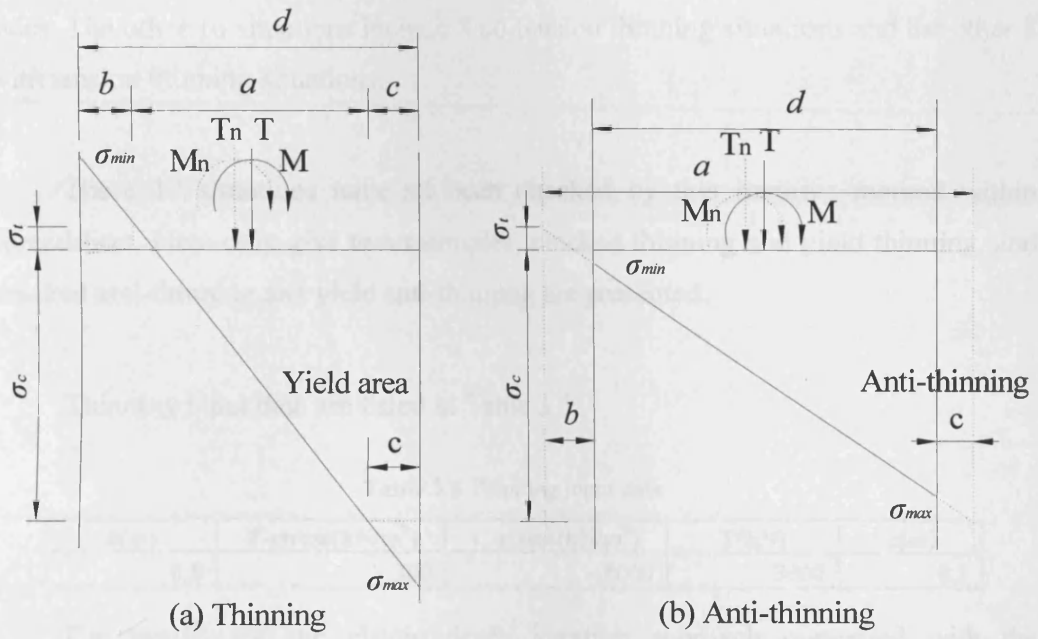

Figure 3.20 Iterative solutions for thinning and anti-thinning

The new elastic length a is then used as the next step d, and the new thrust and moment applied to the centre of the new elastic length are used to determine the next iteration values. When the elastic length change is very small when related to the original length, then the solution of the elastic length is considered to have converged to the correct solution. This solution is then compared with the theoretical value determined in the last section.

3.9.2 Examples of different models

Iterative solutions for thinning and anti-thinning can determine the new lengths for all the models. Here examples of theoretical solutions and the iterative solutions are compared in a standard spreadsheet. These comparisons verify the different methods.

There are four different theoretical models and in total 17 theoretical thinning, anti-thinning, and no thinning situations. One of these situations is no thinning both sides. The other 16 situations include 8 no tension thinning situations and the other 8 with tension thinning situations.

These 17 situations have all been checked by this iterative method within spreadsheet. Here only give two examples, cracked thinning and yield thinning, and cracked anti-thinning and yield anti-thinning are presented.

Thinning input data are listed in Table 3.5.

Table 3.5 Thinning input data

d(m)	T-stress(kN/m^2)	C-stress(kN/m^2)	T(kN)	e(m)
0.8	300	8000	3000	0.2

The results for the elastic depth iterative approach compared with the theoretical results are listed in Table 3.6. The row of 'Elastic depth' is iterative depth results. The 'Difference rate' is defined as the relative difference between the iterative and theoretical solution, i.e. it is iterative result minus the theoretical result then this result is divided by theoretical result.

Table 3.6 shows that at iteration 5 the elastic depth is accurate enough for engineering use.

Table 3.6 Thinning results comparison

	Iteration 1	Iteration 5	Iteration 10	Iteration 20
Elastic depth(m)	0.590	0.351	0.350	0.350
Difference rate	6.89E-01	4.125E-03	2.65E-07	2.128E-09

Figure 3.21 which shows the iterative solution lengths for thinning. crack length and plastic length indicates that all are thinning at the same time and almost converge at the same time. Iteration 5 is considered accurate enough for all three part lengths.

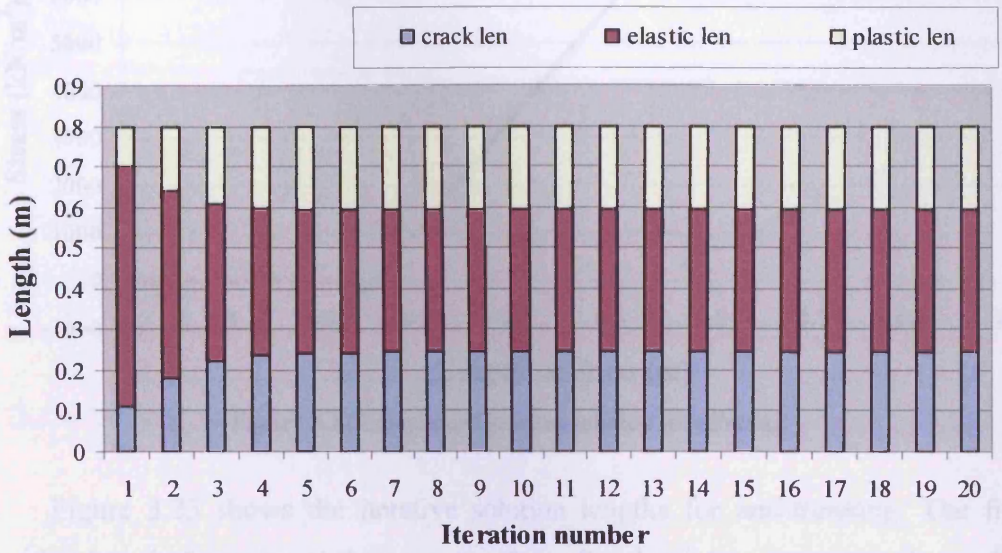

Figure 3.21 Iterative solution for thinning

Figure 3.22 presents the section lengths and stress solution results for Iteration 5. This figure gives a very clear thinning stress distribution over the calculated length.

The anti-thinning input data example is listed in Table 3.7.

Table 3.7 Anti-thinning input data

d(m)	T-stress(kN/m^2)	C-stress(kN/m^2)	T(kN)	e(m)
0.8	300	8000	3000	0.1

Table 3.8 shows the anti-thinning iteration 5 elastic depth is accurate enough for engineering use.

Table 3.8 Anti-thinning results comparison

	Iteration 1	Iteration 5	Iteration 10	Iteration 20
Elastic depth(m)	1.180	1.049	1.049	1.049
Difference rate	1.257E-01	8.576E-05	7.547E-09	2.128E-09

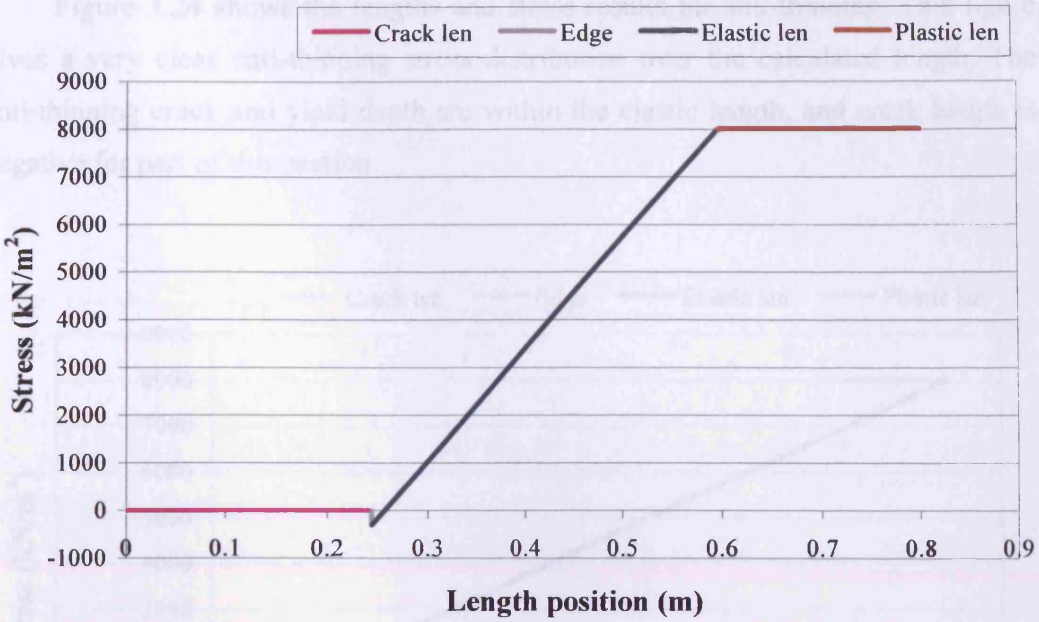

Figure 3.22 Lengths and stresses solution for thinning

Figure 3.23 shows the iterative solution lengths for anti-thinning. The first iteration has the largest anti-thinning step then after that it has progressively smaller and smaller anti-thinning steps. The crack length and plastic length are anti-thinning at the same time and almost converge at the same time. Iteration 5 is again accurate enough for all three part lengths. Anti-thinning crack and yield length are negative in Figure 3.23.

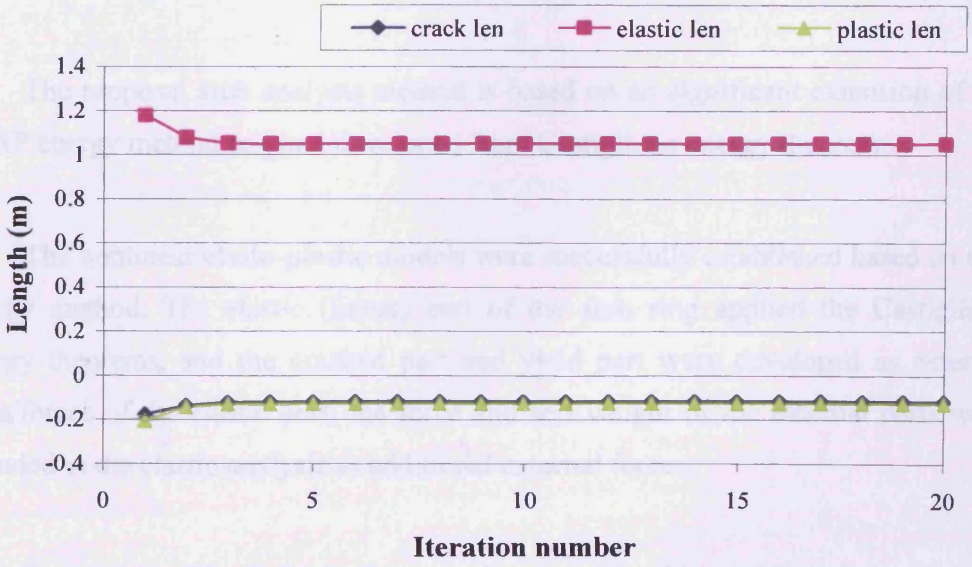

Figure 3.23 Iterative solution for anti-thinning

Figure 3.24 shows the lengths and stress results for anti-thinning. This figure gives a very clear anti-thinning stress distribution over the calculated length. The anti-thinning crack and yield depth are within the elastic length, and crack length is negative for part of this section.

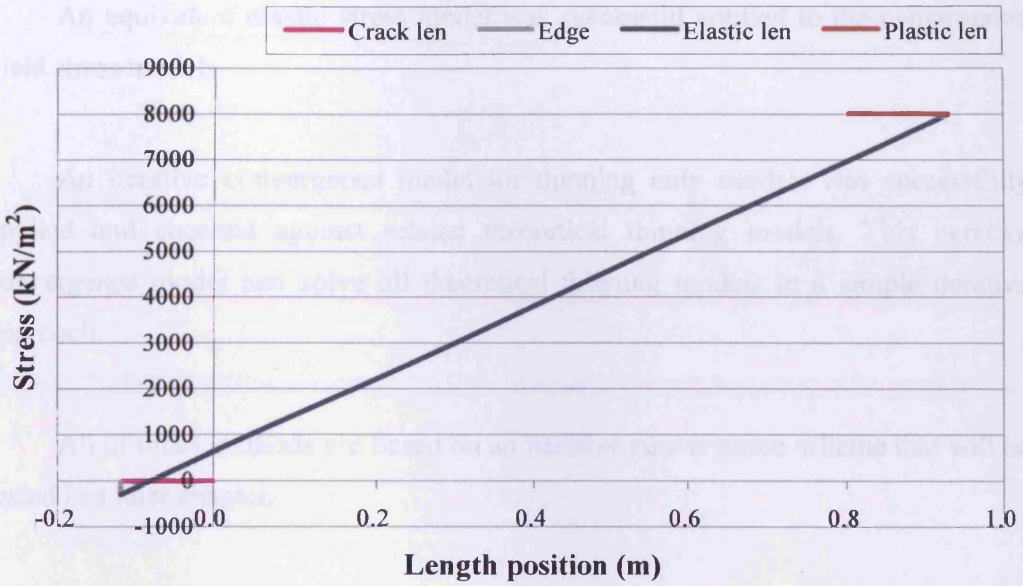

Figure 3.24 Iterative solution stress for anti-thinning

3.10 Conclusions

The proposal arch analysis method is based on an significant extension of the CTAP energy method original developed from Castigliano energy theorems.

The nonlinear elasto-plastic models were successfully established based on this energy method. The elastic (linear) part of the arch ring applied the Castigliano energy theorems, and the cracked part and yield part were developed as external parts/forces of the elastic part, the force and self weight of the external parts were included in the elastic analysis as additional external forces.

A new type of load distribution was developed for this model.

Tensile stress and compressive yield stress components were also successfully developed for this model.

The thinning and anti-thinning can be concluded in Table 3.9.

An equivalent elastic stress model was successful applied to the compressive yield stress models.

An iterative convergence model for thinning only models was successfully applied and checked against related theoretical thinning models. This iterative convergence model can solve all theoretical thinning models in a simple iterative approach.

All of these methods are based on an iterative convergence scheme that will be tested in a later chapter.

Table 3.9 Thinning and anti-thinning conclusion and their main equations (Equ.)

Crack	Yield	Free/limited crack anti-thinning	Free/limited yield anti-thinning	No tension cracked model	Limited Tension cracked model	Compressive yield with no tension cracked model	Compressive yield with a limited tension cracked model
Thinning	**No Yield**			Equ. (3.38)	Equ. (3.54)	Equ. (3.38)	Equ. (3.54)
Thinning	**Thinning**					Equ. (3.64)	Equ. (3.101)
Thinning	**Anti-thinning**		**Free**			Equ. (3.70)	Equ. (3.101)
Thinning	**Anti-thinning**		**Limited**			Equ. (3.75)	Equ. (3.107)
Anti-thinning	**No Yield**	**Free**		Equ. (3.45)	Equ. (3.45)	Equ. (3.45)	Equ. (3.45)
Anti-thinning	**No Yield**	**Limited**		Equ. (3.38)	Equ. (3.54)	Equ. (3.38)	Equ. (3.54)
Anti-thinning	**Thinning**	**Free**				Equ. (3.64)	Equ. (3.101)
Anti-thinning	**Thinning**	**Limited**				Equ. (3.81)	Equ. (3.81)
Anti-thinning	**Anti-thinning**	**Free**	**Free**			Equ. (3.64)	Equ. (3.101)
Anti-thinning	**Anti-thinning**	**Limited**	**Free**			Equ. (3.81)	Equ. (3.81)
Anti-thinning	**Anti-thinning**	**Free**	**Limited**			Equ. (3.75)	Equ. (3.107)
Anti-thinning	**Anti-thinning**	**Limited**	**Limited**			Equ. (3.86)	Equ. (3.86)
No crack	**Thinning**					Equ. (3.91)	Equ. (3.91)
No crack	**Anti-thinning**		**Free**			Equ. (3.81)	Equ. (3.81)
No crack	**Anti-thinning**		**Limited**			Equ. (3.96)	Equ. (3.96)

4 Development of the spreadsheet

4.1 Introduction

One of the principal problems with the acceptance of new approaches to bridge assessment is the combination of suitable pre and post processors, to allow easy application and interpretation of the results, with an analysis "engine" which is well understood and trusted by the assessment engineer. Finite Element analysis is a well accepted "black box" analysis but may be considered as "overkill" for routine assessments. Limit Analysis based assessment methods can be "transparent" but are quite simplistic. The move from assessments based solely on ultimate load towards assessments undertaken on the basis of serviceability requires the development of suitable "transparent" elastic based assessment tools.

The requirement for purpose written 'black box' software for the current study was seen as a significant drawback. The spreadsheet developed in this chapter attempts to rectify this issue by providing an approach that includes all the features of an advanced cracking elastic analysis using a Castigliano method analysis within a standard spreadsheet format familiar to most practicing engineers. The intention was to allow engineers to understand bridge assessments using a procedure that is both fully transparent and suitable for subsequent user modification.

Spreadsheets are in common use by engineers for both tabular based calculations and also for specific sequential type calculations. The application of this Castigliano method spreadsheet contains significant portions of both types of calculations.

The spreadsheet as presented can operate in two ways. Firstly, with the user entering the position and load, or secondly, using the built-in optimisation software, contained within spreadsheets, to get the critical position and/or ultimate or serviceability load. This is an additional feature not present in previous elastic based analysis.

The spreadsheet contains all the calculations needed to analyse all aspects of a single span. The spreadsheet has four main parts: input and output data sheet ('Main'), calculation sheet ('Elements'), advanced setting sheet and result plot sheets.

This chapter contains details of the application of Castigliano energy thinning method to the analysis of single span masonry arch bridges using a standard spreadsheet. The method has been enhanced to include both limited tensile strength in the masonry, compressive yielding at the extreme fibres, new load distributions and the use of an optimiser to automatically determine critical load location . The use of a standard spreadsheet allows the assessment engineer to have full access to all the elements of the analysis within the assessment process and this transparent approach can be used to simulate either a load controlled ultimate load analysis or can be used to simulate the passage of a load train over the structure and thus find the critical load location.

The theory for use in this spreadsheet has been developed in the last chapter. Service and ultimate loads can be applied and results obtained using this spreadsheet. This spreadsheet can directly determine the stress and strain in the arch and it presents a wide range of graphs. Furthermore, the critical failure/serviceability limit load can be obtained by the standard optimisation package within the spreadsheet and it finds the optimum location by the use of simple micro code. This spreadsheet can also analyse a distorted arch by inputting surveyed data, using cubic spline interpolation. The analysis includes the Castigliano theory of arch analysis, the soil masonry interactions, multi-axles, thinning models and load distribution. An example application is given at the end.

This chapter is written so as to allow the reader to become the user so occasionally it reads slightly more like a user manual than a traditional thesis. This is considered justified as the development of this spreadsheet is seen as integral to the development of the serviceability approach developed in later chapters.

4.2 Main sheet

The spreadsheet containing all the calculations needed to analyse all aspects of a single span arch is shown in Figure 4.1. The main spreadsheet is divided into 21 boxes (major elements), A-U, data input boxes including a surveyed data input option, calculation box, results and result charts. All data is in SI units.

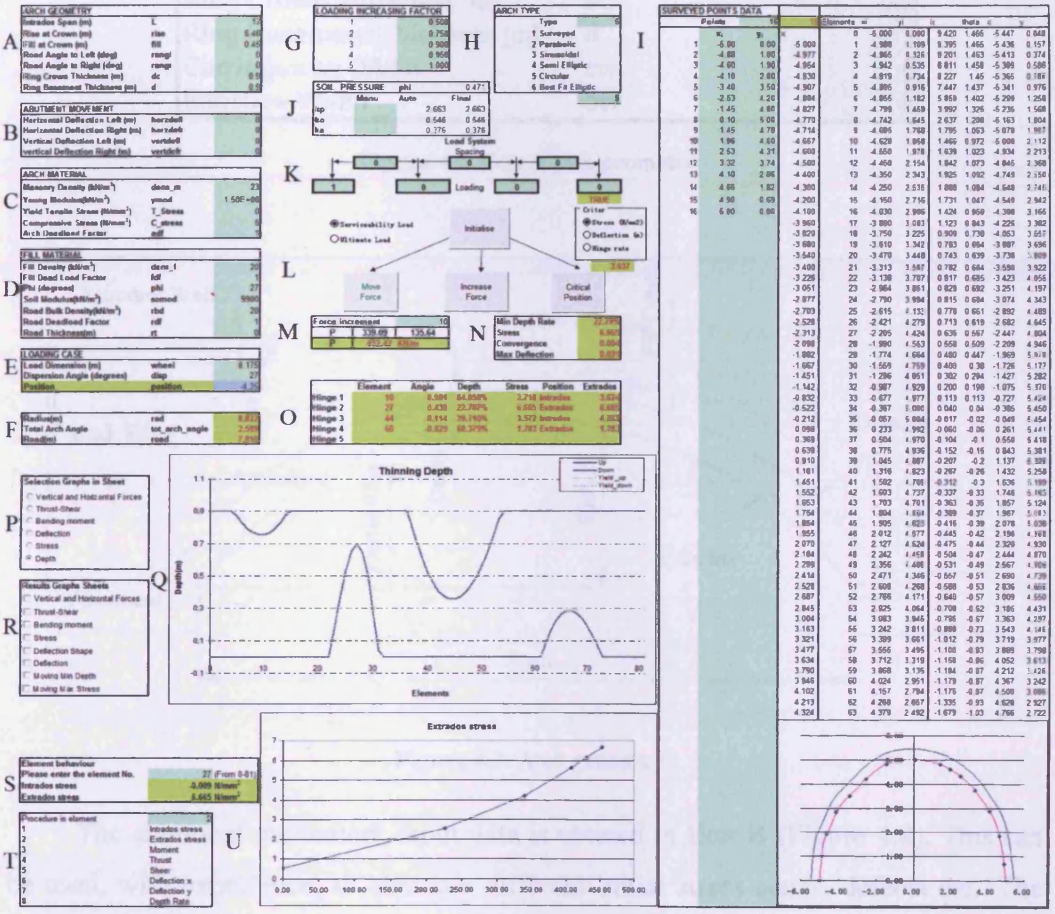

Figure 4.1 Main sheet layout of Castigliano analysis spreadsheet

The basic geometric and material input data is entered in Box A, as illustrated in Figure 4.2 and Figure 4.3, and includes the intrados span, the rise at crown, the fill depth at crown, road angle, the arch ring thickness, carriageway width and effective width. Effective width can be calculated by spreadsheet if keep blank, otherwise user effective width accepted.

Road angle's direction is from right to left, if road climbing, positive, other wise negative.

	ARCH GEOMETRY		
	Intrados Span (m)	L	14
	Rise at Crown (m)	rise	6
	Fill at Crown (m)	fill	0.45
A	Road Angle to Left (deg)	rangl	10
	Road Angle to Right (deg)	rangr	-10
	Ring Crown Thickness (m)	dc	0.9
	Ring Basement Thickness (m)	d	0.9
	Carriageway Width	cw	6
	Effective Width	ew	6

Figure 4.2 Box A arch geometry

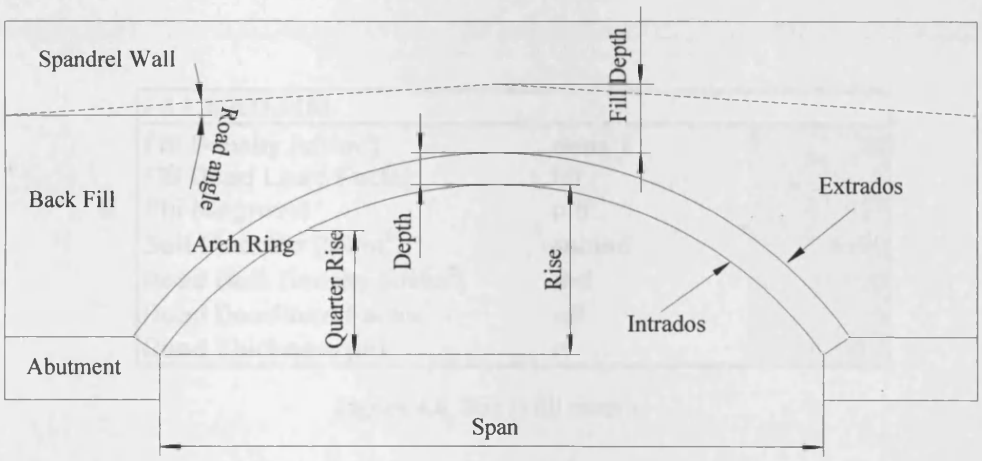

Figure 4.3 Arch geometry

The abutment movement input data is entered in Box B (Figure 4.4). This can be used, with experience, to simulate different initial stress states, defects etc.. The coordinate direction is the same as the arch ring coordinate.

	ABUTMENT MOVEMENT		
	Horizontal Deflection Left (m)	horzdefl	0
B	Horizontal Deflection Right (m)	horzdefr	0
	Vertical Deflection Left (m)	vertdefl	0
	vertical Deflection Right (m)	vertdefr	0

Figure 4.4 Box B abutment movement

The masonry density, arch stiffness, yield tensile strength, compressive stress and arch dead load factor complete the masonry data in box C (Figure 4.5).

	ARCH MATERIAL		
	Masonry Density (kN/m^3)	dens_m	23
C	Young Modulus (kN/m^2)	ymod	1.50E+06
	Yield Tensile Stress (N/mm^2)	T_Stress	0
	Compressive Stress (N/mm^2)	C_stress	10
	Arch Deadload Factor	adf	1

Figure 4.5 Box C arch material

The fill density, fill dead load factor, angle of internal shearing resistance, along with soil modulus, road bulk density, road dead load factor and road thickness complete the fill material data in Box D (Figure 4.6).

	FILL MATERIAL		
	Fill Density (kN/m^3)	dens_f	20
	Fill Dead Load Factor	fdf	1
D	Phi (degrees)	phi	27
	Soil Modulus (kN/m^3)	somod	9900
	Road Bulk Density (kN/m^3)	rbd	20
	Road Deadload Factor	rdf	1
	Road Thickness (m)	rt	0.2

Figure 4.6 Box D fill material

The wheel loads are defined in terms of the loaded length and the dispersion angle, as shown in Figure 4.7, also included is the load location of the principle axle. If the load pattern has more than one axle, then this position means the first right load position. The zero position is in the middle of the bridge. So negative value of position means the position is in the left side of the bridge.

	LOADING CASE		
E	Load Dimension (m)	wheel	0.175
	Dispersion Angle (degrees)	disp	27
	Position	position	-4.25

Figure 4.7 Box E loading case

Box F (Figure 4.8) automatically determines some additional geometric data. Effective Lane width here is the final effective lane width. It can be the data from the user value in the Box A 'effective width' or calculated from lane number multiple by lane width calculated in 'Advanced' sheet.

F	Effective Lane Width (m)	lw	6.000
	Radius (m)	rad	7.083
	Total Arch Angle	tot_arch_angle	2.835
	Road (m)	road	7.350

Figure 4.8 Box F simple calculation

Box G (Figure 4.9) includes the five loading increasing load factors. These factors will be introduced in section 4.2.1.

	LOADING INCREASING FACTOR	
G	1	0.500
	2	0.750
	3	0.900
	4	0.950
	5	1.000

Figure 4.9 Box G loading increasing factors

Box H (Figure 4.10) is the arch geometry type selection. There are six types of arch that can be chosen. First is surveyed arch type. Second is parabolic type. If this type is selected, the parabolic arch will be automatically created in the calculation sheet, the same as Sinusoidal, Semi-Elliptic, Circular and Best Fit Elliptic. Finally, the best fit elliptic type arch also needs the input of the rise at the quarter span. More details will be introduced in the next section.

H

ARCH TYPE	
Type	5
1 Surveyed	
2 Parabolic	
3 Sinusoidal	
4 Semi-Elliptic	
5 Circular	
6 Best Fit Elliptic	

Figure 4.10 Box H arch type

If the arch type is surveyed, the surveyed data have to be input in box I (Figure 4.11). The input data can be as large as 81 points. The spreadsheet will calculate the data and use cubic spline to fit these surveyed points. Then the fitted arch ring is divided into 80 elements. The cubic spline is defined as a function in a Macro. The tabulated value of the elements is given alongside the detailed calculation results of the cubic spline fit, see Figure 4.11.

I

SURVEYED POINTS DATA			
	Points		16
		x_i	y_i
	1	-5.00	0.00
	2	-4.88	1.00
	3	-4.60	1.90
	4	-4.10	2.80
	5	-3.40	3.50
	6	-2.53	4.20
	7	-1.45	4.80
	8	0.10	5.00
	9	1.45	4.78
	10	1.96	4.60
	11	2.53	4.31
	12	3.32	3.74
	13	4.10	2.86
	14	4.66	1.82
	15	4.90	0.69
	16	5.00	0.00

Figure 4.11 Box I surveyed points data

Box J (Figure 4.12) determines the soil Rankine pressure coefficients. The value in this box is calculated from fill material angle, so it is no necessary to input this data. These coefficients of soil pressure can be automatically calculated by the equations

$$k_p = \frac{1 + \sin \phi}{1 - \sin \phi} \tag{4.1}$$

$$k_0 = 1 - \sin \phi \tag{4.2}$$

$$k_a = \frac{1}{k_p} = \frac{1 - \sin \phi}{1 + \sin \phi} \tag{4.3}$$

Also these data can be input by hand, the final value is the value put by hand or the auto value (if the Manu cell is kept blank).

	SOIL PRESSURE	phi		0.471
		Manu	Auto	Final
J	kp		2.663	2.663
	ko		0.546	0.546
	ka		0.376	0.376

Figure 4.12 Box J coefficient of soil pressure

The loading is provided by the vehicle axle loads.

The axle pattern is shown in box K (Figure 4.13) and allows for axles with different spacing and relative loadings. The spaces between loads are any value totalling less than the bridge span, and the load factors of all loads must add up to 1. The check cell below this load system is set to check if these values are correct.

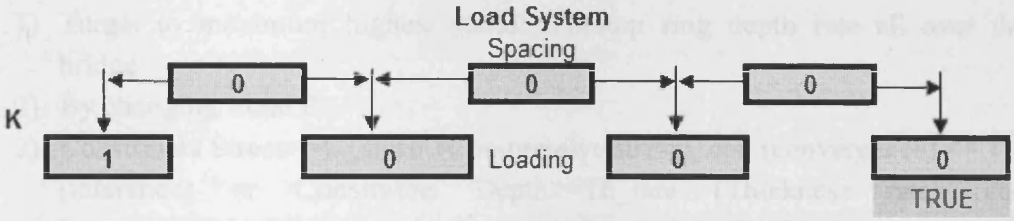

Figure 4.13 Box K load system

The analysis can deal with two types of loading cases showed in box L (Figure 4.14), a moving load case and a stationary incremental loading case. The moving load case can find the most critical position all over the bridge under any service load or ultimate load. The stationary load can be increased to find the ultimate/ serviceability limit condition. The last button combines these two methods to find the limit condition at the critical position.

For the first method of load application, a fixed magnitude of load is allowed to move across the bridge span, at specified movement increments. At each movement increment, the stresses and deflections are calculated and checked for convergence before proceeding with another increment. If a load value greater than the collapse load of the bridge is specified manually, the analysis will fail to converge.

Box L contains the options to select the ultimate limit load or the serviceability limit load, and the serviceability criteria also can be choose to determine the particular serviceability limit load. Box L also contains the buttons to run the spreadsheet optimisation macro. The button 'Initial' is a function using a macro in the spreadsheet, only to set some initial data, for example placing the loading at the quarter point and setting the default force as 40% of the MEXE PAL (Provisional Assessment Load) based on a 2.5m lane width.

'Move Force' button runs the macro that moves the loading position, and the steps data are from Moving steps in the advanced setting sheet which will be introduced in section 4.4.

'Increase Force' uses the solver in the spreadsheet. This button's constraints and optimisation in the following way:

1) Target to maximum highest stress/minimum ring depth rate all over the bridge
2) By changing Load P
3) Constraints Stress<=C_stress (Compressive stress), con (convergence) <= Tol (tolerance) or Constraints Depth>=Th_rate (Thickness rate), con (convergence) <= Tol (tolerance) or Constraints Deflection<=acceptable deflection, con (convergence) <= Tol (tolerance)

'Critical Position' combines the two buttons 'Move Force' and 'Increase Force by Depth'. If already using the button 'Increase Force' in a particular position, it has to be reset by the 'Initialise' button to initialise the load.

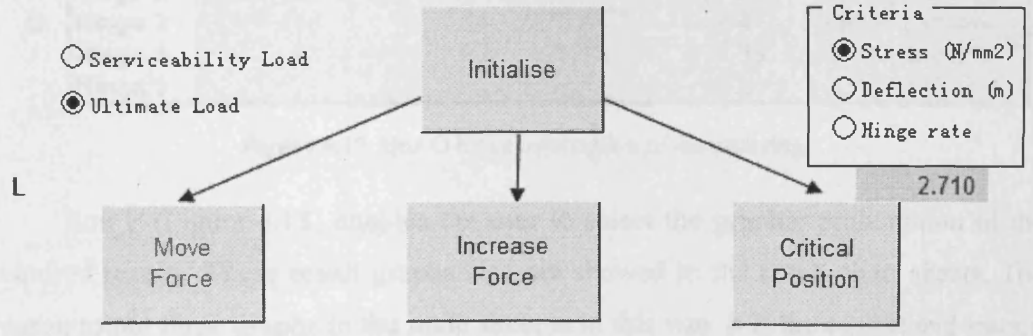

Figure 4.14 Box L buttons to run the spreadsheet optimisation macro

A limit load value or a service load value can be entered by the user into box M (Figure 4.15). The force increment details the initial force increment and the total live load carried by the arch. The white background cells are the 40% MEXE PAL load to initial the load.

M	Force increment	10
	PAL*40%	174.6 kN/2.5m
	P	174.6 kN/m

Figure 4.15 Box M Details of live load carried by the bridge

Box N (Figure 4.16) contains the critical serviceability values calculated by the analysis. These values can then be used to the spreadsheet to check the serviceability criteria or can simply be displayed for user information.

N	Stress (N/mm^2)	1.39
	Deflection (m)	0.0046
	Depth Rate	63.7%

Figure 4.16 Box N control value of the limit value

Box O (Figure 4.17) contains the hinge information calculated by the spreadsheet. This includes the critical element numbers and face as well as the peak stress. These values are used to help to meet the serviceability criteria limit. These discussions will be detailed in chap`ter 6.

O		Element	Stress	Depth	Ver. Def.	Hor. Def.	Position
	Hinge 1	11	4.82	52.2%	-0.0052	0.0041	Intrados
	Hinge 2	28	13.33	11.6%	-0.0539	0.0550	Extrados
	Hinge 3	46	7.14	20.2%	0.0747	0.0534	Intrados
	Hinge 4	68	3.90	28.2%	0.0029	0.0093	Extrados
	Hinge 5						

Figure 4.17 Box O hinge information of the arch ring

Box P (Figure 4.18) enables the user to select the graphic presentation of the required results. These result graphs also are showed in the result chart sheets. The reason to put these graphs in the main sheet is in this way it is the easiest and instant

to find the result graph, and puts all the important output data and graphs on one sheet.

P

Selection Graphs in Sheet

- Vertical and Horizontal Forces
- Thrust-Shear
- Bending moment
- Deflection
- Stress
- Depth

Figure 4.18 Box P graph options of results

Box Q (Figure 4.19) contains the selected chart of the results. The graph selected show the variation of the parameter required along the length of the arch at the current load. The graph selected in Box Q is only displayed adjacent to the box. In this case it is a thinning depth graph showing the location of the incipient hinges. This box for useful for a quick investigation of as range of parameter variations as it shows a range of graphs quickly without changing page.

Q

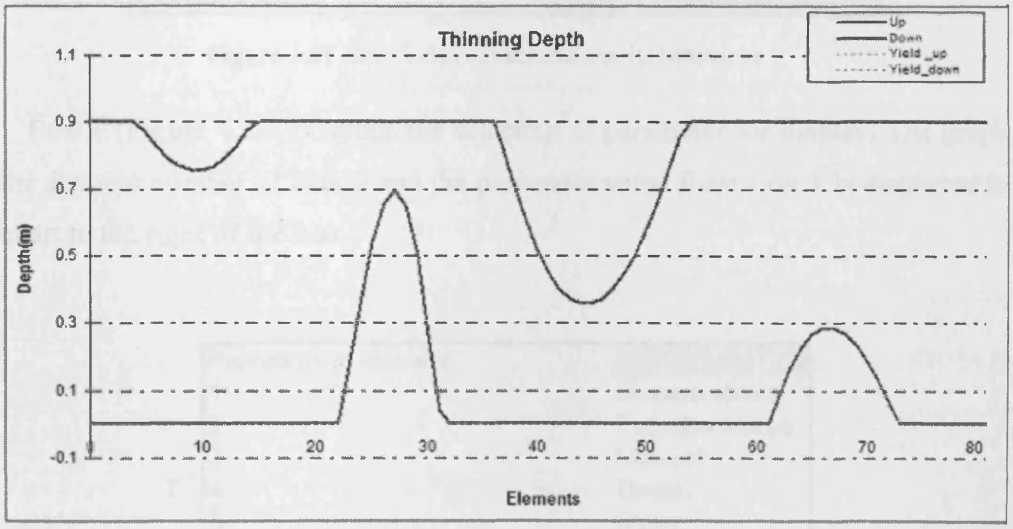

Figure 4.19 Box Q selected result graph

Box R (Figure 4.20) contains the chart sheet selections list. All selected charts are then shown as separate worksheets in the spreadsheet. Obviously, these charts are much larger than the Box Q. So it is useful when looking into greater detail of the arch results or for printing important results.

R

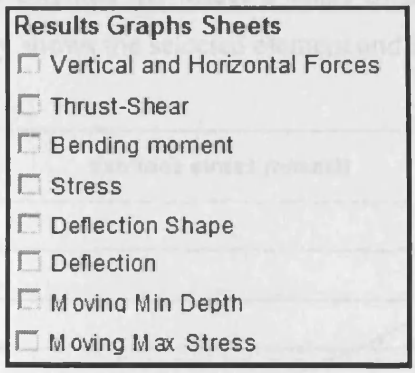

Figure 4.20 Box R result sheets options

Box S and Box T (Figure 4.21 and Figure 4.22) enables the user to investigate all parameters at a particular location along the arch at a range of different loads (or positions). Box S allows the user to enter the element number and displays the intrados and extrados stress at that location.

S

Element behaviour	
Please enter the element No.	27 (From 0-81)
Intrados stress	-0.009 N/mm^2
Extrados stress	6.665 N/mm^2

Figure 4.21 Box S element selection of its behaviour

Box T (Figure 4.22) contains the selection of parameter for display. The graph for the element number of Box S and the parameter value form Box T is displayed in the chart to the right of the box.

T

Procedure in element	2
1	Intrados stress
2	Extrados stress
3	Moment
4	Thrust
5	Sheer
6	Deflection x
7	Deflection y
8	Depth Rate

Figure 4.22 Box T selected element's result graph options

Box U (Figure 4.23) contains the selected chart of the element information results. The result chart only shows the selected element and selected behaviour.

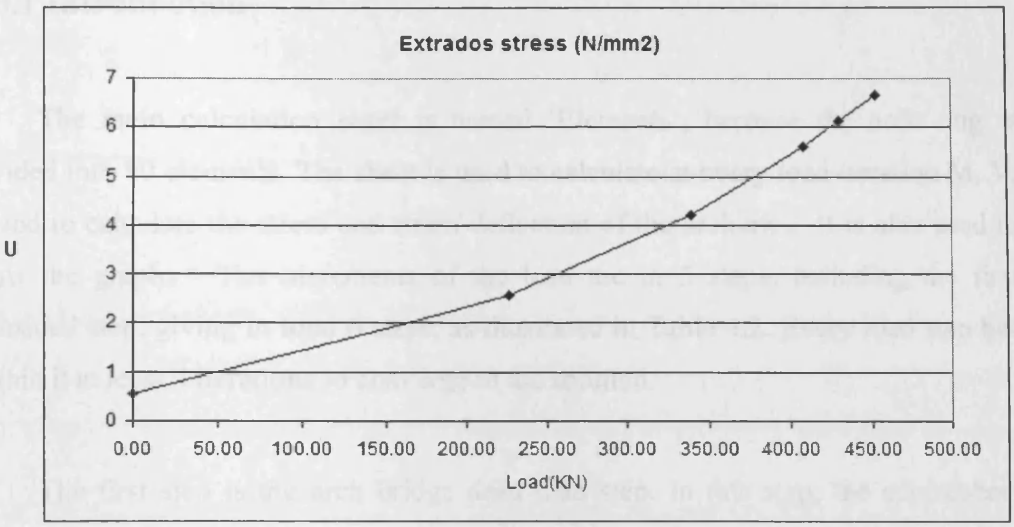

Figure 4.23 Box U selected increasing load result graph

Table 4.1 is the list of the functions of these boxes. In conclusion, the 'Main' sheet is an input and output sheet. The output results are based on the other worksheet named 'Elements'.

Table 4.1 Description of boxes in 'Main' sheet

Box	Description
A	Arch geometric input data
B	Abutment movement input data
C	Arch material input data
D	Fill material input data
E	Loading case input data
F	Simple calculation
G	Loading increasing factors input data
H	Arch type input data
I	Surveyed points input data
J	Coefficient of soil pressure input data
K	Loading pattern
L	Buttons to run critical position and limit(ultimate or serviceability) load using the spreadsheet optimisation macro
M	Limit/service load estimate and force result of the masonry arch bridge
N	Control value of the limit criteria
O	Hinge information of the arch ring
P	Graph options of results
Q	Selected result graph
R	Result sheets options
S	Element selection of its behaviour
T	Selected element's result graph options
U	Selected increasing load result graph

4.3 Calculation sheet

4.3.1 Introduction

The main calculation sheet is named 'Elements', because the arch ring is divided into 80 elements. The sheet is used to calculate at every load iteration M, V, H and to calculate the stress and strain deflection of the arch etc.. It is also used to draw the graphs. The increments of the load are in 5 steps, including the first unloaded step, giving in total 6 steps, as illustrated in Table 4.2. Every load step has within it at least 6 iterations to converge to the solution.

The first step is the arch bridge dead load step. In this step, the spreadsheet calculates the initial forces in the arch and stores these in the spreadsheet. At the end of this step it also calculates the default deflection. That is the deflection as gravity is applied. This step includes 6 iterations from iteration 0 to iteration 8, see table 4.2. The live load is assumed to move the structure from the dead load deflections. This dead load analysis is quite useful in modelling centrifuge tests where most of the dead load is applied by increasing the spinning speed up to the full scale value.

The second step applies half the total load. It includes 6 iterations. The ratio of the load can be changed in box D of the input sheet. The third to fifth steps include 6 iterations from iteration 0 to iteration 5, see table 4.2.

The sixth step is the last step. It includes 9 iteration steps from iteration 0 to iteration 8, see table 4.2. This process has been optimised as discussed later.

The main calculation sheet also includes a series of data for the plotter to use.

Table 4.2 'Elements' sheet layout

Dead load	Iteration 0	.....	Iteration 5
50% live load	Iteration 0	.....	Iteration 5
75% live load	Iteration 0	.....	Iteration 5
90% live load	Iteration 0	.....	Iteration 5
95% live load	Iteration 0	.....	Iteration 5
100% live load	Iteration 0	.....	Iteration 8

Every iteration includes the following items, as illustrated in Figure 4.24: the previous coordinate from last iteration or step, the previous thickness of the arch, the calculation of the horizontal forces and vertical forces of every element, the matrix (as derived from the theory chapter), the solution of the matrix derived by the theory chapter. Then it uses the abutment moment, vertical force and horizontal force *M V H* to determinate the element vertical force, horizontal force and cross section mid point moment, thrust and shear forces. It then calculates the new thickness, coordinate and convergence of the cross section. The convergence is based on the changing rate of the thickness. If the thickness becomes stable, the load is converged. Finally, it calculates the deflection and modifies the horizontal soil forces by active or passive soil force. It then begins the next iteration.

	Angle	x	y	deffet	enert	slopl	dx	dx	dy	r	sigmay	vfdis	dx	dy	r	sigmay	vfdis	dx	dy	r	sigmay	vfdis
1																						
0	1.417	-7.404	0.063	0.819	0.046	0.01	0.002	-3.945	7.281	8.281	0.000	0.000	-3.945	7.281	8.281	0.000	0.000	-3.945	7.281	8.281	0.000	0.000
1	1.400	-7.404	0.197	0.861	0.053	0.27	0.045	-3.923	7.149	8.155	0.000	0.000	-3.923	7.149	8.155	0.000	0.000	-3.923	7.149	8.155	0.000	0.000
2	1.364	-7.373	0.463	0.900	0.061	0.27	0.055	-3.873	6.887	7.902	0.000	0.000	-3.873	6.887	7.902	0.000	0.000	-3.873	6.887	7.902	0.000	0.000
3	1.329	-7.314	0.723	0.900	0.061	0.27	0.064	-3.814	6.627	7.646	0.000	0.000	-3.814	6.627	7.646	0.000	0.000	-3.814	6.627	7.646	0.000	0.000
4	1.293	-7.245	0.981	0.900	0.061	0.27	0.073	-3.745	6.369	7.389	0.000	0.000	-3.745	6.369	7.389	0.000	0.000	-3.745	6.369	7.389	0.000	0.000
5	1.258	-7.167	1.236	0.900	0.061	0.27	0.082	-3.667	6.114	7.129	0.000	0.000	-3.667	6.114	7.129	0.000	0.000	-3.667	6.114	7.129	0.000	0.000
6	1.222	-7.081	1.489	0.900	0.061	0.27	0.091	-3.581	5.861	6.869	0.000	0.000	-3.581	5.861	6.869	0.000	0.000	-3.581	5.861	6.869	0.000	0.000
7	1.187	-6.986	1.738	0.900	0.061	0.27	0.100	-3.485	5.612	6.606	0.000	0.000	-3.485	5.612	6.606	0.000	0.000	-3.485	5.612	6.606	0.000	0.000
8	1.152	-6.881	1.983	0.900	0.061	0.27	0.109	-3.381	5.367	6.343	0.000	0.000	-3.381	5.367	6.343	0.000	0.000	-3.381	5.367	6.343	0.000	0.000
9	1.116	-6.768	2.225	0.900	0.061	0.27	0.117	-3.268	5.125	6.078	0.000	0.000	-3.268	5.125	6.078	0.000	0.000	-3.268	5.125	6.078	0.000	0.000

vforc	hforc	veael	haael	halfv	halfh	at	ct	cee0b	cee1b	cee2b	ceeeb	a(1)	a(2)	a(3)	b(2)	b(3)	c(3)	d(1)	d(2)	d(3)
0.426	0.000	0.000	0.000	0.214	0.000	-0.081	0.000	0.000	0.000	0.000	0.000	0	0	0	0	0	0	0	0	0
11.969	20.313	6.193	10.156	5.980	10.156	-0.039	0.000	0.000	0.080	0.000	0.080	0	0	0	0	-1	5	1	0	0
12.969	19.383	18.657	30.005	6.484	9.652	0.000	0.000	0.000	0.000	5.776	5.861	0	0	0	1	-2	4	4	-10	26
13.869	18.447	32.076	48.920	6.934	9.223	0.000	0.000	0.000	0.000	11.823	17.674	0	0	0	2	-3	4	13	-50	78
14.660	17.508	46.340	66.897	7.330	8.754	0.000	0.000	0.000	0.000	17.673	35.346	0	-1	1	4	-4	4	32	-140	155
15.346	16.570	61.343	83.935	7.673	8.285	0.000	0.000	0.000	0.000	23.486	58.832	1	-1	1	6	-5	4	70	-300	258
15.927	15.636	76.880	100.036	7.963	7.818	0.000	0.000	0.000	0.000	29.261	88.093	1	-2	1	9	-6	4	136	-548	387
16.407	14.712	93.147	115.212	8.203	7.356	0.000	0.000	0.000	0.000	34.996	123.089	1	-3	2	12	-7	4	239	-901	541
16.789	13.799	109.745	129.468	8.394	6.899	0.000	0.000	0.000	0.000	40.684	163.773	1	-4	2	16	-8	4	390	-1376	720
17.076	12.901	126.677	142.818	8.538	6.451	0.000	0.000	0.000	0.000	46.321	210.094	2	-6	3	21	-10	4	601	-1990	923

Vforc	Hforc	M	T	S	eccentricity	Min_Str	Max_Str	a'	a	at	c	ct	sden	deffet	deupp	xnew	ynew	convergence
803	147	-103	816	-23	-0.127	76.589	1924.016	-0.031	0.000	-0.050	0.000	0.000	0.850	0.850	0.475	-7.420	0.065	0.07528
797	158	-123	812	-19	-0.152	-52.581	1938.598	0.000	0.023	-0.061	0.000	0.000	0.839	0.839	0.481	-7.393	0.196	0.02712
785	177	-143	804	-13	-0.178	-165.774	1953.135	0.000	0.070	-0.070	0.000	0.000	0.830	0.830	0.485	-7.339	0.455	0.06436
771	196	-146	796	-6	-0.183	-193.558	1961.918	0.000	0.081	-0.081	0.000	0.000	0.819	0.819	0.490	-7.274	0.713	0.09805
757	214	-146	787	1	-0.186	-208.177	1956.335	0.000	0.087	-0.087	0.000	0.000	0.813	0.813	0.493	-7.203	0.969	0.13541
742	231	-145	777	8	-0.186	-209.446	1936.342	0.000	0.088	-0.088	0.000	0.000	0.812	0.812	0.494	-7.126	1.223	0.18617
726	247	-142	767	15	-0.185	-197.246	1901.959	0.000	0.085	-0.085	0.000	0.000	0.815	0.815	0.492	-7.041	1.474	0.19371
710	263	-137	757	22	-0.181	-171.505	1853.251	0.000	0.076	-0.076	0.000	0.000	0.824	0.824	0.488	-6.950	1.724	0.09254
694	277	-130	746	29	-0.174	-132.188	1790.320	0.000	0.062	-0.062	0.000	0.000	0.838	0.838	0.481	-6.853	1.971	0.07360
677	290	-121	735	36	-0.165	-79.290	1713.288	0.000	0.046	-0.040	0.000	0.000	0.860	0.860	0.470	-6.750	2.217	0.04826

Figure 4.24 Typical iteration in spreadsheet

4.3.2 Geometry

The geometry of the arch ring is expressed by the angle, x and y in the 'Elements' sheet, as illustrated in Figure 4.25, these data are also used to draw the graph of the arch in the 'Arch View' chart sheet. The input geometry includes 6 shape options detailed in the last section. In this section the geometry of these 6 types of arch is detailed.

	Angle	x	y
-1			
0	1.300	-8.934	0.120
1	1.283	-8.892	0.265
2	1.251	-8.802	0.553
3	1.219	-8.703	0.837
4	1.186	-8.594	
5	1.154		
		[illegible]	1.938
	[illegible]	8.350	1.669
76	-1.154	8.477	1.396
77	-1.186	8.594	1.118
78	-1.219	8.703	0.837
79	-1.251	8.802	0.553
80	-1.283	8.892	0.265
81	-1.300	8.934	0.120

Figure 4.25 Geometry related parameters

If the 'Surveyed' option is selected, the spreadsheet fits these data using a cubic spline interpolation. The angles, x and y of the elements are calculated in 'Main' sheet. These parameters are directly used in 'Elements' sheet. The coordinate is geometry is illustrated in Figure 4.26.

If the option is 'Parabolic', the equation of parabolic is given by equation (4.4).

$$y = r - \frac{4rx^2}{L^2} \tag{4.4}$$

If the option is 'Sinusoidal', the equation is given by equation (4.5).

$$y = \frac{\pi r \sin(x + \frac{L}{2})}{L} \tag{4.5}$$

If the option is 'Semi-Elliptic', the equation is given by equation (4.6).

$$y = r\sqrt{L^2 - 4x^2} \tag{4.6}$$

If the option is 'Circular', the equation is given by equation (4.7).

$$y = r - R + r\cos\theta \tag{4.7}$$

If the option is 'Best Fit Elliptic', the equation is given by equation (4.8).

$$y = \frac{b\sqrt{a^2 - x^2}}{a} - b - r \tag{4.8}$$

where

$$a = \frac{Lb}{2\sqrt{2rb - r^2}} \tag{4.9}$$

$$b = \frac{2r_q r - r_q^2}{8r_q - 6r} \tag{4.10}$$

When this option is selected the quarter rise has to be input in the hidden cell below the box H (this becomes unhidden after option 6 is selected) and the value of a and b are calculated in hidden cells of the 'Main' sheet.

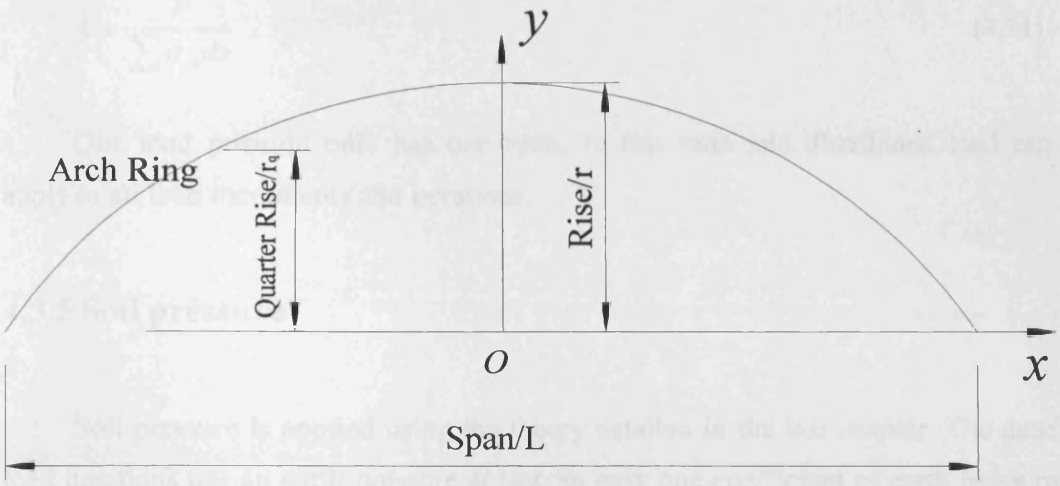

Figure 4.26 Arch geometry coordinate

4.3.3 Dead load

The dead loads applied to the arch include the arch self weight and the soil weight. The resulting forces are applied to the arch elements, and then transferred to the thrust, shear and moment in the middle section of the elements. Deflections are calculated for the dead load as the datum for the total deflection, this is to say, the deflections are defined as zero in the only dead load situation. So soil pressures at the dead load are $k_0 \gamma h$.

4.3.4 Load distribution

The load distribution methods have been detailed in the last chapter. In this section, equation (3.20) and (3.29) are applied in the 'Elements' worksheet.

First equation (3.29) is applied to a particular column, then equation (4.11) determines the ratio *k*.

$$k = \frac{P}{\sum \sigma_p dx} \tag{4.11}$$

One load position only has one ratio, so this ratio and distributed load can apply to all load increments and iterations.

4.3.5 Soil pressure

Soil pressure is applied using the theory detailed in the last chapter. The dead load iterations use an earth pressure at rest, so only one coefficient of earth pressure at rest is applied to the soil pressure. The deflection is only calculated at the last iteration of the dead load defection.

When the load increments are applied to the arch, the deflections change at every increment and iteration, so the related soil pressures are changing too. If the deflection of the arch push the soil, then the soil pressure is tending to passive, otherwise the soil pressure is tending to active.

4.3.6 Deflections

The arch ring deflection is important as its variation determines the soil pressure reaction. The deflection of the arch increases, when the load increases. So, every different load increment must calculate different deflections. And also when the soil pressure changes within the same load condition, the deflections also change slightly, so it is important to calculate the deflections and soil pressure at every iteration until it converges. The deflections in the iterations have to be factored, because the deflection under no soil pressure will be much bigger in some elements than under soil pressure (since it increases with deflection). After using this bigger deflection to increase the soil pressure, the soil pressure will become very large. The solution therefore could have trouble converging, if the deflection is not factored. So in this spreadsheet the deflection is factored by a deflection adjustment factor '*dr*' which value is less than 1 to relax soil reaction by deflection in the 'Advanced' sheet, this is a hidden sheet for the advanced settings.

4.3.7 Forces and moments solution

The forces and moments in the centre of the element are calculated from the energy theory using the matrix developed in Table 3.3 to get the left abutment vertical force, horizontal force and moment in the middle of the element section (the elastic part). From these abutment forces and moments, all the element thrusts, shears and moments in the middle of the section can be obtained.

All the calculation procedures are carried out in the spreadsheet. The horizontal forces, vertical forces and moments of elements are then added and assembled in the matrix shown in Figure 4.27. This is then resolved, using the spreadsheet matrix function MINVERSE(), which returns the inverse matrix for the matrix stored in an array. Then it uses the matrix function MMULT() which returns the matrix product of two arrays. The result is array3 with the same number of rows as array1 and the same number of columns as array2, see Figure 4.27.

	a(1)	a(2)	a(3)	45395	-15563	3547	d(1)	28254465	V	663.052	kN
	b(1)	b(2)	b(3)	-15563	9361	-1742	d(2)	-9273825	H	81.156	kN
	c(1)	c(2)	c(3)	3547	-1742	397	d(3)	2145499	M	-163.939	kN*m
								Array2		Array3	
				0.00007	0.00000	-0.00065					
		MINVERSE		0.00000	0.00058	0.00255	Array1				
				-0.00065	0.00255	0.01955					

Figure 4.27 Energy matrix solution in spreadsheet

The results of *V, H* and *M* are used to determinate the thrusts, shears and moments/eccentric positions of all elements in the arch.

4.3.8 Thinning and anti-thinning

Thinning is the most complicated part of this spreadsheet. So many models, logical cases and equations have to be realized not in code but in the spreadsheet. The logical functions in MS Excel are used to realize the logical cases.

Every section of the thickness is divided into previous iteration elastic thickness, local crack thickness, local anti-thinning thickness, total crack thickness, local yield thickness, local anti-yield thickness, and total yield thickness, as illustrated in Figure 4.28.

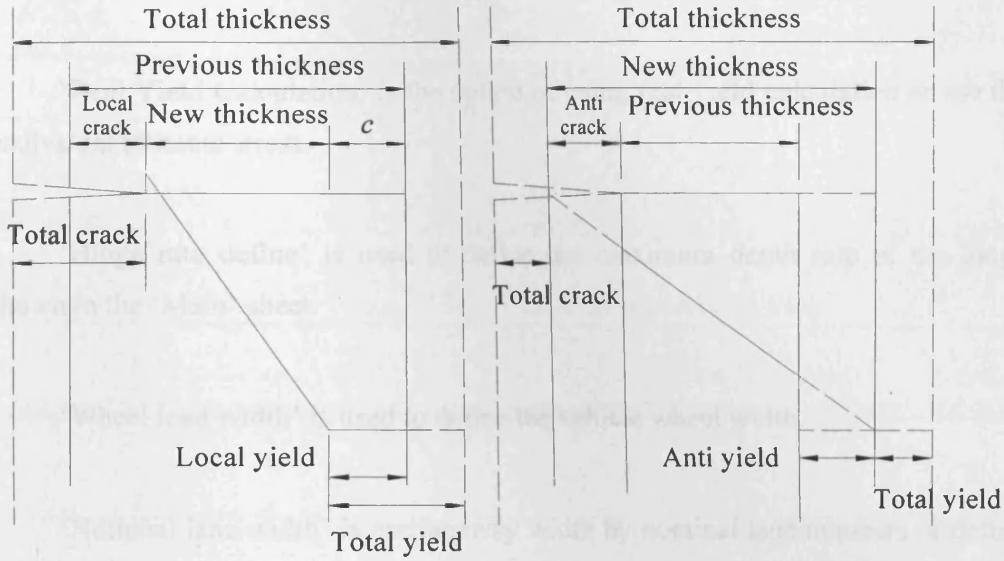

(a) Crack and yield thinning (b) Crack and yield anti-thinning

Figure 4.28 Thinning process definitions

4.4 Advanced setting sheet

This sheet is a hidden sheet. Some advanced settings can be changed in this part. This sheet has four boxes.

Box A, as illustrated in Figure 4.29, contains some control factors.

'Thickness Rate' is the minimum thickness the arch ring can have. This can be used as a serviceability assessment criterion.

'Deflection relaxation' is the factor to relax the calculated deflection.

'Relaxation' is the factor to relax the arch ring thickness.

'Moving Steps' is the numbers of positions to move the load over the whole span of the arch bridge.

'Moving Area' is the start position and the end position which the loads move between.

'Real Yield Calculation' is the option of using real yield calculation or use the equivalent ultimate stress.

'Hinge rate define' is used to define the maximum depth rate of the hinge shown in the 'Main' sheet.

'Wheel load width' is used to define the vehicle wheel width.

'Notional lane width' is carriageway width by nominal lane numbers or define by user, here input data is user defined notional lane width.

	Tolerance	Tol	0.1
	Thickness Rate	Th_rate	0.001
	Deflection relaxation	dr	0.1
A	Relaxation	Relax	1
	Moving Steps	Movstp	20
	Moving Area		4
	Real Yield Calculation	ryc	0
	Hinge rate define	H_rate	0.9
	Wheel load width (m)	wlw	1.8
	Notional lane width (m)		

Figure 4.29 Advanced setting Box A in the 'Advanced' sheet

Box B, as illustrated in Figure 4.30, is Lane width box, this box calculates the number of notional lanes from Box C. Box C, as illustrated in Figure 3.31, is the notional lane number determine method, as illustrated in Figure 4.31.

B			
	Number of Notional Lanes		2.00
	h (m)		1.26
	Notional lane width (m)	nlw	3.00
	Combined effective width (m)		3.00

Figure 4.30 Advanced setting Box B in the 'Advanced' sheet

C			
	Notional Lane Number		6
	0		
	5	1	0
	7.5	2	2
	10.95	3	0
	14.6	4	0
	18.25	5	0
	21.9	6	0

Figure 4.31 Advanced setting Box C in the 'Advanced' sheet

Box D, as illustrated in Figure 4.32, is the serviceability criteria box, this box calculates the stress, deflection and thinning related serviceability criteria.

D						
	Ultimate Stress (N/mm^2)	5	10	15	20	10
	Serviceability Stress (N/mm^2)	2.405306	3.156231	3.390895	3.57863	3.1562308
	Serviceability Deflection (L)	0.000689	0.000902	0.000983	0.00103	0.0009015
	Serviceability First Hinge %	0.287541	0.236167	0.223132	0.2147	0.2361667

Figure 4.32 Advanced setting Box D in the 'Advanced' sheet

4.5 Result chart sheets and a simple example

There are two normal chart sheets and eight hidden chart sheets. The hidden sheets can be displayed from the excel menu or from the 'Q' box in 'Main' sheet. These sheets are briefly introduced below and will be detailed in the example.

The 'Arch View' sheet is the most important sheet. This sheet includes the original arch geometry, load pattern, abutment forces, thrust line and thinning shape.

The 'Depth' sheet shows the original arch depth and the thinning depth including the yielding depth.

The other eight sheets are hidden sheets.

The 'VHForces' sheet includes the Vertical force and the Horizontal force for every arch ring element.

The 'Thrust-Shear' sheet details the Thrust and Shear forces in every arch ring elements.

The 'Bending Moment' sheet is the moment in the ring centre after cracking and yield thinning.

The 'Stress' sheet shows the stress in the extrados and the intrados of arch ring elements. At the same time this sheet also shows the total depth of the arch, because the highest stress is always located in the thinnest part of the arch ring.

The 'Def. Shape' sheet shows the total deflected shape of the arch.

The 'Deflection' sheet gives the separate x direction deflection and y direction deflection of the arch ring elements.

The 'Moving Min Depth' sheet is the minimum depth determined over the entire arch ring element, when the load on the bridge is moved from the right side to the left side.

The 'Moving Stress' sheet is the maximum stress determined in any arch ring element, when the load on the bridge is moved from the right side to the left side.

This example uses a quarter point load to determine the ultimate load and uses a service load to find out the critical load position. This spreadsheet sets the default arch width as 1 metre. This example's input data is listed in Table 4.3.

Table 4.3 Example data

Intrados Span (m)	14
Rise at Crown (m)	6
Fill at Crown (m)	0.45
Ring Thickness (m)	0.9
Masonry Density (kN/m^3)	23
Young Modulus (kN/m^2)	1500000
Yield Tensile Stress (N/mm^2)	0
Compressive Stress (N/mm^2)	10
Fill Density (kN/m^3)	20
Fill Dead Load Factor	1
Phi (degrees)	27
Soil Young Modulus (kN/m^3)	9900
Road Bulk Density (kN/m^3)	20
Road Deadload Factor	1
Road Thickness (m)	0.2
Load Dimension (m)	0.4
Dispersion Angle (degrees)	27
Arch type	circular

The 'Initial button' button in the 'Main' sheet is first used to get an initial position and load, then the 'Increase Force' button is used to get the quarter point ultimate load, the results are shown in Figure 4.33. The arch view chart shows the load pattern, load value, abutment forces, thrust line, original shape and the thinning shape.

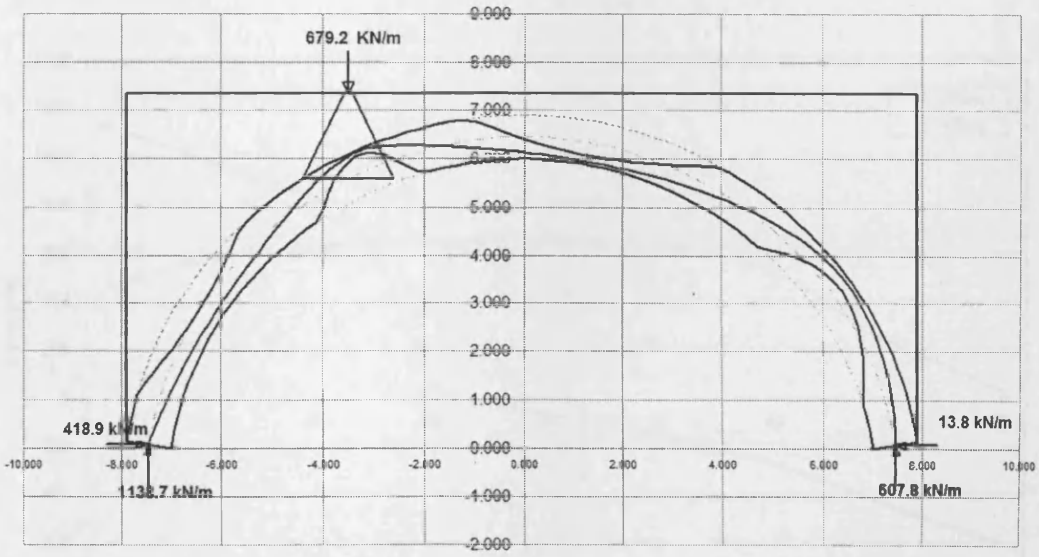

Figure 4.33 Arch view of quarter point ultimate load result

The depth of the arch is showed in Figure 4.34. This chart also includes the yield thickness. This chart gives very clear information about thinning and ring arch thickness.

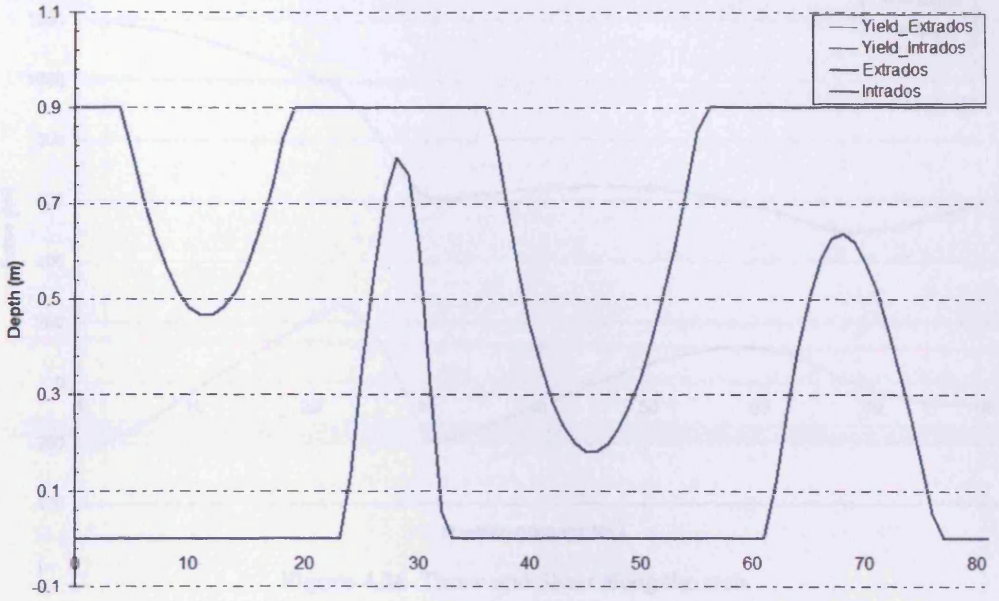

Figure 4.34 Arch ring thinning depth

The vertical forces and horizontal forces are showed in Figure 4.35.

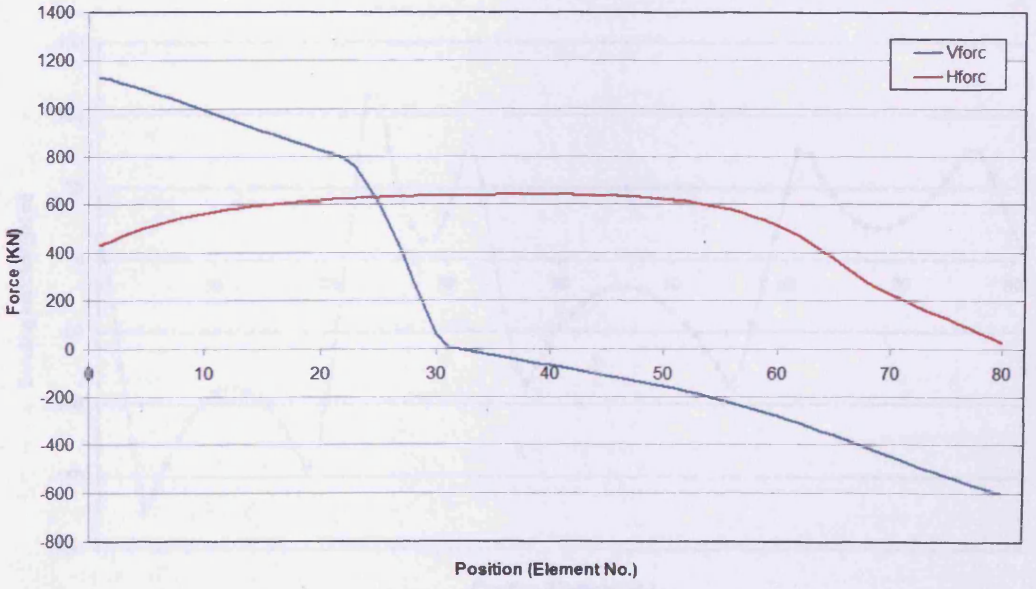

Figure 4.35 Vertical and horizontal forces along the arch

The Thrust forces and Shear forces along the arch ring are showed in Figure 4.36.

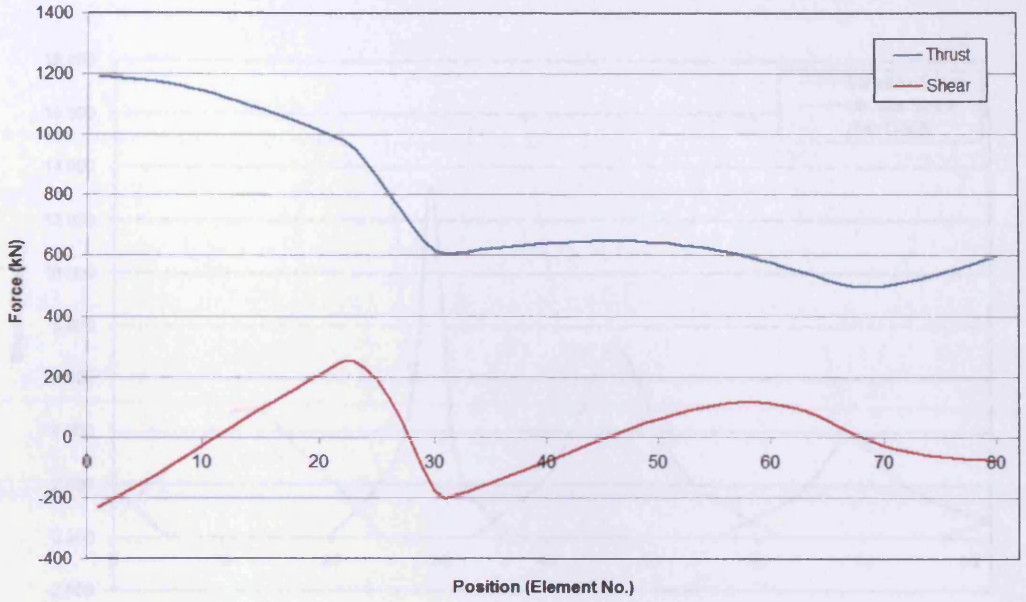

Figure 4.36 Thrust and Shear along the arch

The bending moments along the centreline of the elastic part of the arch ring elements are showed in Figure 4.37. The reversal of the moment is caused by the affect of the thinning of the arch ring.

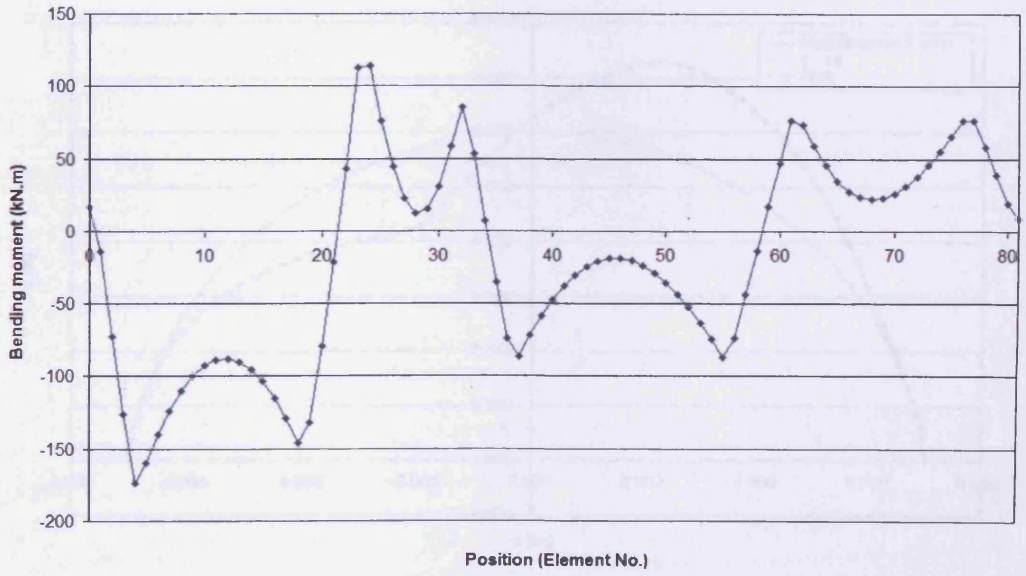

Figure 4.37 Bending moments along the arch

The stresses are showed in Figure 4.38. This chart also includes, in the background, the effective depth of the arch ring. This help to identify where these stresses occur.

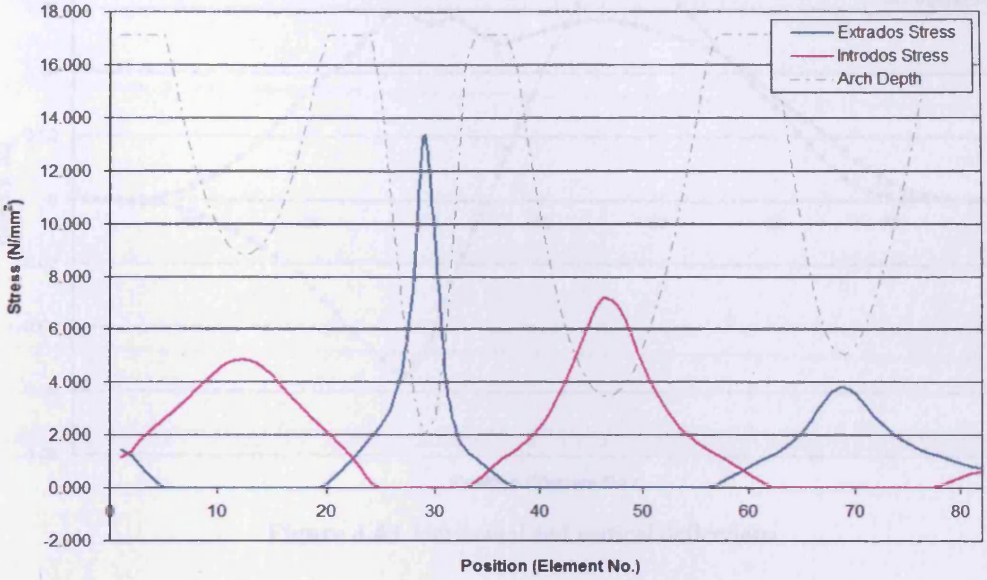

Figure 4.38 Extrados and intrados stress

The deflected shape is showed in Figure 4.39. These are total real deflections multiplied by a magnification factor which showed in the chart. The measured value in this chart multiple by the magnified factor can get the real deflections.

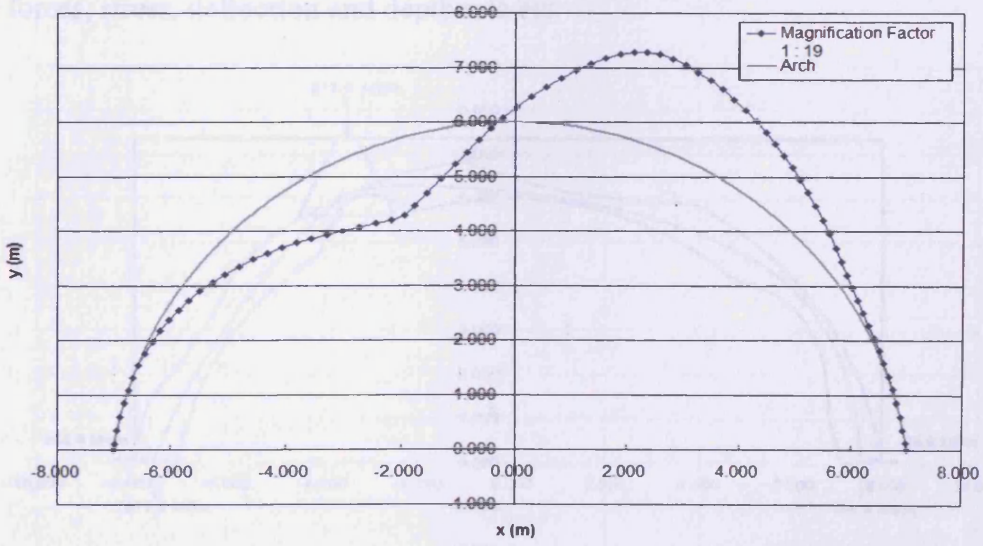

Figure 4.39 Deflected shape

The horizontal deflections and vertical deflections are showed in Figure 4.40. The x deflection is the horizontal deflection value and y deflection is the vertical deflection value.

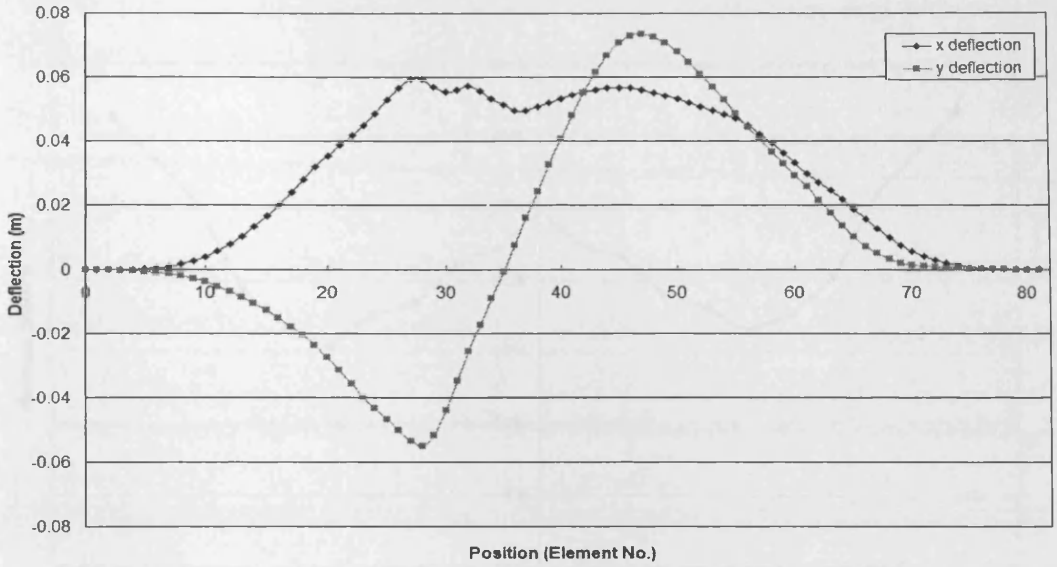

Figure 4.40 Horizontal and vertical deflections

Figure 4.33-4.40 are for an increasing load at one particular position taken up to ultimate load. Changing the load to a smaller value, here using 611kN/m, and applying 'Move Force' to get the critical position, is illustrated in Figure 4.38. The spreadsheet can also display a series of graphs stress, deflection etc., as for the ultimate load. The spreadsheet can apply any service load at any position and check the forces, stress, deflection and depth rate etc.

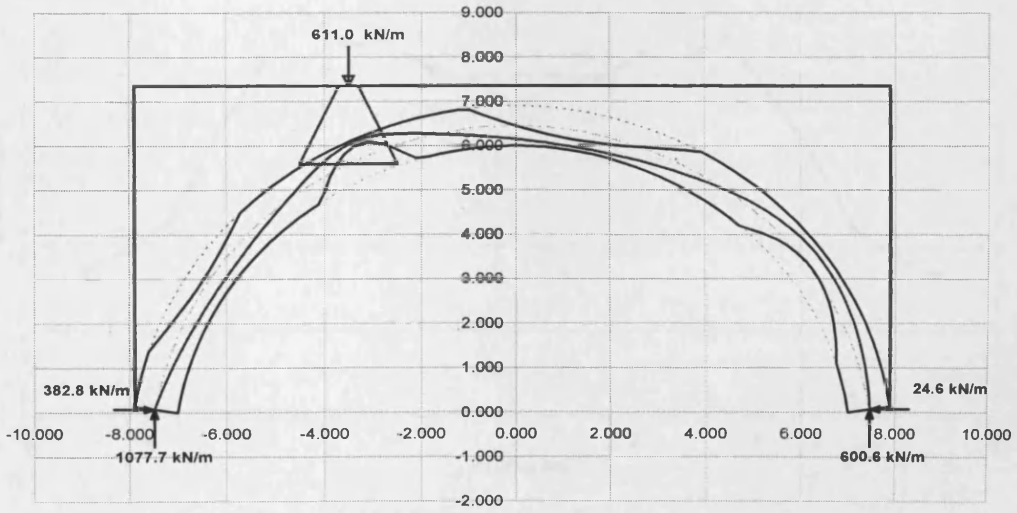

Figure 4.41 Critical position of a service load result

Minimum depth % for a moving load is showed in Figure 4.39. Minimum depth % is the % of the elastic part of the element section to the overall section thickness.

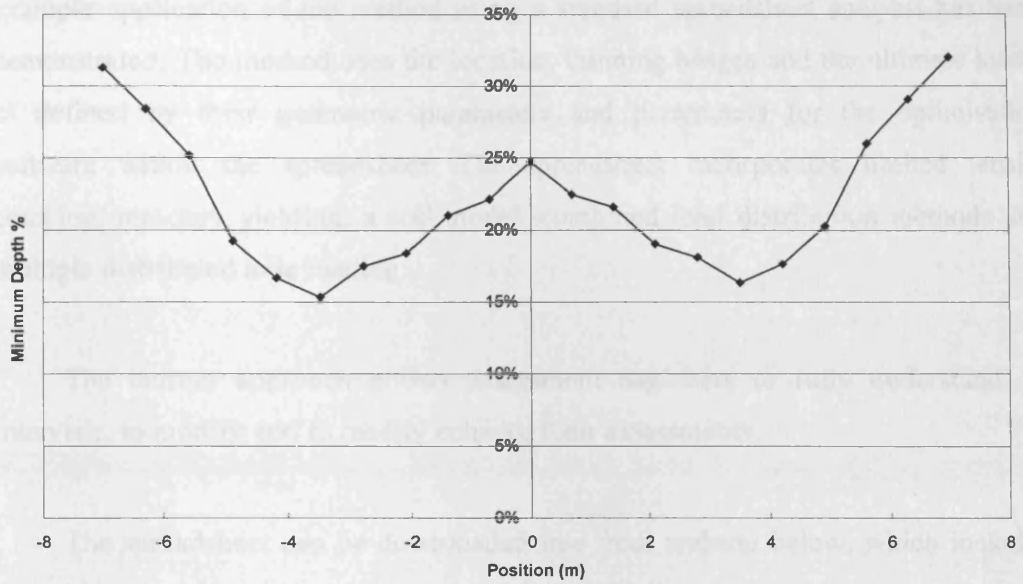

Figure 4.42 Minimum depth % for a moving load

Maximum stress by moving load is showed in Figure 4.43. Maximum stress means the maximum stress an any element along the arch ring, it can swap locations if another element becomes more critical.

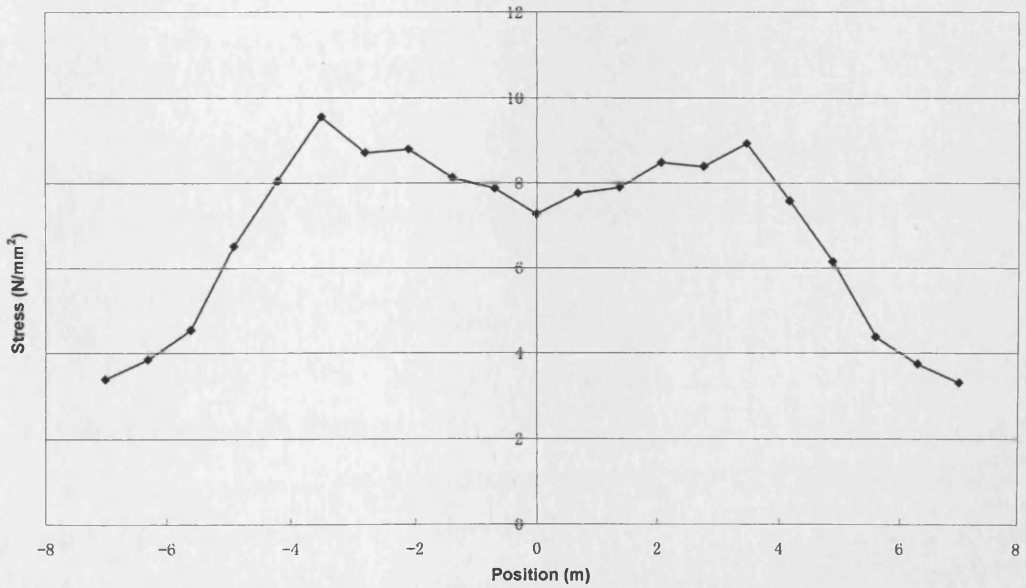

Figure 4.43 Maximum stress for a moving load

4.6 Conclusion

A complex arch thinning Castigliano analysis has been presented and an example application of the method using a standard spreadsheet analysis has been demonstrated. The method uses the location, thinning hinges and the ultimate loads, as defined by their geometric parameters and parameters for the optimisation software within the spreadsheet. The spreadsheet incorporates limited tensile cracking, masonry yielding, a soil model, combined load distribution methods and multiple distributed axle loading.

The current approach allows assessment engineers to fully understand, to intervene, to modify and to readily enhance their assessments.

The spreadsheet can be downloaded free from website below, which includes spreadsheet and instruction for the use of the spreadsheet:

http://masonry.engineering.cf.ac.uk/masonry-research/arch-spreadsheet.html

5 Statistics of Masonry Arch Bridges

5.1 Introduction

The approach adopted in the development of the serviceability load assessment criteria in this work was to test the serviceability criteria against a range of arches and to compare the outcomes with the traditional ultimate load approaches. This is because there is no adequate data on the condition of the existing arches against which to develop the criteria directly from an assessment of the structures condition. In order to properly compare serviceability approaches with the traditional methods it is necessary to assess both methods for a range of arches that is properly representative of the existing bridge stock. The current chapter therefore contains details of the development of the necessary probability distributions of the relevant geometric and material properties.

In this chapters data for 100 bridges including span, rise, ring depth and crown fill depth were gathered from books, papers, reports and the internet. Firstly the bridge database source is detailed, then the statistics are introduced and finally the method applied to the bridge database to get the statistical parameters required.

The statistics in this chapter are used to determine the probability densities of the important bridge geometric parameters. These probability densities and the correlation studies are later used in the simulation of 10,000 bridges. This enables the determination of appropriate serviceability criteria.that exactly matches the average performance of the serviceability methods to the ultimate limit state approach.

5.2 The bridge data source

The 100 bridge data set are from 7 different sources. First is from full scale experimental bridges[28]. Thirteen bridges belong to this group. They were chosen to represent a wide range of the UK bridge stock. The second source is from a book named Masonry Arch Bridges edited by McKibbins et al[1]. Seven bridges belong to this group. The next source is from "Masonry Arch Bridges" edited by J. Page[6]. Five bridges belong to this group. The fourth source is from a series of arch

assessment reports[157, 158, 159, 161, 162, 163, 164, 165, 166, 167] undertaken on a range of UK bridges. Thirteen bridges belong to this group. Totally 38% of the bridges are from publications. These data are more reliable and accurate. The fifth source is from bridges built by Roman Empire[168]. Twenty five bridges belong to this group. The sixth is from the bridges over Thames River[169]. Twenty nine bridges belong to this group. The last source was obtained by searching the internet. Eight bridges belong to this group. Totally 74% bridges are from UK.

The 100 bridges have full data on span, rise and depth of arch. Part of these 100 bridges have fill depth data. Some details of the bridges' data, from the internet (Roman bridges or Thames bridges), were derived from the photos of the bridges. In these cases the spans of the bridge were known, the ratio of the depth to span and rise to span were obtained from measurements taken from photos. For example, as illustrated in Figure 5.1, Pont-Saint-Martin (Italy). Its span is known as 36.7m. Its rise to span ratio and its ring depth to span ratio were estimated from this photo. The real span estimate is 17.0m and the real depth is 1.0m. It is accepted that this is not 100% accurate but the photos were selected as being reasonably central on the arch (as Figure 5.1) so the is unlikely to be significant distortion between vertical and horizontal distances.

Figure 5.1 Example of bridge data from photo Pont-Saint-Martin

Many of the bridges with full data are famous bridges and the more famous the bridge the easier to get the data. In addition the famous bridges by their nature may have unusual features, for example long spans or thin depth rings. There is therefore a danger that this might result in a bias in the statistics, this is considered particularly likely in relation to the span and this will be considered again in the relevant section.

5.3 Arch span statistics

In this section the statistics for the distribution of the spans of masonry arch bridges is considered. The span is the most important geometric property as it is to a large extent defined by the size of the crossing river, road rail etc. All other geometric properties will subsequently be scaled to this parameter. Figure 5.2 shows the cumulative probability density of arch span. The 'selected bridges' are all more then 4m, less than 4m bridges are generally considered as culvert. At the smaller end culverts move towards pipes and an increasing percentage become circular.

Of the 100 'selected bridges' 61 are single span bridges with the other 39 bridges being multi-span bridges. One multi-span bridge is considered as a number of separate single span bridges in this database.

In Figure 5.2, 'From books and reports' refers to the data from books and reports, this is included in 100 bridge database in Table 5.1. 'From Internet' refers to the data from internet this is also included in 100 bridge database. 'Selected 100 Bridges' refers to the 100 selected data. 'All bridges' refers to 378 bridges include all bridges can be found from any source, most of these bridges are only have the span data recorded with but no data on rise, depth, crown fill depth or have bridge photos.

From Figure 5.2 the arch bridges 'from books and reports' distribution is very similar to the 'All bridges' distribution. 'From Internet' bridges generally include more longer span bridges, with about 15% greater than 20m, however, 'From books and reports' only have about 5% in this category.

Table 5.1 Selected 100 bridges with different geometries

No.	Name	Span(m)	Rise(m)	Quarter Rise(m)	h(m)	d(m)	r/L	d/L	h/d	Built	Note	Country
1	Bridgemill	18.3	2.85	2.16		0.71	0.16	0.04			Full Expr	UK
2	Bargower	10.4	5.18	4.49		0.56	0.50	0.05			Full Expr	UK
3	Preston	5.0	1.64	1.37	0.38	0.36	0.33	0.07	1.06		Full Expr	UK
4	Prestwood	6.6	1.43	1.12	0.17	0.22	0.22	0.03	0.75		Full Expr	UK
5	Torksey	4.9	1.15	0.90	0.25	0.34	0.24	0.07	0.72		Full Expr	UK
6	Shinafoot	6.2	1.19	0.91	0.22	0.54	0.19	0.09	0.40		Full Expr	UK
7	Strathmashie	9.4	2.93	2.35	0.41	0.60	0.31	0.06	0.68		Full Expr	UK
8	Barlae	8.5	1.70	1.31		0.45	0.20	0.05			Full Expr	UK
9	Dundeefsm	4.0	2.00	1.73		0.25	0.50	0.06			Full Expr	UK
10	Boltonfsm	6.0	1.00	0.77		0.22	0.17	0.04			Full Expr	UK
11	Croft Breadsall	6.5	2.06	1.78		0.36	0.32	0.06			Full Expr	UK
12	Yardley Wood	6.5	1.98	1.60		0.34	0.30	0.05			Full Expr	UK
13	Alcester Road	6.5	1.93	1.56		0.36	0.30	0.06			Full Expr	UK
14	Elsage Farm Bridge	8.0	3.60			0.80	0.45	0.10			CIRIA	UK
15	Rockshaw Road Overbridge	9.2	4.60			0.80	0.50	0.09			CIRIA	UK
16	Brynich Viaduct	12.0	4.00			0.70	0.33	0.06			CIRIA	UK
17	Hungerford Canal Bridge	7.0	3.00		0.46	0.33	0.43	0.05	1.39		CIRIA	UK
18	Llanharan Bridge	16.0	3.50			0.30	0.22	0.02			CIRIA	UK
19	Gumley Road Bridge	6.7	2.50			0.30	0.37	0.04			CIRIA	UK
20	Egglestone Abbey Bridge	24.0	11.00		0.60	0.50	0.46	0.02	1.20		CIRIA	UK
21	Ellerbeck Bridge	10.2	2.02			0.30	0.20	0.03			Masonry Arch Bridges	UK
22	Monk New Bridge	9.9	2.60			0.75	0.26	0.08			Masonry Arch Bridges	UK
23	Prestwood New Bridge	6.6	1.43			0.40	0.22	0.06			Masonry Arch Bridges	UK
24	Shinafoot New Bridge	7.0	1.00			0.40	0.14	0.06			Masonry Arch Bridges	UK
25	Kimbolton Bridge	8.0	2.00			0.44	0.25	0.06			Masonry Arch Bridges	UK
26	Llandeilo Bridge	44.5	11.00	6.65	0.38	3.50	0.25	0.08	0.11		Cardiff U report	UK

No.	Name	Span(m)	Rise(m)	Quarter Rise(m)	h(m)	d(m)	r/L	d/L	h/d	Built	Note	Country
27	Seiont Bridge	16.6	6.31	5.20	0.58	0.76	0.38	0.05	0.76		Cardiff U report	UK
28	Westlinton and Egremont Bridge	11.7	2.23	1.72	0.18	0.55	0.19	0.05	0.33		Cardiff U report	UK
29	Carersws Bridge	17.3	3.77		0.62	0.65	0.22	0.04	0.96		Cardiff U report	UK
30	Ryhd Y Ferre Bridge	6.5	2.10		0.22	0.45	0.32	0.07	0.49		Cardiff U report	UK
31	Eden Bridge	15.3	2.78		0.32	0.60	0.18	0.04	0.54		Cardiff U report	UK
32	Hen-Efail	6.7	1.74		0.29	0.45	0.26	0.07	0.63		Cardiff U report	UK
33	Pont Factory	11.9	3.01		0.42	0.50	0.25	0.04	0.84		Cardiff U report	UK
34	Pont-Y-Clerc Bridge	14.4	4.71	3.84	0.59	0.43	0.33	0.03	1.37		Cardiff U report	UK
35	Furnace Bridge	9.0	1.38		0.20	0.55	0.15	0.06	0.36		Cardiff U report	UK
36	Trunk Road Bridge1	14.6	2.86			0.60	0.20	0.04			Cardiff U report	UK
37	Trunk Road Bridge2	16.4	3.12			0.60	0.19	0.04			Cardiff U report	UK
38	Trunk Road Bridge3	14.8	2.94			0.60	0.20	0.04			Cardiff U report	UK
39	Clun Bridge1	5.0	1.57			0.70	0.31	0.14			Internet	UK
40	Clun Bridge2	4.3	1.00			0.70	0.23	0.16			Internet	UK
41	English Bridge1	17.0	6.50			1.00	0.38	0.06			Internet	UK
42	English Bridge2	14.5	5.50		0.30	0.90	0.38	0.06	0.33		Internet	UK
43	Welsh Bridge	13.0	5.90		0.30	0.56	0.45	0.04	0.54		Internet	UK
44	Swinford Toll Bridge	10.0	4.50			1.00	0.45	0.10			Internet	UK
45	Thames Head Bridge	7.8	3.30		0.39	0.19	0.42	0.02	2.00		Internet	UK
46	Ha'penny (Lechlade) Bridge	14.2	4.72		0.39	0.39	0.33	0.03	1.00		Internet	UK
47	St.John's Bridge	6.8	3.40		0.28	0.28	0.50	0.04	1.00	1709	Internet	UK
48	Tadpole Bridge	11.9	4.52		0.24	0.71	0.38	0.06	0.33		Internet	UK
49	Godstow Bridge	8.3	2.56			0.56	0.31	0.07			Internet	UK
50	Folly Bridge	6.6	3.12		0.15	0.40	0.47	0.06	0.38		Internet	UK
51	Abingdon Bridge	18.3	4.24			0.45	0.23	0.02			Internet	UK
52	Clifton Hampden Bridge	12.3	4.09			0.70	0.33	0.06			Internet	UK
53	Shillingford Bridge1	16.0	5.26		0.10	0.74	0.33	0.05	0.14		Internet	UK

No.	Name	Span(m)	Rise(m)	Quarter Rise(m)	h(m)	d(m)	r/L	d/L	h/d	Built	Note	Country
54	Shillingford Bridge2	10.8	4.20		0.68	0.68	0.39	0.06	1.00		Internet	UK
55	Shillingford Bridge3	11.0	4.47		0.92	0.53	0.41	0.05	1.74		Internet	UK
56	Wallingford Bridge1	12.4	5.00		0.10	0.78	0.40	0.06	0.13		Internet	UK
57	Wallingford Bridge2	7.6	3.80		0.45	0.55	0.50	0.07	0.82		Internet	UK
58	Wallingford Bridge3	8.3	3.50		0.85	0.65	0.42	0.08	1.31		Internet	UK
59	Moulsford Railway Bridge	16.8	4.20		0.70	0.78	0.25	0.05	0.90		Internet	UK
60	Gatehampton Rly Bridge	19.0	6.96		0.90	0.85	0.37	0.04	1.06	1838	Internet	UK
61	Sonning Bridge	9.8	4.31		0.10	0.60	0.44	0.06	0.17	1775	Internet	UK
62	Henley Bridge	12.0	4.34		0.20	0.40	0.36	0.03	0.50		Internet	UK
63	Maidenhead Bridge	10.2	5.10		0.10	1.13	0.50	0.11	0.09		Internet	UK
64	Maidenhead Railway Bridge	39.0	7.00		0.20	0.91	0.18	0.02	0.22	1838	Internet	UK
65	Runnymede A30 Bridge	51.0	7.01		0.20	0.87	0.14	0.02	0.23	1961	Internet	UK
66	Staines Bridge1	22.2	2.30		0.10	0.80	0.10	0.04	0.13	1832	Internet	UK
67	Staines Bridge2	18.0	2.20		0.10	0.80	0.12	0.04	0.13		Internet	UK
68	Chertsey Bridge	9.8	4.50		0.40	0.50	0.46	0.05	0.80	1785	Internet	UK
69	Kingston Bridge	19.0	7.29		0.10	1.00	0.38	0.05	0.10	1828	Internet	UK
70	Richmond Bridge	6.0	2.00		0.10	0.38	0.33	0.06	0.26	1823	Internet	Australia
71	Richmond Bridge	14.0	5.30		0.25	0.50	0.38	0.04	0.50	1777	Internet	UK
72	Kew Bridge	30.0	5.30		0.40	1.65	0.18	0.06	0.24		Internet	UK
73	Putney Bridge	29.0	3.80		0.10	0.70	0.13	0.02	0.14	1886	Internet	UK
74	Pontypridd bridge	43.0	11.00			0.75	0.26	0.02		1756	Internet	UK
75	Grosvenor Bridge	61.0	15.00			1.90	0.25	0.03		1833	Internet	UK
76	Bridge at Afrin1	11.5	4.60		0.50	0.60	0.40	0.05	0.83		Internet	Syria
77	Bridge at Afrin2	12.5	5.00		0.50	0.60	0.40	0.05	0.83		Internet	Syria
78	Bridge at Afrin3	12.0	4.80		0.50	0.60	0.40	0.05	0.83		Internet	Syria
79	Jisr Banat Ya'qub	4.0	2.00			0.45	0.50	0.11			Internet	Palestine
80	Misis bridge1	5.0	2.50			0.70	0.50	0.14			Internet	Turkey
81	Misis bridge2	6.5	3.00			0.70	0.46	0.11			Internet	Turkey

No.	Name	Span(m)	Rise(m)	Quarter Rise(m)	h(m)	d(m)	r/L	d/L	h/d	Built	Note	Country
82	Misis bridge3	11.0	3.50			0.75	0.32	0.07			Internet	Turkey
83	Misis bridge4	4.0	2.00			0.60	0.50	0.15			Internet	Turkey
84	Pons Aelius	18.0	9.00			0.90	0.50	0.05		122	Internet	Italy
85	Pons Cestius	13.7	6.80		0.10	0.57	0.50	0.04	0.18	-50	Internet	Italy
86	Pons Fabricius	24.2	10.25		0.20	1.70	0.42	0.07	0.12		Internet	Italy
87	Pons Mulvius	18.0	9.00		0.10	1.20	0.50	0.07	0.08		Internet	Italy
88	Pont de Mejez el Bab	6.0	3.00		0.20	0.40	0.50	0.07	0.50	1735	Internet	Tunisia
89	Pont de Pierre	17.1	5.00			0.90	0.29	0.05			Internet	Italy
90	Pont de Sommières	8.5	4.20			0.50	0.49	0.06			Internet	France
91	Pont de Vaison-la-Romaine	17.0	8.50		0.20	1.00	0.50	0.06	0.20		Internet	France
92	Pont Flavien	12.3	5.00			0.85	0.41	0.07			Internet	France
93	Pont Julien1	10.0	5.00			0.50	0.50	0.05			Internet	France
94	Pont Julien2	16.3	8.00			0.60	0.49	0.04			Internet	France
95	Pont Julien3	10.0	5.00			0.50	0.50	0.05			Internet	France
96	Pont-Saint-Martin	36.7	17.00			1.00	0.46	0.03			Internet	Italy
97	Ponte dell'Abbadia1	25.0	12.00			1.20	0.48	0.05			Internet	Italy
98	Ponte dell'Abbadia2	4.0	2.00			0.80	0.50	0.20			Internet	Italy
99	Ponte dell'Abbadia3	4.0	2.00			0.80	0.50	0.20			Internet	Italy
100	Ponte d'Arli	17.0	8.50			0.80	0.50	0.05			Internet	Italy

This supports the earlier conclusion that the general public have little interest in normal or small bridges, but prefer the longer and greater bridges and therefore are more likely to be recorded, so the bridges from internet sources are more likely to be famous bridges with longer span and built a long time ago. 'Selected 100 bridges' include these two set of data. So the distribution curve is between these two curves. It is considered that the 'All' bridges are appropriately representative of the UK bridge stock.

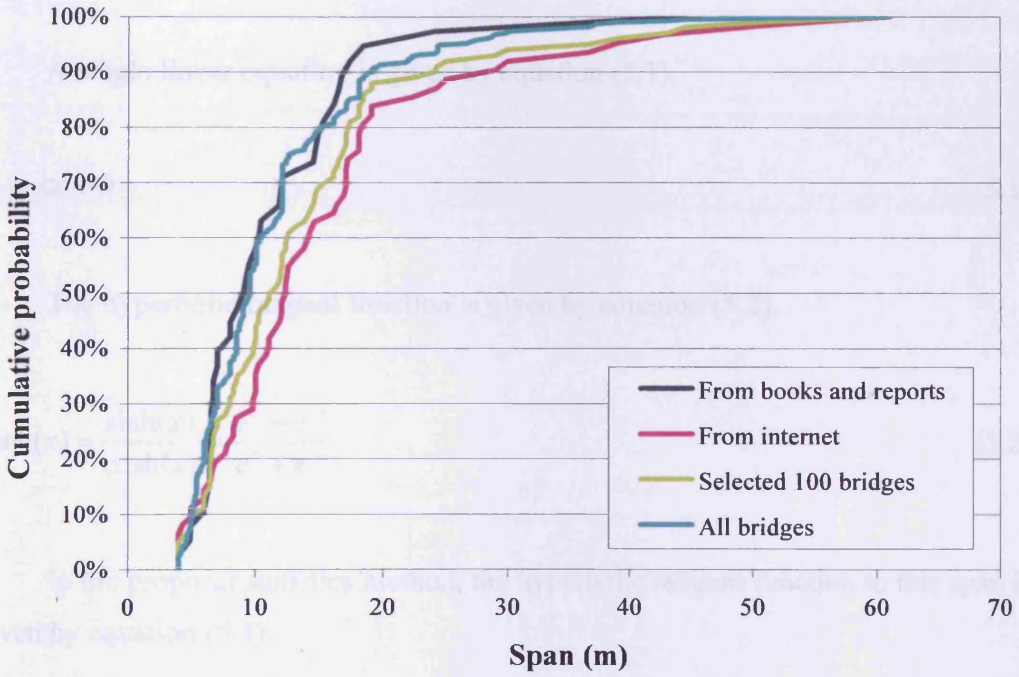

Figure 5.2 Cumulative probability distribution of different source span

To fit the curve, two curves are used, a multilinear regression curve made up of a series of straight lines over defined intervals and the positive half of the hyperbolic tangent function.

John[170] developed a novel method of using the solver function within Excel to fit curves. His method is used to determine the hyperbolic tangent function regression.

The R squared value was used in these statistics to quantify the difference between the curves and the actual data. It was decided to fit curves to the cumulative probability distributions and to then use these to establish the probability density distributions which were required later as part of the development of the serviceability approach.

To undertake the regression for the multilinear approach the spans have to be divided in to a number of groups and then linear regressions are applied to each group.

A single linear equation is given by equation (5.1).

$$y = kx + b \tag{5.1}$$

The hyperbolic tangent function is given by equation (5.2).

$$\tanh(x) = \frac{\sinh(x)}{\cosh(x)} = \frac{e^{x} - e^{-x}}{e^{x} + e^{-x}} \tag{5.2}$$

In the proposal statistics method, the hyperbolic tangent function to this span is given by equation (5.3).

$$y = \tanh(kx + b) \tag{5.3}$$

The R squared value was used to quantify the fit is given by equation (5.4).

$$R^2 = 1 - \frac{SS_{err}}{SS_{tot}} \tag{5.4}$$

The R squared value of the hyperbolic tangent equation is 0.9950 and for the multi- linear curve the R squared value is 0.9951 giving a similar value. The

resulting curves are shown in Figure 5.3. The multi-linear line is made up of 4 separate straight lines and, as expected, clearly provides a slight better visual fit to the data. However, hyperbolic tangent curve has continuous probability shown in Figure 5.3.

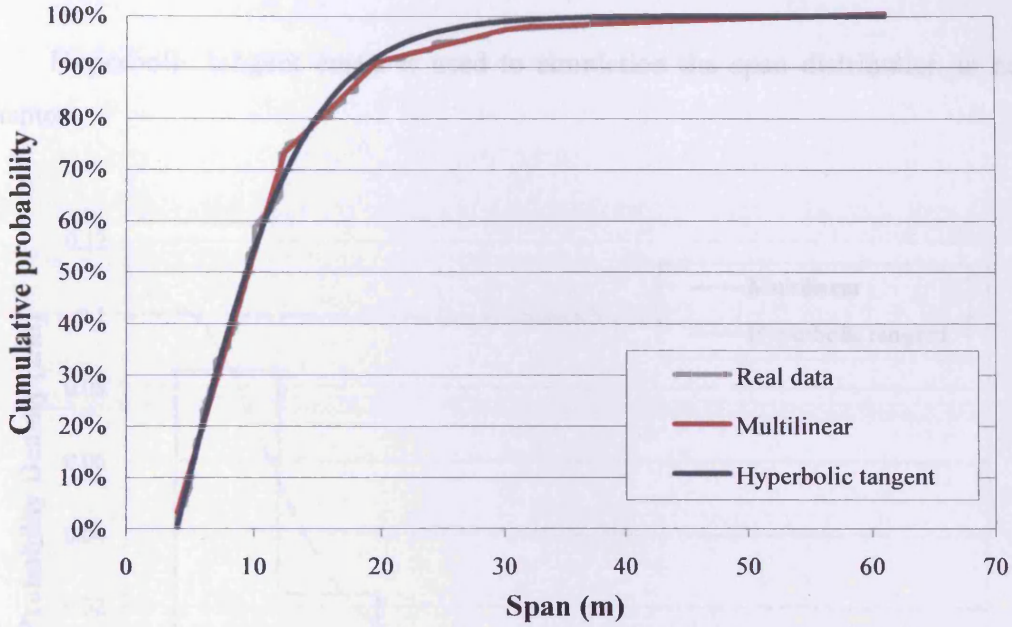

Figure 5.3 Selected 378 bridges cumulative distribution of the arch span and its regression functions

The multilinear plots in the cumulative probability density distributions translate into the 4 zones within the probability density plots. The distribution therefore assumes that there are no arches with a span less than 4 metres and that all spans between 4 and 12 metres have an equal likelihood of occurrence and this constitutes 73.3% of the distribution. Between 12 m and 20 m there is another 18.1% of the sample again with each span having an equal likelihood. Between 20 m and 30 m there is another 6.0% with the final 2.6% made up of bridges between 30 and 60m (the upper limit). The average span is 11.4 m, the median span is 9.5 m, and the mode span in real data is 12 m, in fitted hyperbolic tangent curve is 4 m, and in fitted multilinear curve is 4 m to 12 m with average is 8 m. A typical span is of 10 m is taken to be used in later sections.

In conclusion, the multilinear gives a little bit better fit than the hyperbolic tangent curve, however the hyperbolic tangent curve has a continuous probability curve which is likely to be more representative of real life. For example, 30 m span must be higher probability than 60 m span. Hyperbolic tangent curve can explain this very well, but multilinear curve has the same probability, as illustrated in Figure 5.4.

Hyperbolic tangent curve is used to simulation the span distribution in next chapter.

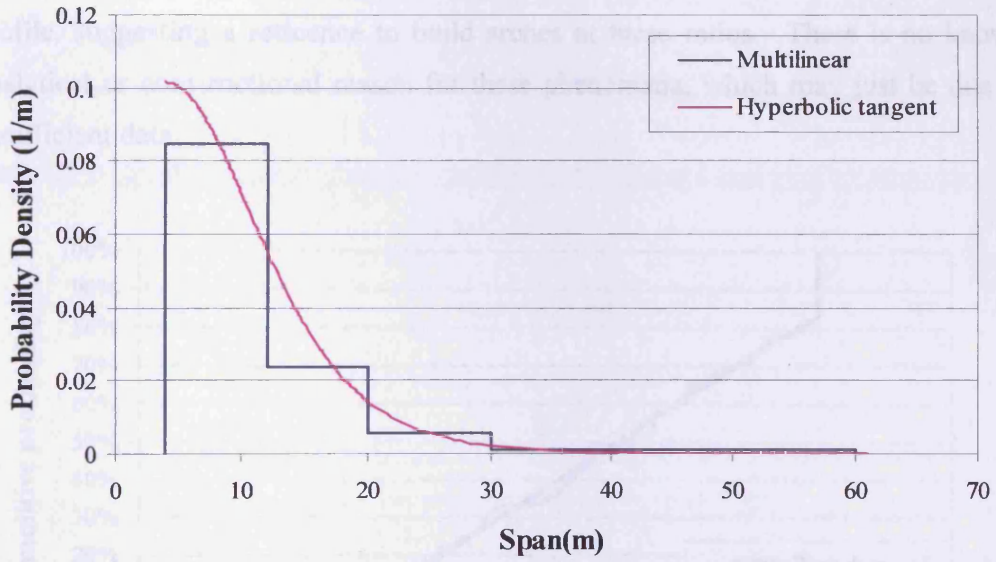

Figure 5.4 Probability density distribution of span

5.4 Arch rise statistics

In this section the statistics of the centreline rise of masonry arch bridges is detailed. Rather than analyse the basic rise statistics it was decided early on that this parameter would need to be linked with the arch span. This was a natural choice as span to rise ratios are regularly referred to in engineering, however the statistics were actually developed for the inverse, the rise/span ratio. The rise to span ratio cumulative probability density distribution, obtained from the data detailed in Table 5.1, is shown in Figure 5.5, which contains both the data points and a multi-linear curve fitting through the data with a ratio less than 0.5. The value of 0.5 which

corresponds to a semicircular arch represents almost the limit of values with few masonry arches, as opposed to numerous brickwork tunnels, being formed of a horseshoe shape. The cumulative probability distribution is bi-linear from 0.10 to 0.17 and 0.17 to 0.50 with the remaining arches, 19% in selected 100 bridges, being semi circular. Semi-circular arches are geometrically easier to construct, naturally provide more headroom for a limited width and are also very visually pleasing. With this exception there appears to be no preferential value for the arch's rise to span ratio. In this cumulative probability density a bi-linear curve is used to fit the real data, as illustrated in Figure 5.5. From the profile there appears to be two rise to span ratio value ranges, at about 0.27 and 0.35, where there are noticeable gaps in the profile, suggesting a reticence to build arches at these ratios. There is no known analytical or constructional reason for these phenomena, which may just be due to insufficient data.

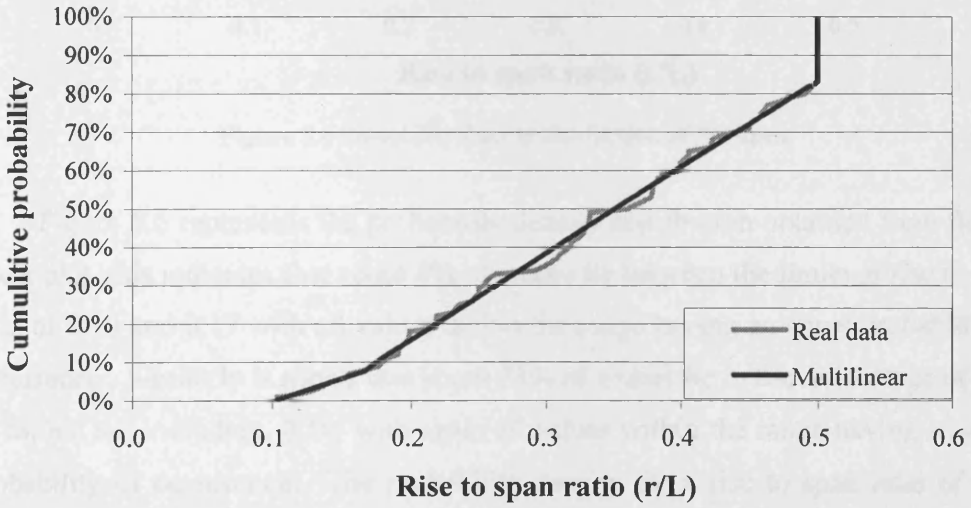

Figure 5.5 Cumulative probability data and a fitted multilinear line for the arch rise to span ratio

The gradient of the fitted bi-linear is used to obtain the approximate probability density distribution.

R squared value of the fitted curve is 0.9975, so the fitted curve can explain real data very well.

From the cumulative probability function 50% of the rise to span ratios are less than 0.36, and the average is 0.35 however, the highest probability density of span is 0.5, as illustrated in Figure 5.5. Considering these results, this defines a typical span to rise ratio as 0.38.

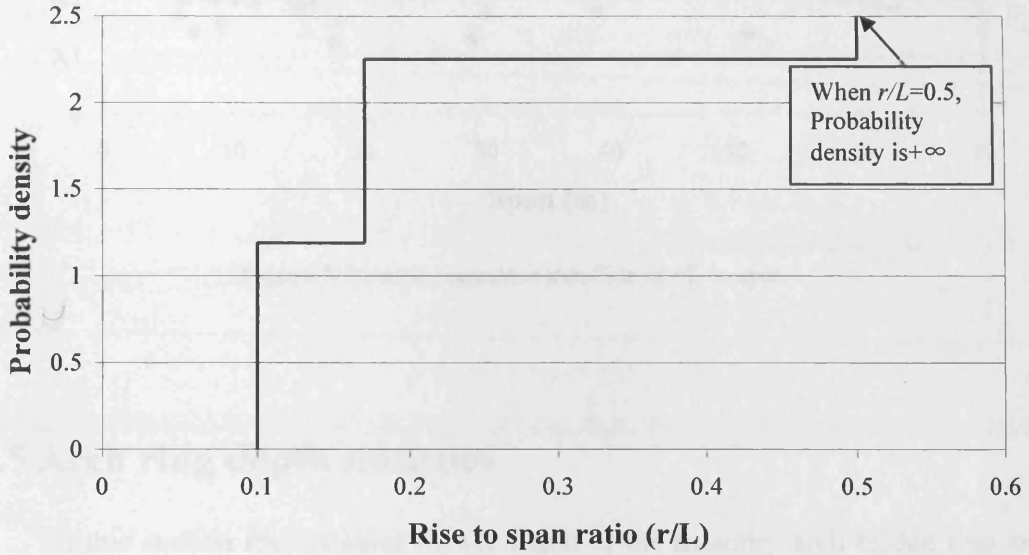

Figure 5.6 Probability density distribution of rise/span

Figure 5.6 represents the probability density distribution obtained from the bi-linear plot, this indicates that about 8% of arches lie between the limits of rise to span ratio of 0.10 and 0.17 with all values within the range having an equal probability of occurrence. Similarly it shows that about 73% of arches lie in the ratio range of 0.17 up to, but not including, 0.50, with again all values within the range having an equal probability of occurrence. The probability density for a rise to span ratio of 0.50 cannot be plotted since all value consider in this range take the value 0.50 but the cumulative probability distribution indicates that 19% of arches have a ratio of 0.50.

The trend of rise to span ratio with span is when span increasing the rise to span ratio is decreasing, as illustrated in Figure 5.7. However, 91.4% of span is between 4 m to 20 m, and the trendline values between the 4 m to 20 m are only slight difference. So it is not big difference to use the independent simulation of span and rise to span ratio.

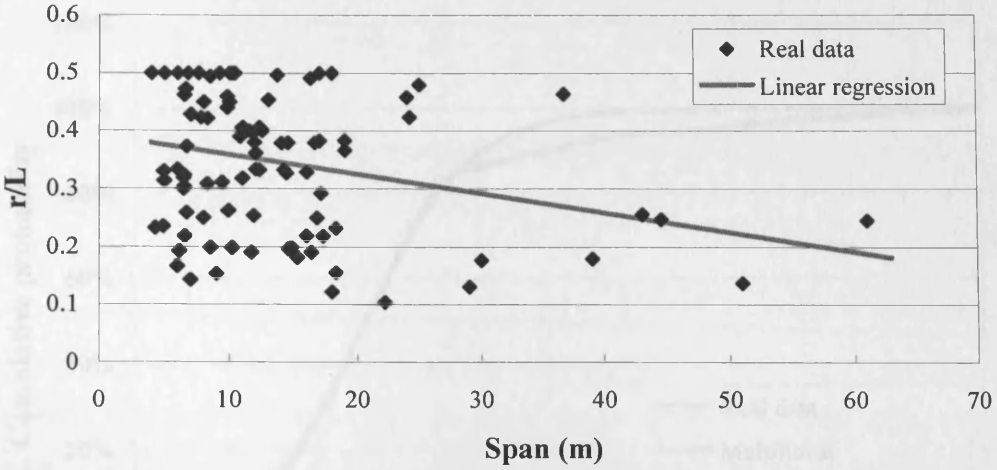

Figure 5.7 Linear regression trendline of r/L to span

5.5 Arch ring depth statistics

In this section the statistics for the depth of the masonry arch bridge ring are developed, this is an important statistic as it is the primary variable that determines the strength and stiffness of the structure. As with section 5.4 the arch ring thickness was considered in its non-dimensional form with the span again being used as a suitable factor to develop the non dimensional parameter. Depth to span ratios are generally considered to be indicative of the flexibility of a structure.

The cumulative probability density distribution of the ratio of the arch ring depth to span is detailed in Figure 5.8 together with two fitted curves, one a hyperbolic tangent curve and the other a multi-linear curve. The average ratio of the depth to span is 0.06 with the highest probability of occurrence being approximately equal between the values of 0.036 and 0.070 with average of 0.053 according to the fitted multilinear regression and 0.052 according to the hyperbolic tangent regression, as illustrated in Figure 5.9. The median value of real data is 0.053. With a typical depth to span ration of 0.053 coupled with a typical span of 10 metres yields a typical depth as 530 mm which is a typical ring brick arch of secondary road or rail crossings.

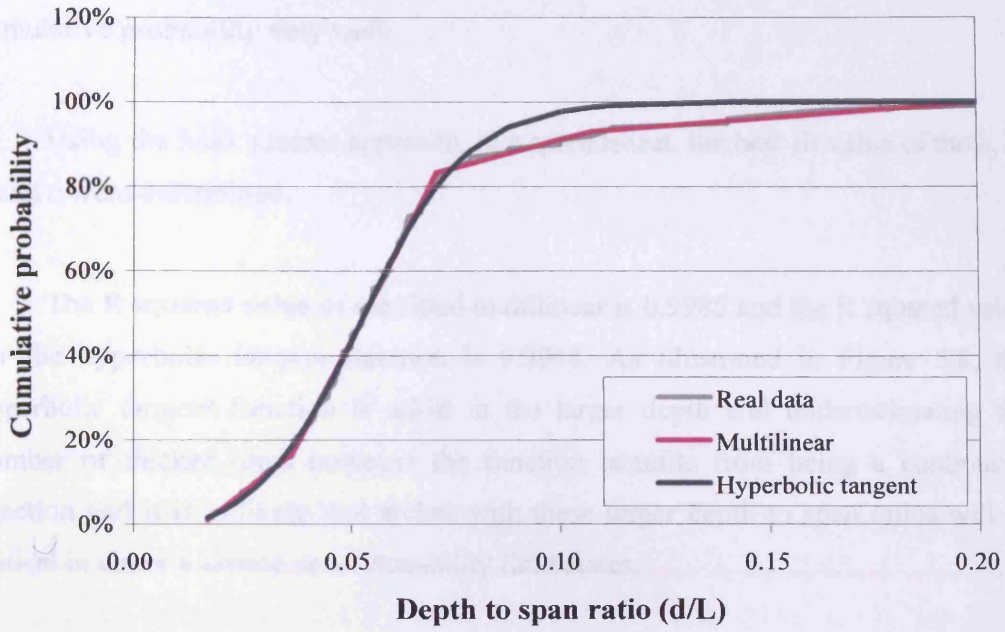

Figure 5.8 Probability density distribution of depth/span

The field data shape of Figure 5.8 is considered to be well represented by a hyperbolic tangent function of the form given by equation (5.5).

$$y = k\tanh(ax+b)+c \tag{5.5}$$

Using the positive half of the hyperbolic tangent function, the y value varies from 0 to 1. However, equation (5.4) may use part of the negative half of the function. yielding equation (5.6) and (5.7)

$$c = 1-k \tag{5.6}$$

$$\tanh(ax+b) <= 1 \tag{5.7}$$

then substituting equations (5.5), (5.6) and (5.7) yields equation (5.8)

$$y <= k+c=1 \tag{5.8}$$

so, the function y can still has a value equal and less than 1. This describes the cumulative probability very well.

Using the least squares approach, in a spreadsheet, the best fit value of the *k*, *a*, *b* and *c* were determined.

The R squared value of the fitted multilinear is 0.9985 and the R squared value for the hyperbolic tangent function is 0.9948. As illustrated in Figure 5.8, the hyperbolic tangent function is adrift at the larger depth end underestimating the number of thicker rings however the function benefits from being a continuous function and it is unlikely that arches with these larger depth to span ratios will be critical in either ultimate or serviceability limit states.

Figure 5.9 shows the resulting probability density functions from the fitted equations. Although the multi-linear approach compared well on Figure 5.8 the resulting probability density plot might have benefited from remodelling of the area between a depth to span ratio of 0.07 and 0.08, however this was left as detailed.

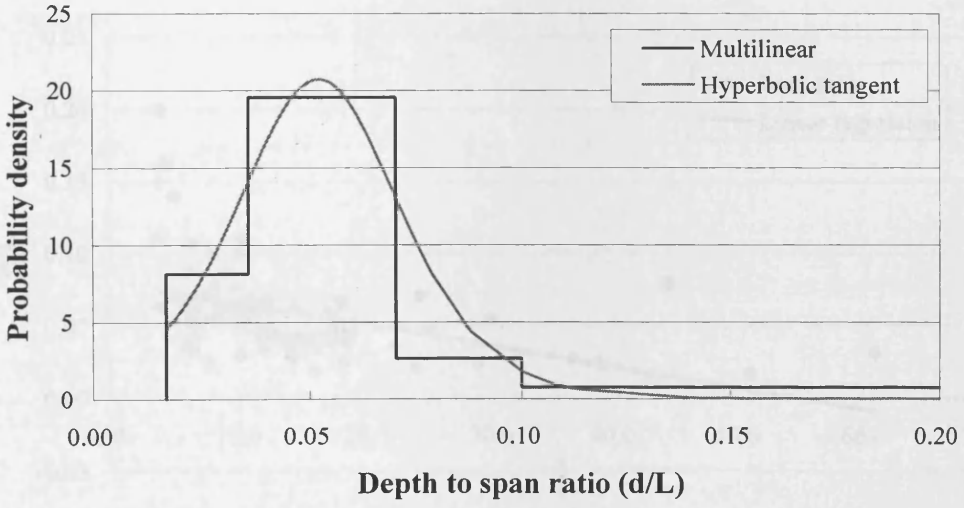

Figure 5.9 Probability density distribution of depth/span

In conclusion, the multilinear gives a little bit better fit than the hyperbolic tangent curve, however the hyperbolic tangent curve has a continuous probability curve which is likely to be more representative of real life. For example, 0.1 *d/L* must be higher probability than 0.2 *d/L* as common sense. Hyperbolic tangent curve can explain this very well, but multilinear curve has the same probability, as illustrated in Figure 5.4.

Hyperbolic tangent curve is used to simulation the span distribution in next chapter.

The trend of *d/L* with span is when span increasing the rise to span ratio is decreasing, as illustrated in Figure 5.10. It is obvious from the figure that the short span has related thicker depth to span ratio and longer span has related thinner depth to span ratio. However, 91.4% of span is between 4 m to 20 m, and the trendline values between the 4 m to 20 m are only slight difference. So it is not big difference to use the independent simulation of span and rise to span ratio. The proposal method does not include this trend, however for future research this affect could be recommended.

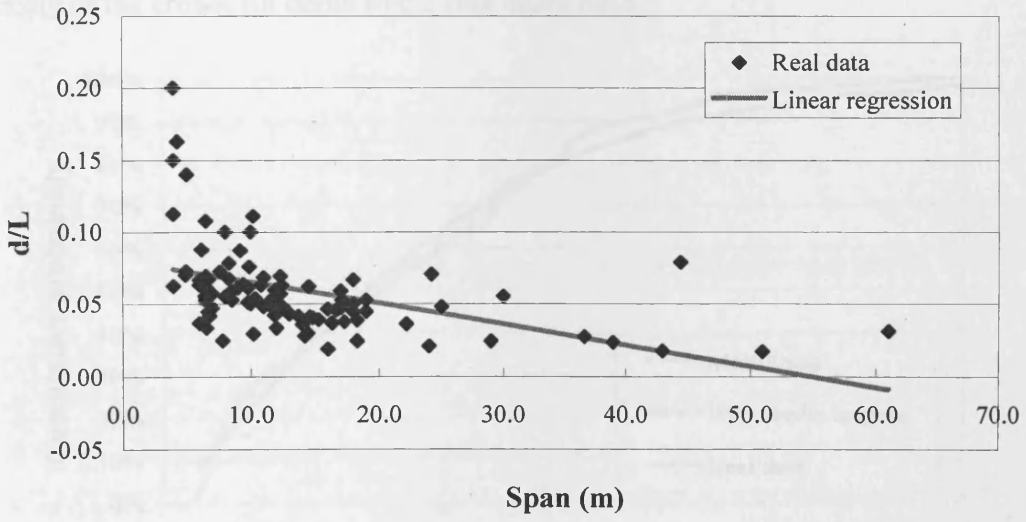

Figure 5.10 Linear regression trendline of d/L to span

5.6 Fill depth statistics

In this section the statistics of the fill depth, as measured above the crown of masonry arch bridges, are developed. Although to date the secondary parameters of rise and arch ring depth have been related to the span, it was considered more appropriate to relate the fill depth to the arch ring depth. This was seen as more appropriate as 1) they were of similar value, 2) they are measured adjacently at the crown and 3) in the same vertical direction.

Figure 5.11 shows the cumulative probability density distribution for the measured data together with the fitted functions of equations (5.1) and (5.3). It is apparent that there are a number of gaps in the data set represented by the horizontal lines where there are no apparent data values, for example between ratio values of 0.6 and 0.8. This was considered to be the result of insufficient data and that there was no practical engineering reason.

As illustrated in Figure 5.11, the R squared value of fitted multilinear curve is 0.9961, and the R squared value of fitted hyperbolic tangent curve is 0.9857. Both models are acceptable. So, both of these models are used to get the probability density of the crown fill depth to the ring depth ratio.

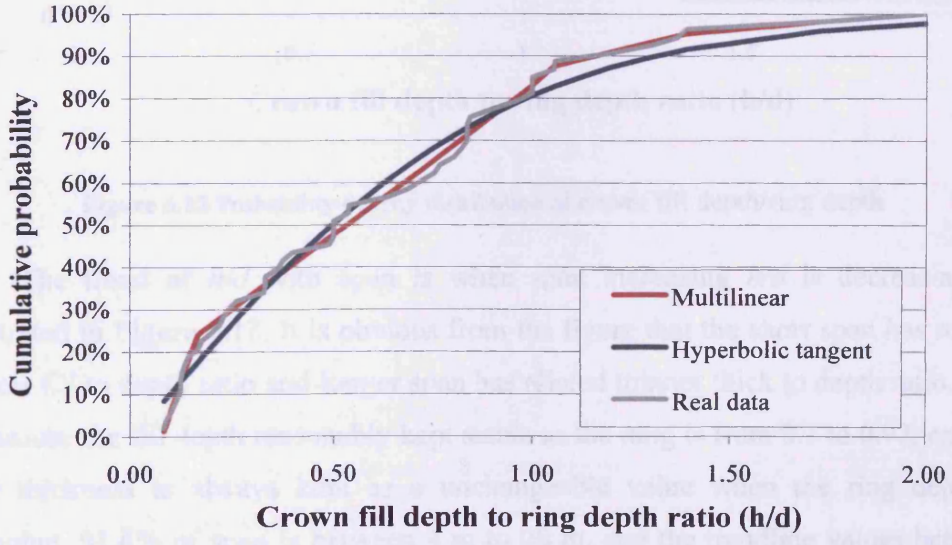

Figure 5.11 Cumulative probability distribution of crown fill depth/ring depth

The average of the *h/d* is 0.61. The median value of real data is 0.50. The highest probability rate is 0.08-0.18 with average is 0.14 according to fitted multilinear model and 0.08 according to fitted hyperbolic tangent model, however from 0.08 to 0.18 the hyperbolic tangent model is fitted very bad, so use the multilinear model mode is the mode value of *h/d*.

So define the typical fill depth to ring depth ratio as 0.5, when typical span is 10 metres then the typical fill depth is 0.27 metres.

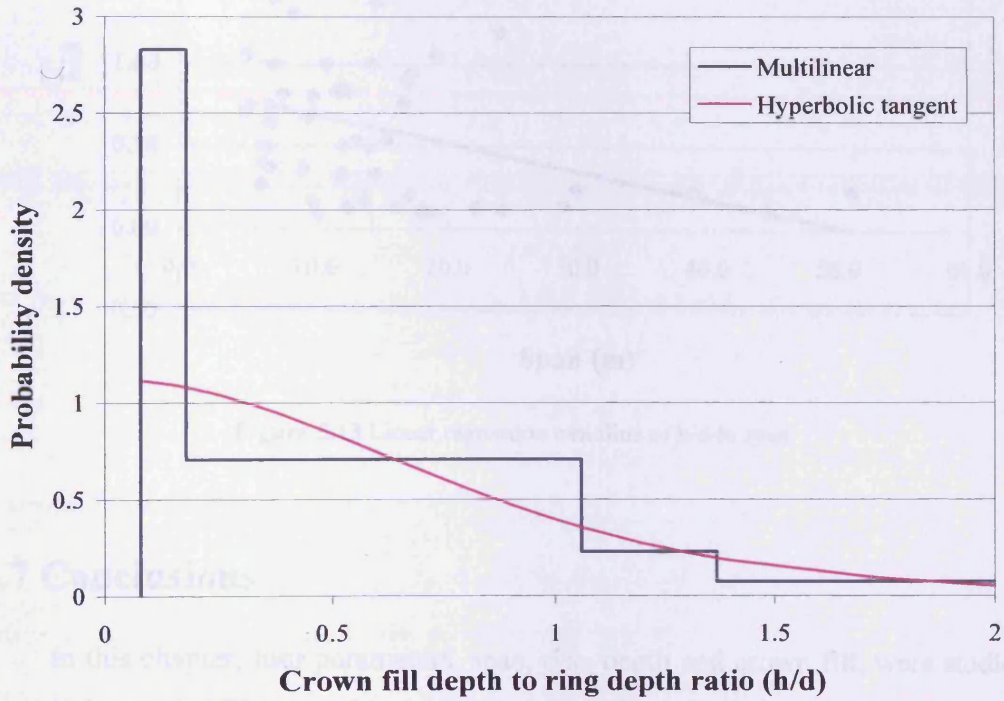

Figure 5.12 Probability density distribution of crown fill depth/ring depth

The trend of *h/d* with span is when span increasing *h/d* is decreasing, as illustrated in Figure 5.13. It is obvious from the figure that the short span has related thicker fill to depth ratio and longer span has related thinner thick to depth ratio. This is because the fill depth reasonably kept stable as the rang is from 0.1 to 0.92, and the road thickness is always kept as a unchangeable value when the ring depth is changing. 91.4% of span is between 4 m to 20 m, and the trendline values between the 4 m to 20 m are about a quarter difference. So it should be included in simulation.

However, the independent simulation of crown fill to ring depth ratio is easier. The proposal method does not include this trend, it is strongly recommended that the future analysis should include this trend, other wise the fill depth will be overestimated in thicker ring depth and underestimated in thinner ring depth.

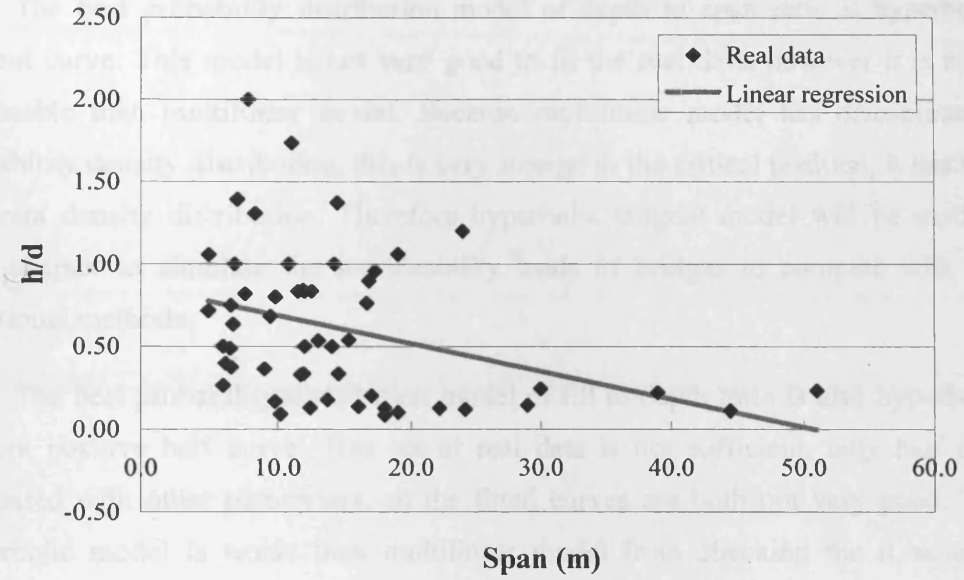

Figure 5.13 Linear regression trendline of h/d to span

5.7 Conclusions

In this chapter, four parameters, span, rise, depth and crown fill, were studied. Cumulative probability was fitted by two types of curve models multilinear model and hyperbolic tangent model. The probability density curve then gets from the fitted cumulative probability curves. Finally, the best model was selected and checked by the R squared value.

The best probability distribution model of span is hyperbolic tangent positive half curve. This model can describe the probability distribution very well. This model will be used in next chapter to simulate the serviceability loads of bridges to compare with the traditional methods.

The best probability distribution model of rise to span ratio is multilinear curve. The longer span has smaller rise to span ratio. However, 91.4% of span is less than 20 metres, and the rise to span ratio within 4 metres to 20 metres is only slight difference. So this relation of span to rise to span ratio will not affect the independent simulation result very much.

The best probability distribution model of depth to span ratio is hyperbolic tangent curve. This model is not very good to fit the real data, however it is more reasonable than multilinear model. Because multilinear model has discontinuous probability density distribution, this is very strange in the critical position, it has two different density distribution. Therefore hyperbolic tangent model will be used in next chapter to simulate the serviceability loads of bridges to compare with the traditional methods.

The best probability distribution model of fill to depth ratio is also hyperbolic tangent positive half curve. This set of real data is not sufficient, only half data compared with other parameters, so the fitted curves are both not very good. The hyperbolic model is worse than multilinear model from checking the R squared value , however, as the same reason as d/L, the hyperbolic is continuous model, and this will be used in next chapter to simulate the serviceability loads of bridges to compare with the traditional methods.

The mean, median, mode and typical value of bridge parameters are listed in Table 5.2. The mode value in table 5.2 uses the mode from selected fitted curves.

Table 5.2 Mean, median, mode and typical value of bridge parameters

	L (m)	r/L	d/L	h/d
Mean	11.5	0.35	0.060	0.61
Median	9.5	0.36	0.053	0.50
Mode	4.0	0.50	0.053	0.14
Typical Value	10.0	0.38	0.053	0.50

From Table 5.2, typical parameters are defined as span is 10 metres, rise to span ratio is 0.38, ring depth to span ratio is 0.053 and crown fill depth to ring depth ratio is 0.5.

Define the typical bridge parameters as span 10 metres, rise 3.8 metres, depth 0.53 metres and fill depth 0.27 metres.

There are no strong correlations between the variables: the ratio of rise to span and span, the ratio of depth to span and span, and the ratio of crown fill to span and span, so that these can be reasonably treated in the next chapter as independent in the simulation of the bridges.

6 Serviceability criteria

6.1 Introduction

A range of serviceability criteria are developed in this chapter. The development of serviceability criteria is much more complex than ultimate limit state criteria since what constitutes a suitable serviceability criteria is much less well defined than the clear engineering concept of overall structural failure. In reviewing approaches to developing the criteria three basic approaches were initially considered, the first was to base the development on a direct examination and interpretation of the recorded evidence of long term bridge performance, the second was to consider the use of complex stress analysis programs, including damage models, linked to advanced understanding of arch construction material mechanical and degradation behaviour. The final approach considered, which was less fundamental and more incremental, was to consider systematically reviewing the implications, on arch bridge assessments, of different serviceability criteria with a view to providing guidance on appropriate levels that would allow an evolution in the assessment method rather than, perhaps, the revolution that would result from the other two approaches. All of these approaches would require the development of a relatively simple engineering model of arch bridge behaviour that would form the analytical base for the subsequent serviceability based assessment method. Each of these three will be discussed in turn.

The owners of the UK bridge stock are acutely aware of the importance of the existing masonry arch infrastructure and are keen to maintain, and not replace, this significant gift from the Victorians. However with such large numbers of structures even carrying out periodic inspections represents a significant task. Modern databases do allow significant volumes of material to be stored, and subsequently queried, so with appropriate bridge management systems in place it should, in theory, be possible to develop a systematic way of interrogating the data to identify general trends in durability. However for arch bridges this is a very complex problem, many

arch bridges, even on the same railway line are substantially different not only in span, general geometry and ground conditions but also in their basic construction materials (bricks, mortar and backfill). In addition there are quite limited records of bridge usage (the live loadings) even for railway bridges where the vehicle passes have historically been timetabled. Assuming that trends in the durability of different types of arch bridge structures could be identified then the next stage would be to analyse the relevant structures at a sufficient detail to try to correlate the database findings with an engineering model of the structures. It is considered that this approach would likely require quite a complex, possibly 3-D, model of the behaviour and it would then be necessary to try to calibrate the damage models to properly replicate real life behaviour. The final stage would then be to develop a simple assessment model, similar to the one developed in Chapters 3 and 4, that was capable of correlating to the complex models. This could be achieved by undertaking a parametric study using the complex model and deriving suitable proxy parameters in the simpler assessment tool. Therefore on the basis of, the difficulty of data access, the questionable value of the data collected and the need to run large numbers of complex models this approach was not followed.

The second approach would not require the direct use of bridge management database systems. The approach would be to develop very complex models of overall arch bridge behaviour and to include within them material models of behaviour that would be able to properly model the material degradation processes directly. This would likely involve significant development of analytical models of brickwork behaviour under repeated loading and would require a large supporting experimental programme; work has been undertaken in this direction but to a limited extent[128-132]. It would also require details of historic loadings similar to the previous approach and the same matching of the outcomes from the complex models to a simpler assessment tool. This approach basically replaces the knowledge about what has historically caused problems, as used in approach one, with detailed fundamental understanding of how the construction materials behave. This second approach is also rejected on the basis of the complex analytical model required and the experimental work required to develop the advanced masonry models, coupled with the additional need to develop a simpler assessment method at the end.

The third approach is less fundamental and follows more incrementally on from recent changes in UK assessment methods. The UK still largely uses the MEXE method (based on a modified working stress model) as its initial approach and it is considered by most that a successful passing assessment using the MEXE method represents sufficient evidence to accept the outcome. There is some recent evidence[172] that this approach is being questioned. The other simple assessment approach is to use an ultimate load model and then to downgrade the result to reflect the questionable judgement that arch bridges start to experience damage at 50% of their ultimate load, as discussed earlier. This latter approach generally uses a mechanism based model of behaviour. The third approach to developing an assessment base method is to investigate a range of serviceability criteria and to pragmatically fix the criteria levels such that they will averagely replicate the existing MEXE or ultimate load approaches and then to consider the circumstances in which the assessments differ from those approaches. If developed such an approach would, in the short to medium term, allow the existing methods to continue but would provide, in parallel, evidence of analysis based concern associated with particular geometric/material parameter values that could, over time, be coupled to inspection evidence, which then would provide the necessary refinement to the approach. Such an approach is considered to be much more likely to be accepted by bridge assessment engineers, as it starts from the existing situation and involves the assessing engineers in the development of the approach. This is the approach adopted for the present study as it represented a good first step in the development of a serviceability based method and was considered to be achievable within the timeframe of the current work.

In order to systematically identify differences between the ultimate load approaches and serviceability based approaches it would be necessary to undertake assessments covering the full range of masonry arch bridge material and geometric parameters. That was the primary reason for developing the statistical basis for the probability of occurrence of a range of arch parameters in Chapter 5. It was accepted at the start that even with an analysis tool as easy to use as the spreadsheet, developed in Chapters 3 and 4, it would not be practicable, or even possible, to undertake sufficient assessments to fully cover these ranges using the actual

assessment tool. It was therefore decided to develop a "surrogate" of the cracking elastic model which retained the essential features but which could be included in a wide ranging parametric modelling study. The development stages of this approach are therefore to:-

1. Identify likely suitable candidates for a serviceability based approach.
2. Apply the serviceability assessment tool (Chapter 4) to a small sample of bridges and develop suitable average parameter values that on average gave similar results to the ULS assessment.
3. Apply these fixed serviceability parameter values to the analysis of a separate wider range of bridges using the same serviceability assessment tool.
4. Use these results to develop a simple empirical model of the assessment tool, and of the ULS approach, and to then check their performance.
5. Apply the simple empirical models to the full range of bridge stock with the correct frequency of usage (Chapter 5) of any value appropriate to its probability of occurrence.
6. Modify the serviceability parameter values until the assessment methods give the same overall mode load as ultimate assessment methods, that is to say, 50% of bridges' allowable load is lower than this model load.
7. Finally quantify types of arches that are more likely to be prone to serviceability failure than ULS.

The development of serviceability assessment criteria using this approach is illustrated in Figure 6.1.

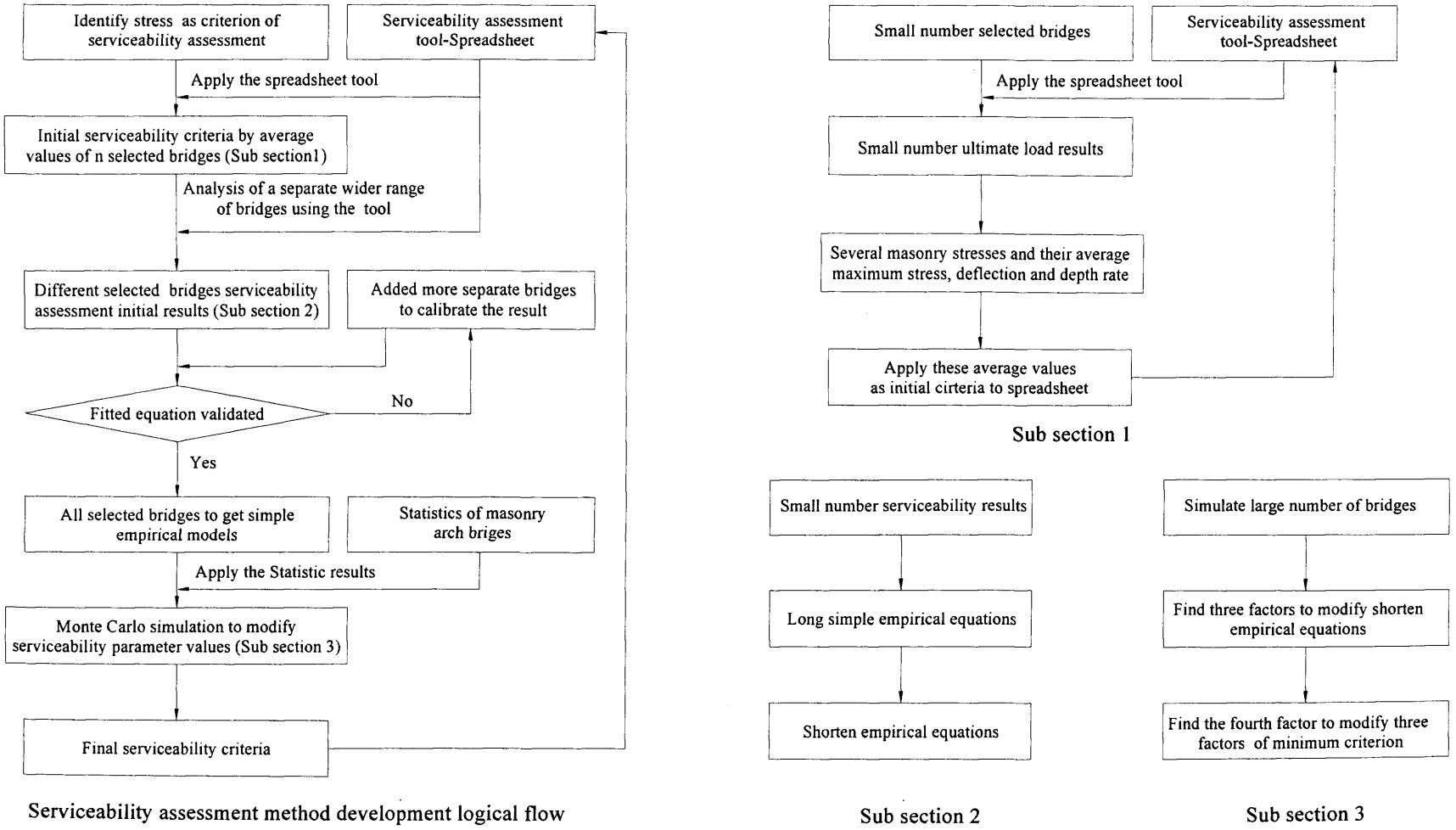

Figure 6.1 Serviceability assessment development logical flow

6.2 Serviceability criterion selection

Serviceability criteria for structures are generally associated with either deflections or stresses, in addition for certain concrete applications, for example water retaining structures, crack widths (depths) are also considered appropriate. Three criteria were initially selected for use with masonry arch bridges there were: - a compressive stress related criterion, a deflection criterion and a criterion associated with the development of cracking, or opening, of a masonry joint.

6.2.1 Stress criterion selection

Following consideration of the stresses developed both with moving load patterns and loading to limit state (ultimate limit or serviceability limit) at the critical load location, using the analysis from Chapter 4, the relevant serviceability stress was defined as the maximum intrados or extrados stress occurring anywhere in the arch ring except at the abutment.

6.2.1.1 Increasing load to limit stress in critical position

Figure 6.2 shows a typical variation of the intrados and extrados compressive stress along a masonry arch bridge for a line load applied at about the third point, also included is the effective arch depth (that area of the arch in compression); the live loading for this figure is at, or about, serviceability level. As illustrated the maximum stress normally happens under the location of the live load. Under ultimate load the stress distribution is similar to this figure only with reduced areas carrying the load and, of course, higher compressive stresses everywhere.

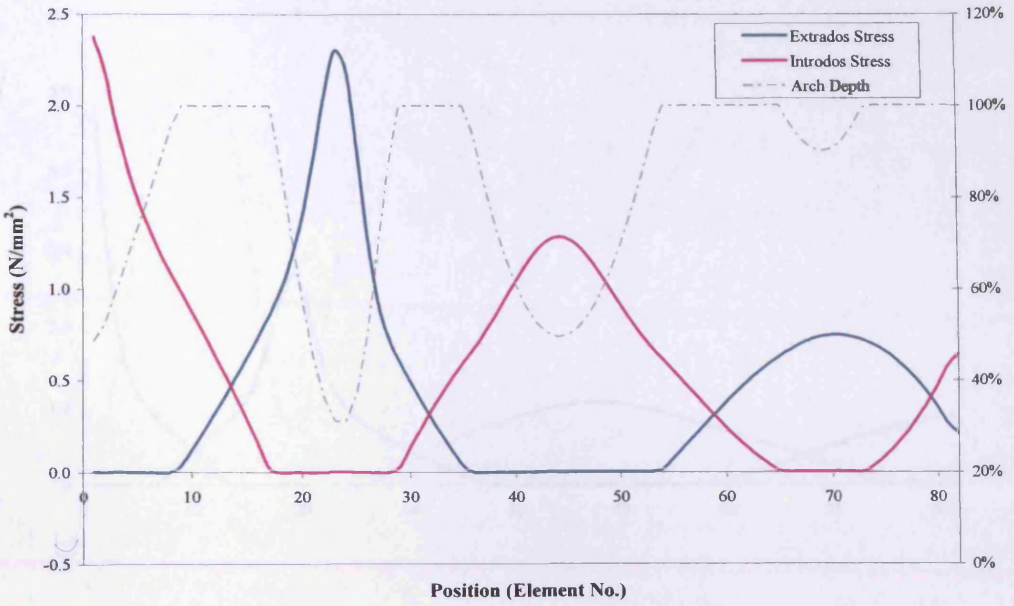

Figure 6.2 Typical bridge (C26) variation of intrados and extrados stress when loaded at the critical location

As illustrated in Figure 6.3, for shallow bridges the maximum stress sometimes occurs close to the abutment, adjacent to the live load. It is considered unlikely that critically high stresses can develop at either abutment and that these stresses are the result of an inadequate representation of the true nature of the support provided in "real" bridges, for example significant additional "backing" material is frequently placed behind the springing of the supports. This structural masonry effectively increases the ring thickness local to the abutments and for the case illustrated in Figure 6.3 would result in a local change in the centreline of the arch which would reduce the predicted intrados stress. Similarly at the hinge remote from the live load, on the right of Figure 6.3, here the line of thrust could actually leave the arch prior to the end of the arch ring provided there was sufficient "backing" material in the structure. **Therefore the location of the maximum stresses considered as the stress criterion are restricted so as not to include either abutment.**

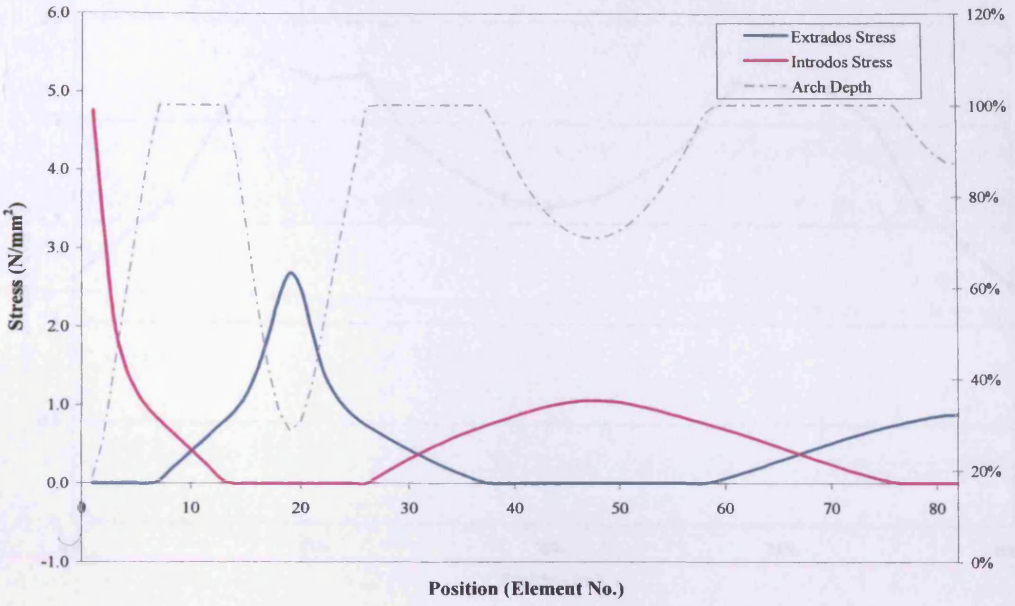

Figure 6.3 Shallow bridge (C04) variation of intrados and extrados stress when loaded at the critical location

6.2.1.2 Moving load over the entire bridge.

Having discounted the abutment stress the variation of peak stress with load position is typically as detailed in Figure 6.4. The serviceability load critical position for a typical masonry arch bridge is near the quarter point, similar to that found for the ultimate load critical position. For a shallow bridge, as illustrated in Figure 6.5, this gives a similar figure to the typical bridge.

Earlier work [59] had limited the stress consideration to the intrados incipient hinge area between the applied load and the abutment remote from the applied load on the basis that the extreme extrados stresses under the applied load were confined by the load above to such an extent that it was not considered a critical location (ie the masonry was considered to be largely in triaxial compression).

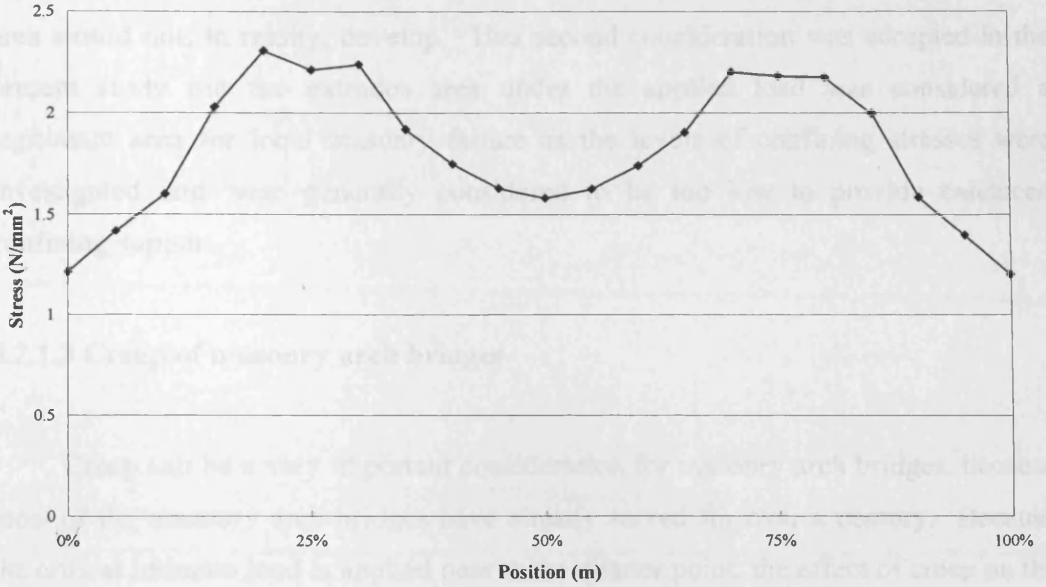

Figure 6.4 Typical bridge variation of peak stress with load location

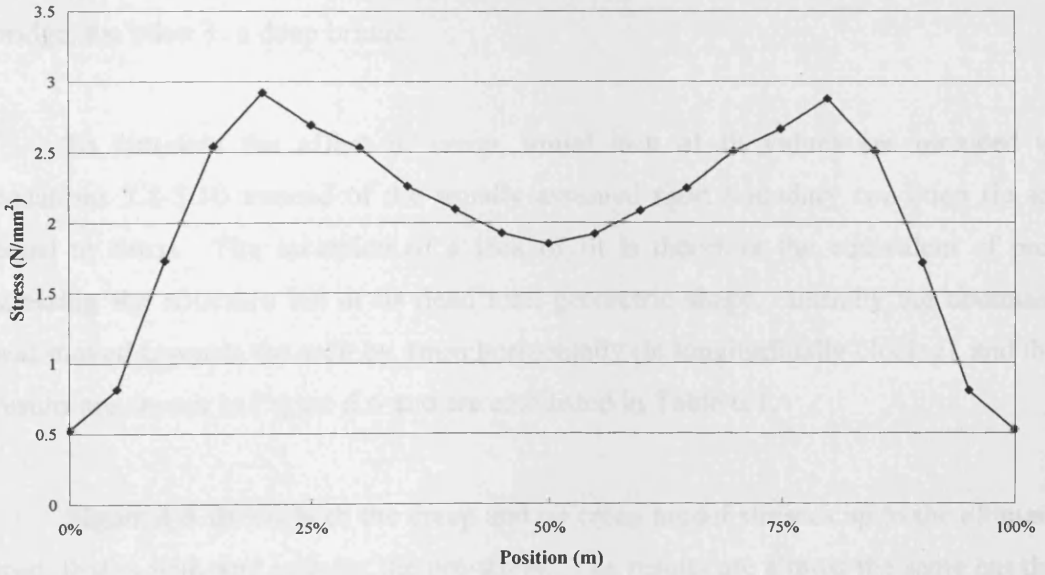

Figure 6.5 Shallow bridge variation of peak stress with load location

The far abutment hinge area was also not considered critical as this is, almost universally, a poorly defined support with there frequently being backing masonry material in this area, that effectively extends the support vertically (as detailed in

section 6.1), such that the extreme extrados stresses predicted by the analysis in this area would not, in reality, develop. This second consideration was accepted in the present study but the extrados area under the applied load was considered a legitimate area for local masonry failure as the levels of confining stresses were investigated and were generally considered to be too low to provide enhanced confining support.

6.2.1.3 Creep of masonry arch bridges

Creep can be a very important consideration for masonry arch bridges, because most of the masonry arch bridges have already served for over a century. Because the critical ultimate load is applied near to the quarter point, the effect of creep on the peak stress at the ultimate load is not significant, but at lower loads the initial stress state is still important, for example when it is assessed by the serviceability limit load. Two types of masonry arch bridges were studied in this section. One is a shallow bridge, the other is a deep bridge.

To simulate the effect of creep, initial lack of fit values are included in equations 3.8-3.10 instead of the usually assumed rigid boundary condition (ie set equal to zero). The inclusion of a lack of fit is therefore the equivalent of pre-stressing the structure but at its dead load geometric shape. Initially the abutment was moved towards the arch by 1mm horizontally (ie longitudinally closing), and the results are shown in Figure 6.6 and are also listed in Table 6.1.

Figure 6.6 shows both the creep and no creep model stresses up to the ultimate load, that is with and without the pre-stress. The results are almost the same but the stresses at the serviceability limit (stress in the central region) are slightly different (near 10% in Table 6.1). When applied, creep in masonry arch bridges would thus allow it to carry about 10% more load than when not applied in the serviceability limit state in a shallow arch.

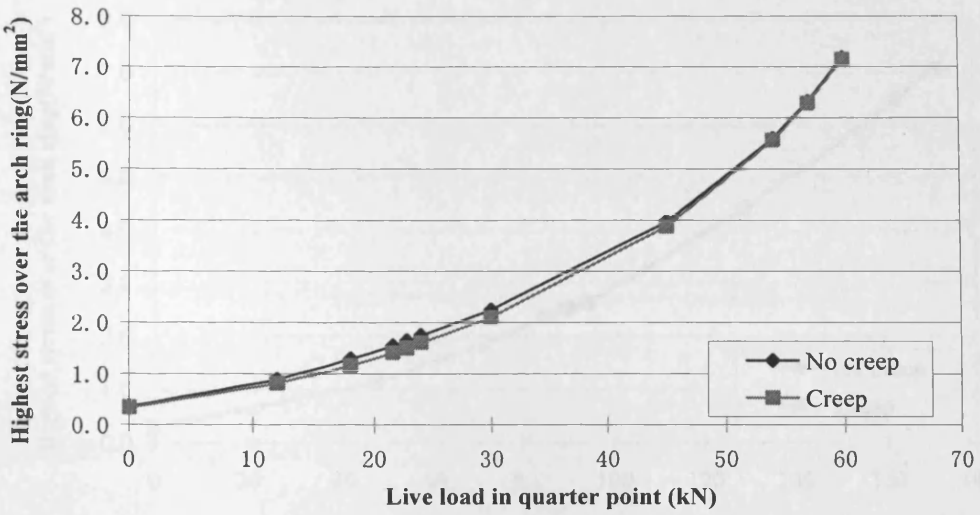

Figure 6.6 Creep effect on the variation of peak stress with load for a shallow masonry arch

Table 6.1 Shallow bridge's creep effect

Force(kN)	No Creep (N/mm^2)	Creep (N/mm^2)	Difference
0.0	0.36	0.34	-5.9%
12.0	0.89	0.81	-9.8%
18.0	1.29	1.16	-9.9%
21.6	1.55	1.41	-8.9%
22.8	1.64	1.50	-8.5%
24.0	1.75	1.61	-8.1%
30.0	2.25	2.10	-6.8%
45.0	3.96	3.88	-2.1%
54.0	5.59	5.56	-0.6%
57.0	6.31	6.28	-0.5%
60.0	7.18	7.15	-0.4%

Figure 6.7 and Table 6.2 shows the equivalent phenomenon except this is now for a deep arch. This shows that creep does not significantly affect the stresses in a deep arch.

Normally, at the critical positions, the creep effect is relatively small, so the effect of creep on masonry arch bridge is not considered further in serviceability and ultimate assessment of masonry arch bridges.

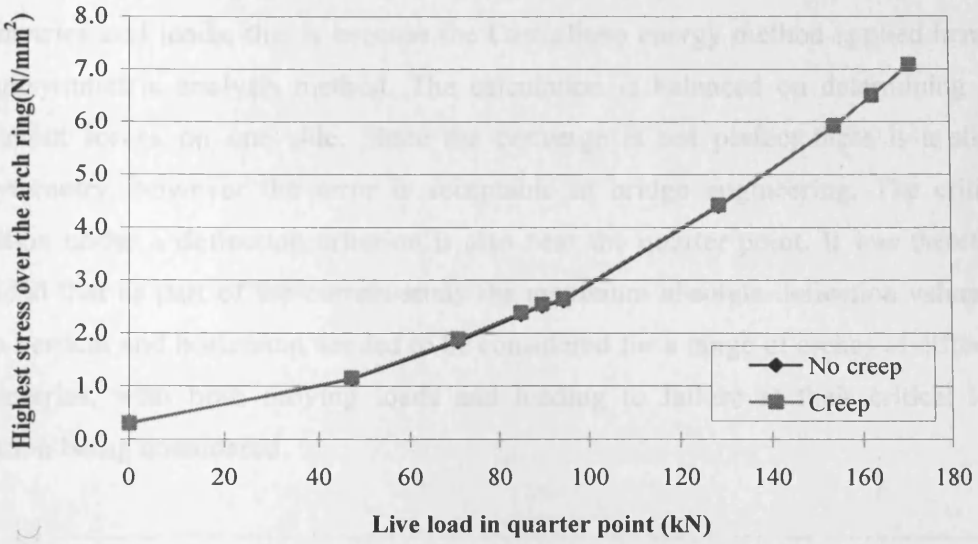

Figure 6.7 Creep effect on the variation of peak stress with load for a deep masonry arch

Table 6.2 Deep bridge's creep effect

Force(kN)	No Creep	Creep	Difference
0.0	0.31	0.30	-1.0%
47.2	1.14	1.16	2.3%
70.8	1.84	1.89	2.3%
84.9	2.35	2.39	1.9%
89.6	2.51	2.55	1.7%
94.3	2.61	2.65	1.5%
128.3	4.40	4.42	0.6%
153.9	5.92	5.93	0.1%
162.5	6.50	6.50	0.1%
171.0	7.08	7.09	0.1%

6.2.2 Deflection criterion selection

Following initial consideration of the deflection plots for both vertical and horizontal deflection, as typically illustrated in Figure 6.8 and the shape of the total deflection as illustrated in Figure 6.9, it was determined that for standard vertical live loading the maximum total deflection is almost always at the position of maximum vertical deflection. Figure 6.10 shows the moving load positions and their maximum

total deflections. Figure 6.10 is very slightly unsymmetric under symmetric geometries and loads, this is because the Castigliano energy method applied here is an unsymmetric analysis method. The calculation is balanced on determining the abutment forces on one side. Since the converge is not perfect there is a slight unsymmetry, however the error is acceptable in bridge engineering. The critical position under a deflection criterion is also near the quarter point. It was therefore decided that as part of the current study the maximum absolute deflection values of both vertical and horizontal needed to be considered for a range of arches of different geometries, with both moving loads and loading to failure at their critical load location being considered.

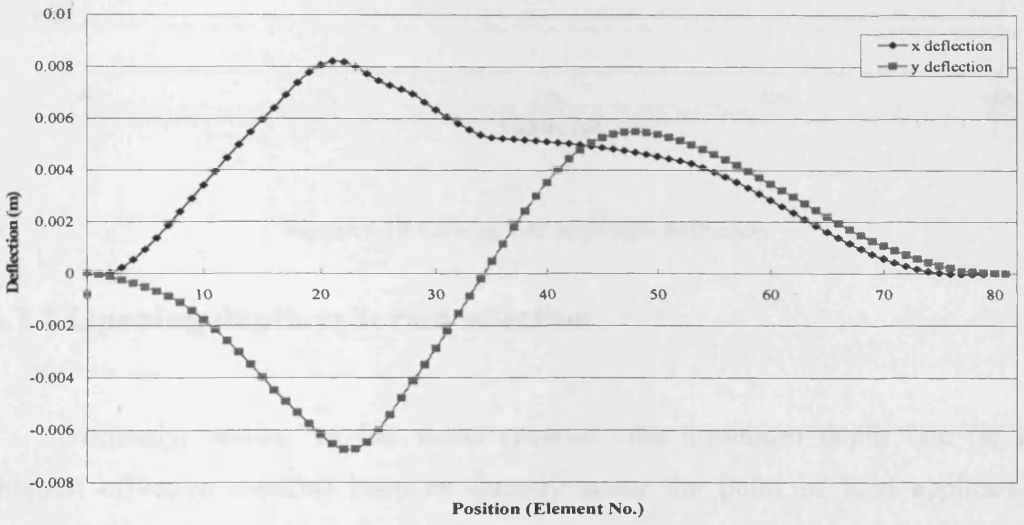

Figure 6.8 Normal bridge vertical and horizontal deflection

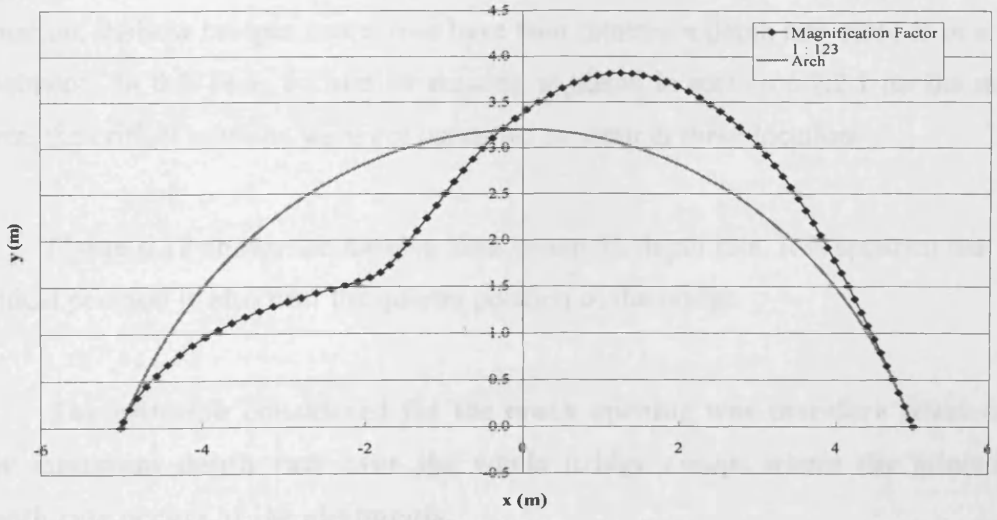

Figure 6.9 Normal bridge total deflection shape

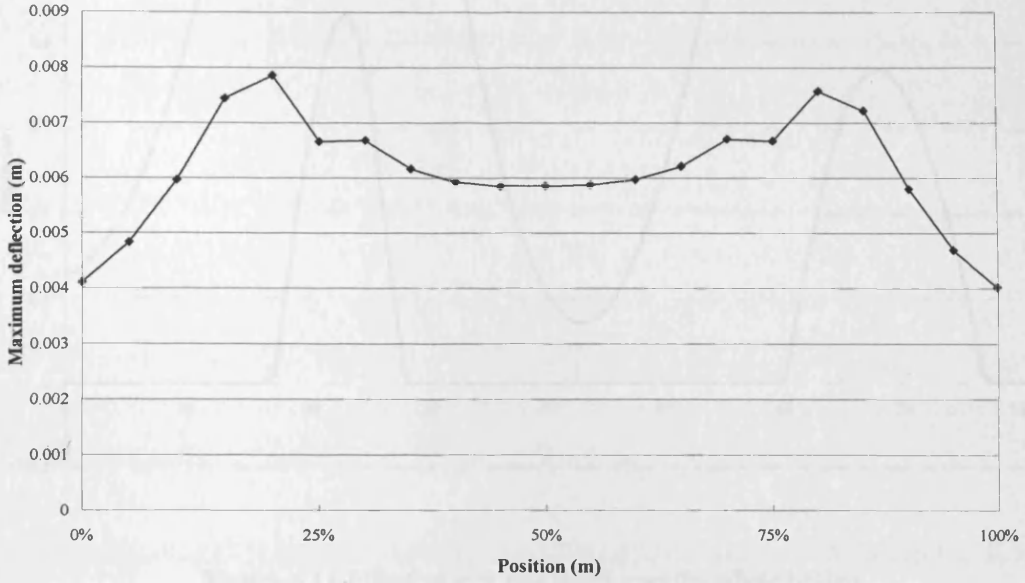

Figure 6.10 Moving load maximum deflection

6.2.3 Opening depth criterion selection

Normally, similar to the stress criterion, the minimum depth rate (ie the thinnest effective section) happens directly under the point of load application. Figure 6.11 shows the variation of the thinning depth across a typical bridge. This typical bridge's minimum depth rate occurs under the live load. As with the stress criterion, shallow bridges sometimes have their minimum depth rate close to or at the abutment,. In this case, for similar reasons, as stated in section 6.2.2.1 for the stress state, the critical sections were not permitted to occur at these locations..

Figure 6.12 shows the moving load minimum depth rate. It is apparent that the critical position is also near the quarter position of the bridge.

The criterion considered for the crack opening was therefore selected as the minimum depth rate over the whole bridge except where the minimum depth rate occurs at the abutments.

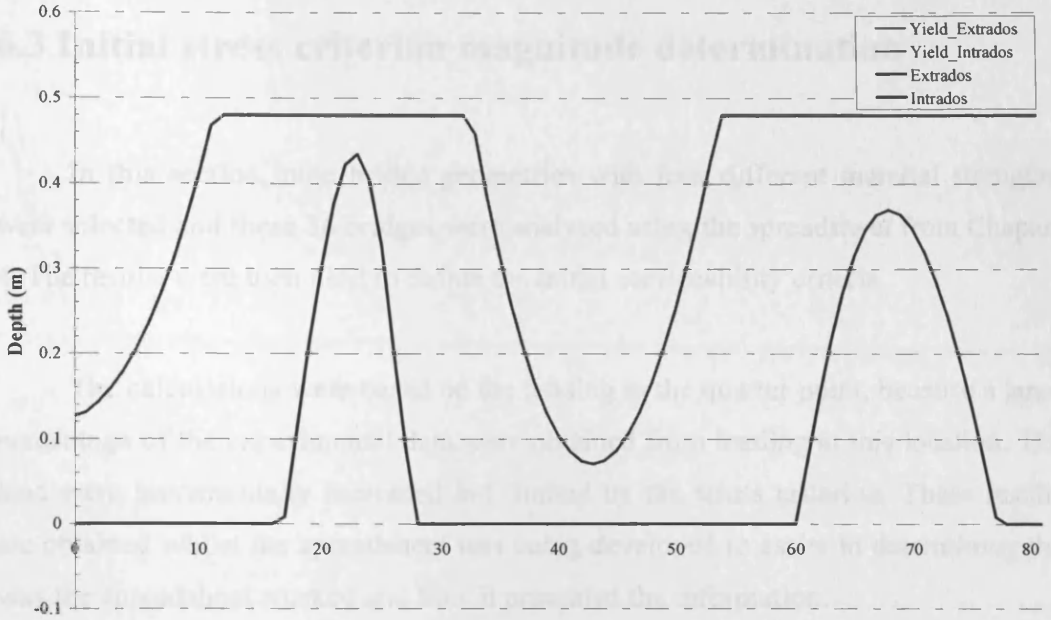

Figure 6.11 Effective arch ring depth over the whole bridge

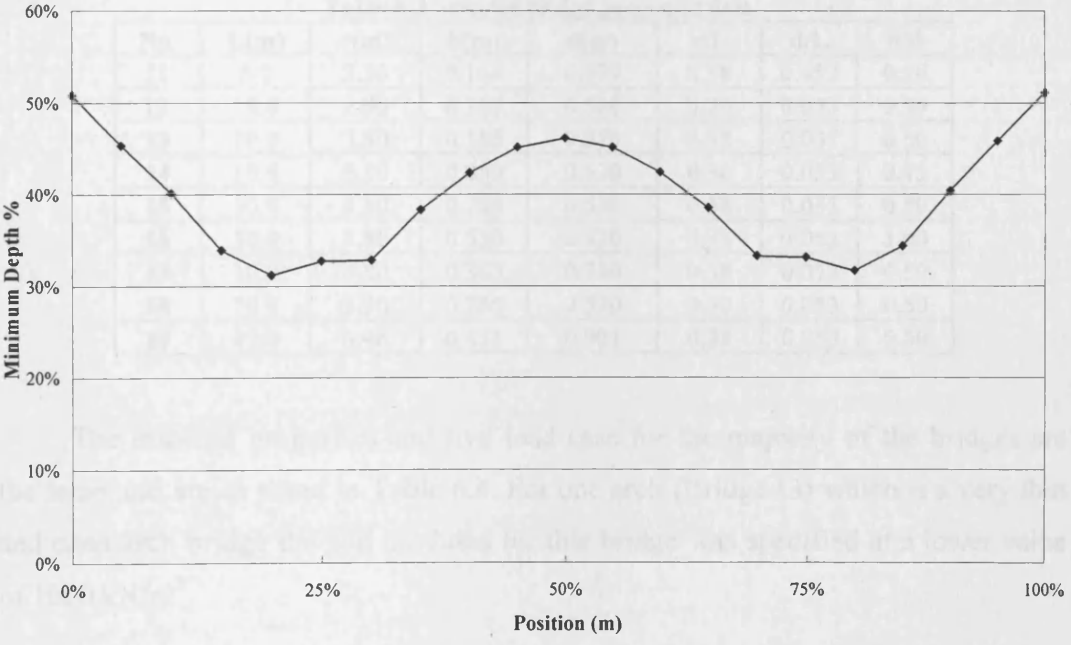

Figure 6.12 Variation of minimum effective arch ring depth with load position

6.3 Initial stress criterion magnitude determination

In this section, nine bridge geometries with four different material strengths were selected and these 36 bridges were analysed using the spreadsheet from Chapter 4. The results were then used to define the initial serviceability criteria.

The calculations were based on the loading in the quarter point, because a large percentage of the experimental data were obtained from loading at this location. The load were incrementally increased but limited by the stress criterion. These results are obtained whilst the spreadsheet was being developed to assist in determining the way the spreadsheet worked and how it presented the information.

Table 6.3 shows the nine bridges' geometric data, L is span, r is rise, h is fill depth, and d is ring thickness. The bridges have 4 different parameters: span, rise to span ratio, ring depth to span ratio and fill depth to ring thickness ratio.

Table 6.3 Selected bridge geometric data

No.	L(m)	r(m)	h(m)	d(m)	r/L	d/L	h/d
I1	6.2	2.36	0.164	0.329	0.38	0.053	0.50
I2	10.0	2.00	0.265	0.530	0.20	0.053	0.50
I3	10.0	3.80	0.185	0.370	0.38	0.037	0.50
I4	10.0	3.80	0.069	0.530	0.38	0.053	0.13
I5	10.0	3.80	0.265	0.530	0.38	0.053	0.50
I6	10.0	3.80	0.530	0.530	0.38	0.053	1.00
I7	10.0	3.80	0.365	0.730	0.38	0.073	0.50
I8	10.0	5.00	0.265	0.530	0.50	0.053	0.50
I9	17.0	6.46	0.451	0.901	0.38	0.053	0.50

The material properties and live load case for the majority of the bridges are the same and are as listed in Table 6.4. For one arch (Bridge I3) which is a very thin and deep arch bridge the soil modulus for this bridge was specified at a lower value of 1000 kN/m^3.

Table 6.4 Bridge material properties and load case

Masonry density (kN/m^3)	Young Modulus (kN/m^2)	Fill Density (kN/m^3)	Phi (degrees)	Soil Modulus (kN/m^3)	Load Dimension (m)	Dispersion Angle (degrees)
23	1.50E+06	20	27	9900	0.175	0.053

The TRL tested a significant number of arch bridges and showed that deformations increase rapidly as the applied load exceeds approximately half the ultimate failure load. In order to avoid causing any permanent structural damage, it was further suggested that a serviceability load could be considered at a value of one half of the ultimate failure load. Table 6.5 details the maximum stresses, maximum deflections and maximum hinge depths for the 9 different bridges at 50% of their ultimate load. Four groups of material strength for the material making up the arch rings were consider and are listed in the table. Ultimate loads based on both quarter point and loading at their most critical point were also determined and the results presented.

Table 6.5 also includes a comparison of the quarter load to the critical position load. The critical positions in the table are all around the quarter point, so the ultimate loads for these two different positions are naturally similar.

Table 6.6 details the initial serviceability criteria selected as a result of the outcomes detailed in Table 6.5. When the ultimate stresses are $5N/mm^2$, $10N/mm^2$, $15N/mm^2$ and $20N/mm^2$, the resulting serviceability stress, deflection and first hinge depth rate are listed in the table. These criterion are ultimate masonry strength related, because the ultimate load is ultimate masonry stress related.

If the stress values are between these range, the serviceability criterion can be obtained using linear interpolation.

6.4 Selected bridges initial serviceability results

In this section, the ultimate and serviceability loads for 43 selected bridges were calculated using the Castigliano spreadsheet, using the initial serviceability criteria developed and detailed in Table 6.6.

Table 6.5 Stress, defection and hinge depths for a range of arch bridges at one half ultimate load

No.	Quarter point ultimate load (kN)	Half load stress (N/mm^2)	Half load deflection	Half load first hinge depth rate	Critical Position	Critical position ultimate load (kN)	Half load stress (N/mm^2)	Half load deflection	Half load first hinge depth rate
I1	87	1.50	0.00045L	31.3%	25%	87	1.50	0.00045L	31.3%
I2	196	2.31	0.00063L	40.8%	20%	191	2.20	0.00057L	40.7%
I3	66	2.22	0.00112L	33.7%	20%	65	2.36	0.00143L	30.5%
I4	162	1.74	0.00050L	35.4%	20%	157	1.73	0.00058L	34.8%
I5	199	1.90	0.00054L	38.4%	25%	199	1.90	0.00054L	38.4%
I6	250	2.19	0.00063L	41.4%	30%	245	2.20	0.00067L	40.8%
I7	401	2.12	0.00056L	35.8%	30%	382	2.23	0.00057L	34.9%
I8	203	1.90	0.00070L	37.5%	25%	203	1.90	0.00070L	37.5%
I9	453	2.41	0.00064L	48.6%	25%	453	2.41	0.00064L	48.6%
5 N/mm^2 Average		**2.03**	**0.00064L**	**38.1%**		**Average**	**2.05**	**0.00068L**	**36.9%**
I1	98	1.80	0.00054L	27.3%	25%	98	1.80	0.00054L	27.3%
I2	246	3. 05	0.00086L	34.0%	20%	234	2.84	0.00076L	34.2%
I3	86	2.90	0.00154L	24.9%	20%	82	3.10	0.00191L	23.4%
I4	190	2.21	0.00064L	29.6%	20%	182	2.12	0.00071L	29.7%
I5	237	2.44	0.00070L	32.0%	25%	237	2.44	0.00070L	32.0%
I6	312	2.92	0.00086L	33.9%	30%	309	3.01	0.00091L	32.9%
I7	499	2.85	0.00076L	29.4%	30%	494	3.17	0.00081L	28.0%
I8	244	2.49	0.00087L	30.7%	20%	243	2.30	0.00080L	32.2%
I9	597	3.40	0.00091L	37.7%	25%	597	3.40	0.00091L	37.7%
10 N/mm^2 Average		**2.63**	**0.00085L**	**31.1%**		**Average**	**2.69**	**0.00089L**	**30.5%**
I1	102	1.92	0.00058L	26.0%	25%	102	1.92	0.00058L	26.0%
I2	266	3.38	0.00097L	31.7%	20%	250	3.11	0.00085L	32.1%
I3	95	3.43	0.00179L	21.5%	20%	85	3.24	0.00200L	22.5%
I4	201	2.41	0.00069L	27.7%	20%	191	2.28	0.00077L	28.0%
I5	252	2.67	0.00077L	29.8%	25%	252	2.67	0.00077L	29.8%
I6	332	3.19	0.00095L	31.8%	25%	332	3.19	0.00095L	31.8%
I7	536	3.17	0.00085L	27.4%	25%	536	3.17	0.00085L	27.4%
I8	259	2.74	0.00095L	28.6%	20%	258	2.51	0.00087L	30.1%
I9	658	3.91	0.00105L	34.0%	25%	658	3.91	0.00105L	34.0%
15 N/mm^2 Average		**2.98**	**0.00096L**	**28.7%**		**Average**	**2.89**	**0.00097L**	**28.9%**
I1	104	1.99	0.00060L	25.4%	25%	104	1.99	0.00060L	25.4%
I2	276	3.57	0.00103L	30.6%	20%	258	3.25	0.00090L	31.3%
I3	99	3.71	0.00191L	20.1%	20%	88	3.45	0.00214L	21.4%
I4	207	2.53	0.00073L	26.7%	20%	196	2.38	0.00080L	27.1%
I5	260	2.81	0.00081L	28.8%	25%	260	2.81	0.00081L	28.8%
I6	342	3.34	0.00100L	30.8%	25%	342	3.34	0.00100L	30.8%
I7	556	3.35	0.00090L	26.4%	25%	556	3.35	0.00090L	26.4%
I8	267	2.88	0.00099L	27.6%	20%	266	2.63	0.00091L	29.0%
I9	693	4.22	0.00114L	32.2%	25%	693	4.22	0.00114L	32.2%
20 N/mm^2 Average		**3.16**	**0.00101L**	**27.6%**		**Average**	**3.05**	**0.00102L**	**27.9%**

Table 6.6 Initial serviceability criteria

Ultimate Stress (N/mm^2)	Quarter Serviceability Stress (N/mm^2)	Quarter Serviceability Deflection	Quarter Serviceability First Hinge Depth Rate	Critical Serviceability Stress (N/mm^2)	Critical Serviceability Deflection	Critical Serviceability First Hinge Depth Rate
5	2.03	0.00064L	38.1%	2.05	0.00068L	37.5%
10	2.63	0.00085L	31.1%	2.69	0.00089L	30.8%
15	2.98	0.00096L	28.7%	2.89	0.00097L	29.1%
20	3.16	0.00101L	27.6%	3.05	0.00102L	28.0%

The selected bridges with different geometries and material properties have three groups. The first group has 19 bridges with several random parameters, and all parameters are not related. The second group uses the same 19 bridges but 10 parameters are related with every different bridge only having a change to one parameter in turn. So each bridge is different with each other but similar with each other. The third group additionally have some random parameter values. The 43 bridges with the 10 parameters are listed in Table 6.7.

Table 6.8 then lists the ultimate and serviceability results of the selected bridges detailed in Table 6.7. These results are all generated from the spreadsheet developed earlier.

The headings of Table 6.8 are explained as below:

- Quarter Ultimate Load (kN): this is a single axle ultimate load at the quarter position of the bridge.
- Load Pos.: this is the critical position of ultimate load, the value is a percentage of the whole span.
- Critical Ultimate Load (kN): this is the critical position single axle ultimate load of the bridge.
- Quarter Stress Ser. Load (kN): quarter position stress based serviceability load.
- Load Pos.: critical position of stress serviceability criterion.
- Critical Stress Ser. Load (kN): critical position stress based serviceability load.
- Quarter Def. Ser. Load (kN): quarter deflection based serviceability load.
- Load Pos. : critical position of deflection based serviceability load.
- Critical Def. Ser. Load (kN): critical position deflection based serviceability load.
- Quarter Hinge Ser. Load (kN): quarter hinge serviceability load.
- Load Pos.: critical position of hinge rate based serviceability load.
- Critical Hinge Ser. Load (kN): critical position hinge rate based serviceability load.
- Min. Ser. Load (kN): minimum value of three criteria based serviceability load

Table 6.7 Selected parameters of masonry bridges for initial testing of the serviceability criterion

No.	L (m)	r/L	d/L	h/d	Ultimate Stress (N/mm^2)	Phi (°)	Soil E (kN/m^3)	Arch E (kN/m^2)	Soil Density (kN/m^3)	Arch Density (kN/m^3)
C01	4	0.32	0.048	0.23	7.0	27	9000	1500000	21	23
C02	5	0.19	0.058	0.36	8.0	29	9700	2000000	20	24
C03	6	0.32	0.040	0.33	9.0	28	7900	1800000	19	23
C04	7	0.12	0.038	0.16	10	25	9900	1600000	18	22
C05	8	0.20	0.047	0.37	15	37	8900	1700000	17	21
C06	9	0.19	0.049	0.43	14	50	6900	2100000	20	23
C07	10	0.32	0.055	0.53	13	47	5000	2500000	21	25
C08	11	0.31	0.051	0.63	12	32	5900	3000000	22	23
C09	12	0.35	0.056	0.33	11	38	9100	1600000	15	22
C10	13	0.25	0.061	0.39	10	27	9200	1400000	16	18
C11	14	0.32	0.044	0.73	9.0	39	6700	2600000	19	23
C12	15	0.20	0.043	0.84	7.0	40	7500	1300000	17	19
C13	16	0.19	0.067	0.96	8.0	44	8500	2800000	18	23
C14	17	0.17	0.060	0.23	6.0	45	6800	2900000	20	24
C15	18	0.26	0.087	0.53	5.0	26	8700	1700000	21	21
C16	19	0.42	0.056	0.73	10	37	9600	1800000	18	23
C17	20	0.50	0.053	0.93	12	36	5000	2000000	17	22
C18	21	0.38	0.048	0.26	6.0	29	5900	1700000	19	21
C19	22	0.34	0.055	0.39	12	31	9900	1500000	20	23
C20	6	0.32	0.048	0.33	7.0	27	9900	1500000	20	23
C21	10	0.19	0.048	0.33	7.0	27	9900	1500000	20	23
C22	10	0.32	0.040	0.33	7.0	27	9900	1500000	20	23
C23	10	0.32	0.048	0.16	7.0	27	9900	1500000	20	23
C24	10	0.32	0.048	0.33	15	27	9900	1500000	20	23
C25	10	0.32	0.048	0.33	7.0	50	9900	1500000	20	23
C26	10	0.32	0.048	0.33	7.0	27	5000	1500000	20	23
C27	10	0.32	0.048	0.33	7.0	27	9900	3000000	20	23
C28	10	0.32	0.048	0.33	7.0	27	9900	1500000	15	23
C29	10	0.32	0.048	0.33	7.0	27	9900	1500000	20	18
C30	10	0.32	0.048	0.33	7.0	27	9900	1500000	20	23
C31	10	0.32	0.048	0.84	7.0	27	9900	1500000	20	23
C32	10	0.32	0.048	1.10	7.0	27	9900	1500000	20	23
C33	10	0.32	0.060	0.33	7.0	27	9900	1500000	20	23
C34	10	0.32	0.087	0.33	7.0	27	9900	1500000	20	23
C35	10	0.42	0.048	0.33	7.0	27	9900	1500000	20	23
C36	10	0.45	0.048	0.33	7.0	27	5000	1500000	20	23
C37	14	0.32	0.048	0.33	7.0	27	9900	1500000	20	23
C38	22	0.32	0.080	0.33	7.0	27	9900	1500000	20	23
C39	5.5	0.26	0.087	0.53	5.0	26	8700	1700000	21	21
C40	7.5	0.25	0.061	0.39	10	27	9200	1400000	16	18
C41	9.5	0.19	0.067	0.96	8.0	44	8500	2800000	18	23
C42	11.5	0.19	0.058	0.36	8.0	29	9700	2000000	20	24
C43	13.5	0.20	0.047	0.37	15	37	8900	1700000	17	21

As shown in Table 6.8, the serviceability loads are normally near one half the ultimate loads, however, a lot of long span bridges have significantly different SLS loads from half ULS loads. So 50% of ultimate load does not work for all arches.

Table 6.8 Ultimate and Serviceability results of selected bridges

No.	Quarter Ultimate Load (kN)	Load Pos.	Critical Ultimate Load (kN)	Quarter Stress Ser. Load (kN)	Load Pos.	Critical Stress Ser. Load (kN)	Quarter Def. Ser. Load (kN)	Load Pos.	Critical Def. Ser. Load (kN)	Quarter Hinge Ser. Load (kN)	Load Pos.	Critical Hinge Ser. Load (kN)	Min. Ser. Load (kN)
C01	27.2	20%	25.5	19.4	20%	19.2	17.9	20%	16.8	9.90	20%	9.80	9.80
C02	83.1	20%	78.0	48.3	25%	48.3	57.4	20%	55.3	35.2	20%	34.6	34.6
C03	41.1	20%	36.8	26.6	20%	25.0	26.7	15%	23.1	17.7	20%	16.0	16.0
C04	68.7	20%	60.3	33.8	20%	31.9	33.9	20%	33.2	33.8	20%	29.7	29.7
C05	126	20%	116	65.1	20%	64.1	71.5	20%	70.1	57.8	20%	54.8	54.8
C06	219	20%	204	83.4	25%	83.4	108	20%	107	90.2	20%	86.4	83.4
C07	328	25%	328	122	35%	118	176	25%	176	116	25%	116	116
C08	302	25%	302	119	25%	119	190	20%	190	133	25%	133	119
C09	346	20%	340	160	35%	149	193	35%	191	151	35%	140	140
C10	405	20%	388	198	25%	198	218	25%	218	214	20%	204	198
C11	333	20%	327	124	25%	124	194	20%	191	166	25%	166	124
C12	305	20%	294	107	25%	107	109	75%	107	186	20%	177	107
C13	1010	25%	1010	283	35%	267	639	30%	632	721	20%	714	267
C14	570	25%	570	185	30%	183	438	25%	438	369	25%	369	183
C15	1320	25%	1320	453	35%	437	777	65%	735	942	25%	942	437
C16	888	25%	888	344	55%	309	456	50%	340	565	30%	546	309
C17	1040	40%	1030	310	40%	271	421	50%	303	529	40%	440	271
C18	461	25%	461	178	80%	162	221	50%	161	272	20%	269	161
C19	1040	25%	1040	350	75%	349	462	50%	396	640	20%	640	349
C20	63.5	20%	61.4	40.1	25%	40.1	40.5	15%	38.1	26.5	25%	26.5	26.5
C21	162	20%	156	75.3	20%	75.0	84.0	25%	84.0	84.0	20%	79.9	75.0
C22	93.2	20%	89.0	50.7	20%	48.2	51.2	15%	40.7	46.3	80%	42.6	40.7
C23	134	25%	134	71.0	25%	71.0	79.2	15%	71.9	60.3	25%	60.3	60.3
C24	181	20%	165	96.8	20%	95.5	103	20%	94	92.7	20%	87.2	87.2
C25	210	20%	195	92.1	30%	84.8	101	70%	97.9	83.7	30%	79.0	79.0

No.	Quarter Ultimate Load (kN)	Load Pos.	Critical Ultimate Load (kN)	Quarter Stress Ser. Load (kN)	Load Pos.	Critical Stress Ser. Load (kN)	Quarter Def. Ser. Load (kN)	Load Pos.	Critical Def. Ser. Load (kN)	Quarter Hinge Ser. Load (kN)	Load Pos.	Critical Hinge Ser. Load (kN)	Min. Ser. Load (kN)
C26	159	20%	147	78.1	20%	75.8	82.6	20%	74.5	71.3	20%	67.7	67.7
C27	159	20%	147	78.0	20%	75.7	118	20%	108	71.2	20%	67.6	67.6
C28	144	20%	138	84.5	30%	79.3	87.1	20%	83.2	71.3	20%	68.8	68.8
C29	146	20%	130	77.4	20%	72.3	83.4	20%	72.2	66.7	20%	59.7	59.7
C30	161	20%	148	82.9	30%	82.3	90.2	20%	81.9	78.0	20%	73.5	73.5
C31	198	25%	198	95.3	25%	95.3	105	50%	103	107	25%	107	95.3
C32	227	20%	221	108	30%	104	115	50%	107	129	20%	125	104
C33	261	25%	261	131	30%	129	151	30%	151	121	25%	121	121
C34	585	30%	577	270	50%	246	346	30%	334	256	30%	244	244
C35	159	20%	154	84.7	25%	84.7	87.8	50%	64.8	75.8	20%	75.5	64.8
C36	173	25%	173	90.1	30%	89.1	86.8	50%	62.8	78.5	75%	78.4	62.8
C37	281	20%	269	125	20%	121	147	20%	132	155	20%	148	121
C38	1710	30%	1640	535	30%	500	812	65%	764	1160	30%	1140	500
C39	224	20%	220	112	25%	112	159	20%	159	86.7	25%	86.7	86.7
C40	149	25%	149	92.0	25%	92.0	95.4	25%	95.4	68.5	25%	68.5	68.5
C41	472	25%	472	168	25%	168	321	25%	321	248	20%	247	168
C42	364	20%	349	142	30%	140	213	25%	213	199	20%	190	140
C43	301	20%	288	119	25%	119	147	25%	147	152	20%	150	119

6.5 Simple empirical assessment models

Functions of empirical models are derived in this section. Functions of ultimate load, serviceability load, and ultimate load by serviceability load are developed, and expressed in terms of the arch's span, rise, arch ring depth, crown fill depth, fill material friction angle, density of the arch and fill material, elastic modulus of the arch and fill material, and the arch material strength.

The initial serviceability and ultimate results are used here to obtain a multi-linear regression equation with 10 parameters. Using the regression statistics information, shortened simple empirical equations are then created with less parameters.

6.5.1 Functions derivation

6.5.1.1 Ultimate load derivation

Equation (6.1) illustrates that the ultimate load is a function of several parameters, introduced above.

$$P_u = f_1(L,r,h,d,\phi,\gamma_a,\gamma_f,E_a,E_f,\sigma_a) \tag{6.1}$$

When compared to the MEXE method PAL expression in equation (2.5) a similar power function was developed as equation (6.2). Before using this equation, several other dimensionally correct equivalent forms of equation and other kind of non-dimensional equations were tried. However, the selected equation fits the spreadsheet data and results most accurately.

$$P_u = k_1 L^{\alpha_1}\left(\frac{r}{L}\right)^{\beta_1}\left(\frac{h}{d}+1\right)^{\gamma_1}\left(\frac{d}{L}\right)^{\delta_1}\phi^{\varepsilon_1}\gamma_a{}^{\zeta_1}\gamma_f{}^{\eta_1}E_a{}^{\theta_1}E_f{}^{\iota_1}\sigma_a{}^{\kappa_1} \tag{6.2}$$

Rather than use the soil angle of shearing resistance directly which might have a zero value, it was decided this would be better modelled by the soil passive pressure Rankine coefficient used in Chapter 4. Then equation (6.2) could be changed into equation (6.3):

$$P_u = k_1 L^{\alpha_1}\left(\frac{r}{L}\right)^{\beta_1}\left(\frac{h}{d}+1\right)^{\gamma_1}\left(\frac{d}{L}\right)^{\delta_1} k_p{}^{\varepsilon_1}\gamma_a{}^{\zeta_1}\gamma_f{}^{\eta_1}E_a{}^{\theta_1}E_f{}^{\iota_1}\sigma_a{}^{\kappa_1} \tag{6.3}$$

6.5.1.2 Serviceability load derivation

Following on from the ultimate load, the serviceability load could also be expressed in a similar form, as detailed in equation (6.4).

$$P_s = f_2(L, r, h, d, \phi, \gamma_a, \gamma_f, E_a, E_f, \sigma_a) \tag{6.4}$$

As the stress of the arch has a direct relation (multi-linear used in the proposal method) with the serviceability criteria. So the serviceability load also can be expressed by the equation (6.5).

$$P_s = f_2(L, r, h, d, \phi, \gamma_a, \gamma_f, E_a, E_f, C_s) \tag{6.5}$$

Where C_s is the serviceability parameter under consideration and may be associated with stress, deflection or arch ring opening. Equation (6.6) is developed following the same reason as above to fit the serviceability loads from the elastic analysis spreadsheet calculation.

$$P_s = k_2 L^{\alpha_2}\left(\frac{r}{L}\right)^{\beta_2}\left(\frac{h}{d}+1\right)^{\gamma_2}\left(\frac{d}{L}\right)^{\delta_2} k_p{}^{\varepsilon_2}\gamma_a{}^{\zeta_2}\gamma_f{}^{\eta_2}E_a{}^{\theta_2}E_f{}^{\iota_2}C_s{}^{\kappa_2} \tag{6.6}$$

The functions derived above are all in the form of power based equations. So, the approach uses a log-transformation, then the functions can be regressed be using multi-linear regression to obtain the coefficients of the functions.

6.5.2 Ultimate load simple empirical model

Logs are initially taken of both sides of Equation (6.3) and then the new equation is the a multi-linear equation, and the regression data analysis in MS Excel is used to obtain the ultimate load regression equation coefficients. Here the ultimate load is used, with the geometric and material parameters, to drive the regression.

Following the multi linear regression, the critical statistical results are listed in Table 6.9. These are detailed for a sample of 38 bridges with 5 bridges initially being held back to check the regression equation.

The R-squared value of a regression is the fraction of the variation in the dependent variable that is predicted by the independent variables. The R-squared value is generally of secondary importance. The P value details the confidence that each individual variable has some correlation with the dependent variable, which is the most important thing.

The t statistic is the coefficient divided by its standard error. The standard error is an estimate of the standard deviation of the coefficient, the amount it varies across cases. It could be thought of as a measure of the precision with which the regression coefficient was measured. If an absolute coefficient was large compared to its standard error, then it was probably different from 0. So, the larger the absolute t Stat the more accurate and important the parameter is.

Another number to be aware of is the P value for the regression as a whole. Because independent variables may be correlated, a condition known as multi-co-linearity, the coefficients of individual variables may be insignificant when the regression as a whole is significant. Intuitively, this is because highly correlated independent variables are explaining the same part of the variation in the dependent variable. However, in these empirical equations, the independent variables are not correlated. So this is not considered in the results. The results are listed ordered by P value and t-stat.

If 95% of the distribution is closer to the mean than the value on the coefficient, then there is a P value of 5%. This is also referred to a significance level of 5%. A P of 5% or less is the generally accepted point at which to reject the null hypothesis. With a P value of 5% there is only a 5% chance that seeing results would have come up in a random distribution, so it can be said with a 95% probability of being correct that the variable is having some effect, assuming the model is specified correctly. So, the smaller the P-value the more important the parameter is.

In simple or multiple linear regression, the size of the coefficient for each independent variable demonstrates the size of the effect that the variable is having on the dependent variable, and the sign on the coefficient (positive or negative) gives the direction of the effect. In regression with a single independent variable, the coefficient demonstrates how much the dependent variable is expected to increase (if the coefficient is positive) or decrease (if the coefficient is negative) when that independent variable increases by one. In regression with multiple independent variables, the coefficients indicates how much the dependent variable is expected to increase when that independent variable increases by one, holding all the other independent variables constant.

Table 6.9 Ultimate load regression results of 38 selected bridges

	Coefficients	Standard Error	t Stat	P-value	Lower 95%	Upper 95%
α_1 (Span)	1.748	0.050	34.829	0.000	1.645	1.851
δ_1 (Depth)	2.129	0.094	22.671	0.000	1.937	2.322
γ_1 (Fill)	0.814	0.117	6.955	0.000	0.574	1.055
κ_1 (Stress)	0.324	0.063	5.097	0.000	0.193	0.454
$\log_{10} k_l$	2.455	0.734	3.346	0.002	0.950	3.961
$\zeta_1(\gamma_a)$	0.684	0.274	2.498	0.019	0.122	1.245
ε_1 (k_p)	0.147	0.062	2.376	0.025	0.020	0.274
θ_1 (E_a)	-0.094	0.089	-1.061	0.298	-0.276	0.088
β_1 (Rise)	-0.064	0.062	-1.021	0.316	-0.192	0.064
ι_1 (E_f)	-0.057	0.079	-0.714	0.481	-0.220	0.106
$\eta_1(\gamma_f)$	0.142	0.205	0.693	0.494	-0.279	0.564

Figure 6.13 shows the comparison between the application of the regression equation (to 38 bridges) and the primary results that formed it. A perfect regression would capture the entire science and would result in all points lying on a 45 degree line. As illustrated in Figure 6.13, the regression is based on the data from 38 selected bridges with the results of five more bridges, not used in forming the initial regression, being separately illustrated. The equation results are very close to the spreadsheet results, so the regression equation is considered acceptable. The amount of selected bridges appears to have been sufficient to get a relatively accurate empirical equation. The regression equation is a very good to fit the spreadsheet results when the loads are small. It is not important at very large loads, as accuracy in assessment is not required for bridges that are clearly well above any real live load.

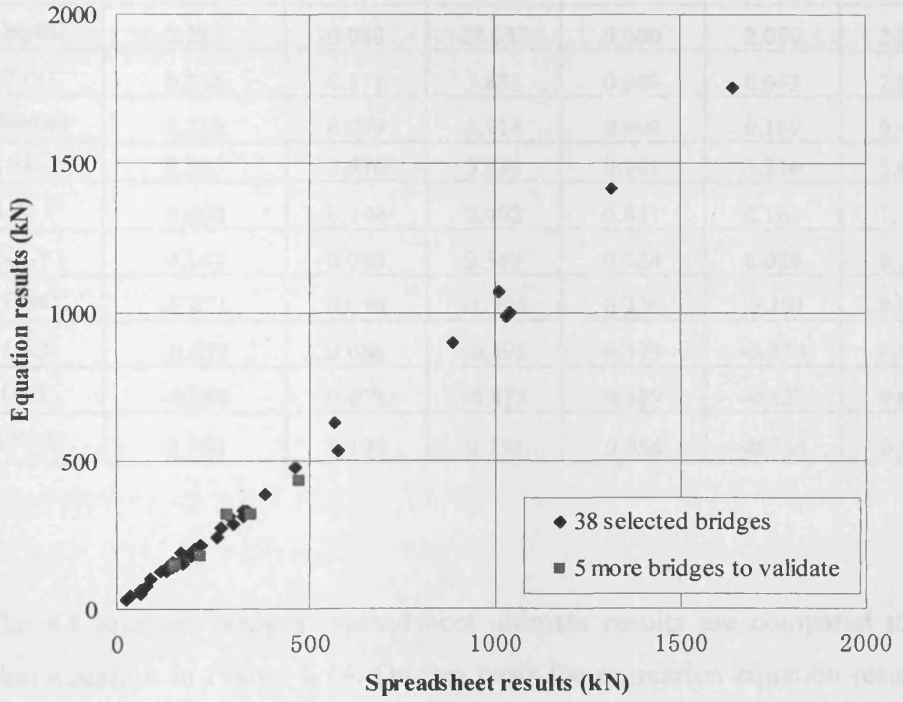

Figure 6.13 Ultimate equation results regressed from selected bridges compared with spreadsheet results with more bridges to validate

Finally, all 43 sets of bridge data were utilised to get the final empirical equation. In this regression, the results are listed in Table 6.10. The regression R squared was 0.992 for this ultimate load regression.

From Table 6.10, the coefficients are listed in the order of smallest P value to highest P value and highest absolute t-stat value to the lowest absolute value.

The first three parameters are clearly the main geometric parameters. It may be considered surprising that the arch shape, as defined by the rise to span ratio is not included in this important group but generally as the arch rise increases the increased tendency for the arch to sway is counterbalanced by the increased support provided by the restraining fill. Thus although the hinge positions and the mode of failure may change the value of the ultimate load changes little.

Table 6.10 Ultimate load regression results of all 43 selected bridges

	Coefficients	**Standard Error**	**t Stat**	**P-value**	**Lower 95%**	**Upper 95%**
α_1 (Span)	1.708	0.041	41.156	0.000	1.623	1.792
δ_1 (Depth)	2.213	0.080	27.633	0.000	2.050	2.377
γ_1 (Fill)	0.868	0.111	7.835	0.000	0.643	1.094
κ_1 (Stress)	0.289	0.059	4.914	0.000	0.169	0.408
$\log_{10} k_1$	2.593	0.676	3.836	0.001	1.216	3.970
$\zeta_1(\gamma_a)$	0.660	0.244	2.702	0.011	0.163	1.158
ε_1 (k_p)	0.143	0.060	2.369	0.024	0.020	0.266
β_1 (Rise)	-0.071	0.059	-1.208	0.236	-0.191	0.049
θ_1 (E_a)	-0.077	0.086	-0.893	0.379	-0.253	0.099
ι_1 (E_f)	-0.068	0.078	-0.873	0.389	-0.227	0.091
$\eta_1(\gamma_f)$	0.150	0.198	0.754	0.456	-0.255	0.554

The 43 selected bridges' spreadsheet ultimate results are compared to their regression equation in Figure 6.14. On this basis the regression equation results are considered acceptable to estimate the ultimate loads.

At this stage it was necessary to consider which geometric/materials parameters were to be retained in the process to develop the serviceability based assessment.; as detailed in Figure 6.1 Table 6.10 details all the parameters considered to date and, within the limitations of the modelling used, provides statistical information on their contribution to the "real" behaviour.

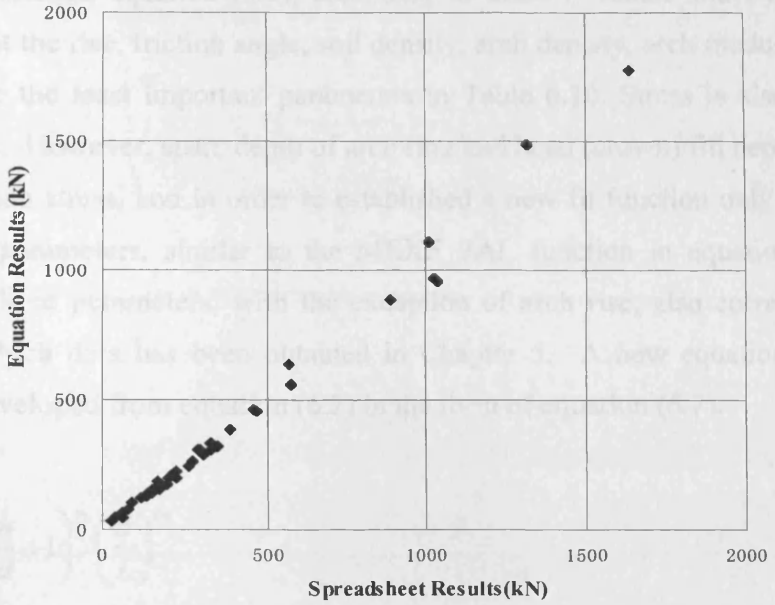

Figure 6.14 Ultimate equation results regressed from all selected bridges compared with spreadsheet results

In addition to consideration of the parameter contribution to the behaviour it is necessary to consider the availability of information on the overall distribution of the parameters values within the existing bridge stock. For example what information is available on the distribution of arch compressive strength or arch modulus? Whilst is may be possible to define reasonable upper and lower bounds for most parameters, little is known about the distribution between. It would of course be possible/reasonable to assume a normal distribution but the inclusion of a whole series of normally distributed parameters within the next stage, the Monte Carlo simulation, as detailed in Figure 6.1, would likely not contribute much to understanding. It was therefore decided to retain the most statistically important characteristics within the process and those for which reasonable population distributions were known, or could be assumed, and to investigate the effects of the less important parameters by considering them separately/individually within the Monte Carlo simulation stage.

It was also decided to use the opportunity of having this data to look at how well a simple regression equation, involving substantially less variables, could model arch behaviour at ultimate load as a possible substitute for the MEXE equation.

To shortened equation (6.6), according to these P values and t-values, it is apparent that the rise, friction angle, soil density, arch density, arch modulus and soil modulus are the least important parameters in Table 6.10. Stress is also relatively unimportant. However, span, depth of arch ring and head (crown) fill depth are more important than stress, and in order to established a new fit function only these main geometries parameters, similar to the MEXE PAL function in equation (2.5) are retained. These parameters, with the exception of arch rise, also correspond with those for which data has been obtained in Chapter 5. A new equation (6.7) was therefore developed from equation (6.2) in the form of equation (6.7).

$$P_u = k_3 L^{\alpha_3}\left(\frac{h}{d}+1\right)^{\gamma_3}\left(\frac{d}{L}\right)^{\delta_3} \tag{6.7}$$

Applying logs to equation (6.7) as before again results in a multi-linear regression; the parameters coefficients of which are listed in Table 6.11.

The result of k_3 value is 1178, so a new function of ultimate load is created in equation (6.8).

$$P_u = 1178 \cdot L^{1.73}\left(\frac{h}{d}+1\right)^{1.00}\left(\frac{d}{L}\right)^{2.06} \text{ (kN/m)} \tag{6.8}$$

Table 6.11 Ultimate load regression results of selected parameters

	Coefficients	**Standard Error**	**t Stat**	**P-value**	**Lower 95%**	**Upper 95%**
α_3 (Span)	1.725	0.061	28.233	0.000	1.601	1.849
$\log_{10} k_3$	3.071	0.174	17.640	0.000	2.719	3.423
δ_3 (Depth)	2.062	0.117	17.595	0.000	1.825	2.299
γ_3 (Fill)	1.000	0.160	6.242	0.000	0.676	1.324

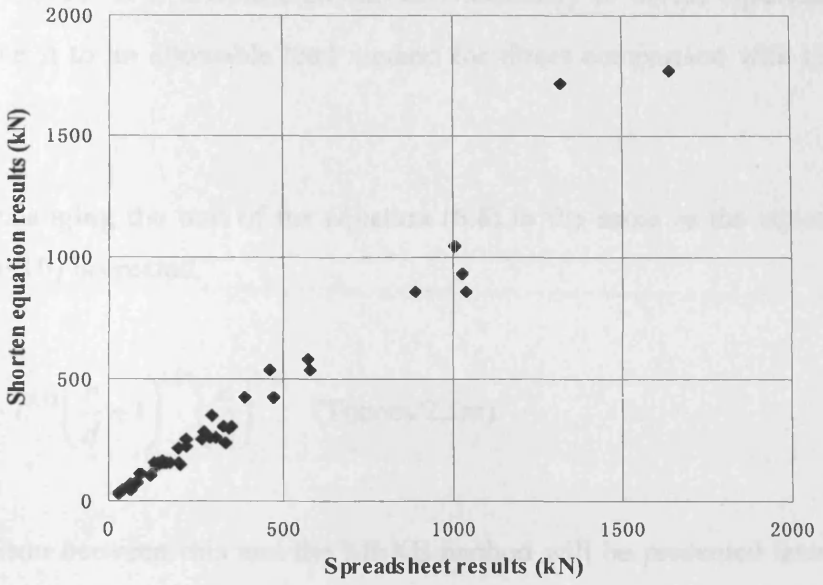

Figure 6.15 Shortened ultimate equation results compared with spreadsheet results

The differences between the shortened equation (6.8) for the ultimate load results and spreadsheet results of the selected 43 bridges (include the 5 verifying bridges) are compared in Figure 6.15.

The MEXE equation (2.5) is widely used by engineers, and to be able to compare equation (6.8) it is necessary to modify the units to a more familiar unit. The arch bridge road unit is 1m in equation (6.8) but 2.5m in equation (2.5) and the unit of load is kN in equation (6.8) but Tons in equation (2.5). Like the MEXE method[22,23], the shortened equation should have some modifying factors to obtain the final modified maximum theoretical single axle failure load. These factors include , F_p and F_m. and finally include F_e , F_j, F_{cM} and γ_{fl} to get the allowable axle load. It is recommended by BD21/97[22] that for a single axle, the allowable axle load should be obtained using the equation (6.9).

Allowable single axle load $\times \gamma_{fl}$ = Theoretical maximum single axle failure load $\times F_j \times F_{cM}$ =Shortened equation load $\times F_e \times F_{sr} \times F_p \times F_m \times F_j \times F_{cM}$ (6.9)

where $\gamma_{fl} = 3.4$. It is therefore additionally necessary to divide equation (6.8) by 3.4 to move it to an allowable load method for direct comparison with the MEXE PAL.

So, changing the unit of the equation (6.8) to the same as the equation (2.5), equation (6.10) is created.

$$P_A = 86.6 \cdot L^{1.73}\left(\frac{h}{d}+1\right)^{1.00}\left(\frac{d}{L}\right)^{2.06} \quad \text{(Tonnes/2.5m).} \tag{6.10}$$

A comparison between this and the MEXE method will be presented later once the remaining models are developed.

6.5.3 Stress based serviceability criterion simple empirical model

Equation (6.6) is used in the current section to provide a simple model of the serviceability load.

First the 38 bridges were used to get an initial empirical equation from a multi-linear regression. Here the serviceability stress is used as C_s, with the geometric and material parameters, to drive the regression. As illustrated in Figure 6.16, the stress based serviceability empirical equation results represent the stress based serviceability spreadsheet results quite well. The five additional validation bridges validate the equation results. So the selected bridges are considered sufficient to get a stable empirical equation.

Finally the 43 bridges were used to get the serviceability empirical equation. The results of this regression are listed in Table 6.12 with the comparative results presented in Figure 6.17. The overall regression R square was 0.989 for the serviceability load regression.

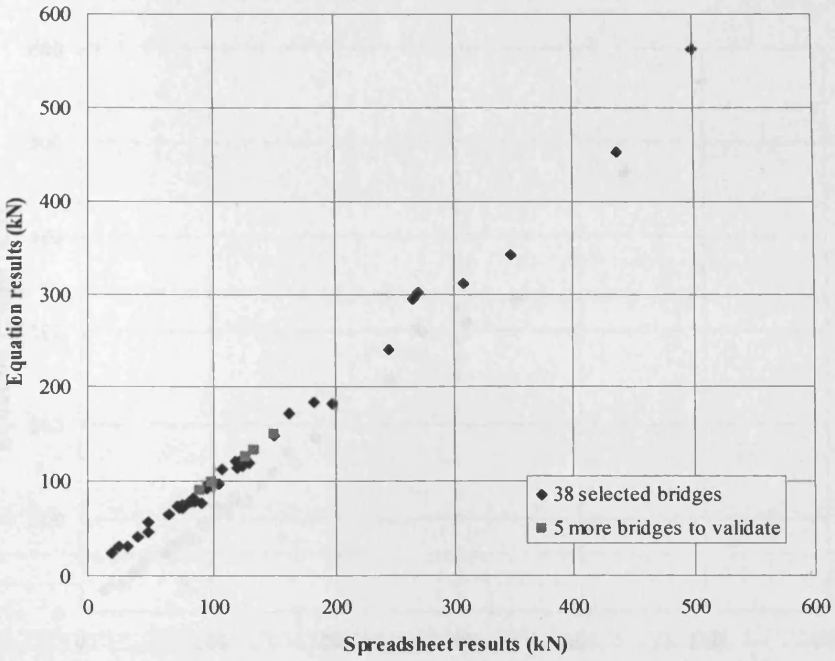

Figure 6.16 Stress based serviceability equation results regressed from selected bridges compared with spreadsheet results with more bridges to validate

In Table 6.12, the coefficients are list in the order of smallest P value to highest P value and the highest absolute t-stat value to the lowest absolute value. According to these P values and t-values, it is apparent that rise, friction angle, soil density, arch density, arch modulus and soil modulus are not important parameters in the table.

Table 6.12 Stress based serviceability load regression results of selected bridges

	Coefficients	Standard Error	t Stat	P-value	Lower 95%	Upper 95%
α_2 (Span)	1.254	0.038	32.734	0.000	1.176	1.332
δ_2 (Depth)	1.940	0.074	26.221	0.000	1.789	2.090
κ_2 (Stress)	0.919	0.166	5.549	0.000	0.582	1.256
γ_2 (Fill)	0.530	0.102	5.181	0.000	0.321	0.738
$\log_{10} k_2$	2.766	0.625	4.426	0.000	1.493	4.039
θ_2 (E_a)	-0.125	0.080	-1.556	0.130	-0.288	0.039
β_2 (Rise)	0.074	0.054	1.369	0.181	-0.036	0.185
$\zeta_2(\gamma_a)$	0.299	0.225	1.324	0.195	-0.161	0.758
ι_2 (E_f)	0.081	0.072	1.118	0.272	-0.066	0.227
$\eta_2(\gamma_f)$	0.081	0.187	0.434	0.667	-0.299	0.461
ε_2 (k_p)	0.008	0.055	0.147	0.884	-0.104	0.121

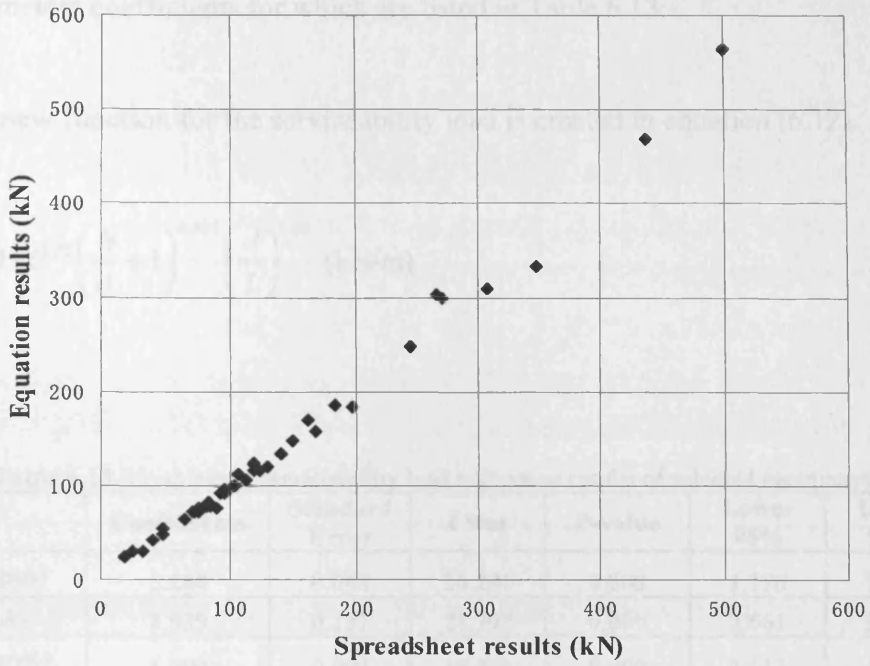

Figure 6.17 Stress based serviceability equation results regressed from all selected bridges compared with spreadsheet results

The 43 selected bridges' spreadsheet ultimate results are compared to their equation serviceability results, as illustrated in Figure 6.17. The equation results estimate the spreadsheet results quite well. So the equation results are considered acceptable to estimate the stress based serviceability loads.

In the derivation of a simpler assessment tool, based on the regression model, stress is considered of moderate of importance in Table 6.12. However, span and depth of arch ring are more important than stress, and in order to established a new function with only the geometric parameters, similar to the MEXE PAL function in equation (2.5), retained. The new equation (6.11) can be therefore be extracted from equation (6.6).

$$P_s = k_4 L^{\alpha_4} \left(\frac{h}{d}+1\right)^{\gamma_4} \left(\frac{d}{L}\right)^{\delta_4} \tag{6.11}$$

Again taking logs to both sides of the equation allows a multi-linear regression, the parameters coefficients for which are listed in Table 6.13.

A new function for the serviceability load is created in equation (6.12).

$$P_s = 869 \cdot L^{1.27}\left(\frac{h}{d}+1\right)^{0.527}\left(\frac{d}{L}\right)^{1.80} \text{ (kN/m)} \qquad (6.12)$$

Table 6.13 Stress based serviceability load regression results of selected parameters

	Coefficients	Standard Error	t Stat	P-value	Lower 95%	Upper 95%
α_4 (Span)	1.268	0.048	26.291	0.000	1.170	1.365
$\log_{10} k_4$	2.939	0.137	21.392	0.000	2.661	3.217
δ_4 (Depth)	1.800	0.093	19.461	0.000	1.613	1.987
γ_4 (Fill)	0.527	0.126	4.172	0.000	0.272	0.783

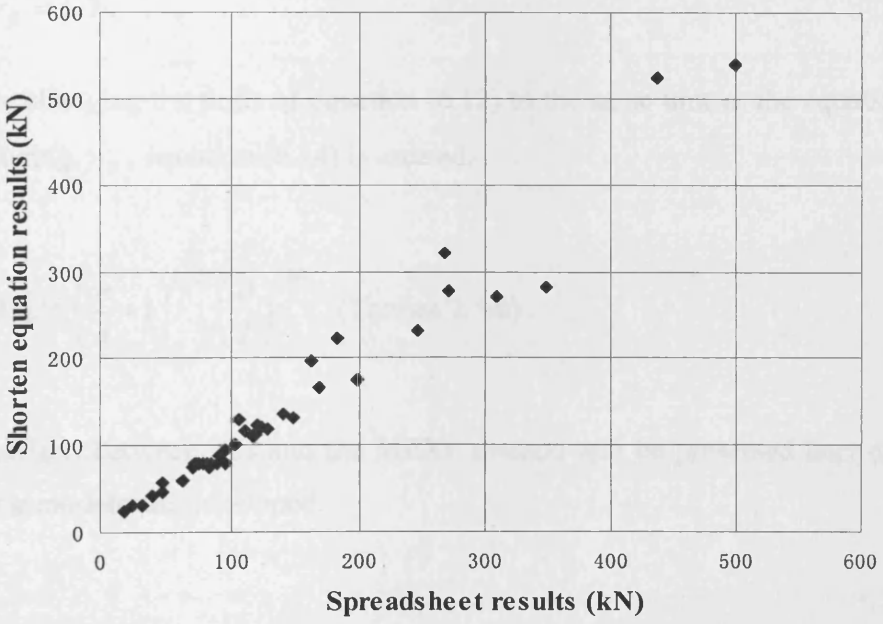

Figure 6.18 Shortened stress based serviceability equation results compared with spreadsheet results

The differences between the shortened equation ultimate load results and the full spreadsheet results using the selected 43 bridges (including 5 verification bridges) are compared in Figure 6.18.

Comparison with the MEXE equation (2.5), widely used by engineers, here, requires equation (6.12) to be modified to a more familiar unit. The arch bridge road unit width is 1m in equation (6.12) but 2.5m in equation (6.2) and the unit of load is kN in equation (6.12) but Ton in equation (6.2). Like the ultimate empirical short equation results, the shortened equation of serviceability should have some modifying factors to get the final modified maximum theoretical single axle failure load. These factors include F_p and F_m. And finally include F_e , F_j, F_{cM} and γ_{fl} to get the allowable axle load. It is recommended by BD21/97[22] that for a single axle, the allowable axle load should be obtained using the equation (6.13).

Allowable single axle load $\times \gamma_{fl}$ = Theoretical maximum serviceability single axle failure load$\times F_j \times F_{cM}$=Shortened equation load$\times F_e \times F_{sr} \times F_p \times F_m \times F_j \times F_{cM}$ (6.13)

where $\gamma_{fl} = 1.7$.

So, changing the units of equation (6.12) to the same unit as the equation (6.2) and including γ_{fl}, equation (6.14) is created.

$$P_s = 128 \cdot L^{1.27}\left(\frac{h}{d}+1\right)^{0.527}\left(\frac{d}{L}\right)^{1.80} \quad \text{(Tonnes/2.5m)} \qquad (6.14)$$

A comparison between this and the MEXE method will be presented later once the remaining models are developed.

6.5.4 Deflection based serviceability criterion simple empirical model

Equation (6.6) is also used to obtain the deflection based serviceability load. Following the method adopted above the 38 bridges were first used to get the initial empirical equation by multi-linear regression. As illustrated in Figure 6.19, the equation results compares quite well with the spreadsheet result and the five additional bridges validate the equation results. So the selected bridges are sufficient to get a stable empirical equation.

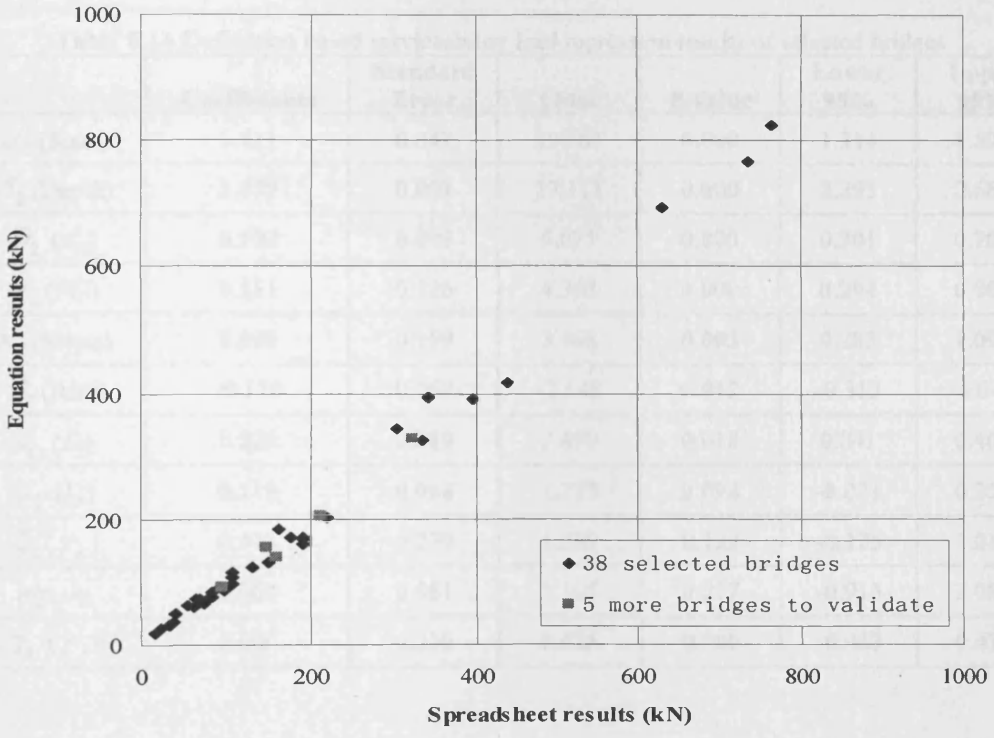

Figure 6.19 Deflection based serviceability equation results regressed from selected bridges compared with spreadsheet results with more bridges to validate

Finally the full 43 bridges are used to obtain the final serviceability empirical equation by multi-linear regression. In this regression, the results are listed in Table 6.14. Regression R squared was 0.989 for the stress serviceability load regression.

From the table, the coefficients are again listed in the order of smallest P value to highest P value and the highest absolute t-stat value to the lowest absolute value. According to these P value and t-value, it is apparent that rise, friction angle, soil density, arch density and soil modulus are not important parameters in the table. Arch modulus and stress have some importance, the arch modulus is not surprising given its importance in determining deflection. However, in order to get a function only containing geometric parameters, these parameters are not included in proposal shortened equation. So the equation (6.6) can be shortened to equation (6.15).

$$P_s = 4820 \cdot L^{1.39}\left(\frac{h}{d}+1\right)^{0.87}\left(\frac{d}{L}\right)^{2.47} \text{ (kN/m)} \tag{6.15}$$

Table 6.14 Deflection based serviceability load regression results of selected bridges

	Coefficients	Standard Error	t Stat	P-value	Lower 95%	Upper 95%
α_2 (Span)	1.411	0.047	29.763	0.000	1.314	1.507
δ_2 (Depth)	2.479	0.091	27.111	0.000	2.293	2.665
θ_2 (E_a)	0.502	0.099	5.071	0.000	0.301	0.704
γ_2 (Fill)	0.551	0.126	4.358	0.000	0.294	0.809
κ_2 (Stress)	0.690	0.199	3.468	0.002	0.285	1.095
β_2 (Rise)	-0.178	0.067	-2.649	0.012	-0.315	-0.041
ι_2 (E_f)	0.223	0.089	2.499	0.018	0.041	0.405
ε_2 (k_p)	0.118	0.068	1.727	0.094	-0.021	0.257
$\zeta_2(\gamma_a)$	0.443	0.279	1.589	0.122	-0.125	1.011
$\log_{10}k_2$	1.085	0.981	1.105	0.277	-0.915	3.084
η_2 (γ_f)	0.006	0.230	0.025	0.980	-0.463	0.474

Changing the units of the equation (6.15) to the same unit as the equation (2.5), and using the same γ_{fl}, as above equation (6.16) is created.

$$P_s = 709 \cdot L^{1.39}\left(\frac{h}{d}+1\right)^{0.87}\left(\frac{d}{L}\right)^{2.47} \text{ (Tonnes/2.5)} \tag{6.16}$$

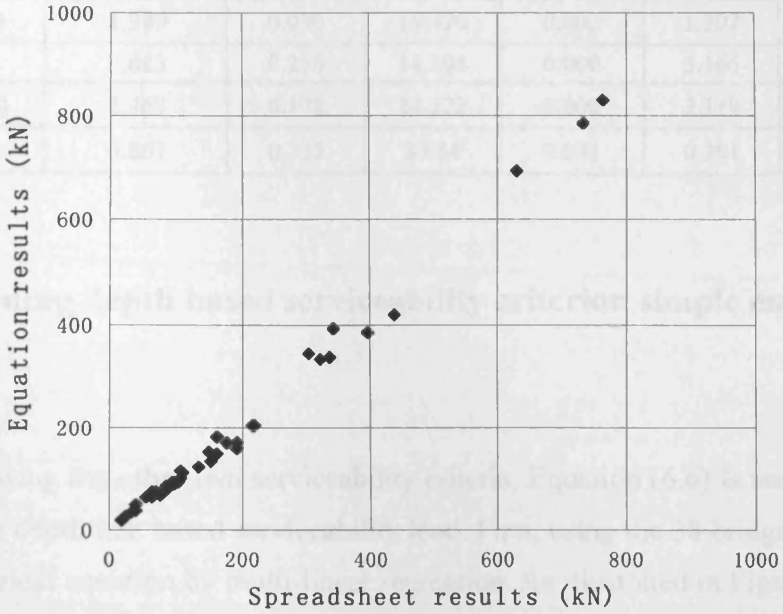

Figure 6.20 Deflection based serviceability equation results regressed from all selected bridges compared with spreadsheet results

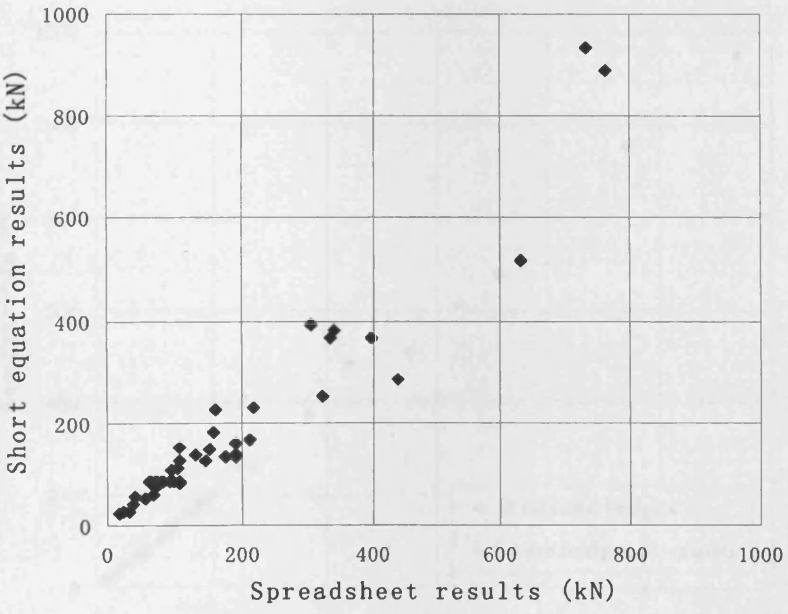

Figure 6.21 Shortened deflection based serviceability equation results compared with spreadsheet results

Table 6.15 Deflection based serviceability load regression results of selected parameters

	Coefficients	Standard Error	t Stat	P-value	Lower 95%	Upper 95%
α_4 (Span)	1.389	0.090	15.470	0.000	1.207	1.571
$\log_{10} k_4$	3.683	0.256	14.398	0.000	3.166	4.201
δ_4 (Depth)	2.467	0.172	14.322	0.000	2.119	2.815
γ_4 (Fill)	0.867	0.235	3.684	0.001	0.391	1.343

6.5.5 Opening depth based serviceability criterion simple empirical model

Following the other two serviceability criteria, Equation (6.6) is used to obtain the thinning depth rate based serviceability load. First, using the 38 bridges to get the initial empirical equation by multi-linear regression. As illustrated in Figure 6.22, the equation results compare quite well to the spreadsheet. and the five additional bridges validate the equation results. So the selected bridges are sufficient to get a stable empirical equation.

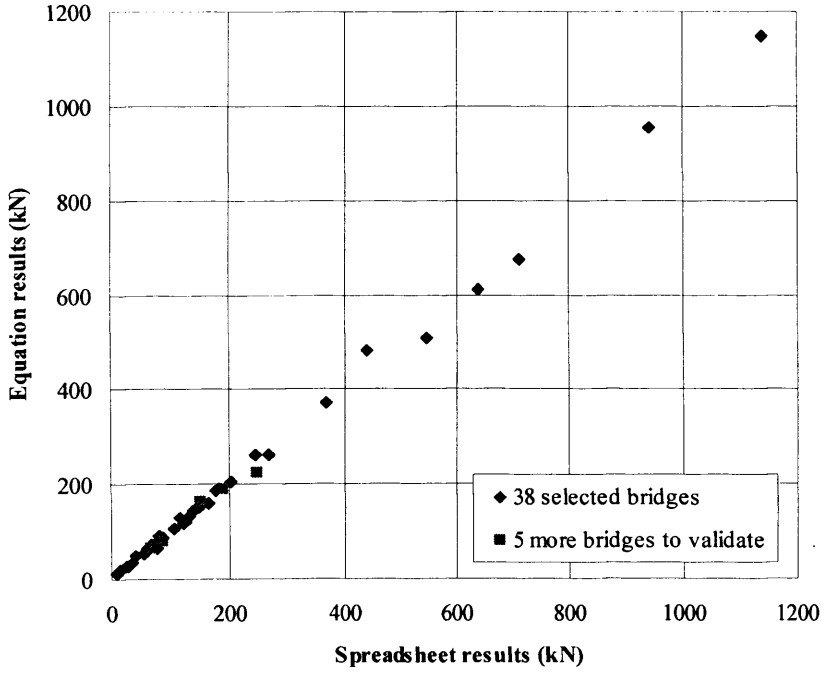

Figure 6.22 Opening depth based serviceability equation results regressed from selected bridges compared with spreadsheet results with more bridges to validate

Finally the 43 bridges are used to get the final serviceability empirical equation by linear regression. In this regression, the results are listed in Table 6.16. Regression R squared was 0.996 for the serviceability load regression, this is slightly better than the earlier regressions.

From the table, coefficients are listed in the order of smallest P value to highest P value and the highest absolute t-stat value to the lowest absolute value. According to these P value and t-value, it is apparent that the friction angle, soil density and soil modulus are not important parameters in the table. Arch modulus, arch density, and stress are relatively important. However, in order to get a function only contains geometric values, these parameters are not included in the proposal shortened equation. Rise is also of some important in this regression, but its the absolute value is small, so rise is not as important as the other geometric parameters, in order to compare with the other two shortened equations, rise is not applied in the accepted shortened equation. So the equation (6.6) can be briefed as equation (6.17).

Table 6.16 Opening depth based serviceability load regression results of selected bridges

	Coefficients	Standard Error	t Stat	P-value	Lower 95%	Upper 95%
α_2 (Span)	2.074	0.035	59.361	0.000	2.003	2.145
δ_2 (Depth)	2.154	0.067	32.125	0.000	2.018	2.291
γ_2 (Fill)	1.124	0.093	12.049	0.000	0.934	1.314
β_2 (Rise)	-0.334	0.050	6.734	0.000	-0.435	-0.233
$\zeta_2(\gamma_a)$	0.862	0.206	4.192	0.000	0.443	1.281
κ_2 (Stress)	-0.783	0.194	4.035	0.000	-1.179	-0.388
θ_2 (E_a)	-0.110	0.073	1.504	0.142	-0.259	0.039
$\log_{10}k_2$	0.847	0.576	1.469	0.152	-0.327	2.021
η_2 (γ_f)	0.240	0.170	1.413	0.167	-0.106	0.585
ι_2 (E_f)	0.080	0.066	1.220	0.231	-0.054	0.214
ε_2 (k_p)	0.001	0.050	0.020	0.984	-0.102	0.104

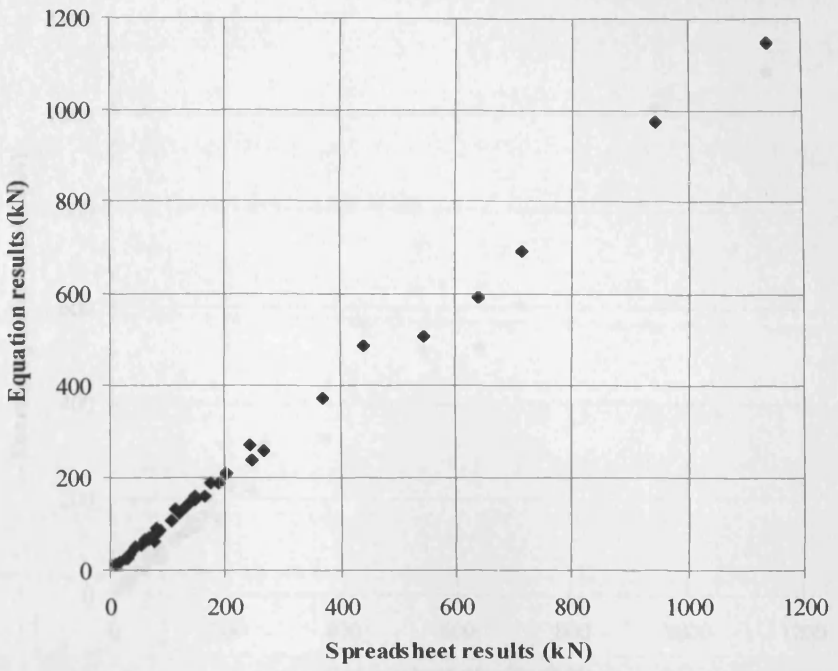

Figure 6.23 Opening depth based serviceability results compared with spreadsheet results

The same method as the detailed above was applied to obtain the unknown coefficients of equation (6.11). The selected parameter values and its statistic information are listed in Table 6.17. The final opening depth serviceability load equation can then obtained from equation (6.17).

$$P_s = 354 \cdot L^{2.00}\left(\frac{h}{d}+1\right)^{1.08}\left(\frac{d}{L}\right)^{2.13} \text{ (kN/m)} \qquad (6.17)$$

Changing the units of the equation (6.17) to the same unit as the equation (2.5), and using the same γ_{fl}, as above equation (6.18) is created.

$$P_s = 52.1 \cdot L^{2.00}\left(\frac{h}{d}+1\right)^{1.08}\left(\frac{d}{L}\right)^{2.13} \text{ (Tonnes/2.5m)} \qquad (6.18)$$

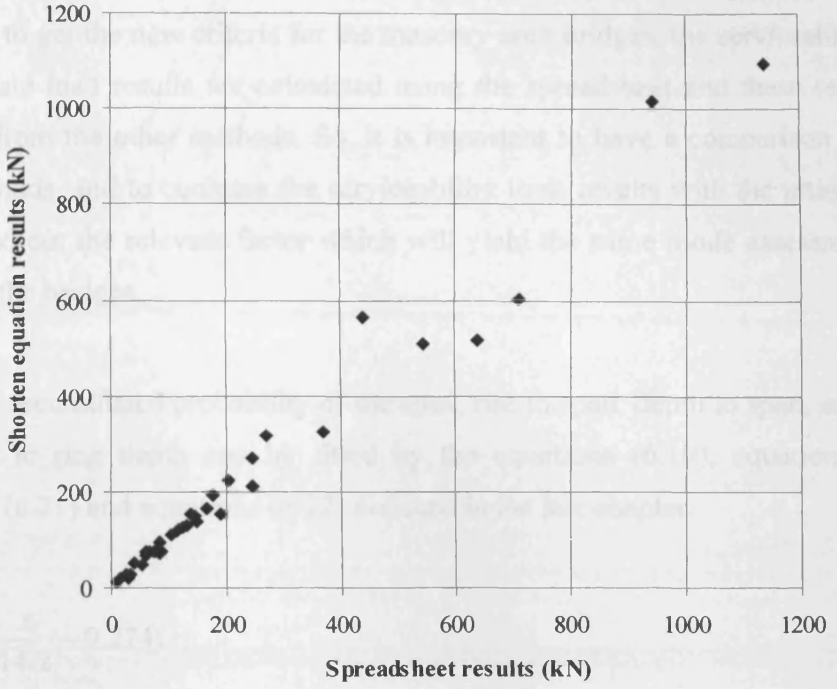

Figure 6.24 Shortened opening depth based serviceability equation results compared with spreadsheet results

Table 6.17 Opening depth based serviceability load regression results of selected parameters

	Coefficients	Standard Error	t Stat	P-value	Lower 95%	Upper 95%
α_4 (Span)	2.003	0.059	33.84	0.000	1.883	2.122
δ_4 (Depth)	2.126	0.114	18.73	0.000	1.896	2.356
$\log_{10} k_4$	2.549	0.169	15.12	0.000	2.208	2.890
γ_4 (Fill)	1.078	0.155	6.95	0.000	0.764	1.392

6.6 Simulations to modify the serviceability parameter values

Monte Carlo simulations were used to investigate 10,000 bridges with different spans, rise to span ratios, thickness of ring to span ratios and fill material depth to thickness of ring ratios. Using the shortened equations to simulate the serviceability loads and the results compared to the half ultimate load assessments. Given that different factors are applied to the serviceability loads, the overall serviceability

loads are 50% greater than half ultimate loads. Then using the longer serviceability equations to get the new criteria for the masonry arch bridges, the serviceability load and ultimate load results are calculated using the spreadsheet and these results are different from the other methods. So, it is important to have a comparison with the other methods, and to compare the serviceability limit results with the ultimate load and to find out the relevant factor which will yield the same mode assessment load values of the bridges.

The accumulated probability of the span, rise to span, depth to span, and crown fill depth to ring depth can by fitted by the equations (6.19), equations (6.20), equations (6.21) and equations (6.22) deduced in the last chapter.

$$y = \tanh(\frac{x}{14.2} - 0.274) \tag{6.19}$$

$$\begin{cases} y = 1.17x - 0.121, x \in (0.1,0.19) \\ y = 2.14x - 0.298, x \in (0.19,0.5) \\ x = 0.5, y \in (0.77,1) \end{cases} \tag{6.20}$$

$$y = 0.518\tanh(\frac{x}{0.0248} - 2.13) + 0.482 \tag{6.21}$$

$$y = \tanh(\frac{x}{0.867} - 0.0753) \tag{6.22}$$

As listed in Table 6.18, the real masonry parameters such as stress, k_p, soil modulus, fill density, masonry density and masonry Young modulus etc. are assumed as normally distributed with the values obtained from previous considerations of appropriated values used in comparisons with the ultimate load experimental results.

Table 6.18 Normal distribution factors of masonry arch bridge material parameters

Bridge	k_p	Soil Modulus (kN/m^3)	Fill Density (kN/m^3)	Masonry Density (kN/m^3)	Young Modulus (N/mm^2)
Bridgemill	5.83	5100	19.0	21.0	4400
Bargower	4.60	9000	20.0	24.0	3300
Preston	3.54	18000	20.0	22.0	3000
Prestwood	4.02	14300	20.0	20.0	4100
Torksey	4.20	19000	18.0	21.0	400
Shinafoot	4.20	15100	18.0	26.0	3000
Dundee	5.83	23000	22.1	24.5	6000
Bolton	9.47	15500	21.8	22.6	6400
Strathmashie	3.54	9900	20.0	26.0	1500
Barlae	4.60	9500	20.0	21.0	3000
Average	4.98	13840	19.9	22.8	3510
Standard Deviation	1.77	5442	1.4	2.2	1833

The stress distribution uses the same method, but is obtained from different bridges. The results show the average as 8.6 N/mm^2 with a standard deviation of 2.7 N/mm^2.

So, using the Monte Carlo method to simulate the bridges' span, rise by span, depth by span and crown fill depth by arch ring depth, stress, k_p, soil modulus, fill density, masonry density and masonry young modulus, and then applying these data to regression function equation (6.3) and (6.6) to get the ultimate and serviceability empirical results. The final adjusted serviceability criteria are listed in Table 6.19.

Table 6.19 Final serviceability criteria

Ultimate Stress (N/mm^2)	5	10	15	20
Serviceability Stress (N/mm^2)	2.18	2.87	3.08	3.25
Serviceability Deflection (L)	0.00057	0.000746	0.000813	0.000854
Serviceability First Hinge %	34.8	28.6	27.0	26.0

The stress criteria listed in Table 6.18 is less than half maximum load, only when the arch material is extremely weak, then the fatigue limit should be considered in the assessment. In conclusion the fatigue limit is always lower than the stress criteria based serviceability limit load, except when the arch material is extremely weak.

The use of the minimum criterion is a different assessment criterion which uses the minimum values of the serviceability loads and when compared with the half ultimate loads with the same mode value; so this minimum criterion is based on the three serviceability criteria. So the final adjusted minimum criterion for three serviceability criteria are listed in Table 6.20.

Table 6.20 Final serviceability criteria of minimum criterion

Ultimate Stress (N/mm^2)	5	10	15	20
Serviceability Stress (N/mm^2)	2.41	3.16	3.39	3.58
Serviceability Deflection (L)	0.000689	0.000902	0.000983	0.001033
Serviceability First Hinge %	0.288	0.236	0.223	0.215

6.7 Modified shortened simple empirical serviceability load regressions

The form of the shortened version of SLS equation was modified until the modal values of the results for ULS equation (6.10) and that for the stress based SLS were the same. The resulting simple (shortened) empirical stress based SLS equation is given as equation (6.23).

$$P_s = 135 \cdot L^{1.27}\left(\frac{h}{d}+1\right)^{0.527}\left(\frac{d}{L}\right)^{1.80} \text{ (Tonnes/2.5m)} \tag{6.23}$$

The same method was applied to the deflection based SLS equation and opening depth based SLS equation, the modified equations are list in equation (6.24) and (6.25)

$$P_s = 627 \cdot L^{1.39}\left(\frac{h}{d}+1\right)^{0.87}\left(\frac{d}{L}\right)^{2.47} \text{ (Tonnes/2.5m)} \tag{6.24}$$

$$P_s = 55.2 \cdot L^{2.00}\left(\frac{h}{d}+1\right)^{1.08}\left(\frac{d}{L}\right)^{2.13} \text{ (Tonnes/2.5m)} \tag{6.25}$$

Application of equations (6.10) and (6.23) or (6.24) or (6.25) to a large number of bridges will result in 50% of the bridges having a higher ULS load capacity and 50% a higher SLS capacity and, as the sample bridges have been selected in proportion to their occurrence, on average a bridge owner should get the same overall level of assessment limit failures from both approaches.

6.8 Different serviceability assessment results compared with ultimate results

In this section, a comparison between the shortened equation results and the spreadsheet results is detailed.

The basis for the current approach to serviceability was to determine values which on average produce similar numbers of assessment failures. But fundamental to the approach is that the different serviceability approaches will produce different assessment loads for each bridge analysed and that, over time, assessing engineers will be able to compare the results of the different approaches with their assessment of the actual condition of each bridge. It is then anticipated that this will help identify the "best" serviceability based approach. It is therefore important at the start to gain some understanding of which serviceability method favours which geometric, material bridge parameters.

To start with the serviceability methods need to be compared with the ULS approach. First it is necessary to define a new function as the ratio of the serviceability load to ultimate load, as equation (6.26).

$$f_s = \frac{P_s}{P_u} = \frac{f_2(L,r,h,d,\phi,\rho_a,\rho_f,E_a,E_f,\sigma_a)}{f_1(L,r,h,d,\phi,\rho_a,\rho_f,E_a,E_f,\sigma_a)} = f_3(L,r,h,d,\phi,\rho_a,\rho_f,E_a,E_f,\sigma_a) \qquad (6.26)$$

Using the spreadsheet twice once for the SLS and the ULS approach the two separate values can be determined for each arch and the ratio used directly to form a regression equation. Using this approach f_s is expressed as equation (6.27).

$$f_s = k_3 L^{\alpha_3}\left(\frac{r}{L}\right)^{\beta_3}\left(\frac{h}{d}+1\right)^{\gamma_3}\left(\frac{d}{L}\right)^{\delta_3} k_p{}^{\varepsilon_3}\gamma_a{}^{\zeta_3}\gamma_f{}^{\eta_3}E_a{}^{\theta_3}E_f{}^{\iota_3}\sigma_a{}^{\kappa_3} \tag{6.27}$$

So to obtain comparison data, the first approach is to use the empirical equations to obtain the equation (6.26). The second method uses equation (6.27) as the model already well fits the results obtained from the spreadsheet results of the three different criterion serviceability loads and the corresponding ultimate loads. The first method is chosen to compare these results. It is the easiest way to compare the shortened equations directly. This current work initially uses the shortened empirical equations to obtain equation (6.26) and compares the difference between different methods. The figures changing the most important factors: span and arch ring thickness. Crown fill depth to arch ring thickness uses the typical value 0.5, the figures will be explained in detail.

It then also compares the spreadsheet results to validate the equation results.

6.8.1 Shortened equation comparisons

6.8.1.1 Stress criterion

Using equation (6.26) a comparison between the stress based serviceability shortened empirical equation results with the corresponding ultimate results is determined by equation (6.28).

$$f_{su} = \frac{P_s}{P_u} = \frac{135\cdot L^{1.27}\left(\frac{h}{d}+1\right)^{0.527}\left(\frac{d}{L}\right)^{1.8}}{86.6\cdot L^{1.73}\left(\frac{h}{d}+1\right)\left(\frac{d}{L}\right)^{2.06}} = 1.56\cdot L^{-0.46}\left(\frac{h}{d}+1\right)^{-0.473}\left(\frac{d}{L}\right)^{-0.26} \tag{6.28}$$

As illustrated in Figure 6.25, the comparison of the two different methods is clear. Figure 6.25, 6.26 and 6.27 are presented this way to indicate which types of

structure (span and ring thickness, which are most important factors to the masonry arch bridge capacity) are over/under predicted by SLS when compared to ULS.

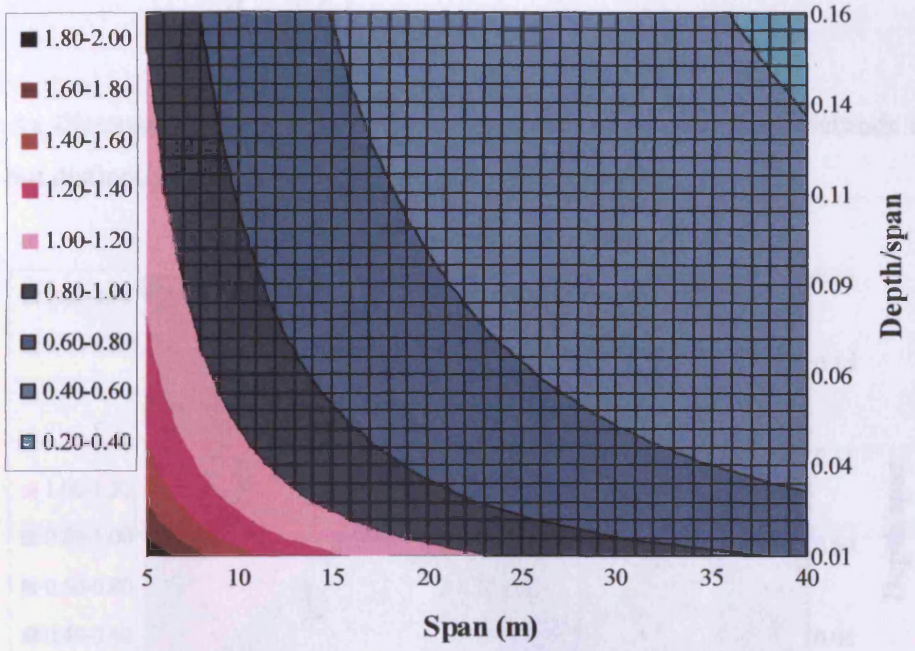

Figure 6.25 Stress based serviceability results compared with ultimate load results

From Figure 6.25, the red area is that where the serviceability assessment loads are greater than ultimate load, and the blue area is the region where they are less. So at a span of 10m and a ring depth of 0.5m both methods produce a similar assessment load. It is important to remember in consideration of this figure that the areas, greater than and less than, do not need to be equal, even though the on average the number of failures are equal, because the area covered by the figure is not representative of the probability of occurrence of the these arch geometric parameters For smaller spans the stress based serviceability results in higher loads but as the span increases and the ring depth increases, the ultimate assessment loads become relatively larger.

6.8.1.2 Deflection criterion

Using equation (6.26) a comparison of deflection based serviceability shortened empirical equation results with the corresponding ultimate results in equation (6.29).

$$f_{su} = \frac{P_s}{P_u} = \frac{627 \cdot L^{1.39}(\frac{h}{d}+1)^{0.87}\left(\frac{d}{L}\right)^{2.47}}{86.6 \cdot L^{1.73}(\frac{h}{d}+1)\left(\frac{d}{L}\right)^{2.06}} = 7.24 \cdot L^{-0.34}(\frac{h}{d}+1)^{-0.13}\left(\frac{d}{L}\right)^{0.41} \quad (6.29)$$

As illustrated in Figure 6.26, the comparison of the different methods is again clear but distinctly different from the stress based approach..

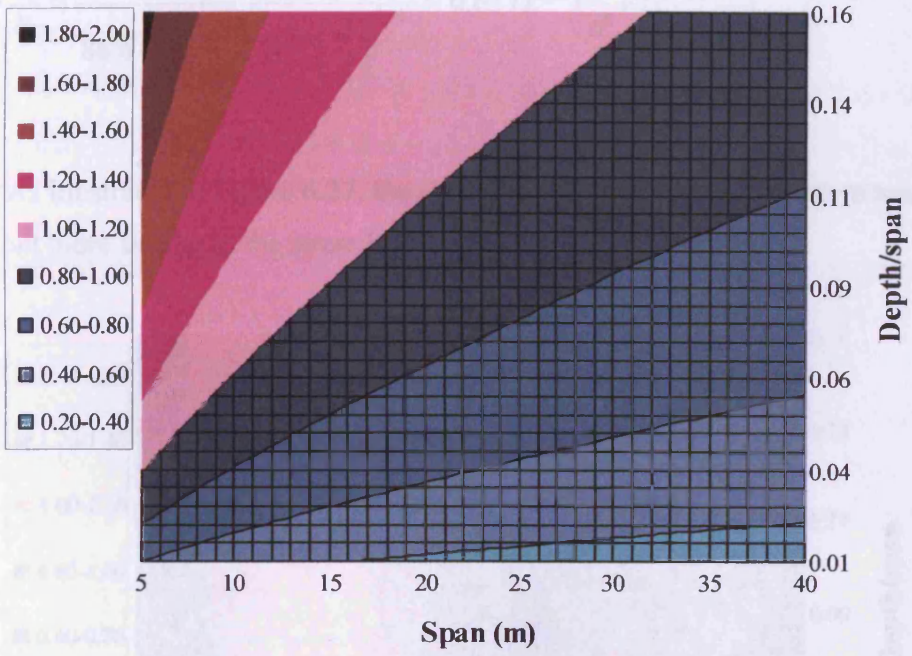

Figure 6.26 Deflection based serviceability results compared with ultimate load results

In Figure 6.26, the red area is where the serviceability assessment loads are greater than the ultimate load, and in the blue area they are less than. At constant span an increase in ring depth results in a greater increase in the serviceability based approach when compared to the ultimate load results. Conversely at a constant depth/span ratio an increase in the span results in a relative increase in the ultimate load results.

6.8.1.3 Opening depth criterion

Using equation (6.26) a comparison of the opening based serviceability shortened empirical equation results with the corresponding ultimate results is determined by equation (6.30).

$$f_{su} = \frac{P_s}{P_u} = \frac{55.2 \cdot L^{2.00}\left(\frac{h}{d}+1\right)^{1.08}\left(\frac{d}{L}\right)^{2.13}}{86.6 \cdot L^{1.73}\left(\frac{h}{d}+1\right)^{1.00}\left(\frac{d}{L}\right)^{2.06}} = 0.637 L^{0.27}\left(\frac{h}{d}+1\right)^{0.08}\left(\frac{d}{L}\right)^{0.07} \tag{6.30}$$

As illustrated in Figure 6.27, the comparison of different methods is again very clear but more similar to the stress based/ultimate load comparison.

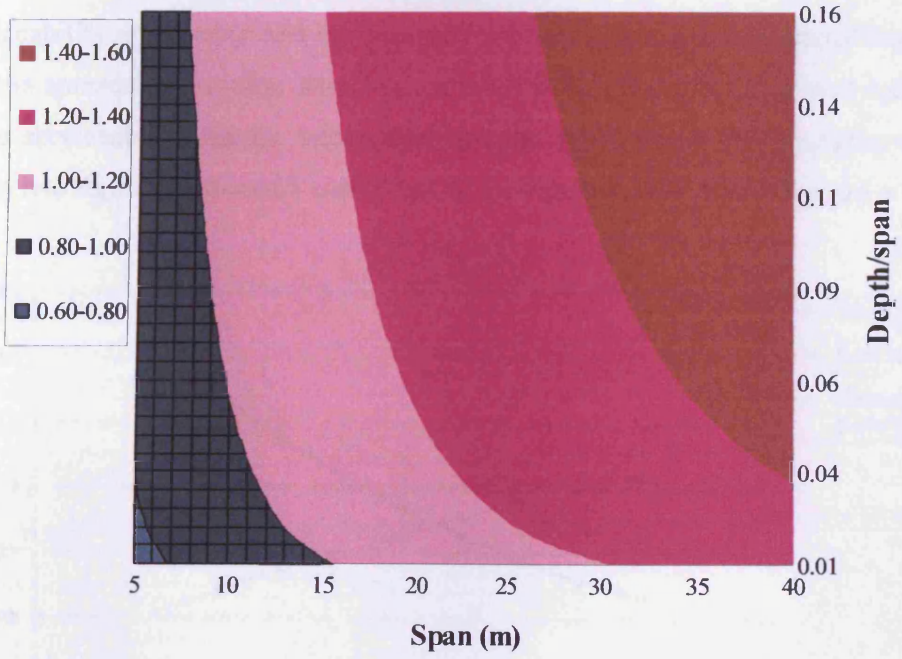

Figure 6.27 Opening depth based serviceability results compared with ultimate load results

In Figure 6.27, the red area is again where the serviceability assessment loads are greater than the ultimate load, and in the blue area are less than. For a 10m arch with a ring depth of 0.7m the two methods result in approximately the same

assessment load. For larger spans the ultimate load approach leads to higher assessment loads and the effect of the depth/span ratio is less significant than for the other two serviceability based approaches.

6.8.2 Spreadsheet results comparisons

The shortened empirical equations results has been compared in the previous section. However, the spreadsheet results comparisons are perhaps considered more reliable. In this section, different results are compared by different span, rise, depth and crown fill with the same other parameters to validate the equation results. All these parameters take the typical data values detailed in Chapter 5 and earlier in this chapter.

Illustrated in Figure 6.28 and Figure 6.29 are comparisons between the three serviceability approaches and the ultimate load results using the shortened equations and the spreadsheet results. Small spans result in larger stress based and deflection based serviceability results, but smaller opening depth based serviceability results. These two figures well match each other, so the equation results are deemed reliable.

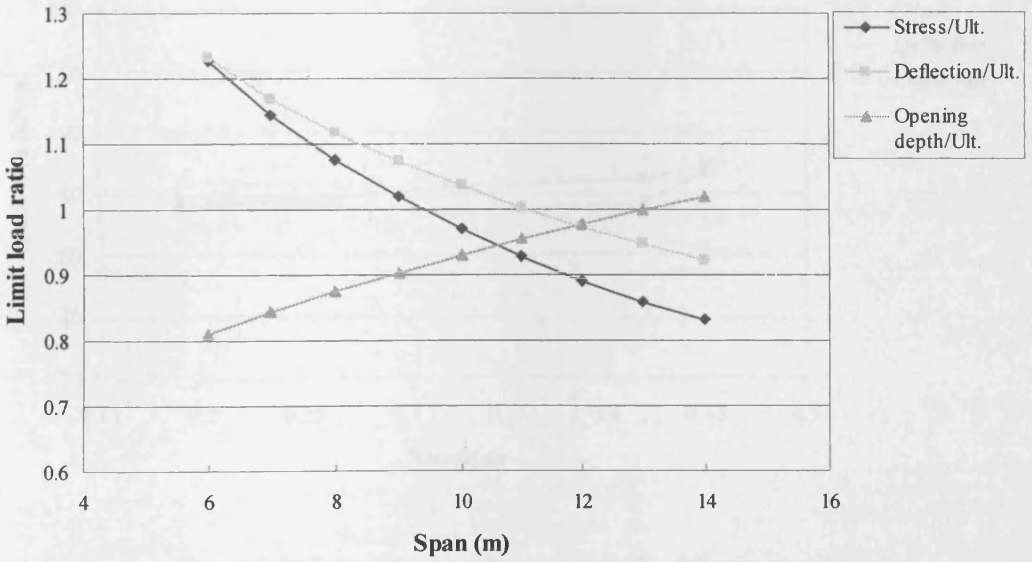

Figure 6.28 Equation results comparison by different span

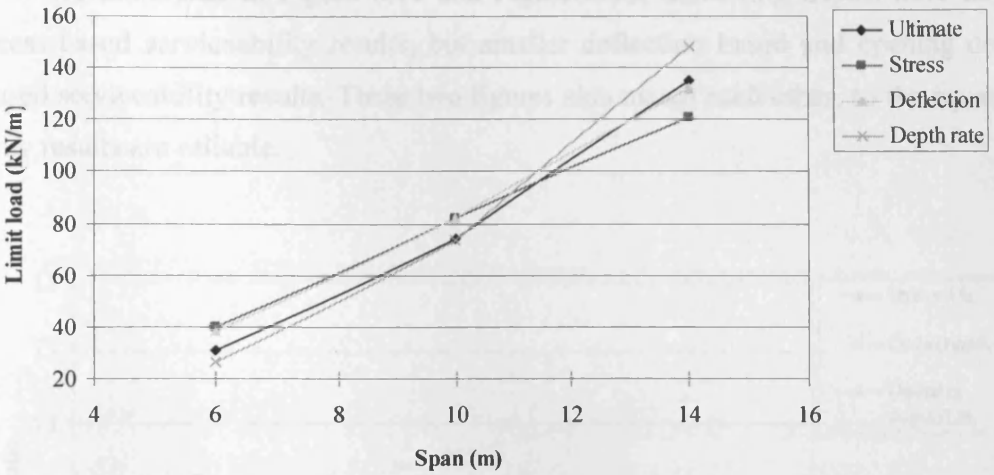

Figure 6.29 Spreadsheet results comparison by different span

Following this a range of other parameters are presented for comparison based on the spreadsheet results. As illustrated in Figure 6.30, rise is not a very important parameter.

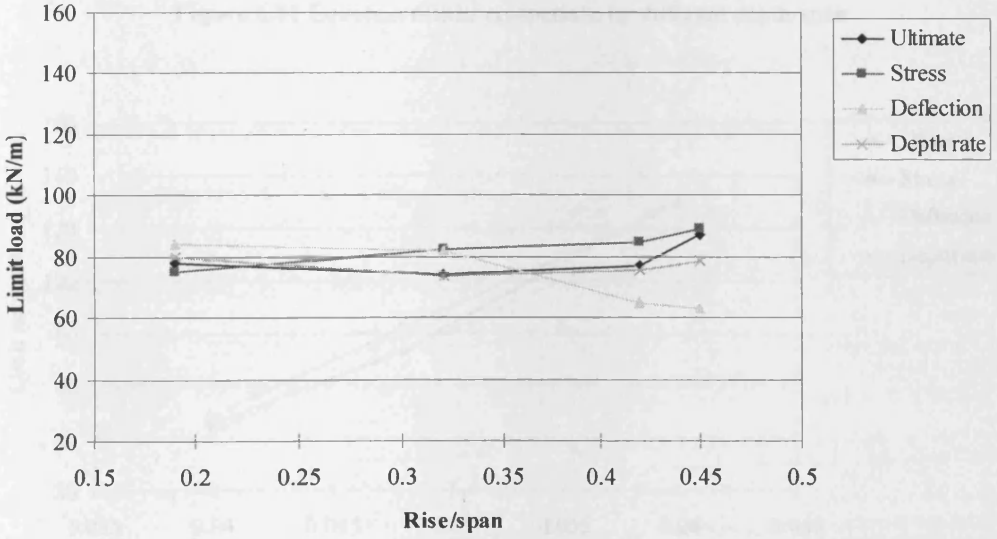

Figure 6.30 Spreadsheet results comparison by different rise/span

As illustrated in Figure 6.31 and Figure 6.32, small ring depths have larger stress based serviceability results, but smaller deflection based and opening depth based serviceability results. These two figures also match each other, so the equation only results are reliable.

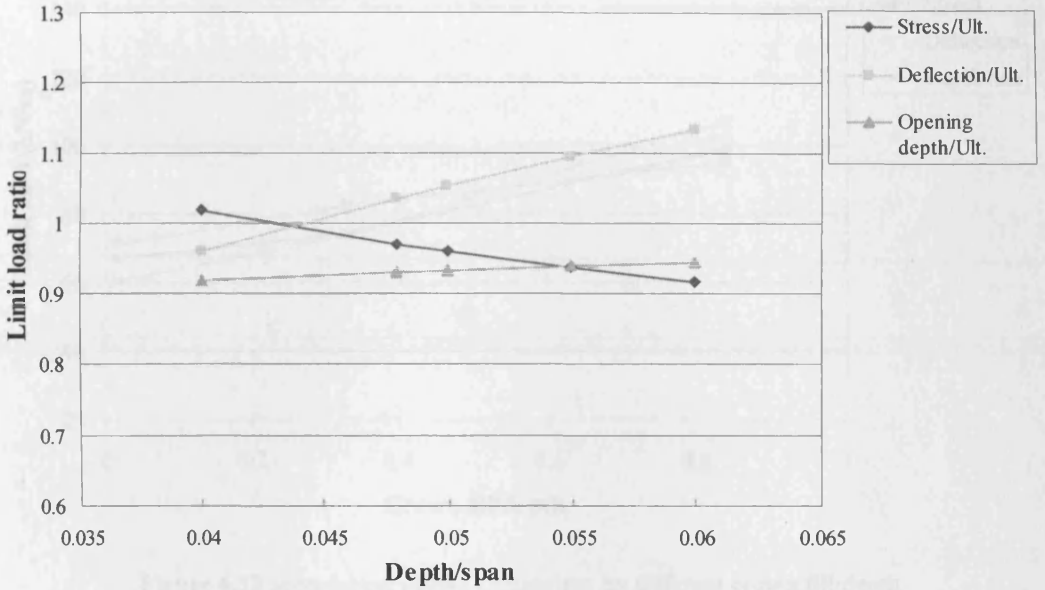

Figure 6.31 Equation results comparison by different depth/span

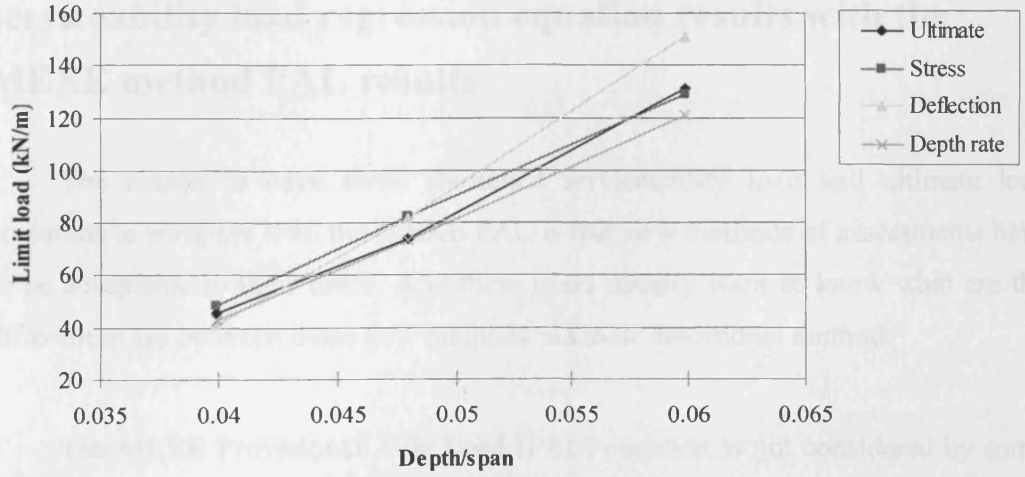

Figure 6.32 Spreadsheet results comparison by different depth/span

Illustrated in Figure 6.33, are the results for the effect of the crown fill depth. The results suggest a similar effect for each approach but with the opening depth effect proportionally increasing in importance as the fill depth increases.

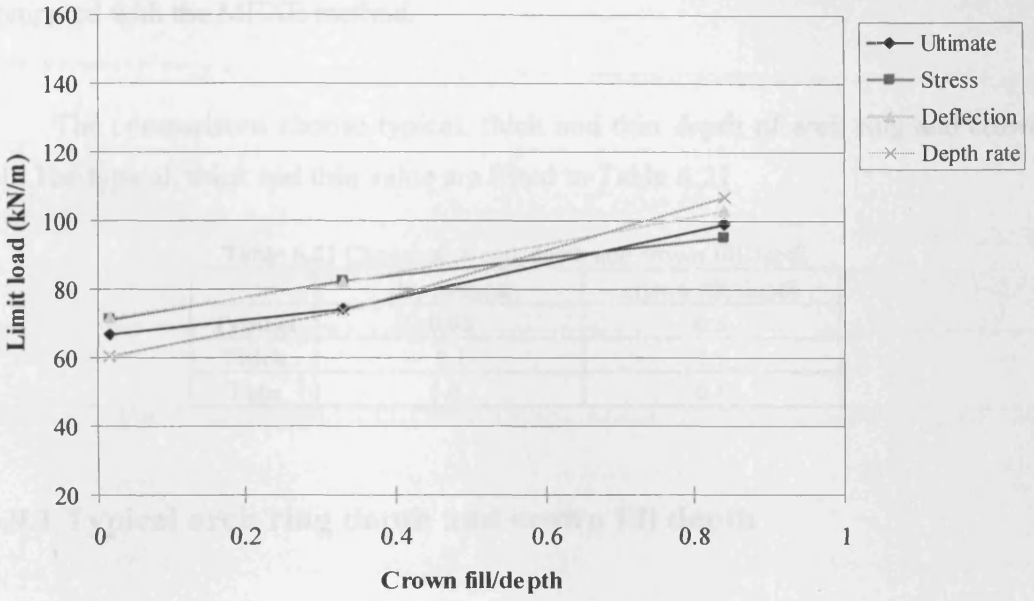

Figure 6.33 Spreadsheet results comparison by different crown fill/depth

6.9 Comparison of shortened ultimate load and serviceability load regression equation results with the MEXE method PAL results

The reason to have three shortened serviceability load and ultimate load equations to compare with the MEXE PAL is that new methods of assessments have to be acceptable to their users. And these users usually want to know what are the differences are between these new methods \nd their traditional method.

The MEXE Provisional Axle Load (PAL) equation is not considered by some to be very good at predicting an acceptable answer because the equation has the same importance for the fill depth and arch ring depth (both squared in bracket). However, from this study, it is apparent that from a structural analysis consideration the arch

ring depth is much more important than crown fill depth. So the MEXE PAL is relatively overweighing the crown fill depth.

Here, these new serviceability loads and elastic method ultimate load are compared with the MEXE method.

The comparisons choose typical, thick and thin depth of arch ring and crown fill. The typical, thick and thin value are listed in Table 6.21.

Table 6.21 Chosen arch ring depth and crown fill depth

	depth/span	crown fill/depth
Typical	0.05	0.5
Thick	0.1	1.5
Thin	0.02	0.1

6.9.1 Typical arch ring depth and crown fill depth

For a typical bridge, the MEXE method load tends to be higher for short spans and too low for long span, this means that in short spans MEXE is not conservative, however, for long span, it is perhaps too conservative. For the length from 10m to 15m the MEXE method is similar to the other four methods. So perhaps this is why the MEXE method has survived for so long. The stress based serviceability limit state method and the deflection based serviceability limit state method are close to the MEXE method in typical arch ring depth and crown fill depth, as illustrated in Figure 6.34.

6.9.2 Thick arch ring depth

As illustrated in Figure 6.35, for thick arch ring depth bridges, the responses for the different methods are similar to those for the typical bridges. However the deflection based SLS method gives larger values for large span bridges. This is because the thicker arch ring depth can leads to smaller deflections. In this situation, the stress based SLS gives the closest result to the MEXE method.

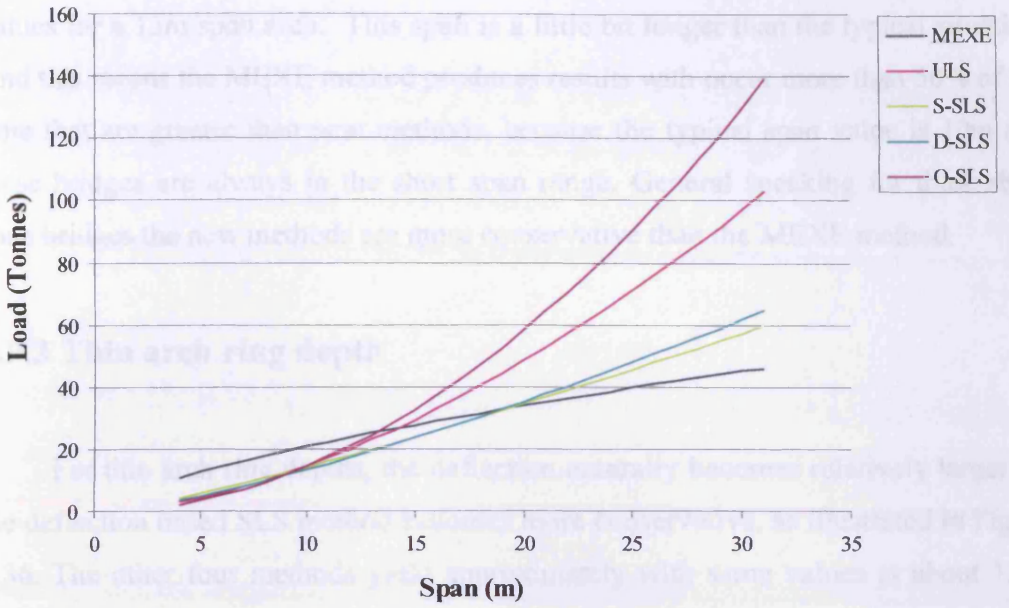

Figure 6.34 Different assessment method results comparison of typical bridges

The stress based SLS method is a little bit different from the other four methods, it appears more conservative because the thick arch ring depth significantly decreases the high stress in the structure.

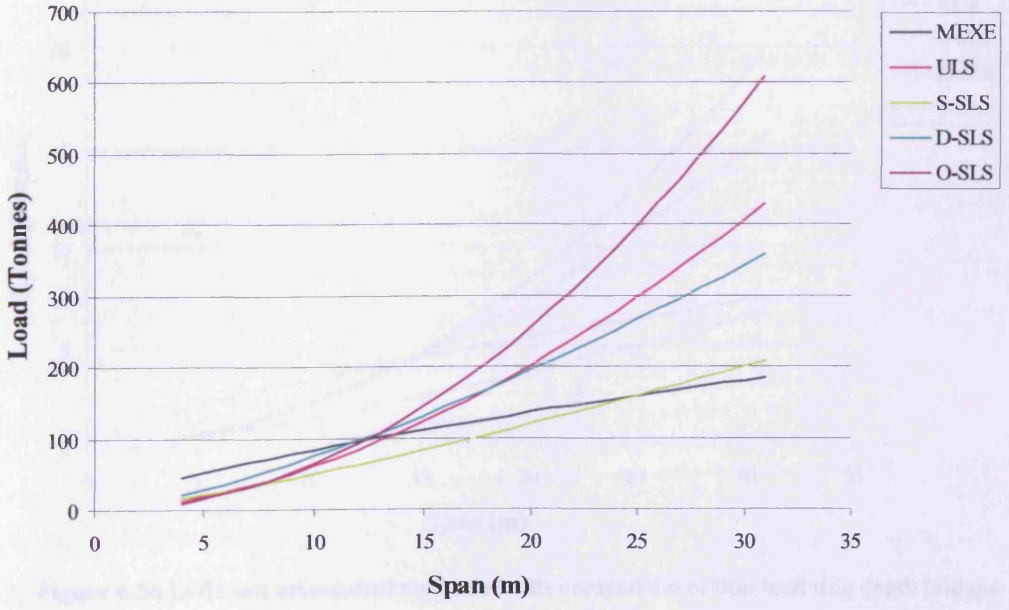

Figure 6.35 Different assessment method results comparison of thick arch ring depth bridges

With the exception of the stress approach the other four methods yield similar values for a 13m span arch. This span is a little bit longer than the typical situation. And this means the MEXE method produces results with occur more than 50% of the time that are greater than new methods, because the typical span value is 10m and these bridges are always in the short span range. General speaking for thick short span bridges the new methods are more conservative than the MEXE method.

6.9.3 Thin arch ring depth

For thin arch ring depths, the deflection naturally becomes relatively larger, so the deflection based SLS method becomes more conservative, as illustrated in Figure 6.36. The other four methods yield approximately with same values at about 15m, this is a slightly longer span than the typical situation. This means that thin arch ring depth bridges are assessed less conservatively using the MEXE method than for typical bridges. Because the MEXE equation is less sensitive than the new serviceability methods.

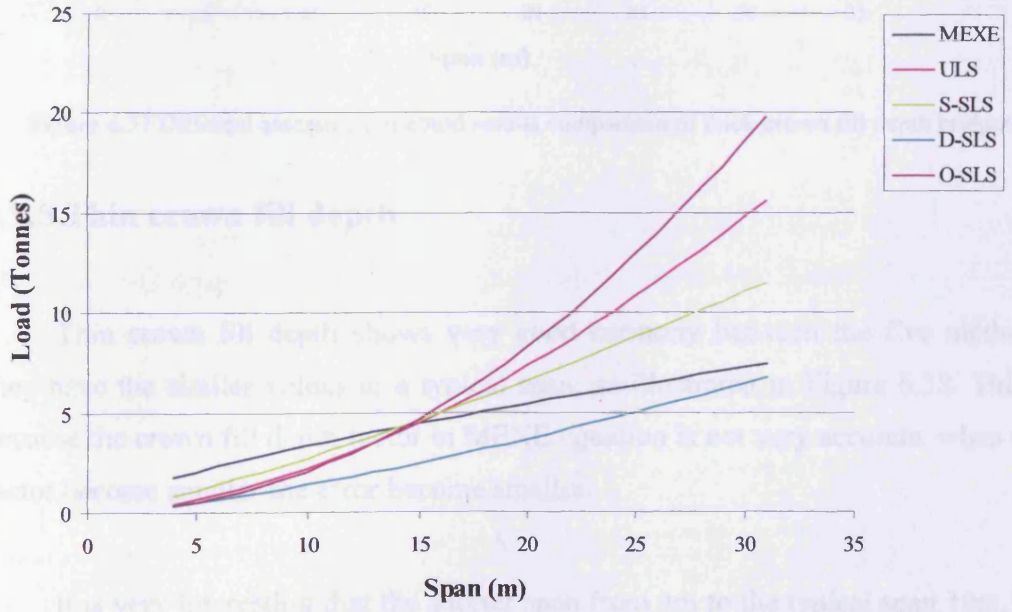

Figure 6.36 Different assessment method results comparison of thin arch ring depth bridges

6.9.4 Thick crown fill depth

The MEXE methods use of a thick crown fill depth is not supported by structural considerations, and results in a lack of conservatism. The MEXE equation take too much account of the crown fill effect, so when the crown fill depth is large, the results will become unreasonable, as illustrated in Figure 6.37.

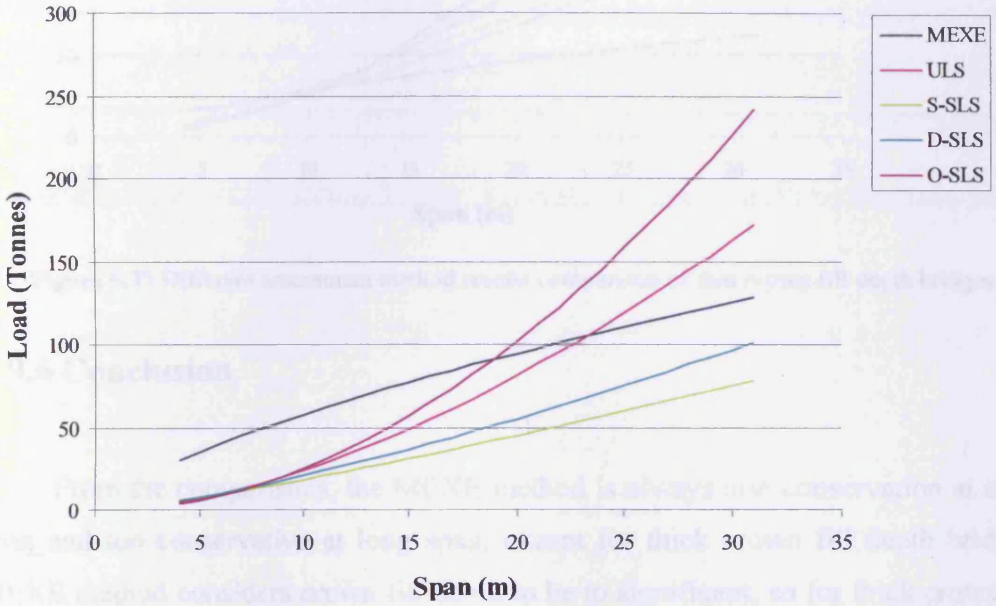

Figure 6.37 Different assessment method results comparison of thick crown fill depth bridges

6.9.5 Thin crown fill depth

Thin crown fill depth shows very good harmony between the five methods, they have the similar values at a typical span, as illustrated in Figure 6.38. This is because the crown fill depth factor in MEXE equation is not very accurate, when this factor become smaller the error become smaller.

It is very interesting that the shorter span from 4m to the typical span 10m, the five methods have very similar results.

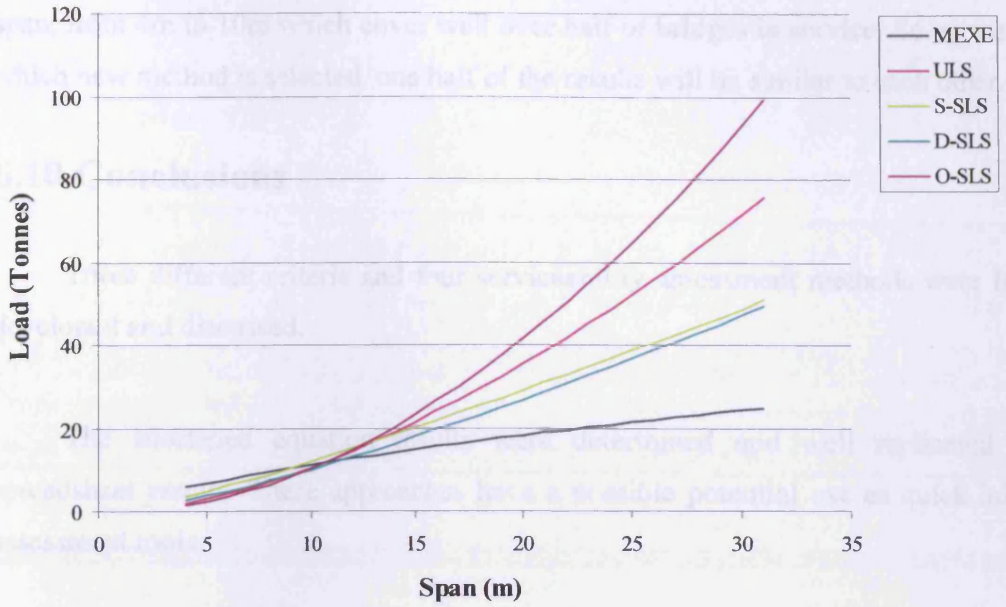

Figure 6.38 Different assessment method results comparison of thin crown fill depth bridges

6.9.6 Conclusion

From the comparisons, the MEXE method is always non conservation at short span and too conservative at long span, except for thick crown fill depth bridges. MEXE method considers crown fill depth to be to significant, so for thick crown fill depth, the method always appears as not conservative.

The stress based SLS method is most close to the traditional MEXE method, except for the thick crown fill depth. So it may be easier for assessing engineers to accept stress based SLS method, as the method changes more gently, less dramatically and evolution is generally more acceptable than revolution.

Opening depth based SLS method always appears as not conservative at long spans.

It is interesting that the four new methods have quite similar results at short span, from 4m to 10m which cover well over half of bridges in service. So no matter which new method is selected, one half of the results will be similar to each other.

6.10 Conclusions

Three different criteria and four serviceability assessment methods were fully developed and discussed.

The shortened equation results were determined and well replicated the spreadsheet results. These approaches have a possible potential use as quick initial assessment tools.

Because the new methods has 50% of their assessment results greater than the traditional results and the other 50% less than, the bridge owners/assessing engineers are more likely to try these new methods.

All the methods have been successfully developed and included in a complex spreadsheet, which is totally transparent and gives all users the opportunity to modify the spreadsheet. The results are so easy to obtain as the input can be created in a standard file and the output readily adapted to form an auditable result sheet. Because the results and the figures are in standard spreadsheet, they can be easily copied.

Compared to the traditional methods, the chapter shows that the new approach based on a more scientific approach are worth trying.

Stress based serviceability method is the closest to the MEXE method, so this method is recommended to be used first. This method will be more acceptable than the other methods, because the change is more gentle and the use of stress based criteria is quite standard in engineering.

7. Serviceability assessment examples

7.1 Introduction

In this chapter, five of the full scale tests carried out to failure by the Transport and Road Research Laboratory (now the TRL) are introduced and the serviceability method developed in the previous chapter are applied to these test results. Both the Cardiff spreadsheet serviceability and ultimate analysis are compared with the full scale results. The serviceability based assessments of these masonry arch bridges are carried out as examples of how to apply the developed serviceability criteria to real structures.

7.2 Test bridge information

The TRL undertook a large number of full scale tests on both existing real structures as well as laboratory built arches. This is in addition to laboratory work on a large number of smaller scale models. The full scale field tests were generally on structures that were any way due for demolition but were selected on the basis of trying to cover a range of material types, geometric shapes, spans and arch conditions. Because these structures were selected as being representative of the population of the UK masonry arch bridges they make an ideal group to apply the newly developed serviceability based assessment method. In the end five of the structures were selected for comparison namely, Torksey Bridge, Shinafoot Bridge, Prestwood Bridge, Preston Bridge and Strathmashie Bridge

Preston Bridge was considered suitable by the TRRL because it fell in a different category of bridges in their program. This was in the category of bridges with a span between 5 to 10 metres and span to rise ratio of between 3 to 5. The MEXE condition factor was 0.8 and the experimental based ultimate load was 2100kN.

The test on the brick arch bridge at Torksey, in Lincolnshire, to collapse was the fifth of the series of tests that had been carried out by the TRRL. Prior to the test, this bridge was in poor condition and some outward movement of the spandrel walls had been noted. As a result of this movement, some cracks had been noticed between the spandrel walls and the arch ring. Bricks were also found to be missing from the abutment walls above the water level. Most of the damage to the bridge was repaired before proceeding with the test. Assessment of this bridge has therefore been carried out based on the data supplied by the TRL. Some other properties of the fill and of the voussoirs, which are required by the spreadsheet, have had to be assumed for this assessment. All unknown necessary parameters were set to the typical values. These unknown values were generally relatively unimportant to the results according to the last chapter's discussion. This bridge lies in the category of a bridge having a span to rise ratio of between 3 to 5, and having a condition factor of 0.7 based on the MEXE method of assessment. The load was applied on this bridge at a quarter span, over a road width of 750mm and the ultimate load applied was 1080kN.

Shinafoot Bridge was offered to TRRL by Tayside Regional Council for their research work into the assessment of the load capacity of masonry arch bridges. This was because it was due to be replaced as a result of some minor outward movement and some indication of longitudinal cracking on the inside edge of the east spandrel wall. Apart from the above damage, the bridge was described as being in fairly good conditions prior to the test, this had a MEXE condition factor of 0.9, with span in the range of 5m to 10m and span/rise in 3 to 5 range. The experimental ultimate load was 2524kN.

Strathmashie Bridge was built with rubble masonry using stone voussoirs about 150 years ago. Prior to the load test which took place in 1988, it had been out of use since the 1930s. It was described as being in very poor condition prior to the test, and had a longitudinal crack about one metre in from the south face of the bridge and had very little visible mortar between the voussoirs. Despite these conditions, it was still in a geometrically reasonable state without any signs of distortion. The MEXE condition factor was 0.5, span/rise was 3.15. The experimental ultimate load was 1320kN.

Prestwood Bridge was an accommodation bridge that linked the Staffordshire and Worcestershire canal in Prestwood. It was described prior to the test as being in poor condition. This was because of the distorted shape of the parapets which had been completely removed due to its condition in 1984. This bridge's span/rise ratio was 4.6, and had a very thin arch ring depth which was 220mm. The span was also between 5m to 10m. The MEXE condition factor was low at 0.5. The ultimate load was 228kN.

7.3 Assessments of five bridges

The bridge data and recorded ultimate loads are listed in Table 7.1 together with any exceptional details. The results show that the spreadsheet ultimate load results at the quarter span are quite close to the real experimental results.

All these five bridges will be assessed by the new methods in detail.

7.3.1 Preston bridge assessments

As explained in section 7.2, Preston bridge is a typical bridge which will be explain first. As shown in Table 7.2, the critical load positions for the four different methods are the same, located in the quarter point. The four different methods have very close or similar assessment results. That supports the previous chapter regarding the comparison of the five methods, when the span is short, the four new methods can give very similar results.

7.3.1.1 Ultimate assessment

As shown in Figure 7.1. the minimum ultimate load is located in the quarter point, the minimum depth and the maximum stress just under the load position, as illustrated in Figure 7.2 and 7.3.

Table 7.1 Full test bridges data, results and Cardiff spreadsheet results

Geometric Data	**Preston Bridge**	**Torksey Bridge**	**Shinafoot Bridge**	**Strathmashie Bridge**	**Prestwood Bridge**
Span (mm)	4950	4902	6160	9425	6550
Rise (mm)	1636	1154	1185	2990	1428
Quarter rise (mm)	1370	904	910	2345	1117
Depth at crown (mm)	360	343	390	600	220
Depth at abutment (mm)	360	343	542	600	220
Fill depth (mm)	380	246	215	410	165
Width (mm)	5820	7045	7395	5810	4180
Material Properties					
Voussoir density (kN/m^3)	22.5	21	23	25	20
Fill density (kN/m^3)	21.5	20	20	20	20
Young's modulus of voussoirs (kN/m^2)	15000000	10000000	4000000	15000000	7500000
Angle of internal friction	34	30	30	37	37
Crushing strength of voussoirs (N/mm^2)	14	10	7.7	16	7.7
Modulus of subgrade reaction (kN/m^3)	100000	50000	45000	50000	50000
Note:		Brick work			skew
Real experimental result (kN)	2100	1080	2524	1320	228
Spreadsheet quarter ultimate load (kN)	1540	1160	2484	2280	197

Table 7.2 Ultimate and serviceability spreadsheet results of real bridges

Bridge Names	**Quarter Half Ultimate Load (kN)**	**Load Pos.**	**Critical Half Ultimate Load (kN)**	**Quarter Stress Ser. Load (kN)**	**Load Pos.**	**Critical Stress Ser. Load (kN)**	**Quarter Def. Ser. Load (kN)**	**Load Pos.**	**Critical Def. Ser. Load (kN)**	**Quarter Hinge Ser. Load (kN)**	**Load Pos.**	**Critical Hinge Ser. Load (kN)**	**Stress Ser. Shortened Equation Load (kN)**	**Def. Ser. Shortened Equation Load (kN)**	**Hinge Ser. Shortened Equation Load (kN)**
Preston Bridge	770	25%	770	969	30%	967	908	70%	904	995	25%	995	504	748	414
Torksey Bridge	580	25%	580	750	25%	750	703	25%	703	694	20%	693	511	695	372
Shinafoot Bridge	1242	20%	1162	1120	50%	918	1093	50%	932	1334	20%	1240	758	1056	612
Strathmashie Bridge	1140	30%	1089	1002	30%	921	2576	20%	2528	1067	30%	1008	807	1106	908
Prestwood Bridge	99	20%	89	129	20%	121	107	80%	101	123	20%	110	118	102	84

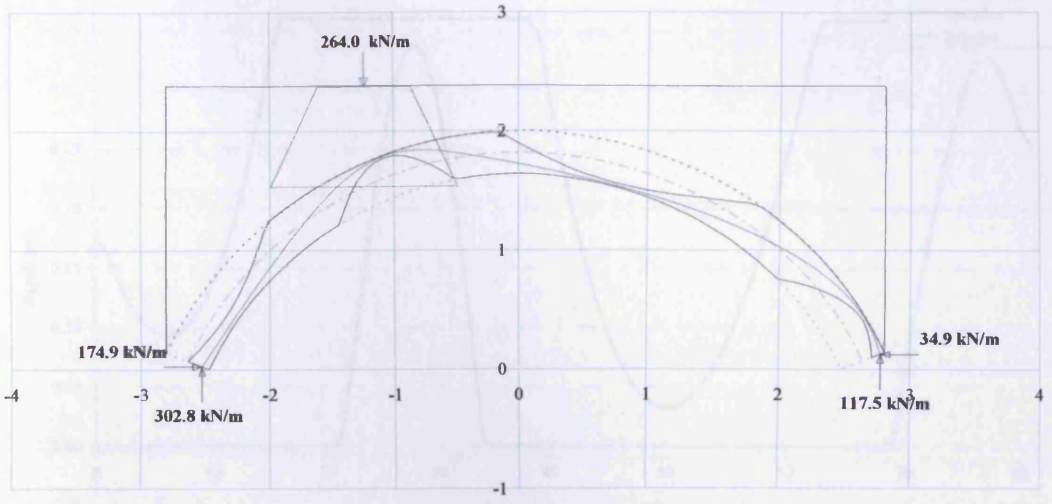

Figure 7.1 The ultimate load of Preston bridge

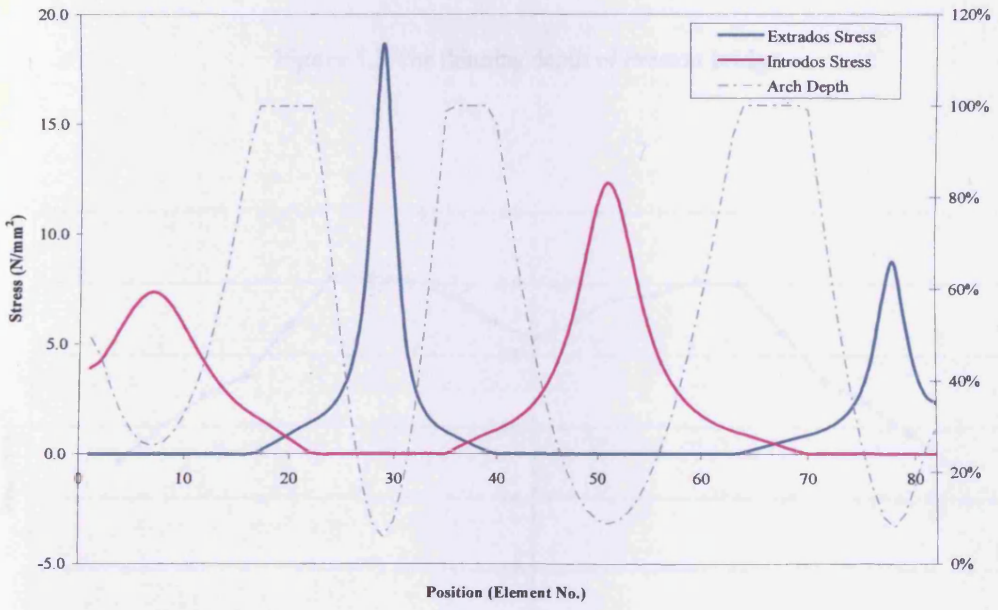

Figure 7.2 The stress over Preston bridge

7.3.1.2 Stress based SLS assessment

As shown in Table 7.2 and Figure 7.4, the moving load maximum stress is quite similar in the quarter point area. So, the critical load of SLS is almost the same as the quarter point and the 30% point.

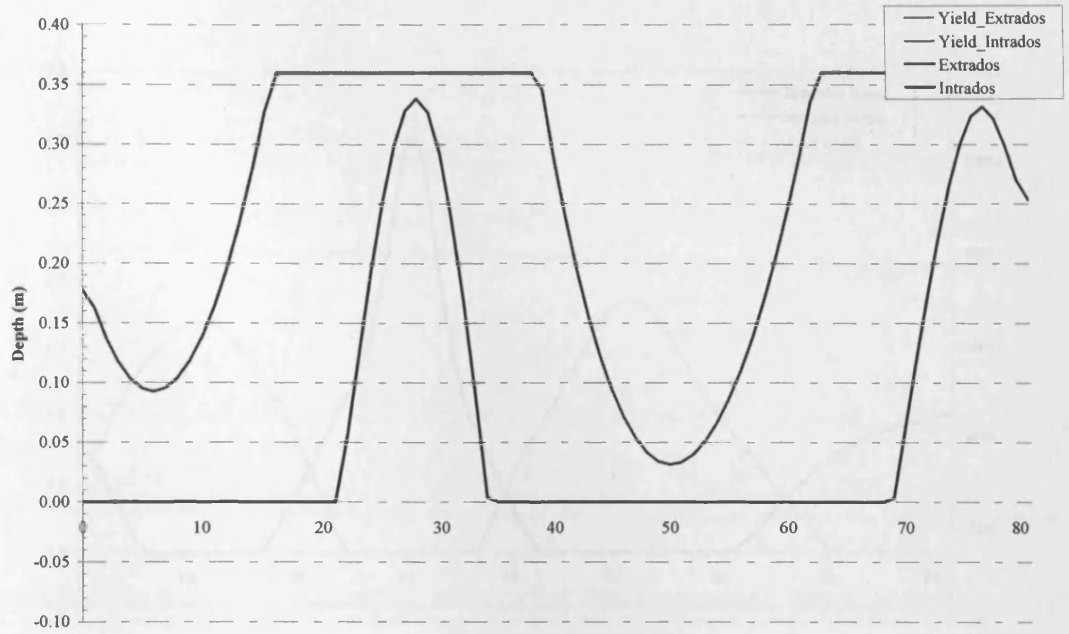

Figure 7.3 The thinning depth of Preston bridge

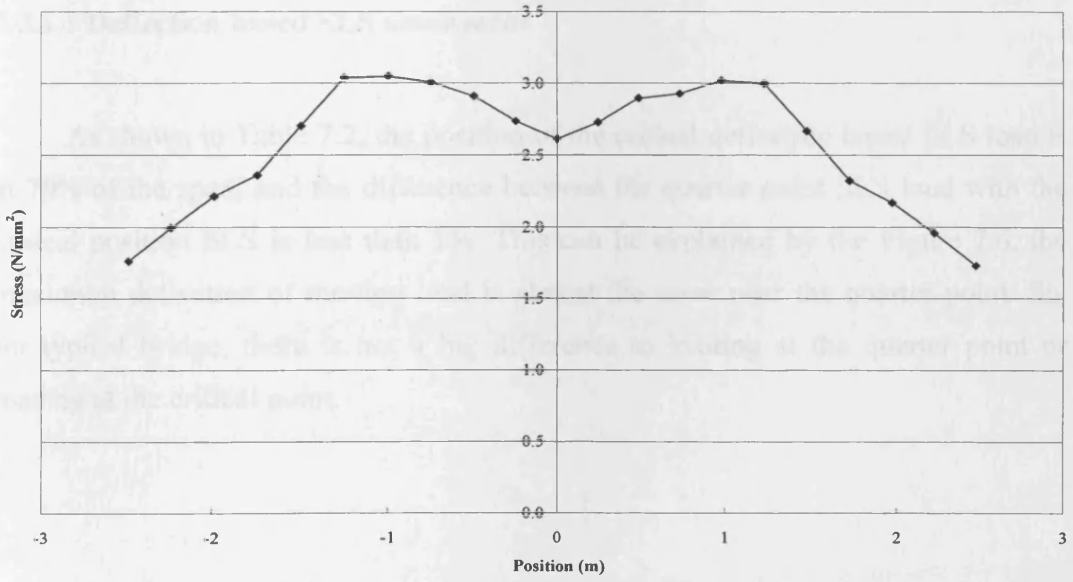

Figure 7.4 The maximum stress when moving load over Preston bridge

As illustrated in Figure 7.5, the maximum stress is located under the load position as is the minimum depth.

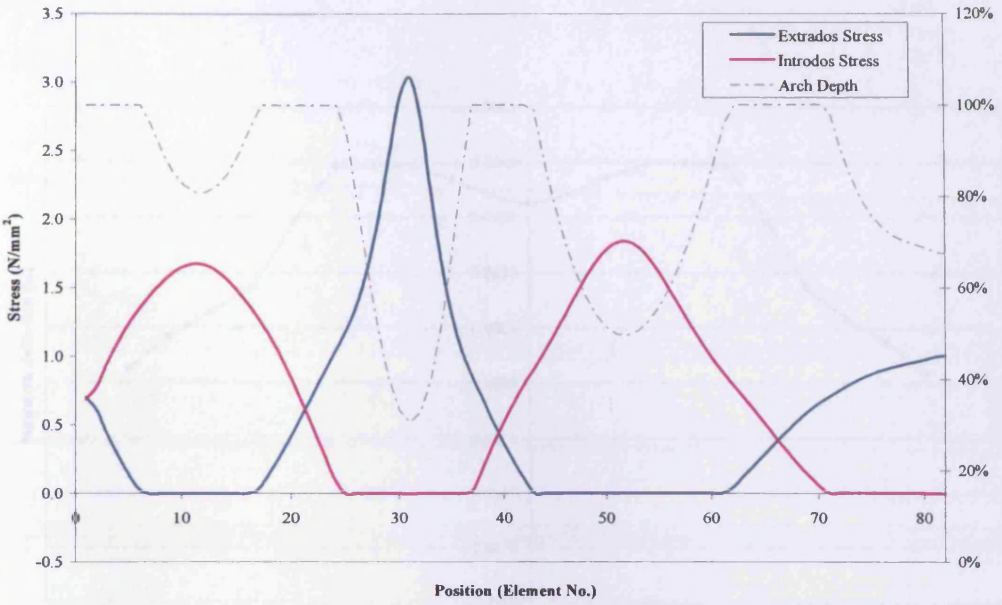

Figure 7.5 The stress over Preston bridge under the stress based SLS load

7.3.1.3 Deflection based SLS assessment

As shown in Table 7.2, the position of the critical deflection based SLS load is at 70% of the span, and the difference between the quarter point SLS load with the critical position SLS is less than 1%. This can be explained by the Figure 7.6, the maximum deflection of moving load is almost the same near the quarter point. So, for typical bridge, there is not a big difference to loading at the quarter point or loading at the critical point.

7.3.1.4 Opening depth based SLS assessment

For the opening depth based SLS, the moving load minimum depth rate is very important, as illustrated in Figure 7.7. Typically the minimum depth rate of the moving load minimum depth rate is at the quarter point.

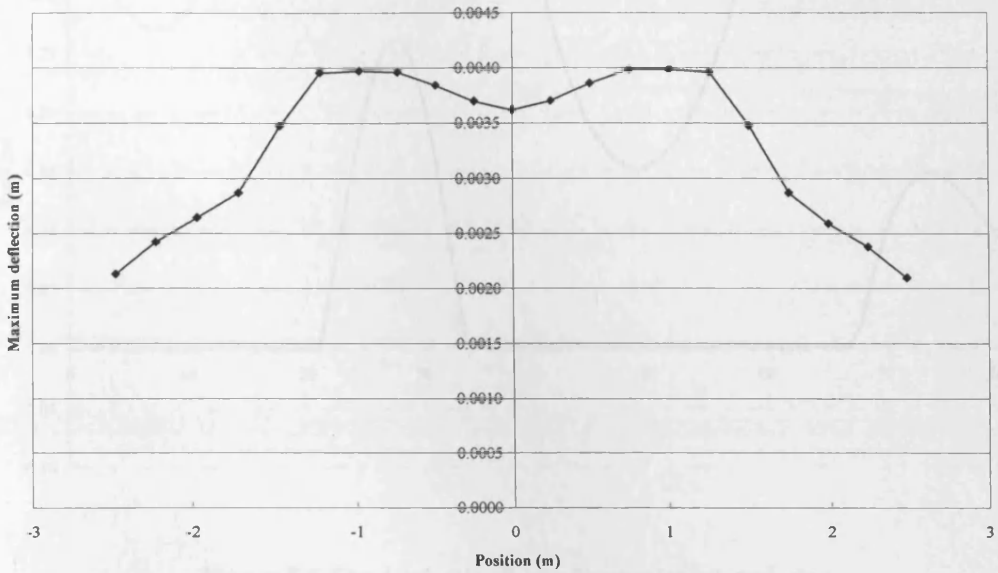

Figure 7.6 The maximum deflection when moving load over Preston bridge

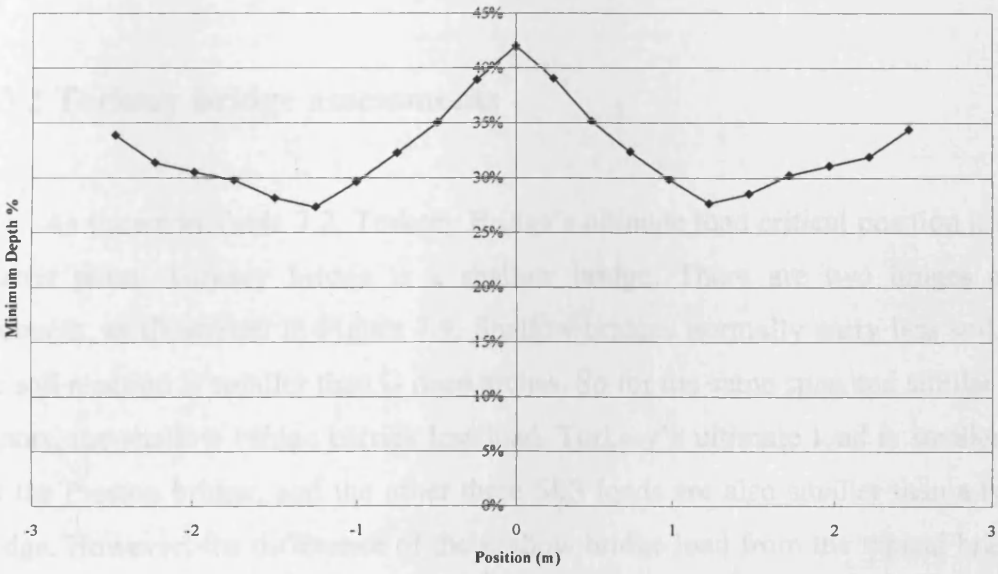

Figure 7.7 The minimum depth when moving load over Preston bridge

As illustrated in Figure 7.8, normally the minimum depth rate of the opening depth based SLS over all the arch ring occurs at the position under the critical load. The four further hinges are not developing one after each other, but are developing at the same time.

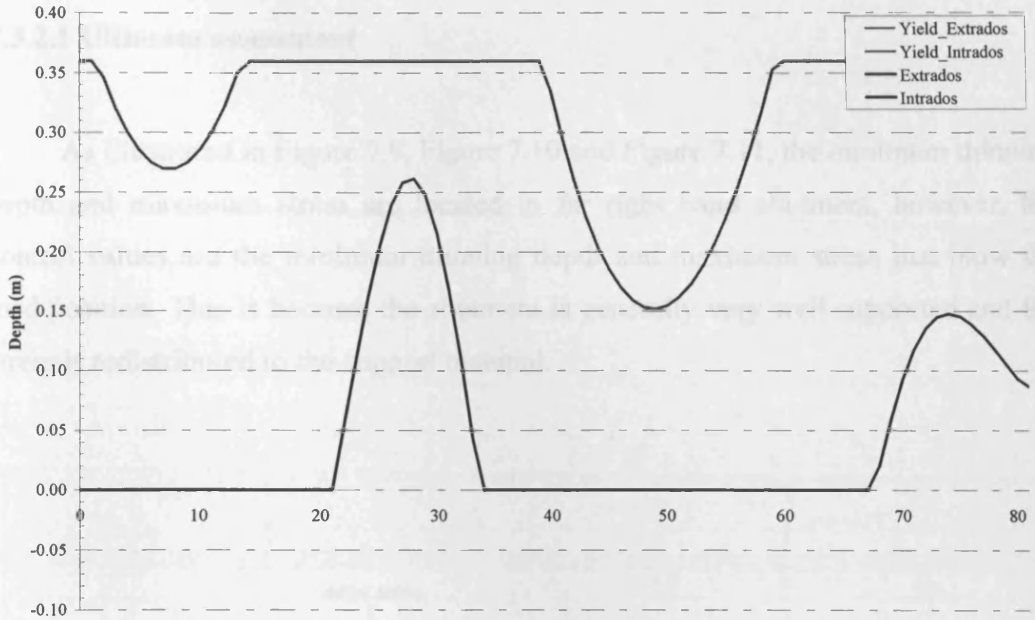

Figure 7.8 The depth rate all over Preston bridge arch ring

7.3.2 Torksey bridge assessments

As shown in Table 7.2, Torksey Bridge's ultimate load critical position is at the quarter point. Torksey bridge is a shallow bridge. There are two hinges at the abutment, as illustrated in Figure 7.9. Shallow bridges normally carry less soil, then the soil reaction is smaller than is deep arches. So for the same span and similar other factors, the shallow bridge carries less load. Torksey's ultimate load is smaller than for the Preston bridge, and the other three SLS loads are also smaller than a typical bridge. However, the difference of the shallow bridge load from the typical bridge is not significant. There is about a 20% difference between the loads of the shallow bridge and the loads of typical bridge (Preston) bridge. The differences are also contributed by the different arch ring depth and head fill depth.

7.3.2.1 Ultimate assessment

As illustrated in Figure 7.9, Figure 7.10 and Figure 7.11, the minimum thinning depth and maximum stress are located in far right hand abutment, however, the control values are the minimum thinning depth and maximum stress just blow the load position. This is because the abutment is generally very well supported and the stress is redistributed to the support material.

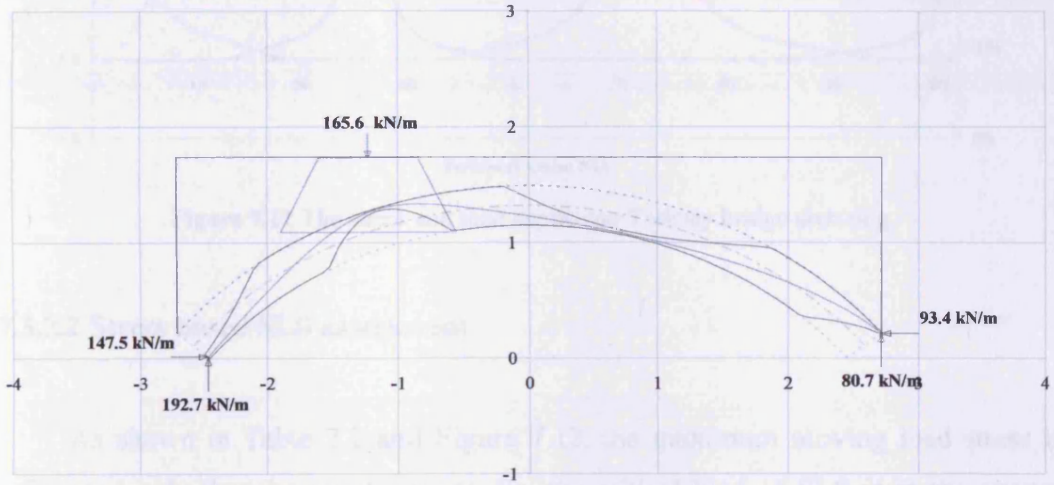

Figure 7.9 The ultimate load of Torksey bridge

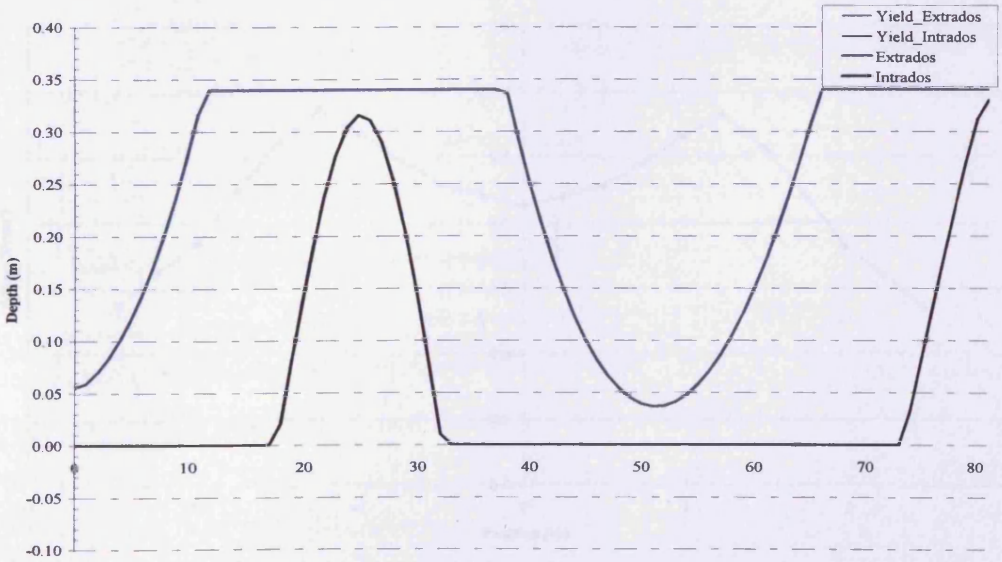

Figure 7.10 The thinning depth over Torksey bridge arch ring

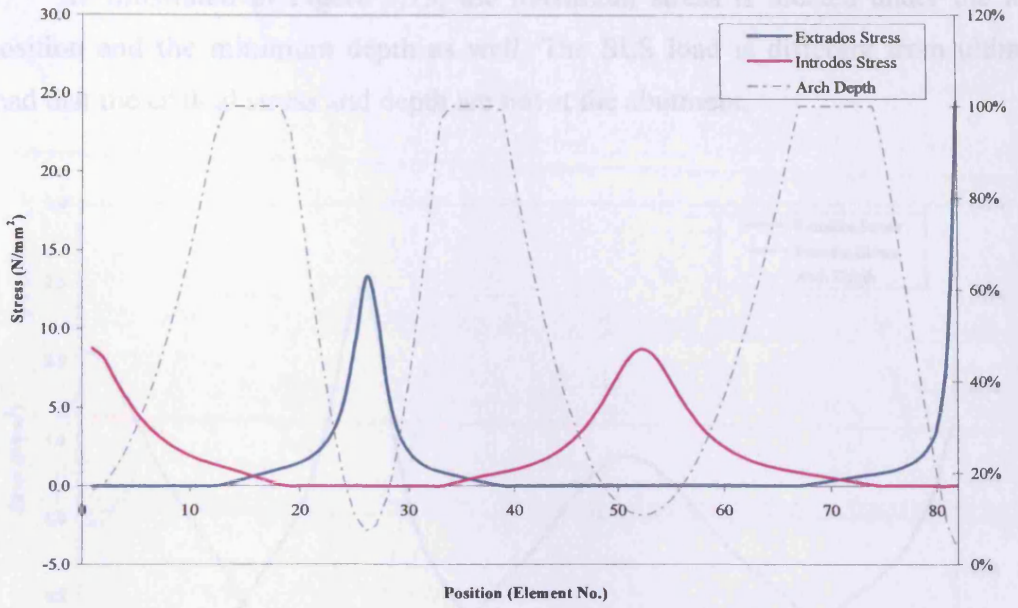

Figure 7.11 The stress and total depth over Torksey bridge arch ring

7.3.2.2 Stress based SLS assessment

As shown in Table 7.2 and Figure 7.12, the maximum moving load stress is quite obviously that the quarter point. So, the critical load of SLS is at the quarter point. This shallow arch has a very clear critical position.

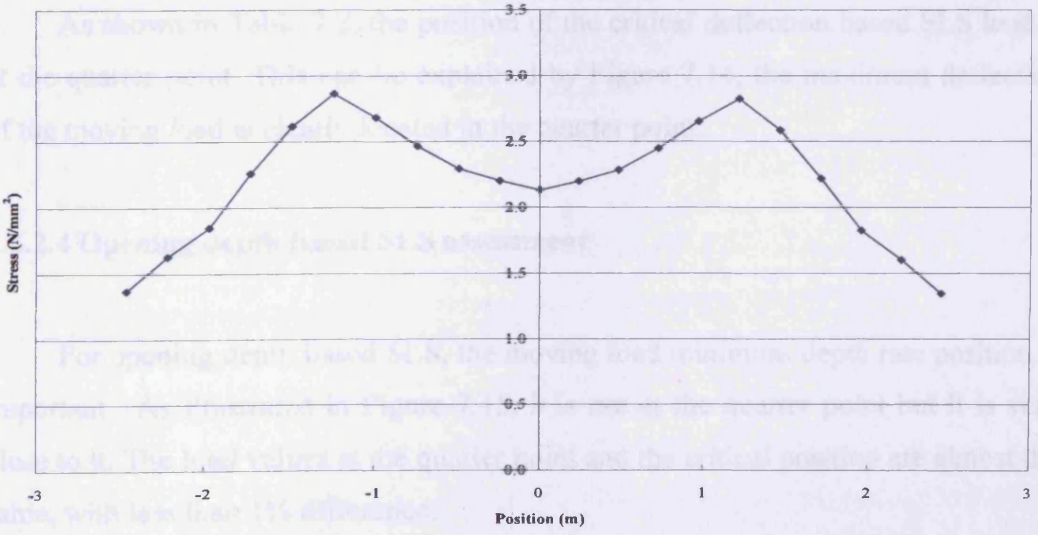

Figure 7.12 The maximum stress when moving load over Torksey bridge

As illustrated in Figure 7.13, the maximum stress is located under the load position and the minimum depth as well. The SLS load is different from ultimate load that the critical stress and depth are not at the abutment.

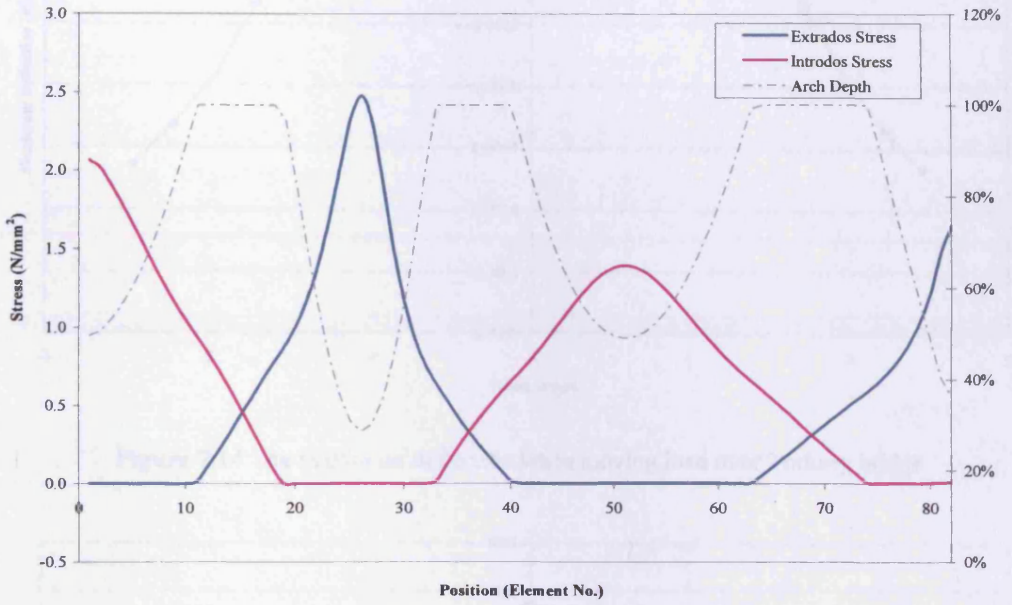

Figure 7.13 The stress over Torksey bridge under the stress based SLS load

7.3.2.3 Deflection based SLS assessment

As shown in Table 7.2, the position of the critical deflection based SLS load is at the quarter point. This can be explained by Figure 7.14, the maximum deflection of the moving load is clearly located in the quarter point.

7.3.2.4 Opening depth based SLS assessment

For opening depth based SLS, the moving load minimum depth rate position is important. As illustrated in Figure 7.15, it is not at the quarter point but it is very close to it. The load values at the quarter point and the critical position are almost the same, with less than 1% difference.

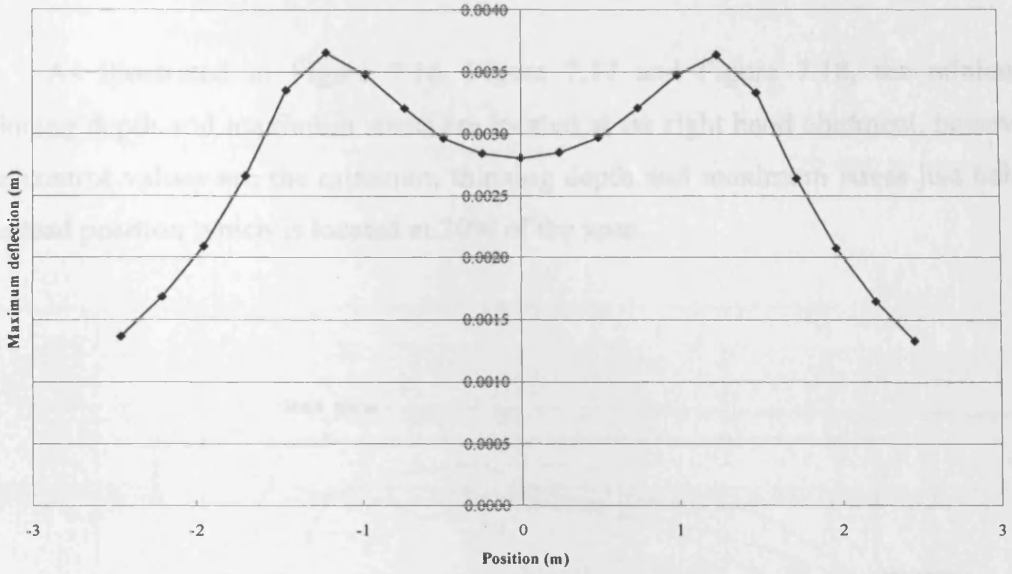

Figure 7.14 The maximum deflection when moving load over Torksey bridge

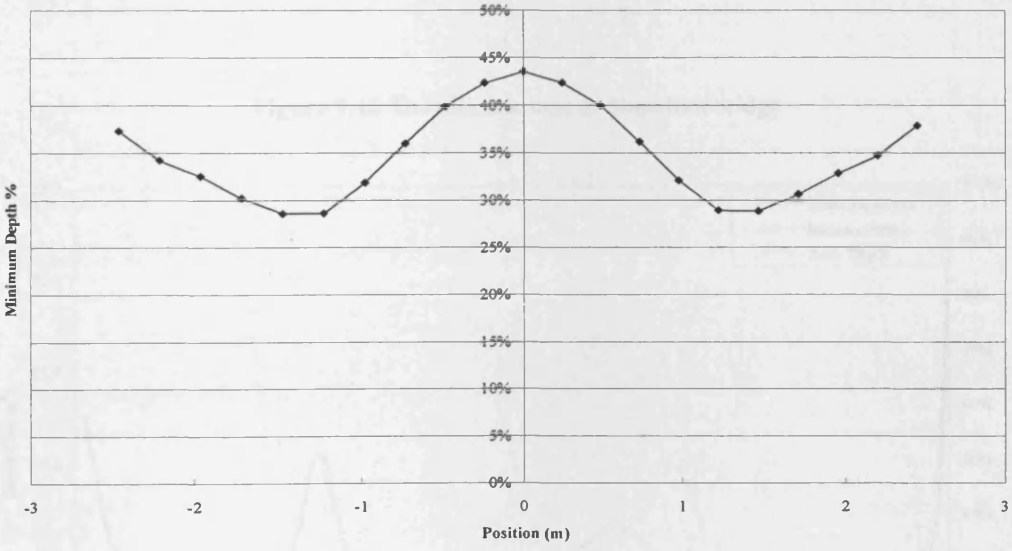

Figure 7.15 The minimum depth when moving load over the bridge

7.3.3 Shinafoot bridge assessments

As shown in Table 7.2, Shinafoot bridge's ultimate load critical position is at 20% of the span. Shinafoot bridge is even shallower than Torksey with its arch ring thickness also different. There are also two hinges at the abutment, as illustrated in Figure 7.16.

7.3.3.1 Ultimate assessment

As illustrated in Figure 7.16, Figure 7.17 and Figure 7.18, the minimum thinning depth and maximum stress are located at far right hand abutment, however, the control values are the minimum thinning depth and maximum stress just below the load position which is located at 20% of the span.

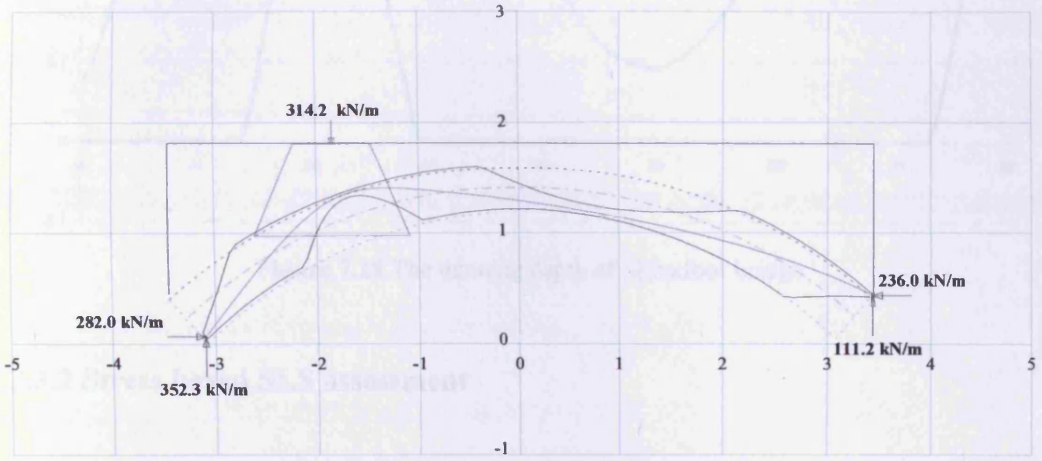

Figure 7.16 The ultimate load of Shinafoot bridge

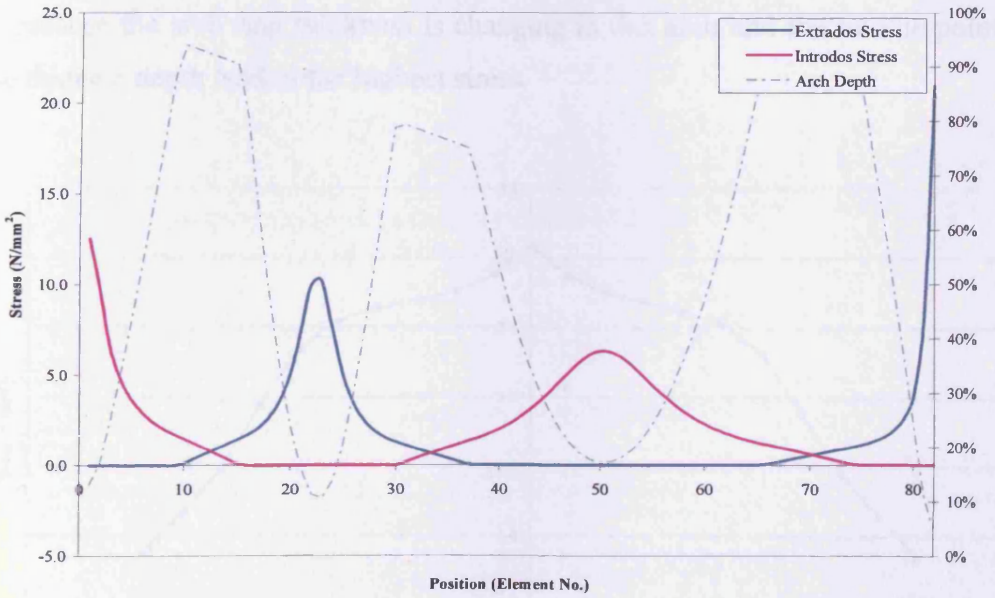

Figure 7.17 The stress over Shinafoot bridge

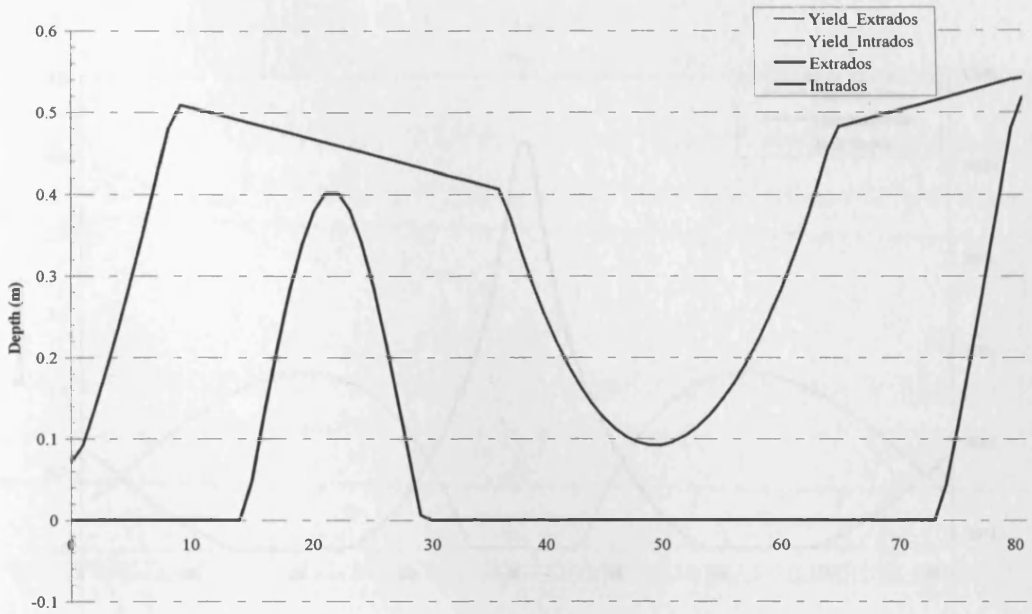

Figure 7.18 The thinning depth of Shinafoot bridge

7.3.3.2 Stress based SLS assessment

As shown in Table 7.2 and Figure 7.19, the moving load maximum stress is in the middle point (crown). This is significantly different from the quarter point. This is because the arch ring thickness is changing in this arch and the middle point with the thinnest depth lead to the highest stress.

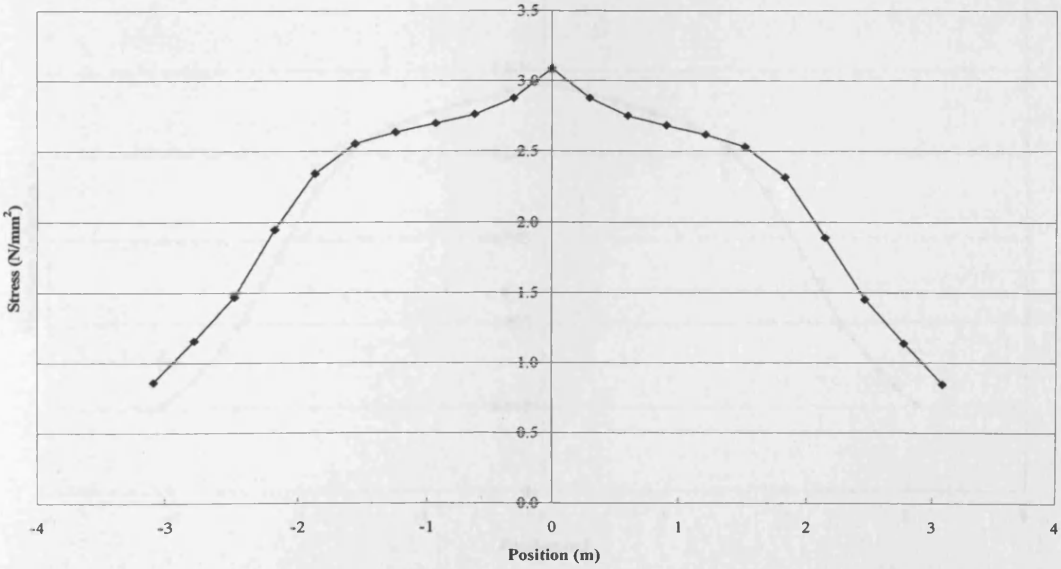

Figure 7.19 The maximum stress when moving load over Shinafoot bridge

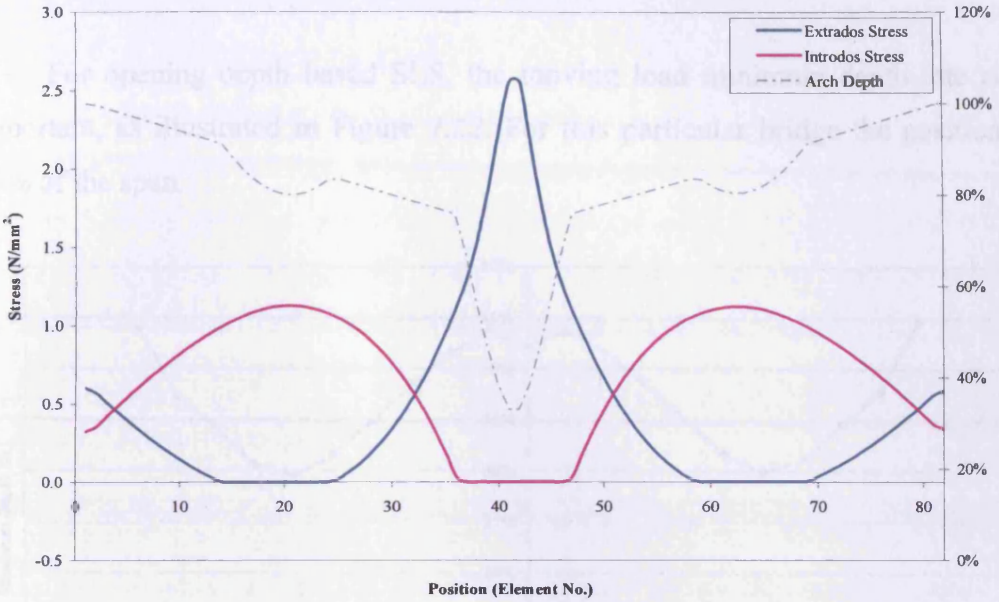

Figure 7.20 The stress over Shinafoot bridge under the stress based SLS load

7.3.3.3 Deflection based SLS assessment

As shown in Figure 7.21, the position of the critical deflection base SLS load is at 50% of the span. This is also because the changing thickness making the middle point thinnest, then the deflection highest.

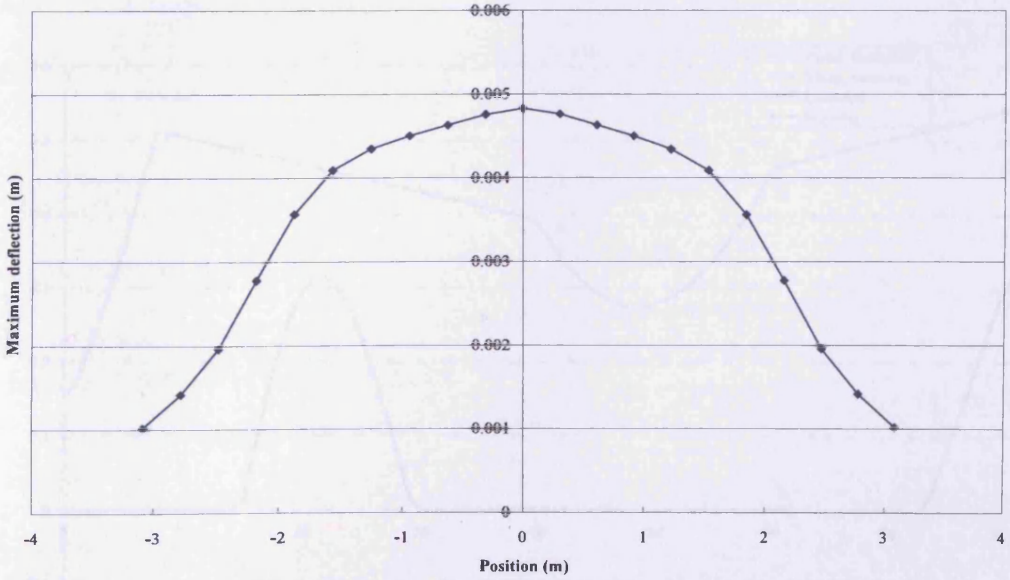

Figure 7.21 The maximum deflection when moving load over Shinafoot bridge

7.3.3.4 Opening depth based SLS assessment

For opening depth based SLS, the moving load minimum depth rate is very important, as illustrated in Figure 7.22. For this particular bridge the position is at 20% of the span.

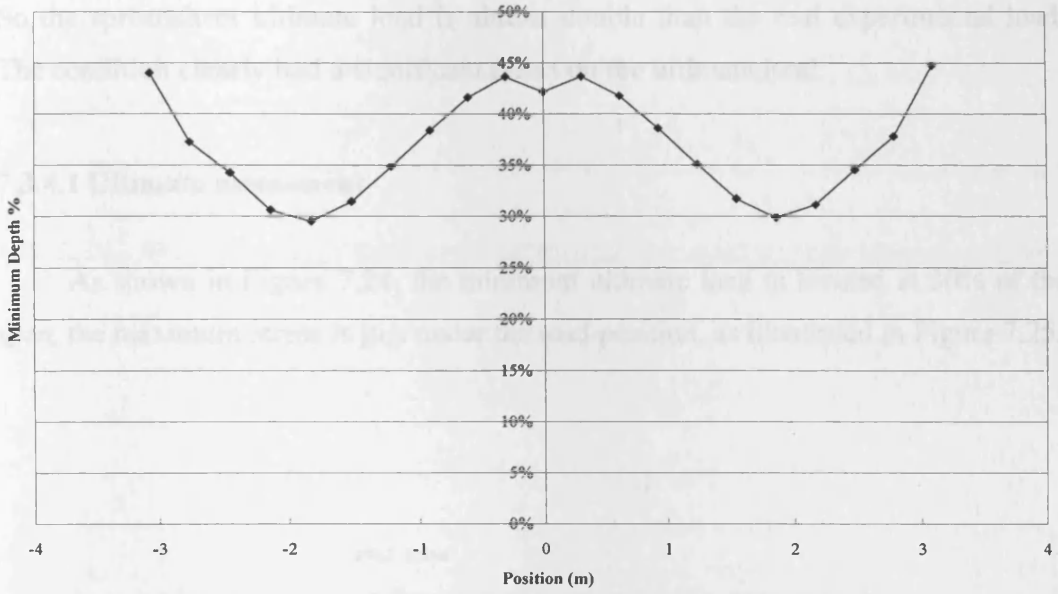

Figure 7.22 The minimum depth when moving load over Shinafoot bridge

As illustrated in Figure 7.23, normally the minimum depth rate all over the arch ring happens in the position under the critical load.

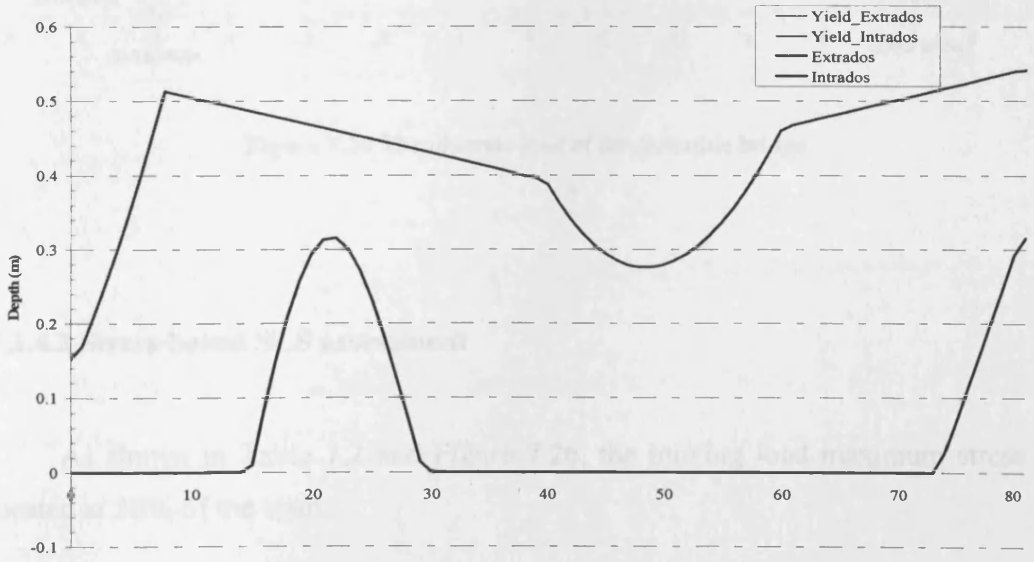

Figure 7.23 The depth rate all over Shinafoot bridge arch ring

7.3.4 Strathmashie bridge assessments

As shown in Table 7.2, Strathmashie bridge's ultimate load critical position is at 30% of span. And Strathmashie bridge is a typical rise to span which is much deeper than the previous three bridges. This bridge also had a very poor condition. So the spreadsheet ultimate load is almost double than the real experimental load. The condition clearly had a significant effect on the ultimate load.

7.3.4.1 Ultimate assessment

As shown in Figure 7.24, the minimum ultimate load is located at 30% of the span, the maximum stress is just under the load position, as illustrated in Figure 7.25.

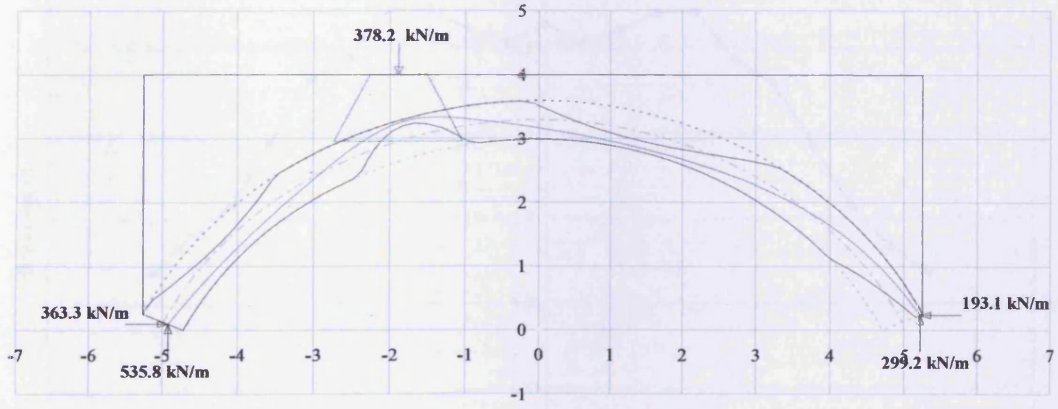

Figure 7.24 The ultimate load of Strathmashie bridge

7.3.4.2 Stress based SLS assessment

As shown in Table 7.2 and Figure 7.26, the moving load maximum stress is located at 30% of the span.

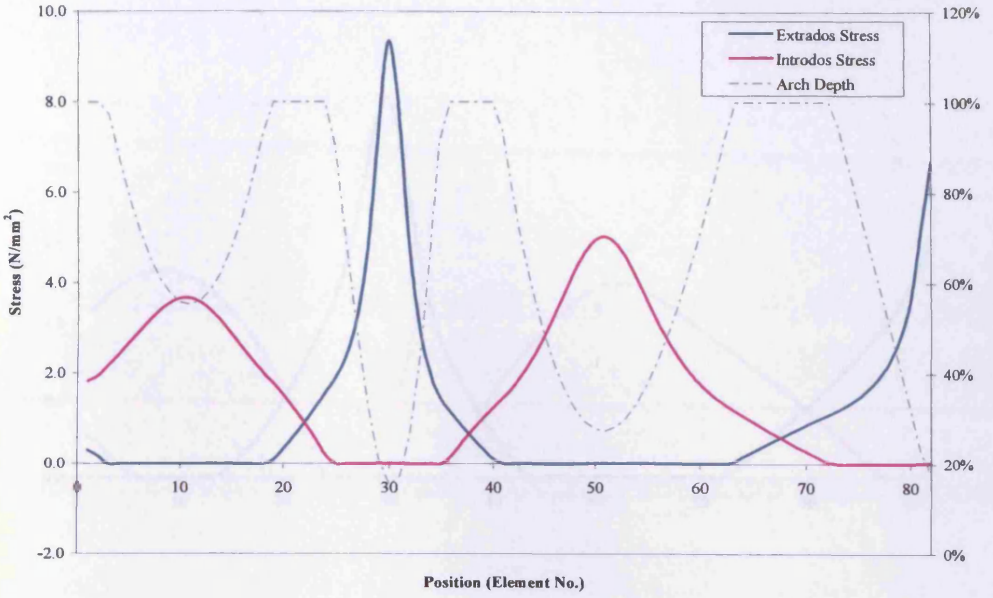

Figure 7.25 The stress over Strathmashie bridge

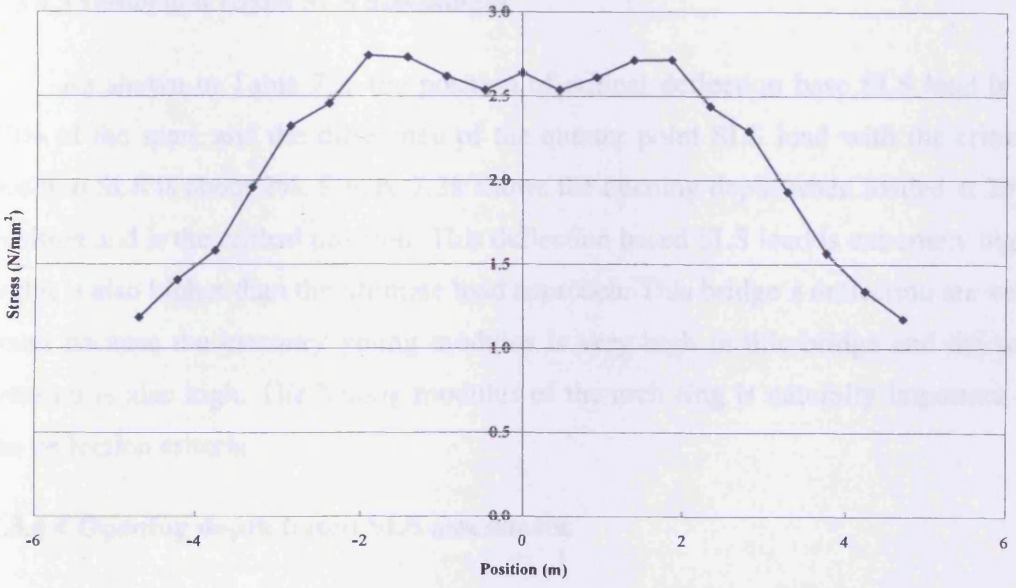

Figure 7.26 The maximum stress when moving load over Strathmashie bridge

As illustrated in Figure 7.27, the maximum stress located is under the load position and the minimum opening depth as well.

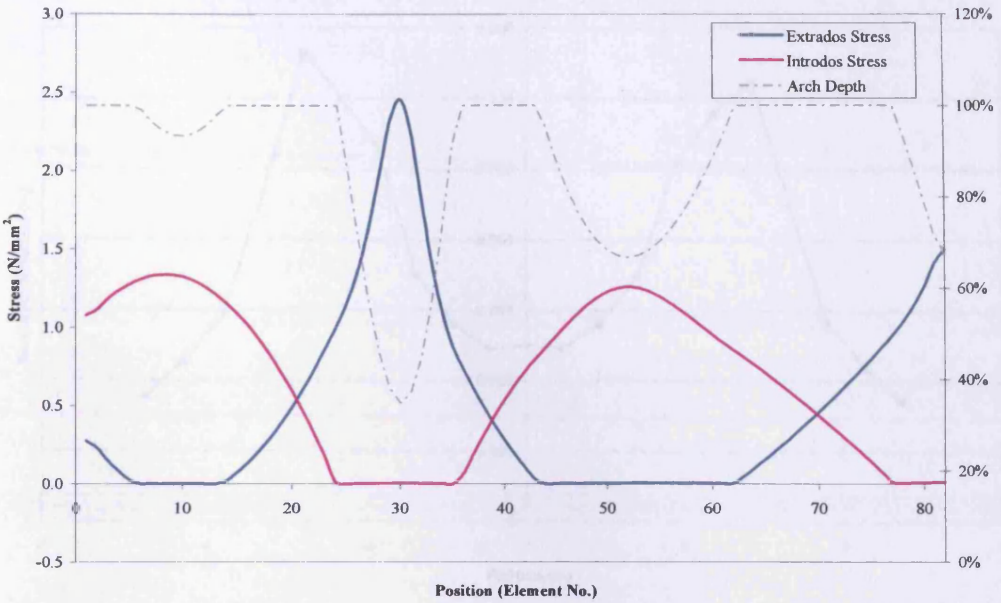

Figure 7.27 The stress over Strathmashie bridge under the stress based SLS load

7.3.4.3 Deflection based SLS assessment

As shown in Table 7.2, the position of critical deflection base SLS load is at 20% of the span, and the difference of the quarter point SLS load with the critical position SLS is about 2%. Figure 7.28 shows the opening depth when loaded at 20% position and is the critical position. This deflection based SLS load is extremely high, and it is also higher than the ultimate load approach. This bridge's deflection are very small because the masonry young modulus is very high in this bridge and the soil reaction is also high. The Young modulus of the arch ring is naturally important to the deflection criteria.

7.3.4.4 Opening depth based SLS assessment

For the opening depth based SLS, the moving load minimum depth rate is very important, as illustrated in Figure 7.29. The critical load is located in 30% of the span. From the figure, from the quarter point to the other side quarter point, the minimum depth rate is very similar, so the difference between different positions is very small. Here the loads are 6% difference between quarter point and critical point.

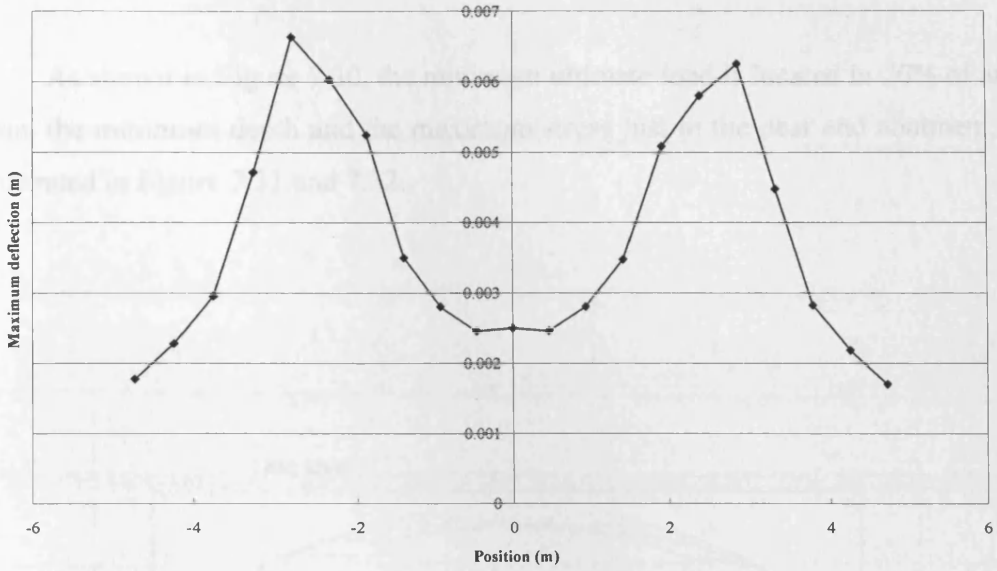

Figure 7.28 The maximum deflection when moving load over Strathmashie bridge

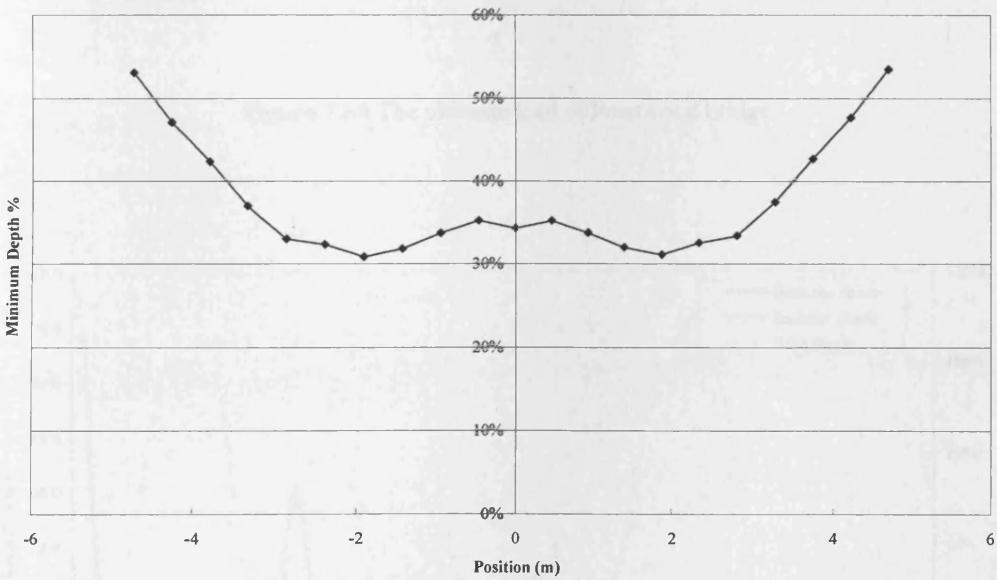

Figure 7.29 The minimum depth when moving load over Strathmashie bridge

7.3.5 Prestwood bridge assessments

The last bridge, Prestwood bridge, is a very thin bridge.

7.3.5.1 Ultimate assessment

As shown in Figure 7.30, the minimum ultimate load is located in 20% of arch span, the minimum depth and the maximum stress just in the near end abutment, as illustrated in Figure 7.31 and 7.32.

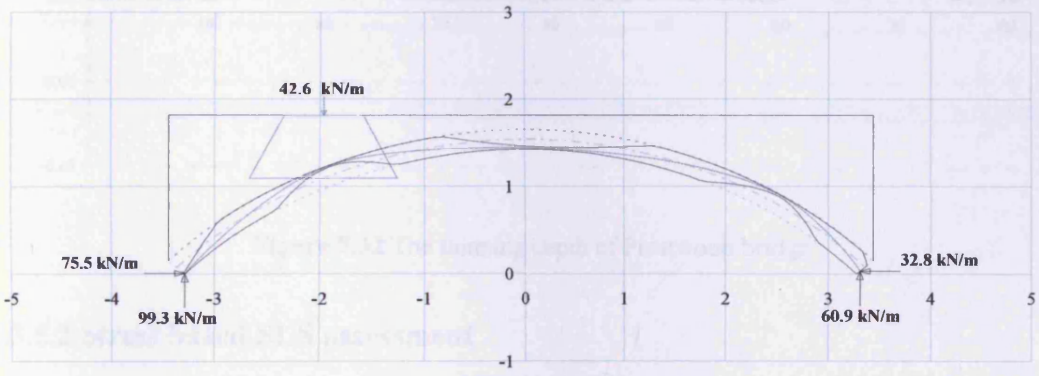

Figure 7.30 The ultimate load of Prestwood bridge

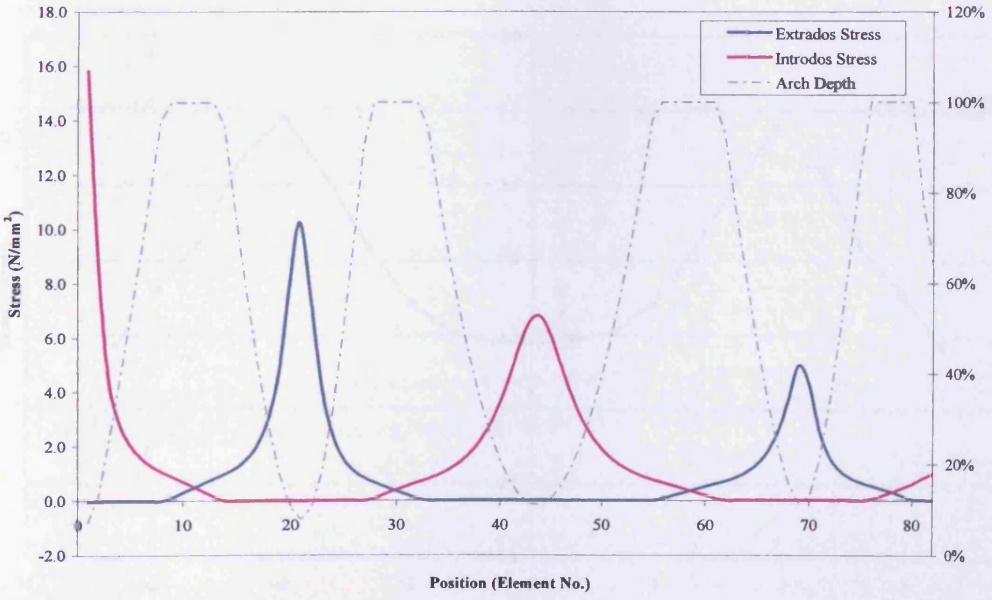

Figure 7.31 The stress over Prestwood bridge

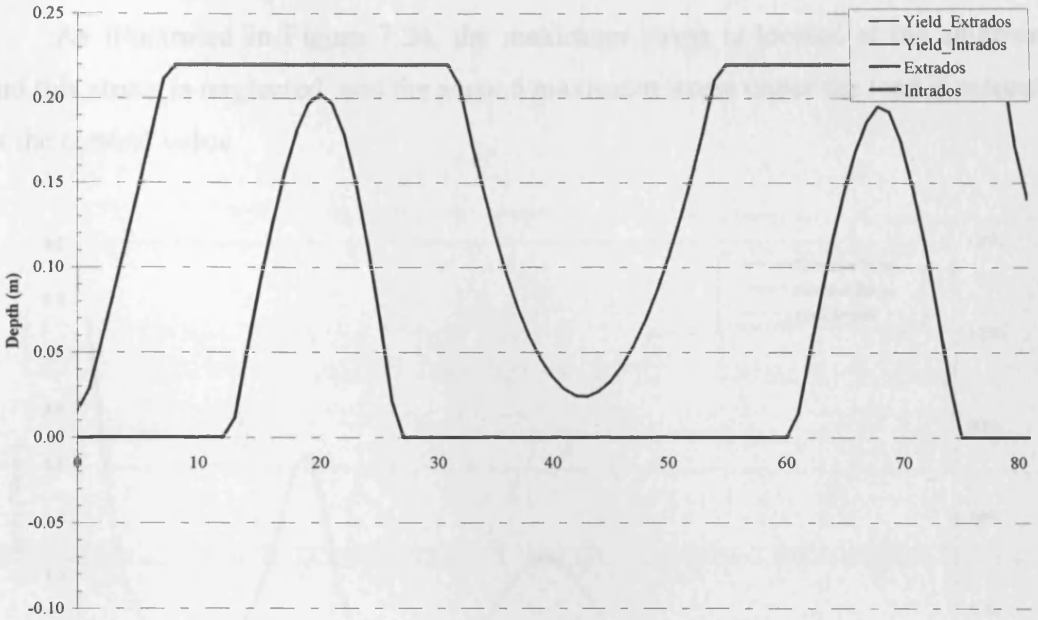

Figure 7.32 The thinning depth of Prestwood bridge

7.3.5.2 Stress based SLS assessment

As shown in Table 7.2and Figure 7.33, the moving load maximum stress is located at 20% of span.

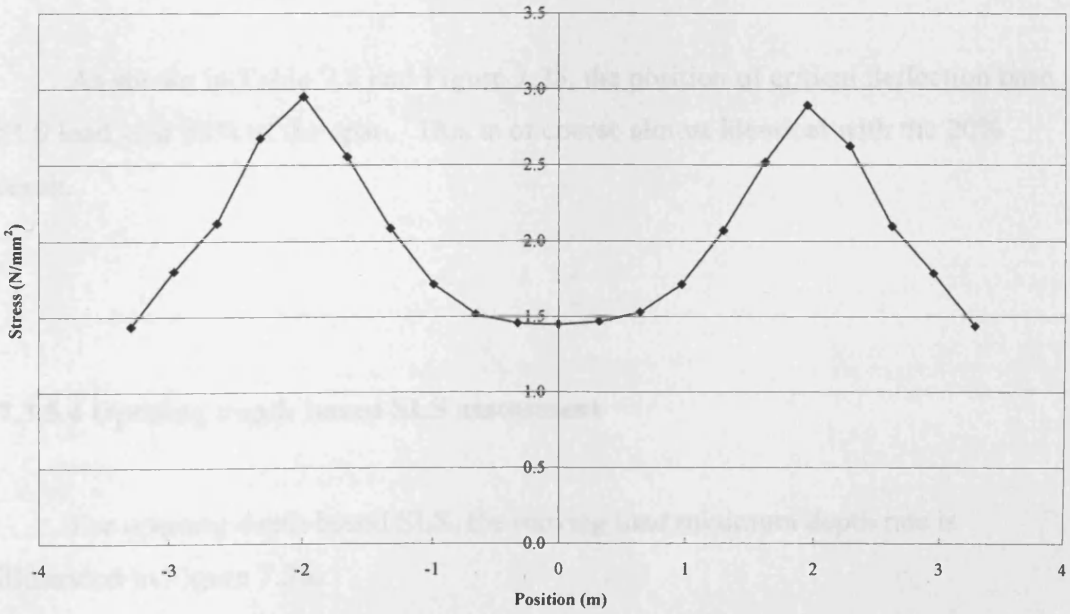

Figure 7.33 The maximum stress when moving load over Prestwood bridge

As illustrated in Figure 7.34, the maximum stress is located at the abutment and this stress is neglected, and the second maximum stress under the load is selected as the control value.

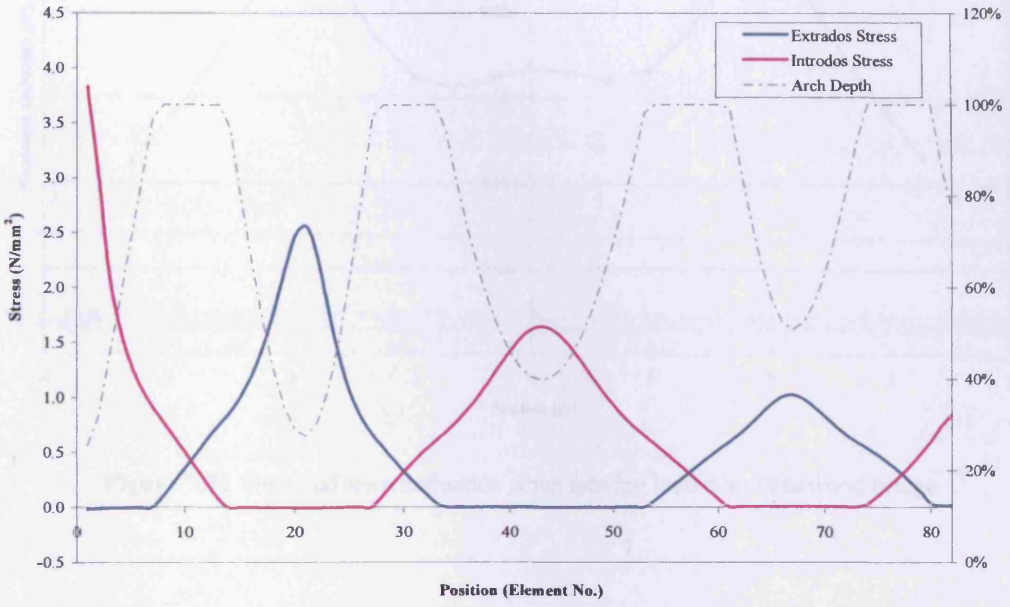

Figure 7.34 The stress over Prestwood bridge under the stress based SLS load

7.3.5.3 Deflection based SLS assessment

As shown in Table 7.2 and Figure 7.35, the position of critical deflection base SLS load is at 80% of the span. This is of course almost identical with the 20% result.

7.3.5.4 Opening depth based SLS assessment

For opening depth based SLS, the moving load minimum depth rate is illustrated in Figure 7.36.

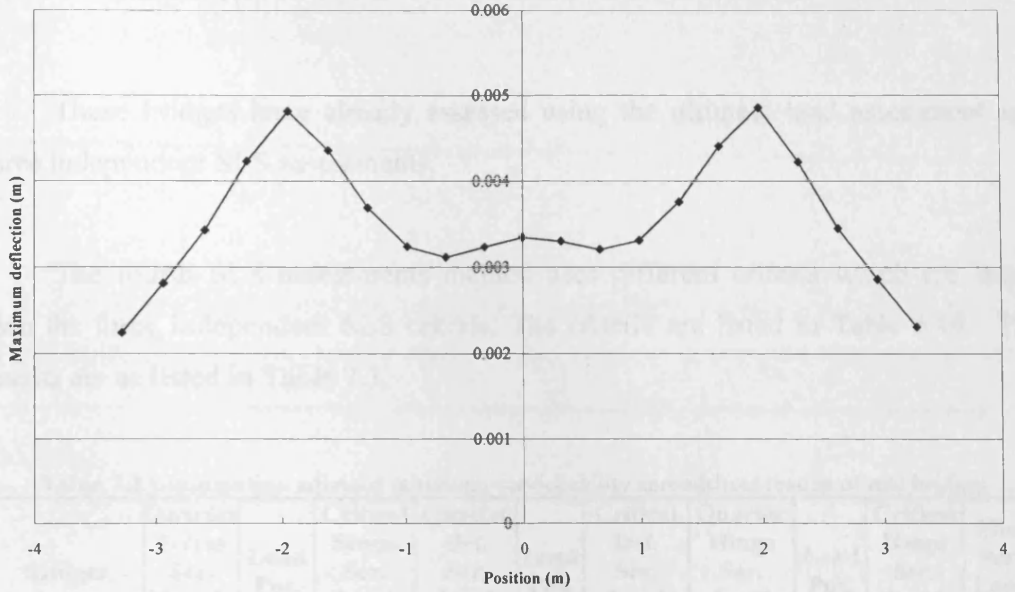

Figure 7.35 The maximum deflection when moving load over Prestwood bridge

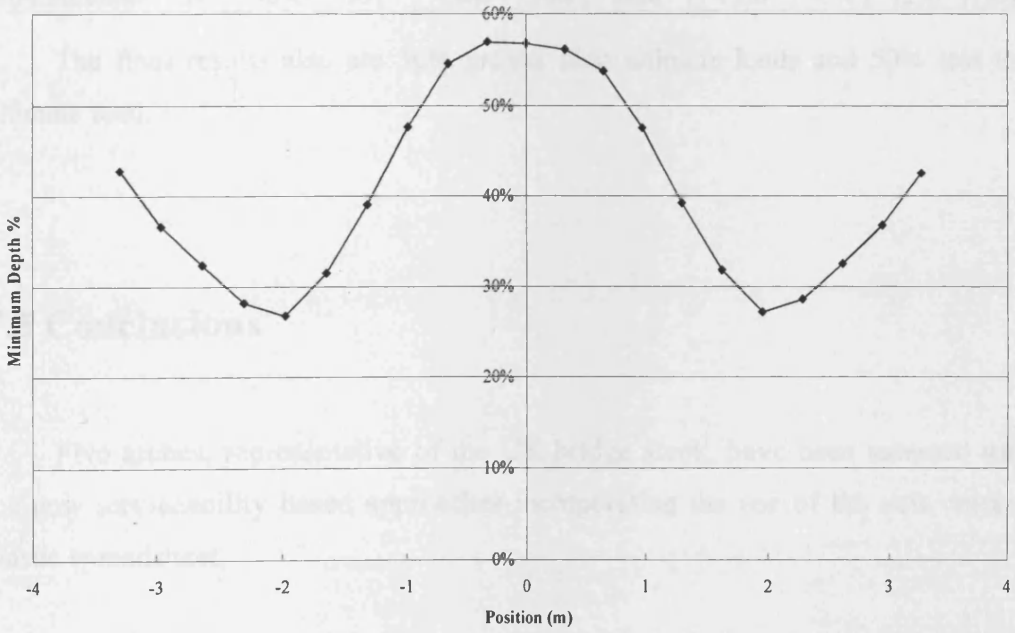

Figure 7.36 The minimum depth when moving load over Prestwood bridge

7.4 Minimum criterion based SLS assessments

These bridges have already assessed using the ultimate load assessment and three independent SLS assessments.

The fourth SLS assessments method uses different criteria which are larger than the three independent SLS criteria. The criteria are listed in Table 6.19. The results are as listed in Table 7.3.

Table 7.3 Ultimate and adjusted minimum serviceability spreadsheet results of real bridges

Bridges	Quarter Stress Ser. Load (kN)	Load Pos.	Critical Stress Ser. Load (kN)	Quarter Def. Ser. Load (kN)	Load Pos.	Critical Def. Ser. Load (kN)	Quarter Hinge Ser. Load (kN)	Load Pos.	Critical Hinge Ser. Load (kN)	Min. Ser. Load (kN)
Torksey	786	25%	786	769	25%	769	798	20%	792	769
Shinafoot	1220	20%	1220	1270	25%	1270	1570	20%	1440	1220
Prestwood	136	20%	127	118	20%	111	139	20%	125	111
Preston	1020	25%	1020	994	25%	994	1110	25%	1110	994
Strathmashie	1080	30%	991	2680	20%	2620	1320	30%	1270	991

The final results also are 50% greater than ultimate loads and 50% less than ultimate load.

7.5 Conclusions

Five arches, representative of the UK bridge stock, have been assessed using the new serviceability based approaches incorporating the use of the new cracking elastic spreadsheet.

All the bridges have been analysed successfully using the new spreadsheet without any convergence/iteration difficulty and using standard settings.

The Figures showing the results of the application of the spreadsheet demonstrate part of the range of output of both stationary and moving loads

The selected examples, covered typical bridge, different condition bridges, different material types, different geometric shapes and different spans.

From assessing these different bridges, the new methods are deemed to be successfully applied not just to these bridges but the range of bridges covered by these structures. This can strengthen the confidence of using these new methods to any bridges.

Cardiff Arch Spreadsheet appears to be a good tool to find the ultimate load and the three new serviceability assessment loads using the new method developed.

8 Conclusions and Recommendations

8.1 Conclusions

The main objective of this thesis was to develop serviceability assessments of masonry arch bridges. Three independent serviceability criteria and one minimum based serviceability criterion have been developed to determine the serviceability limit loads. The process to determine appropriate values for the new serviceability criteria were developed and then followed. A series of bridges were assessed with the new serviceability assessment methods.

A Castigliano method spreadsheet has also been developed to assess the masonry bridges at both serviceability and ultimate load.

The following general conclusion can be drawn with regards to the spreadsheet:

The spreadsheet is suitable for assessing ultimate limit load as well as serviceability limit load and any service load.

The bridge geometries distribution is studied and the distribution of cumulative probability and probability density of the span, rise to span ratio, depth to span ratio and crown fill depth to arch ring depth ratio were fitted by hyperbolic functions and a multi-linear function. Except for the rise to span ratio which used a linear distribution, the other parameters were distributed by hyperbolic functions.

The following conclusions can be drawn with regards to the creep analysis in unloaded masonry arch bridges:

The creep can increase the shallow bridge serviceability loads about 10%, but not increase the ultimate load and not affect the deep bridges significantly.

Three criteria of serviceability limit assessments and one minimum criterion are developed. And three shortened serviceability equations and one ultimate shortened simple equation have been developed for instant assessments for bridge engineers. These shortened equations have been compared with the MEXE equation. The results show that the new methods are worthy of consideration and possibly better than MEXE.

The serviceability assessment methods systematically developed in this work could prove very useful to bridge assessment engineers, they allow an evolutionary approach and easily obtained solution. The shortened equation can be used as a quick solution and are validated to the spreadsheet results. These methods resolved the problems of bridge owners and engineers not easily knowing the stress, deflection and cracking of bridges. They are potentialy excellent tools to manage the daily traffic load and other special loads of the bridges.

8.2 Recommendations

According to the results obtained during the study it seems that the research can be extended to some more areas, which were not covered by this thesis due to the time limitation of the project. It is suggested that the study can be extended to the following areas:

The current serviceability assessment of masonry arch bridges was restricted to the single span structures. It is suggested that this study can be extended to the multi span arches.

The database of the bridges geometries can be added to and ideally up to 1000 real bridges included.

After having additional bridges, the criteria also need more bridges to better define the probabilities. Ideally up to 400 bridges. And the Monte Carlo simulation

also can use more bridges possibly up to 100,000 bridges as the probabilities are better defined.

Work must now be undertaken to prosecute the new methods developed such that as planned, over time, experience gained using the new serviceability criteria will allow the suggested limiting values to be refined as the criteria are better matched to the condition of the actual assessed structures.

References

1. McKibbins L., Melbourne C., Sawar N. and Sicilia Gaillard C. (2006). Masonry arch bridges-condition, appraisal and remedial treatment. London, CIRIA.
2. Howe M. A. (1987). A treatise on arches. New York, John Wiley and Sons.
3. Lu D. Q. (1992). Chinese stone bridges, Peoples Transportation Press.
4. Ng K. H. (1999). Analysis of masonry arch bridges. School of the built Environment. Edinburgh, Nappier University.
5. Cox D. and Hslsall R. (1996). Brickwork Arch Bridges. Windsor, Brick Development Association.
6. Page J. (1993). Masonry arch bridge- state of the art review. London, Transport Research Laboratory, HMSO.
7. Roberts T.M., Hughes T.G. and Goutis G. (2003). Progressive damage to masonry arch bridges caused by repeated traffic loading. Final Report, Network Rail Sponsored Contract RCNG139, Cardiff University, School of Engineering, 1-44.
8. Roberts T.M., Hughes T.G. and Dandamudi V.R. (2004). Progressive damage to masonry arch bridges caused by repeated traffic loading phase 2. Final Report, Network Rail Sponsored Contract RCNG144, Cardiff University, School of Engineering, 1-54.
9. Roberts T. M., Hughes T. G., Dandamudi V. R. and Bell B. (2006). Quasi-static and high cycle fatigue strength of brick masonry, Construction and Building Materials, 20, 9, 603-614.
10. Roberts T.M., Hughes T.G. and Uran N. (2006). Progressive damage to masonry arch bridges caused by repeated traffic loading phase 3. Final Report, Network Rail Sponsored Contract RCNG167, Cardiff University, School of Engineering, 1-89.
11. Roberts T.M. and Hughes T.G. (2007).Serviceability of masonry arch railway bridges, Arch'07, Proc. 5th Int. Conf. Arch bridges, 315-322.
12. Hendry A. W., Sinha B. P. and Davies S. R. (1987). Load Bearing Brickwork Design. Ellis, Horwood Ltd, West Sussex.
13. Hendry A. W., Sinha B. P. and Davies S. R. (1997). Design of Masonry Structures. E & F N, Spon, London.
14. Page J. (1998). Load test on two arch bridges at Torrksey and Shinafoot. Crowthorn, UK, Department of Transport, TRRL Research Report 159.

15. Clark G. W. (1994). Bridge analysis testing and cost causation: serviceability of brick masonry. British Rail Research Report LR-CE5-151.

16. Royles R. and Hendry A. W. (1991). Model tests on masonry arches. Proceedings - Institution of Civil Engineers, Engrs. Structs & Bldgs 91(June): 299-321.

17. Fairfield C. A. and Ponniah D. A. (1994). Model tests to determine the effect of fill on buried arches. Proceedings of the Institution of Civil Engineers, Structure and Buildings 104: 471-482.

18. Heyman J. (1980). The estimation of the strength of masonry arches. Proceeding of the Institution of Civil Engineers. 69: 921-937.

19. Heyman J. (1982). The masonry arch. Chichester, Ellis Horwood Ltd.

20. Crisfield M. A. and Page J. (1990). Assessment of the load carrying capacity of arch bridges. The Maintenance of Brick and Stone Masonry Structures. A. M. Sowden. London, E&F.N. Spon, 81-113.

21. Hughes T. G. and Blackler M. J. (1997). A review of the UK masonry arch assessment methods. Proceeding of the Institution of Civil Engineers, Structures and Building 122(August): 305-315.

22. Orban Z.(2007).UIC Project on assessment, inspection and maintenance of masonry railway bridges, Arch'07, Proc. 5th Int. Conf. Arch bridges, 3-12.

23. Schueremans L. and Van Gemert D. (2001). Assessment of existing structures using probabilistic methods-state of the art, Computer methods in structural masonry-5, Proc. Fifth Int. Symp. Computer methods in structural masonry, 255-262.

24. Schueremans L. and Van Gemert D. (2001). Assessment of existing structures using probabilistic methods-new approaches, Computer methods in structural masonry-5, Proc. Fifth Int. Symp. Computer methods in structural masonry, 271-279.

25. Casas J.R. (2001). Reliability-based assessment of existing arch bridges, Proc. 3rd International Arch Bridges Conference, Paris, 379-384.

26. Pippard A. J. S. (1951). A study of the voussoir arch. London, National Building Studies, Research Paper No 11.

27. Davey N. (1953). Tests on road bridges. London, HMSO, National Building Studies, Research Paper No 16.

28. Department of Transport (2001). BA 16/97 Amendment No.2 - The Assessment of Highway Bridges and Structures. London, Department of Transport, HMSO.

29. Department of Transport (2001). BD 21/01 - The Assessment of Highway Bridges and Structures. London, Department of Transport, HMSO.

30. Hughes T. G. (2005), William Edwards Bridge, ICE Bridge Engineering, 71-80.

31. Pippard A. J. S., Tranter E. et al. (1936). The mechanics of the voussoir arch. Proceeding of the Institution of Civil Engineers. 4(Dec.): 281-306.

32. Pippard A. J. S. and Ashby R. (1939). An experimental study of the voussoir arch. Proceeding of the Institution of Civil Engineers. 10(Jan.): 383-406.

33. Pippard A. J. S. and Chitty L. (1942). Repeated load tests on a voussoir arch. Proceeding of the Institution of Civil Engineers, 79-86.

34. Harvey W. J. (1988). Application of the mechanism analysis to masonry arches. The Structural Engineer 66, 5, 77-84.

35. Sharman M.T. and Harvey W.J. (1995). Assessment of Castle Bridge. Proc. ICE Structs&Bldgs, 110, 28-33.

36. Crisfield M. A. and Packham A. J. (1987). A mechanism program for computing the strength of masonry arch bridges. Crowthorne, Department of Transport.

37. Livesley R.K. (1978). Limit analysis of structures formed from rigid blocks, Int.J. Numerical Methods in Engineering, 12, 1853-1871.

38. Livesley R.K. (1992). The collapse analysis of masonry arch bridges, Proc. Conf. App. Solid Mechanics 4, Elsevier, 261-274.

39. Livesley R.K. (1992). A computational model for the limit analysis of 3-dimensional masonry structures, Meccanica, 27, No.3, 161-172.

40. Gilbert M. (1993). The behaviour of masonry arch bridges containing defects, PhD thesis, University of Manchester.

41. Gilbert M. and Melbourne C. (1994). Rigid-block analysis of masonry structures, The Structural Engineer, Vol. 72, No.21, 356-361.

42. Gilbert M. and Melbourne C. (1995). Analysis of multi-ring arch bridges, Arch Bridges, Thomas Telford, London, 225-238.

43. Melbourne C. and Gilbert M. (1995). The behaviour of Multi ring Brickwork Arch Bridges. The Structural Engineer 73, 3, 39-47.

44. Gilbert M. (1998). On the analysis of multi-ring brickwork arch bridges, Proc. 2nd International Arch Bridges Conference, Venice, Italy, 109-118.

45. Gilbert M. (2001). RING: 2D rigid-block analysis program for masonry arch bridges, Proc. 3rd International Arch Bridges Conference, Paris, 459-464.

46. Gilbert M. and Ahmed H.M. (2004). Developments to the RING masonry arch bridge analysis software, Proc. 4th International Arch Bridges Conference, Barcelona, 263-272.

47. Gilbert M., Casapulla C. and Ahmed H.M.(2006). Limit analysis of masonry block structures with non-associative frictional joints using linear programming. Computers and Structures. 84, 873-887.

48. Gilbert M. (2007). Limit analysis applied to masonry arch bridges: state-of-the-art and recent developments, Arch'07, Proc. 5th Int. Conf. Arch bridges, 13-28.

49. Gilbert M., Nguyen D.P. and Smith C.C. (2007).Computational limit analysis of soil-arch interaction in masonry arch bridges, Arch'07, Proc. 5th Int. Conf. Arch bridges, 633-640.

50. Begg D.W. and Fishwick R.J. (1995). Numerical analysis of rigid block structures including sliding, Proc 3rd Int. Symp. Comp. Meth. Struct. Mas., Portugal, eds. Middleton J. and Pande G. N.

51. Baggio C. and Trovalusci P. (1998). Limit analysis for no-tension and frictional three-dimensional discrete systems, Mechanics of Structures and Machines, 26, 3, 287-304.

52. Orduna A. and Lourenco P.B. (2001). Limit analysis as a tool for the simplified assessment of ancient masonry structures, Historical Constructions 2001-Possibilities of numerical and experimental techniques, Proc. 3rd International Seminar, Portugal, 511-520.

53. Hughes T.G., Burroughs P.O., Hee S.C. and Soms E. (2001). Spreadsheet based mechanism analysis, Computer methods in structural masonry-5, Proc. Fifth Int. Symp. Computer methods in structural masonry, 37-42.

54. Hughes T. G. (1995). Analysis and assessment of twin-span masonry arch bridges, Proc. Inst Civ. Engrs Structs & Bldgs, 110, Nov., 373-382.

55. Harvey B. and Maunder E. (2001). Thrust line analysis of complex masonry structures using spreadsheets, Historical Constructions 2001-Possibilities of numerical and experimental techniques, Proc. 3rd International Seminar, Portugal, 521-528.

56. Brencich A., Gambarotta L. and Sterpi E. (2007). Stochastic distribution of compressive strength: effects on the load carrying capacity of masonry arches, Arch'07, Proc. 5th Int. Conf. Arch bridges, 641-648.

57. Castigliano C.A.P. (1879). The theory of equilibrium of elastic systems and its applications. Torino: A.F.Negro.

58. Bridle R. J. and Hughes T. G. (1990). Energy method for arch bridge analysis. Proceedings - Institution of Civil Engineers, Part 2: Research and Theory 89, 375-385.

59. University of Wales College of Cardiff (1990). Cardiff/TRRL masonry arch assessment package (CTAP) user manual, Version 1.0.

60. Mott MacDonald Ltd. and University of Wales College of Cardiff (1990). Cardiff/TRRL masonry arch assessment package (CTAP) assessment manual, Version 1.0.

61. Garrity S.W., Toropov V.V. and Turovtsev G.V. (2001). An energy formulation for structural masonry and its applications to nonlinear analysis of arch bridges, Proc. 3rd International Arch Bridges Conference, Paris, 423-436.

62. Molins C. and Roca P. (1998). Capacity of masonry arches and spatial structures, Journal of Structural Engineering ASCE, 124,6 , 653-663.

63. Molins C. and Roca P. (1998). Load capacity of multi-arch masonry bridges, Proc. 2nd International Arch Bridges Conference, Venice, Italy, 213-222.

64. Molins C., Roca P. and Pujo A. (2001). Numerical simulation of the structural behaviour of single, multi-arch and open-spandrel arch masonry bridges, Proc. 3rd International Arch Bridges Conference, Paris, 523-530.

65. Molins C., Roca P. and Casas J. (2007). Structural analysis of a large span masonry arch bridges under railway loads, Arch'07, Proc. 5th Int. Conf. Arch bridges, 585-592.

66. Roca P., Molins C., Hughes T.G. and Sicilia C. (1998). Numerical simulation of experiments in arch bridges, Proc. 2nd International Arch Bridges Conference, Venice, Italy, 195-204.

67. Towler K. and Sawko F. (1982). Limit state behaviour of brickwork arches. 6th International Brick Masonry Conference. Rome, Italy.

68. Towler K. (1985). Applications of non-linear finite element codes to masonry arches. 2nd international Conference on Civil and Structural Engineering Computing. Edinburgh, Civil-Comp Press.

69. Sawko F. and Towler K. (1982). Structural behaviour of brick arches, Proc. ICE Structs&Bldgs, 110, 160-168.

70. Sawko F. and Towler K. (1985). A proposed numerical model for structural masonry, J. Brit. Mas. Soc., 5, 22-27.

71. Crisfield M. A. (1984). A finite element computer program for the analysis of arches. Crowthorne, Department of Transport, TRRL Report LR1115.

72. Crisfield M. A. (1985). Finite element and mechanism methods for the analysis of masonry and brickwork arches. Crowthorne, Department of Transport, TRRL Research Report 19.

73. Crisfield M. A. and Wills, J. (1986). Nonlinear analysis of concrete and masonry structures. Finite element methods for nonlinear problems. B. e. al. Berlin, Springer-Verlag.

74. Crisfield M. A. (1988). Numerical methods for the non-linear analysis of bridges. Computers and Structures, 30, No.3, 637-644.

75. Choo B. S., Coutie M. G., et al. (1991). Finite-element analysis of masonry arch bridges using tapered elements. Proceedings - Institution of Civil Engineers, Part 2: Research and Theory 91: 755-770.

76. Loo Y.C. and Yang Y. (1991). Cracking and failure analysis of masonry arch bridges. Journal of Structural Engineering 117(6): 1641-1659.

77. Boothby T. E., Domalik D. E., et al. (1998). Service load response of masonry arch bridges. Journal of Structural Engineering 124(1): 17-23.

78. Fanning P.J. and Boothby T.E. (2001). Nonlinear three dimensional simulations of service load tests on a 32m stone arch bridge in Ireland, Proc. 3rd International Arch Bridges Conference, Paris, 373-378.

79. Boothby T. E. and Roberts B. J. (2001). Transverse behaviour of masonry arch bridges. Structural Engineer 79(9): 21-26.

80. Fanning P. J., Boothby, T. E. et al. (2001). Longitudinal and transverse effects in masonry arch assessment. Construction and Building Materials 15: 51-60.

81. Fanning P. J. and Boothby T. E. (2001). Three-dimensional modelling and full-scale testing of stone arch bridges. Computers and Structures 79(29-30): 2645-2662.

82. Middleton J., Pande G.N., Kralj B. and Gazzola F. (1997). Three dimensional finite element analysis of masonry structures using homogenisation: application to arch structures, Computer methods in structural masonry-4, Proc. Fourth Int. Symp. Computer methods in structural masonry, 208-219.

83. Frunzio G., Monaco M. and Gesualdo A. (2001). 3D F.E.M. analysis of a Roman arch bridges, Historical Constructions 2001-Possibilities of numerical and experimental techniques, Proc. 3rd International Seminar, Portugal, 591-598.

84. Kaminski T. (2007).Three-dimensional modelling of masonry arch bridges based on predetermined, Arch'07, Proc. 5th Int. Conf. Arch bridges, 525-532.

85. Ng K. H., Fairfield C. A., et al. (1999). Finite-element analysis of masonry arch bridges. Proceedings of the Institution of Civil Engineers, Structures and Buildings 134(2): 119-127.

86. Loo Y. C. (1995). Collapse load analysis of masonry arch bridges. First International Conference on Arch Bridges, Bolton, UK, Thomas Telford.

87. Brencich A., De Francesco U. and Gambarotta L. (2001). Non linear elasto-plastic collapse analysis of multi-span masonry arch bridges, Proc. 3rd International Arch Bridges Conference, Paris, 513-522.

88. Brencich A., De Francesco U. and Gambarotta L. (2001). Elastic no tensile resistant - plastic analysis of masonry arch bridges as an extension of Castigliano's method. Proc 9th Canadian Masonry Symposium, Fredericton.

89. Brencich, A., De Francesco U. and Gambarotta, L. (2001). On the collapse mechanisms of multi-span masonry bridges, Computer methods in structural masonry-5, Proc. Fifth Int. Symp. Computer methods in structural masonry, 9-19.

90. Brencich A. and De Francesco U. (2004). Assessment of multispan masonry arch bridges. I: Simplified approach, Journal of Bridge Engineering, Vol. 9, No.6, 582-590.

91. Brencich A. and De Francesco U. (2004). Assessment of multispan masonry arch bridges. II: Simplified approach, Journal of Bridge Engineering, Vol. 9, No.6, 591-598.

92. Cavicchi A. and Gambarotta L. (2007).Load carrying capacity of masonry bridges: numerical evaluation of the influence of fill and spandrels, Arch'07, Proc. 5th Int. Conf. Arch bridges, 609-616.

93. Hughes T.G. and Baker M.J. (1997). A finite element model of arch ring behaviour, Computer methods in structural masonry-4, Proc. Fourth Int. Symp. Computer methods in structural masonry, 200-207.

94. Sililia C. (2000). Centrifuge and Finite Element Modelling of Pontypridd Bridge, Proc. 12th International Brick/Masonry Conference, Madrid, Spain,1707-1718.

95. Sicilia C., Hughes T.G. and Pande G.N. (2001). The capabilities of centrifuge modelling and homogenisation techniques for the in-service analysis of historical constructions, Historical Constructions 2001-Possibilities of numerical and experimental techniques, Proc. 3rd International Seminar, Portugal, 453-462.

96. Sicilia C. (2001). A study of 3-D masonry arch structures using centrifuge models and FE analysis. PhD thesis, University of Wales, Cardiff and Swansea.

97. Sicilia C., Pande G.N. and Hughes T.G. (2001). Numerical modelling of masonry arch bridges, Computer methods in structural masonry-5, Proc. Fifth Int. Symp. Computer methods in structural masonry, 20-27.

98. Sicilia C., Pande G. and Hughes T.G. (2001). A homogenisation-based FE model for the analysis of masonry arch bridges, Proc. 3rd International Arch Bridges Conference, Paris, 465-470.

99. Betti M., Drosopoulos G.A. and Stravroulakis G.E. (2007). On the collapse analysis of single span masonry /stone arch bridges with fill interaction, Arch'07, Proc. 5th Int. Conf. Arch bridges, 617-624.

100. Chiorino M.A., Icardi A.G., Rolando S.V. and Testa M.F. (2001). Mechanism and finite element failure analysis of Mosca's bridge, Proc. 3rd International Arch Bridges Conference, Paris, 365-372.

101. Oliveira D.V., Maruccio C. and Lourenco P.B. (2007). Numerical modelling of a load test on a masonry arch bridge, Arch'07, Proc. 5th Int. Conf. Arch bridges, 577-584.

102. Cucchiara C., Giambanco C. and Failla A. (2000). Numerical modelling of masonry arches via interface model, Proc. 12th International Brick/Masonry Conference, Madrid, Spain, 449-463.

103. Dede T. and Ural A. (2007). A finite element program for historical stone arch bridges, Arch'07, Proc. 5th Int. Conf. Arch bridges, 533-542.

104. Wang J. and Melbourne C. (2007). Finite element analyses of soil-structure interaction in masonry arch bridges, Arch'07, Proc. 5th Int. Conf. Arch bridges, 515-524.

105. Shin H.S. and Pande G.N. (2001). Intelligent finite elements in masonry research, Computer methods in structural masonry-5, Proc. Fifth Int. Symp. Computer methods in structural masonry, 221-230.

106. Lemos J.V. (1995). Assessment of the ultimate load of a masonry arch using discrete elements, Computer methods in structural masonry-3, Proc. Third Int. Symp. Computer methods in structural masonry, 294-302.

107. Lemos J.V. (1997). Discrete element modelling of the seismic Behaviour of stone masonry, Computer methods in structural masonry-4, Proc. Fourth Int. Symp. Computer methods in structural masonry, 220-227.

108. Rouxinol G.A.F., Providencia P. and Lemos J.V. (2007). Bridgemill Bridge bearing capacity assessment by a discrete element method, Arch'07, Proc. 5th Int. Conf. Arch bridges, 669-676.

109. Melbourne C. (2001). An overview of experimental masonry arch bridge research in the UK, Proc. 3rd International Arch Bridges Conference, Paris, 343-350.

110. Chettoe C. S. and Henderson W. (1957). Masonry arch bridges: a study. Proceeding of the Institution of Civil Engineers. 7(Aug.): 723-744.

111. Hendry A. W., Davies S.R. and Royles R. (1985). Test on stone masonry arch at Bridgemill-Girvan. Crowthorn, UK, Department of transport, TRRL Contractor Report 7.

112. Hendry A. W. (1986). Load test to collapse on a masonry arch bridge at Bargower, Strathclyde. Crowthorne, Department of Transport. TRRL Contractor Report 26.

113. Page J. (1987). Load tests to collapse on two arch bridges at Preston, Shropshire and Prestwood, Staffordshire. Crowthorne, Department of Transport. TRRL Research Report 110.

114. Page J. (1989). Load tests to collapse on two arch bridges at Strathmashie and Barlae. Crowthorne, Department of Transport. TRRL Research Report 201.

115. Page J. (1996). Load tests to collapse on two arch bridges at Torksey and Shinafoot. Crowthorne, Department of Transport. TRRL Research Report 159.

116. Harvey W. J. (1989). Load test on a full scale model four metre span masonry arch bridge. Crowthorne, Department of Transport. TRRL Contractor Report 155.

117. Melbourne C. and Walker P. J. (1989). Load test to collapse on a full scale model six metre span brick arch bridge. Crowthorne, Department of Transport. TRRL Contractor Report 189.

118. Fairfield C. A. and Ponniah D. A. (1994). The effect of fill buried model arches. Proceedings of the Institution of Civil Engineers, Engrs. Structs & Bldgs, 358-371.

119. Melbourne C. (1998). The collapse behaviour of a multi-span skewed brickwork and bridge, Proc. 2nd International Arch Bridges Conference, Venice, Italy, 289-294.

120. Roca P. and Molins C. (2004). Experiments on arch bridges, Proc. 4th International Arch Bridges Conference, Barcelona, 365-374.

121. Melbourne C. and Walker P. J. (1988). Load test to collapse of model brickwork masonry arches. 8th International Brick and Block Masonry Conference. New York, Elsevier Applied Science: 991-1002.

122. Melbourne C. (1990). The assessment of masonry arch bridges-the effects of defects. Proceedings of the First International Conference on Bridge Management.

123. Melbourne C., Begimgil M., et al. (1995). The load test to collapse of a 5M span brickwork arch bridge with tied spandrel walls. Arch bridges, Bolton, Tomas Telford.

124. Hughes T.G., Davies M.C.R. and Taunton P.R. (1998). The influence of soil and masonry type on the strength of masonry arch bridges, Proc. 2nd International Arch Bridges Conference, Venice, Italy, 321-330.

125. Hughes T.G., Davies M.C.R. and Taunton P.R. (1998). The small scale modelling of masonry arch bridges using a centrifuge, Proc. Inst. Civ. Engrs., Structures & Building Journal, 128, 49-58.

126. Hughes T.G. and Kitching N.(2000). Small scale testing of masonry, Proc. 12th International Brick/Masonry Conference, Madrid, Spain, 893-902.

127. Davies M.C.R., Hughes T.G. and Taunton P.R. (1997). Considerations in the small scale modelling of masonry arch bridges, Proc. 1st International Conference of Arch Bridges, Bolton, 365-374.

128. Burroughs P., Baralos P., Hughes T. and Davies M. (2000). Soil effects and the service loading of masonry arch bridges, Proc. 12th International Brick/Masonry Conference, Madrid, Spain, 341-351.

129. Taunton P.R. (1997). Centrifuge modelling of soil/masonry structure interaction, PhD thesis, Cardiff University.

130. Gilbert M. et al. (2006). An experimental study of soil-arch interaction in masonry bridges. IABMAS'06-Third International Conference on Bridge Maintenance, Safety and Management, 779-780.

131. Gilbert M. et al (2007). Small and large-scale experimental studies of soil-arch interaction in masonry bridges, Arch'07, Proc. 5th Int. Conf. Arch bridges, 381-388.

132. Burroughs P.O., Baralos P., Hughes T.G. and Davies M.C.R. (2001). Serviceability load effects on masonry arch brdiges, Proc. 3rd International Arch Bridges Conference, Paris, 397-402.

133. Page A. W. and Hendry A. W. (1988). Design rules for concentrated loads on masonry. The Structural Engineer, Vol 66, No 17/6, 273-281.

134. Hendry A. W. (1990). Masonry properties for assessing arch bridges. TRRL Contractor Report 244, Department of Transport.

135. Hatzini kolas M., Longworth J. and Warwaruk J. (1980). Failure modes of eccentrically loaded concrete block masonry walls. ACT Journal, July-August.

136. Pande G. N., Kralj B. and Middleton J. (1994). Analysis of the compressive strength of masonry given by the equation $fk=K(fb)\alpha(fm)\beta$. The Structural Engineer, Vol 7, No 1/4, 7-12.

137. Drysdale R. C. and Hamid A. A. (1982). Effect of eccentricity on the compressive strength of brickwork. J of the British Ceramic Society, Vol 30, 140-148.

138. Al Shebani M.M. and Sinha S.N. (2000). Cyclic compressive loading unloading curves of brick masonry. Structural Engineering and Mechanics, Vol 9, No 4, 375-382.

139. De Courcy J. W. (1988). Test of brick masonry models under cyclic compressive loading. Proc 8th Int Brick and Block Masonry Conference, Dublin, Vol 1, 395-405.

140. Macchi G. (1985). Behaviour of masonry under cyclic actions and seismic design. Proc 6th Int Brick Masonry Conference, Rome, LI-LXXIV.

141. Melbourne C. and Alnuaimi M.M. (2001). The behaviour of multi-ring brickwork arches subjected to cyclic loading, Proc. 3rd International Arch Bridges Conference, Paris, 243-248.

142. Melbourne C., Tomor A. and Wang J. (2004). Cyclic load capacity and endurance limit of multi-ring masonry arches, Proc. 4th International Arch Bridges Conference, Barcelona, 375-384.

143. Lemos J.V. (2001). Modelling the behaviour of a stone masonry arch structure under cyclic loads, Computer methods in structural masonry-5, Proc. Fifth Int. Symp. Computer methods in structural masonry, 101-108.

144. Brown G. (1997). A study of the effect of damage on the dynamic response of masonry arch bridges. PhD Thesis, department of Engineering, University of Reading.

145. Bintrim J.W., Laman J.A. and Boothby T.E. (1998). Dynamic testing of masonry arch bridges, Proc. 2nd International Arch Bridges Conference, Venice, Italy, 295-304.

146. Harvey B. and Houghton W. (2004). Dynamic effects in arch bridges-A field study, Proc. 4th International Arch Bridges Conference, Barcelona, 162-171.

147. Harvey W. J. (1991). Stability strength elasticity and thrust lines in masonry arches. The Structural Engineer, Vol 69, No 9.

148. Choo B. S. and Hogg V. (1995). Determination of the serviceability limit state for masonry arch bridges. Arch Bridges, Thomas Telford, London, 529-536.

149. Mola F. and Palermo A. (2001). Structural effects of constructional techniques on the service behaviour of arch bridges, Proc. 3rd International Arch Bridges Conference, Paris, 471-476.

150. Hughes T.G. and Wu L. (2007).The development of in-situ stress in masonry tunnels, Arch'07, Proc. 5th Int. Conf. Arch bridges, 389-396.

151. Wu L. (2006). Finite element analysis of creep in masonry tunnels, MSc thesis, Cardiff University.

152. Hogg V. and Choo B. S. (1994). Serviceability requirements for masonry arch bridges. Research Project Report, 1-31.

153. Melbourne C., Wang J. and Tomor A. (2007).A new masonry arch bridge assessment strategy (SMART), Arch'07, Proc. 5th Int. Conf. Arch bridges, 227-236.

154. Brook C. and Mullet P. (2004). Service load testing, numerical simulation and strengthening of masonry arch bridges, Proc. 4th International Arch Bridges Conference, Barcelona, 489-498.

155. Boussinesq J. (1885). Application des Potentiels à l'Etude de l'Equilibre et du Mouvement des Solides Elastiques, Gauthier-Villard, Paris, 235.

156. Roberts T. M., Hughes T. G. (2007). Modeling compressive strength of eccentrically loaded masonry, Procs ICE, Construction Materials, 160, CM1, 7-13.

157. Cardiff University (1991). The assessment of Llandeilo Bridge, bridge assessment report by Cardiff University.

158. Cardiff University (1991). The assessment of Seiont Bridge, bridge assessment report by Cardiff university.

159. Cardiff University (1991). The assessment of Westlinton and Egremont Bridge, bridge assessment report by Cardiff University.

160. Cardiff University (1991). The assessment of Carersws Bridge, bridge assessment report by Cardiff University.

161. Cardiff University (1991). The assessment of Ryhd Y Ferre Bridge, bridge assessment report by Cardiff University.

162. Cardiff University (1991). The assessment of Eden Bridge, bridge assessment report by Cardiff University.

163. Cardiff University (1991). The assessment of Hen-Efail, bridge assessment report by Cardiff University.

164. Cardiff University (1991). The assessment of Pont Factory, bridge assessment report by Cardiff University.

165. Cardiff University (1991). The assessment of Pont-Y-Clerc Bridge, bridge assessment report by Cardiff University.

166. Cardiff University (1991). The assessment of Furnace Bridge, bridge assessment report by Cardiff University.

167. Cardiff University (1991). The assessment of Trunk Road Bridge, bridge assessment report by Cardiff University.

168. World Wide Website (2007). List of Roman bridges, http://en.wikipedia.org /wiki/List_of_Roman_bridges, wikipedia.

169. World Wide Website (2006). Thames bridges, http://www.riverthames.co.uk /bridges/4689.htm, wikipedia.

170. John E.G. (1998). Simplified curve fitting using spreadsheet add-ins, Int. J. Engng Ed. Vol.14, 5, 375-380.

171. Roberts T. M., Hughes T. G. (2007). Modelling compressive strength of eccentrically loaded masonry, Procs ICE, Construction Materials, 160, CM1, 7-13.

172. Harvey B. (2005). Some problems with arch bridge assessment and potential solutions, Structural Engineer 84(3): 45-50.